

$\alpha$ -CAPTURE AND  $\alpha$ -ELASTIC SCATTERING ON P-NUCLEI TO PROBE THE  
HAUSER-FESHBACH FRAMEWORK

A Dissertation

Submitted to the Graduate School  
of the University of Notre Dame  
in Partial Fulfillment of the Requirements  
for the Degree of

Doctor of Philosophy

by

Annalia Palumbo

---

Michael Wiescher, Director

Graduate Program in Physics

Notre Dame, Indiana

July 2009

© Copyright by  
Annalia Palumbo  
2009  
All right reserved

$\alpha$ -CAPTURE AND  $\alpha$ -ELASTIC SCATTERING ON P-NUCLEI TO PROBE THE  
HAUSER FESHBACH FRAMEWORK

Abstract

by

Annalia Palumbo

The thirty five neutron deficient stable nuclei known as the p-nuclei are synthesized in a series of photodisintegration reactions of the  $(\gamma,n)$ ,  $(\gamma,p)$  and  $(\gamma,\alpha)$  type in a hot  $\gamma$ -flux environment.

Abundance calculations involve an extended network of about 20,000 nuclear reactions of almost 2000 nuclei. The bulk of these rates are calculated theoretically with the statistical Hauser Feshbach Model (HF Model). Of particular importance in the p-process modeling are the  $(\gamma,\alpha)$  branchings.

Even though in the astrophysical environment it is photodisintegration reactions that synthesize the p-nuclei, in the laboratory it is the inverse process that is generally measured. By detailed balance, it is possible to arrive at the relevant reactions. The experimental data for  $\alpha$ -capture reactions is scarce since at the p-process temperatures (2-3 GK), the  $\alpha$ -particle energies are typically of a few MeV and the corresponding cross

sections very small. In addition, the results show a significant deviation compared to the model predictions.

The HF cross sections are governed by transmission coefficients. These are extracted from an appropriate optical model potential (OMP). The  $\alpha$ -nucleus potential in particular is poorly known at low energies mainly due to the lack of relevant data. The observed inconsistencies between the predicted and measured ( $\alpha,\gamma$ ) rates may be due to problems with this  $\alpha$ -potential parameter.

To explore the applicability of the Hauser Feshbach model, to extend the experimental database of  $\alpha$ -capture reactions on p-nuclei, to test the global parameterizations that currently exist, and to constrain the  $\alpha$ -nucleus potential, the  $\alpha$ -capture cross section of  $^{106}\text{Cd}(\alpha,\gamma)^{110}\text{Sn}$  and the local  $\alpha$ -nucleus potentials of  $^{106}\text{Cd}$ ,  $^{118}\text{Sn}$ , and  $^{120,124,126,128,130}\text{Te}$  have been measured and extracted. The experiments have been carried out at the University of Notre Dame. The results are presented here.

*“Imagination is more important than knowledge”*

-Albert Einstein

## CONTENTS

FIGURES.....	v
TABLES .....	ix
CHAPTER 1 INTRODUCTION .....	1
1.1 Stellar burning phases.....	4
1.2 Supernova Type II.....	5
1.3 Nucleosynthesis of the heavy elements .....	5
1.3.1 The s-process .....	6
1.3.2 The r-process.....	7
1.3.3 The p-process.....	8
CHAPTER 2 ASTROPHYSICAL FRAMEWORK.....	13
2.1 The S-factor .....	13
2.2 Reaction rates and the Gamow window.....	14
2.3 Detailed Balance theorem.....	16
2.4 Input for Network Calculations .....	17
CHAPTER 3 THEORY .....	20
3.1 Overview: One Piece of the Puzzle .....	20
3.2 HF formalism.....	21
3.2.1 The potential dependence of the HF transmission coefficients .....	25
3.3 Optical Potential.....	26
3.3.1 Coulomb potential.....	26
3.3.2 Nuclear Potential.....	27
3.3.3 Double Folding Potential .....	30
3.4 Scattering Theory.....	33
3.4.1 Elastic scattering on a nuclear potential.....	34
3.4.2 Elastic scattering on a Coulomb field .....	36
CHAPTER 4 ACTIVATION EXPERIMENTS .....	38
4.1 Overview.....	38
4.1.1 Beamline set-up .....	41
4.1.2 Enriched $^{106}\text{Cd}$ and $^{120}\text{Te}$ targets.....	43
4.1.3 Counting Set-up .....	43
4.1.4 Electronics.....	45
4.1.5 Efficiency Determination.....	47
4.2 Activations .....	50

4.2.1 Cross Section calculation.....	54
4.3 Results.....	58
CHAPTER 5 ELASTIC SCATTERING EXPERIMENTS .....	66
5.1 $\alpha$ -scattering on p-nuclei.....	66
5.1.1 Enriched $^{120,124,126,128,130}\text{Te}$ , $^{118}\text{Sn}$ and $^{106}\text{Cd}$ targets.....	68
5.1.2 Detection System .....	69
5.1.3 Electronics.....	71
5.1.4 Solid Angle Determination .....	72
5.2 Data Analysis.....	75
CHAPTER 6 RESULTS AND CONCLUSIONS .....	80
6.1 $\alpha$ -nucleus potentials.....	80
6.1.1 Comparison to current Models.....	82
6.1.2 An improved $\alpha$ -nucleus global potential? .....	91
6.2 Optical Model Analysis .....	94
6.2.1 Cross Section Calculation.....	94
6.2.2 Local Potentials.....	97
6.2.3 Real part.....	99
6.2.4 Imaginary Part.....	104
6.2.5 Parameterizations.....	110
6.2.6 Comparison of Local Potentials.....	115
6.3 Astrophysical Implications .....	118
6.3.1 Extrapolation of the potentials.....	119
6.3.2 The S-factor of $^{106}\text{Cd}(\alpha,\gamma)^{110}\text{Sn}$ .....	120
6.3.3 The S-factor of $^{106}\text{Cd}(\alpha,n)^{109}\text{Sn}$ and $^{106}\text{Cd}(\alpha,p)^{109}\text{In}$ .....	122
6.3.4 The S-factor of $^{120}\text{Te}(\alpha,n)^{123}\text{Xe}$ .....	125
6.4 Local Potentials: A user's guide .....	128
6.5 Resonances.....	130
CHAPTER 7 CONCLUSION AND OUTLOOK.....	131
APPENDIX A TARGET INVENTORY .....	133
APPENDIX B SUMMING CORRECTIONS .....	134
APPENDIX C NORMALIZED CROSS SECTIONS.....	140
APPENDIX D GLOBAL POTENTIALS .....	147
APPENDIX E LOCAL POTENTIALS.....	180
REFERENCES .....	213

## FIGURES

- Figure 1.1 Schematic representation of the neutron capture processes in astrophysical scenarios. The s–process path along the valley of stability is marked by the red solid arrows. Once an unstable nucleus is created within this process after several  $(n,\gamma)$  reactions, because of the low neutron capture rate, it decays back to stability. During r–process nucleosynthesis, after several successive neutron capture reactions, very neutron rich species (thick dashed pink line) are produced. Once the neutron flux disappears, these nuclei  $\beta^-$  decay (dotted pink arrows) back to stability [10]. ..... 7
- Figure 1.2 Abundance distribution in the solar system above the iron peak normalized to  $\text{Si} = 10^6$  (bold line). Elements created solely within one of the described neutron capture (s–only, open squares; r–only, filled circles) or photodisintegration (p–only, open circles) processes are also displayed. It is possible to observe the different structures originating from each of the neutron capture processes [10]. 10
- Figure 1.3 P-Process abundance evolution for a 25 solar mass star considering 14 different mass layers of the O-Ne burning zone [19]. ..... 12
- Figure 3.1  $\chi^2_{red}$  in the study of the different potential families for the reaction  $^{89}\text{Y}(\alpha,\alpha)^{89}\text{Y}$  at  $E \approx 19$  MeV. The best description of the experimental cross sections is observed for the families 3, 4, and 5 [10]. ..... 30
- Figure 3.2 Schematic representation of the double folding parameterization [10]. ..... 31
- Figure 4.1 The  $p$ -process reaction flow in the Cd-Sn region. For simplicity, only even-even isotopes are shown, hence the  $(\gamma,n)$  arrow indicates two subsequent neutron emissions. Stable isotopes are indicated by bold squares. The solid arrows show the main reaction flow path, whereas dashed arrows indicate weaker branchings [63,64]. ..... 39
- Figure 4.2: The  $\alpha$ -induced reactions on  $^{106}\text{Cd}$  and the decay of the reaction products [64]. ..... 40
- Figure 4.3 A collimated Si surface barrier detector was mounted at  $135^\circ$  with respect to the beam axis to monitor the stability of the target [65,66]. ..... 42
- Figure 4.4 Two clover detectors placed in close geometry to measure offline  $\gamma$ -activity 44

Figure 4.5 Schematic view of the inside of the clover counting set-up. The Pb is lined with 3 mm Cu plates [65].	44
Figure 4.6 Electronics set-up for activation measurements.	47
Figure 4.7 Photopeak efficiency determined from $^{152}\text{Eu}$ .	49
Figure 4.8 The $^{106}\text{Cd}(\alpha,\gamma)^{110}\text{Sn}$ reaction at the lowest measured energy.	51
Figure 4.9 The $^{106}\text{Cd} + \alpha$ reactions that are open at $E_{\text{lab}} = 11.5$ MeV.	52
Figure 4.10 Activation spectrum of $^{120}\text{Te}(\alpha,n)^{123}\text{Xe}$ at $E_{\text{lab}} = 10.5$ MeV.	53
Figure 4.11 Decay scheme for $^{106}\text{Cd}(\alpha,\gamma)^{110}\text{Sn}$	55
Figure 4.12 Simplified decay scheme of the $^{120}\text{Te}(\alpha,n)^{123}\text{Xe}$ reaction (the two dominant $\gamma$ -transitions used in the analysis are shown).	55
Figure 4.13 Simplified decay scheme of $^{106}\text{Cd}(\alpha,p)^{109}\text{In}$ .	58
Figure 4.14 Cross Section and S-factor of $^{106}\text{Cd}(\alpha,\gamma)^{110}\text{Sn}$	63
Figure 4.15 Cross Section and S factor of $^{106}\text{Cd}(\alpha,p)^{109}\text{In}$	64
Figure 4.16 Cross Section and S factor of $^{120}\text{Te}(\alpha,n)^{123}\text{Xe}$ . Results using the 149 keV $\gamma$ -transition are shown.	65
Figure 5.1 Inside view of the scattering chamber. The left view shows the Si pin diode detectors mounted on a rotatable table and the two fixed monitor detectors. The right view shows the moveable (both transitional and rotational) target ladder...	70
Figure 5.2 Forward (left) and Backward (right) orientations of the detectors and targets.	71
Figure 5.3 Electronics set-up for elastic scattering measurements.	73
Figure 5.4 Ratio of the diameters of the collimators obtained from the offline method versus the online method (1 <sup>st</sup> two methods). A deviation of 1% is obtained.	74
Figure 5.5 Spectra of $^{120}\text{Te}$ at the highest energy and most backward angle and lowest energy and most forward angle.	76
Figure 6.1 Mass dependence (arising from the difference in neutron number) of the experimental cross section of $^{112}\text{Sn}$ (p-nucleus) versus $^{124}\text{Sn}$ compared to the cross section obtained using standard global potentials [37]. The Rutherford normalized cross sections are shown as a function of center-of-mass angle.	83

Figure 6.2 Mass dependence (due to neutron number) of $^{120}\text{Te}/^{130}\text{Te}$ at 17 MeV (left) and 27 MeV (right) compared to the cross section obtained from standard potentials [86,89,90,91,92,94].....	85
Figure 6.3 Mass dependence (due to neutron number) of $^{120}\text{Te}/^{130}\text{Te}$ at 19 MeV (left) and 22 MeV (right) compared to the cross section obtained from standard potentials [86,89,90,91,92,94].....	86
Figure 6.4 The Rutherford normalized cross section of $^{120}\text{Te}$ (top) and $^{130}\text{Te}$ (bottom) is compared to the global potentials of [86,89,90,91,92,94]. The Avrigeanu potential gives a very accurate representation at low energies but at the high energy it overestimates the diffraction pattern.....	88
Figure 6.6 The Rutherford normalized cross section of $^{106}\text{Cd}$ and $^{118}\text{Sn}$ is compared to the global potentials of [86,89,90,91,92,94]. The Avrigeanu potential reproduces the scattering data at 17 MeV but it clearly overestimates it at 27 MeV.....	90
Figure 6.7 Rutherford normalized cross section of $^{106}\text{Cd}(\alpha,\alpha)^{106}\text{Cd}$ at 27 MeV compared to a modified Avrigeanu potential. The potential with the matching McFadden/Satchler diffuseness parameter in the real part (0.52) matches the amplitude of the diffraction pattern. The red line shows a modification of the Avrigeanu potential by assuming a value of 1.22 for the real radius. Here the diffraction pattern is damped. Both overestimate the cross section in magnitude. ....	92
Figure 6.8 Rutherford normalized cross section of $^{106}\text{Cd}(\alpha,\alpha)^{106}\text{Cd}$ at 22 and 24.5 MeV compared to a modified Avrigeanu potential (diffuseness parameter in the real part (0.52)). ....	93
Figure 6.9 Amplitude and phase shift (as a function of the number of partial waves) derived in an S matrix calculation performed for $^{120}\text{Te}$ at a bombarding energy of 27 MeV. ....	96
Figure 6.10 Comparison of the Rutherford normalized cross section calculated from the local potential of $^{126}\text{Te}$ at all energies to the experimental data (no normalization has been applied).....	97
Figure 6.11 Rutherford normalized cross section calculated from the local potential of $^{106}\text{Cd}$ at 24.5 MeV. Shown is the 4% normalization applied to the cross section derived from the local potential (illustrative purposes only). The first few points fall off of the unnormalized curve but the rest are unaffected.....	98
Figure 6.12 $\lambda_{R,0}$ parameterized as a function of center-of-mass energy for $^{120}\text{Te}$ . ....	101
Figure 6.13 $W_V$ and $a_V$ parameterized as a function of center-of-mass energy for $^{130}\text{Te}$ . ....	106

Figure 6.14 Volume integral values ( $J_R$ ) from previous studies on semi-magic and doubly magic nuclei.....	111
Figure 6.15 Strength of the real potential for all isotopes of this study.....	111
Figure 6.16 The BR parameterization applied to $^{128,130}\text{Te}$ .....	113
Figure 6.17 S-factor of $^{106}\text{Cd}(\alpha,\gamma)$ using the local potentials of $^{106}\text{Cd}$ obtained in study along with the values obtained from the standard settings of NON-SMOKER [77,78,79,110,111].....	122
Figure 6.18 Experimental S-factors of $^{106}\text{Cd}(\alpha,n)^{109}\text{Sn}$ and $^{106}\text{Cd}(\alpha,p)^{109}\text{In}$ compared to the theoretical S-factor values obtained from the local potential and NON-SMOKER [77,78,79,110,111]. .....	124
Figure 6.19 S-factor of $^{120}\text{Te}(\alpha,n)^{123}\text{Xe}$ preliminary experimental values compared to the theoretical S-factors values derived from the $^{120}\text{Te}$ local potential considered in this study and the global potential of McFadden/Satchler (standard settings of NON-SMOKER) [77,78,79,86,110,111]. The values are those of the 149 keV $\gamma$ -line.....	126
Figure B1 Decay scheme defining some of the parameters used in coincidence summing.....	134

## TABLES

Table 1.1 List of all 35 $p$ -nuclei .....	9
Table 4.1 Decay parameters of $^{106}\text{Cd}+\alpha$ reaction products and of $^{120}\text{Te}(\alpha,n)^{123}\text{Xe}$ .....	54
Table 4.2 Cross Section and S-Factor of $^{106}\text{Cd}(\alpha,\gamma)^{110}\text{Sn}$ .....	60
Table 4.3 Cross Section and S-Factor of $^{106}\text{Cd}(\alpha,p)^{109}\text{In}$ .....	61
Table 4.4 Cross Section and S-factor of $^{120}\text{Te}(\alpha,n)^{123}\text{Xe}$ .....	61
Table 5.1 Enrichment.....	67
Table 6.1 Nuclear properties of the nuclei from this study.....	81
Table 6.2 Double folding parameterization results from fits for all isotopes. ....	100
Table 6.3 Values for the parameterization of $\lambda$ .....	101
Table 6.4 Values of the parameterization of the real part for $^{106}\text{Cd}$ from 22 - 27 MeV	102
Table 6.5 Value of $J_R$ for $\lambda = w = 1$ .....	103
Table 6.6 Values of $J_R$ ( $\lambda = w = 1$ ) for all previous studied nuclei (with exception of $^{112}\text{Sn}$ which was unlisted). ....	104
Table 6.7 The surface to volume contribution of the imaginary potential for all isotopes. ....	105
Table 6.8 Imaginary Parameters for $^{106}\text{Cd}$ , $^{120}\text{Te}$ , $^{126}\text{Te}$ .....	107
Table 6.9 Imaginary geometry terms parameterized as a function of energy.....	108
Table 6.10 Imaginary geometry parameters and width ( $w$ ) for $^{112,124}\text{Sn}$ [39].....	109
Table 6.11 Parameterization of the depth and diffuseness of the surface terms as a function of neutron number .....	109
Table 6.12 Values for the BR parameterization applied to $^{128,130}\text{Te}$ .....	112

Table 6.13 Relationship of volume depth ( $W_V$ ) to neutron number (* is a closed subshell).....	114
Table 6.14 Solutions of $^{106}\text{Cd}(\alpha,\alpha)^{106}\text{Cd}$ obtained from this study and [81] .....	116
Table 6.15 Parameters of the real and imaginary part of the local potentials derived from this study and [81].....	117
Table 6.16 Values of the strength potential of the real part at the approximate effective burning temperatures of the Gamow window for the $^{106}\text{Cd}+\alpha$ and $^{120}\text{Te}+\alpha$ systems.....	120
Table 6.17 $^{120}\text{Te}(\alpha,n)^{123}\text{I}$ : experimental S-factor compared to NON-SMOKER .....	127
Table 6.18 Local potential parameters.....	129
Table B1 Photopeak efficiency derived from $^{152}\text{Eu}$ .....	137
Table B2 Photopeak efficiency derived from $^{133}\text{Ba}$ .....	138
Table B3 Photopeak efficiency values derived from the log-log fit using $^{152}\text{Eu}$ .....	139

# CHAPTER 1

## INTRODUCTION

*“In principio erat Verbum”*

To understand the lure of astrophysics, one has only to gaze up at the sky on a dark night and see the illumination offered by the stars. It is this celestial brilliance that inspires so many of us but that seems to touch a chord of longing deep within an astrophysicist. This longing is not only to gaze but to understand the mechanism responsible for this brilliance. A nuclear physicist, on the other hand, expresses their passion through precision. Unlocking the secrets of the atomic nuclei and their interaction with one another requires dedication and efficiency and the knowledge therein gives power to those willing to probe its mysteries. But a nuclear astrophysicist is not contented by staying within one realm. Their great ambition drives them, step by agonizing step, to bring the celestial to earth. The heavens are the inspiration but the laboratory is the playing field.

Saying that the goal of nuclear astrophysics is to understand how the heavy elements formed is true, but it is also trite. As Carl Sagan said: “We are all made of star stuff”. Nuclear astrophysics is about understanding our origins. It is not about starting at

the very beginning where conditions were very dense, hot, totally alien and very difficult to probe. Instead, we start at a place that seems to be more familiar, a place where we trust the extrapolation to the present. It may not be primordial nucleosynthesis but it still is nucleosynthesis and placing it on a terrestrial plane of existence is revolutionary.

Thomas Kuhn tells us “scientific advancement is not evolutionary, but rather is a series of peaceful interludes punctuated by intellectually violent revolutions, and in those revolutions one conceptual world view is replaced by another.” Here then the grand ambition of the nuclear astrophysicist is revealed - a paradigm shift. Understanding the formation of the elements is not then just an esoteric pastime but rather it is about the possible application of a faraway nucleosynthesis process for practical purposes.

Some of the first questions addressed in this field were “How does the Sun shine?” “What are its working mechanisms?”. This question was answered in the 1950’s by Burbidge, Burbidge, Fowler, and Hoyle [1] and simultaneously by Cameron [2] who put it in the framework of a nuclear physics perspective (fusion reactions between protons were the Sun’s main energy source). In addition, they postulated how all of the elements we find in nature were produced. At first, it seemed that the picture proposed by [1,2] was capable of explaining the origin and abundance of almost all stable (and long-living unstable) isotopes in our Solar System. Network calculations of the nucleosynthesis path of the abundance distribution as a function of time showed the necessity of improving the descriptions of the different astrophysical processes and the astrophysical sites of synthesis.

Unfortunately, many of the reaction rates (average value of the product of the relative velocity of the interacting nuclei times their cross section) necessary to accurately model the synthesis path of the p-process are experimentally unknown and they must rely on theoretical estimates. These rates, which are necessary inputs into the network simulation, are mainly determined via what is known as the statistical model of compound nuclear reactions. Of particular importance for the determination of the  $(\gamma, \alpha)$  rates is the  $\alpha$ -nucleus optical potential. Its relevance, application, and determination will be discussed in the forthcoming chapters.

## 1.1 Stellar burning phases

The first stage of a star's life cycle involves the burning of hydrogen in thermal and hydrostatic equilibrium. This can proceed via either the pp chain or the CNO cycle. At low temperatures, it is the pp chain that is mainly responsible for the synthesis. Higher temperatures allow nuclei with higher coulomb barriers to be penetrated and hence the CNO cycle becomes more efficient for temperatures in excess of 18 MK [3,4].

When hydrogen burning ceases in the center of the star, the helium core contracts under gravity and grows hotter. This increased temperature promotes hydrogen burning in a shell surrounding the core. As this hydrogen burning continues in the shell, more helium is produced and deposited onto a helium core which becomes hotter and denser. Helium burning is severely hindered by the absence of stable nuclei with mass 5 and mass 8. The only way forward is for three alpha particles to fuse in a two step reaction to form  $^{12}\text{C}$ . As helium is consumed in the center of the star, helium burning migrates to a shell surrounding a central core of C and O, leading to an onion-like structure for the star in which there is an outer hydrogen burning layer, an inner helium burning layer and a core of C and O.

For stars with masses greater than about 8-10 solar masses, carbon begins to burn [5]. The most likely reactions in carbon burning are  $^{12}\text{C}(^{12}\text{C},\text{p})^{23}\text{Na}$  and  $^{12}\text{C}(^{12}\text{C},\alpha)^{20}\text{Ne}$ . At the end of core carbon burning, the core consists mainly of  $^{16}\text{O}$ ,  $^{20}\text{Ne}$ ,  $^{23}\text{Na}$ , and  $^{24}\text{Mg}$  (most of the  $^{12}\text{C}$  nuclei have been consumed). Neon burning will proceed primarily through the photodisintegration reaction:  $^{20}\text{Ne}(\gamma,\alpha)^{16}\text{O}$ . The  $\alpha$  particles that are liberated in the primary reaction will be captured by the remaining  $^{20}\text{Ne}$  and form  $^{24}\text{Mg}$ .

After the neon fuel has been consumed, the  $^{16}\text{O}(^{16}\text{O},\alpha)^{28}\text{Si}$  reaction is the most likely to occur since it has the lowest Coulomb barrier. The last burning phase is Si burning. The nucleosynthesis up to the Fe/Ni region occurs via photodisintegrations of lower mass nuclei and by alpha captures liberated from the  $^{28}\text{Si}(\gamma,\alpha)^{24}\text{Mg}$  reaction.

## 1.2 Supernova Type II

Due to the formation of an envelope over the central region after the end of each burning phase, the star looks like an onion with various skins of different compositions. The internal pressure cannot halt the gravitational collapse and the core shrinks. As the temperature increases, the iron group nuclei are photodisintegrated into neutrons and protons with the latter capturing free electrons ( $e + p \rightarrow \nu_e + n$ ). The neutrinos escape and the decrease of electron pressure decreases the internal pressure and the core continues to collapse to a nucleus of neutrons ( $\rho \approx 10^{14} \text{ g / cm}^3$ ). The collapse is thus halted but the outer layers are still falling and they will rebound forming a shock front. The shockwave will again induce burning in the outer layers (C, Ne, O, Si) and will create p-nuclei in the O-Ne layer (Section 1.3.3).

## 1.3 Nucleosynthesis of the heavy elements

Since the binding energy per nucleon reaches a peak in the Fe/Ni region, further fusion processes cannot take place due to the high Coulomb barrier. Current astrophysical models account for the production of the majority of the nuclear isotopes beyond the  $A \approx 56$  region by neutron captures (the s- and r-process).

### 1.3.1 The s-process

The slow-neutron capture process (s-process) occurs at relatively low neutron densities ( $10^6 \text{ cm}^{-3}$ ) and intermediate temperatures ( $T \approx 1\text{-}3 \times 10^8 \text{ K}$ ). Under these conditions, the rate of neutron capture is slow relative to the rate of  $\beta^-$  decay. Approximately half of the isotopes heavier than iron are produced in this way.

The synthesis takes place during the Hydrogen-Helium intershell burning phase of Asymptotic Giant Branch (AGB) stars at relatively low temperatures ( $1 \times 10^8 \text{ K}$ ) [6]. During this phase, the mean neutron capture rate is only about one per year (this is what keeps the path close to the valley of stability). Fig.1 shows a schematic representation of the s-process. The main neutron source component comes from the  $^{13}\text{C}(\alpha, n)^{16}\text{O}$  reaction while there is an additional neutron contribution that comes from  $^{22}\text{Ne}(\alpha, n)^{25}\text{Mg}$ . In addition, this reaction is the main neutron source driving the synthesis of nuclides in the  $A \approx 60\text{-}90$  mass range [7,8]. This happens during the Helium core burning phase of massive stars at higher temperatures ( $T \approx 3 \times 10^8 \text{ K}$ ) [7]. The size of the  $^{22}\text{Ne}(\alpha, n)^{25}\text{Mg}$  reaction rate used in stellar models can have a significant effect on the predicted abundances of the p isotopes (Section 1.3.3) [9].

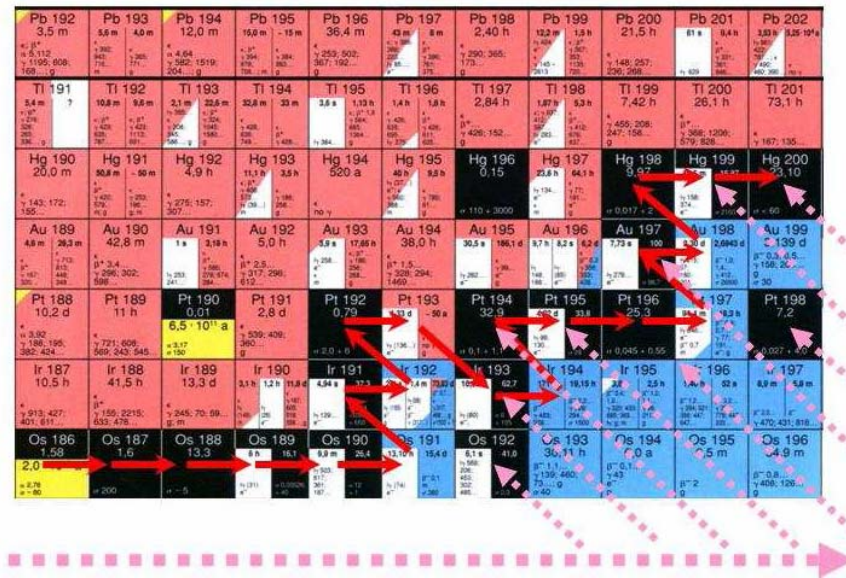


Figure 1.1 Schematic representation of the neutron capture processes in astrophysical scenarios. The s–process path along the valley of stability is marked by the red solid arrows. Once an unstable nucleus is created within this process after several  $(n,\gamma)$  reactions, because of the low neutron capture rate, it decays back to stability. During r–process nucleosynthesis, after several successive neutron capture reactions, very neutron rich species (thick dashed pink line) are produced. Once the neutron flux disappears, these nuclei  $\beta^-$  decay (dotted pink arrows) back to stability [10].

### 1.3.2 The r-process

Compared to the s-process, the time scale for the rapid neutron capture process (r-process) is on the order of a few seconds. In such an intense neutron flux ( $N_n \approx 10^{21}/\text{cm}^3$ ), very neutron rich species are created. A series of neutron captures will occur until an equilibrium is reached between  $(\gamma,n)$  and  $(n,\gamma)$  reactions (Fig. 1.1). At this point, there is an accumulation of material until a  $\beta^-$  decay occurs (moving up to the next higher  $Z$ ), and the process repeats. Equilibrium is generally established for nuclei with

large binding energies (neutron separation energy). A longer waiting point half life corresponds to a greater abundance of these isotopes. An enhancement in the production of nuclei with closed shells is observed.

### 1.3.3 The p-process

The 35 stable neutron deficient nuclei ranging from  $^{74}\text{Se}$  to  $^{196}\text{Hg}$  are shielded from neutron capture processes and require a different mechanism of production. These are the p-nuclei (they contain more protons relative to other stable isotopes of the same element). A list of the p-nuclei and their associated abundances is given in Table 1.1. The solar system abundances of the p-nuclei are displayed in Fig. 1.2 where they are compared to abundances that originate from the s- and r- processes. They are typically smaller by a factor of 100. The abundance pattern for these proton-rich nuclei is similar to that of the neutron-rich isotopes, as enhancements in the abundance of those nuclei with closed nuclear shells ( $^{92}\text{Mo}$ ,  $N=50$ ; Sn isotopes,  $Z=50$ ;  $^{144}\text{Sm}$ ,  $N=82$ ) are evident.

Burbidge et al. [1] proposed a process in which  $(p,\gamma)$  reactions or  $(\gamma,n)$  reactions were responsible for the synthesis of a number of proton rich isotopes. Very high temperatures ( $T_9 = 2-3$ ) and proton densities ( $\geq 10^2 \text{ g/cm}^3$ ) are required in this scenario. Due to the increasing Coulomb barrier for heavy nuclei, proton capture is negligible for nuclei with  $Z \geq 54$  [11]. For the heavier species, nucleosynthesis works mainly via photodisintegration reactions, producing very proton rich nuclei via  $(\gamma,n)$ ,  $(\gamma,\alpha)$  and  $(\gamma,p)$  reactions.

TABLE 1.1  
LIST OF ALL 35 *p*-NUCLEI

Nucleus	Abundance [Si=10 <sup>6</sup> ]	Isotopic abundance(%)	Nucleus	Abundance [Si=10 <sup>6</sup> ]	Isotopic abundance(%)
<sup>74</sup> Se	0.55	0.88	<sup>132</sup> Ba	4.53x10 <sup>-3</sup>	0.1
<sup>78</sup> Kr	0.153	0.34	<sup>138</sup> La	4.09x10 <sup>-4</sup>	0.09
<sup>84</sup> Sr	0.132	0.56	<sup>136</sup> Ce	2.16x10 <sup>-3</sup>	0.19
<sup>92</sup> Mo	0.378	14.84	<sup>138</sup> Ce	2.84x10 <sup>-3</sup>	0.25
<sup>94</sup> Mo	0.236	9.25	<sup>144</sup> Sm	8.0x10 <sup>-3</sup>	3.1
<sup>96</sup> Ru	0.103	5.52	<sup>152</sup> Gd	6.6x10 <sup>-4</sup>	0.2
<sup>98</sup> Ru	0.035	1.88	<sup>156</sup> Dy	2.21x10 <sup>-4</sup>	0.06
<sup>102</sup> Pd	0.0142	1.02	<sup>158</sup> Dy	3.78x10 <sup>-4</sup>	0.1
<sup>106</sup> Cd	0.0201	1.25	<sup>162</sup> Er	3.51x10 <sup>-4</sup>	0.14
<sup>108</sup> Cd	0.0143	0.89	<sup>164</sup> Er	4.04x10 <sup>-3</sup>	1.61
<sup>113</sup> In	7.9x10 <sup>-3</sup>	4.3	<sup>168</sup> Yb	3.22x10 <sup>-4</sup>	0.13
<sup>112</sup> Sn	0.0372	0.97	<sup>174</sup> Hf	2.49x10 <sup>-4</sup>	0.16
<sup>114</sup> Sn	0.0252	0.66	<sup>180</sup> Ta	2.48x10 <sup>-6</sup>	0.01
<sup>115</sup> Sn	0.0129	0.34	<sup>180</sup> W	1.73x10 <sup>-4</sup>	0.13
<sup>120</sup> Te	4.3x10 <sup>-3</sup>	0.09	<sup>184</sup> Os	1.22x10 <sup>-4</sup>	0.02
<sup>124</sup> Xe	5.71x10 <sup>-3</sup>	0.12	<sup>190</sup> Pt	1.7x10 <sup>-4</sup>	0.01
<sup>126</sup> Xe	5.09x10 <sup>-3</sup>	0.11	<sup>196</sup> Hg	5.2x10 <sup>-4</sup>	0.15
<sup>130</sup> Ba	4.76x10 <sup>-3</sup>	0.11			

The solar abundance (normalized to Si = 10<sup>6</sup>) data are taken from [12].

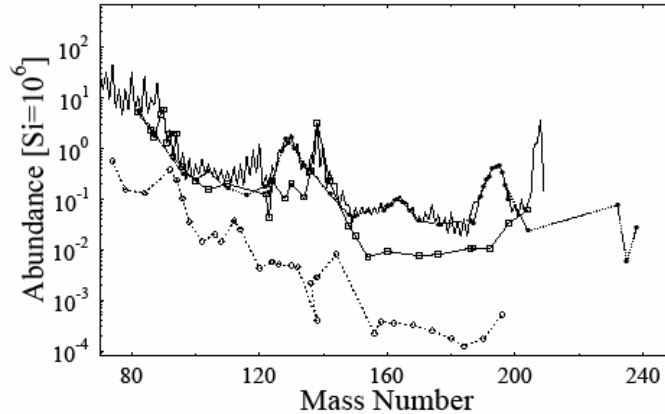


Figure 1.2 Abundance distribution in the solar system above the iron peak normalized to  $\text{Si} = 10^6$  (bold line). Elements created solely within one of the described neutron capture (s-only, open squares; r-only, filled circles) or photodisintegration (p-only, open circles) processes are also displayed. It is possible to observe the different structures originating from each of the neutron capture processes [10].

The currently favored astrophysical site for p-process nucleosynthesis is a Type II supernova [13,14,15,16]. The shock front heats the O-Ne layer to temperatures of 2-3 GK which is sufficient for photodisintegrations to occur (temperatures of 1.5 GK are required). S-process seed [17] is converted by subsequent  $(\gamma, n)$  reactions toward the neutron-deficient region. As the flow moves along the isotopic chain, the neutron separation energy increases. When the  $(\gamma, p)$  or  $(\gamma, \alpha)$  reaction dominates over the  $(\gamma, n)$  reaction (the branch point is satisfied by the decay constants:  $\lambda_{\gamma p} + \lambda_{\gamma \alpha} > \lambda_{\gamma n}$ ) [18], the flow will then branch off to an isotope of a different element. Once the photon bath disappears, some  $\beta$ -decays,  $e^-$  captures, or  $(n, \gamma)$  reactions can possibly complete the nuclear flow [13].

An accurate determination of the  $(\gamma,\alpha)$ ,  $(\gamma,p)$  and  $(\gamma,n)$  reaction rates is extremely important for nuclei at which the p-process path branches. Figure 1.3 shows the abundance evolution in 14 different O-Ne layers for a 25 solar mass star during 1s of the explosion [19]. The general trend is that in the higher mass region ( $A = 140$ ), a global variation of the  $(\alpha,\gamma)$  and  $(\gamma,\alpha)$  rates has a very strong impact on the p-abundances [19]. In addition, the s-process component  $^{22}\text{Ne}(\alpha,n)$  strongly enhances the p-process seed abundances in the  $A \approx 60-90$  region [9]. Most of the p-nuclei are reproduced to within a factor of 3 of their solar system values; however, a number of discrepancies exist. Mainly the underproduction of the light p-nuclei:  $^{92}\text{Mo}$ ,  $^{94}\text{Mo}$ ,  $^{96}\text{Ru}$ , and  $^{98}\text{Ru}$ . There has been some speculation that the  $^{22}\text{Ne}(\alpha,n)$  source might be more efficient than previously thought which would cause a substantial enhancement in the abundances of  $^{92}\text{Mo}$  and  $^{96}\text{Ru}$  [9]; however, this would result in an enormous overproduction of the s-process nuclei. In addition to  $^{92,94}\text{Mo}$  and  $^{96,98}\text{Ru}$ ,  $^{113}\text{In}$ ,  $^{115}\text{Sn}$  and  $^{138}\text{La}$  are also underproduced in most calculations [13,20,21]. Several other astrophysical sites have been considered for the production of p-nuclei, including supernovae of Type Ia [22]; however, none of these other sites solves the underproduction problem.

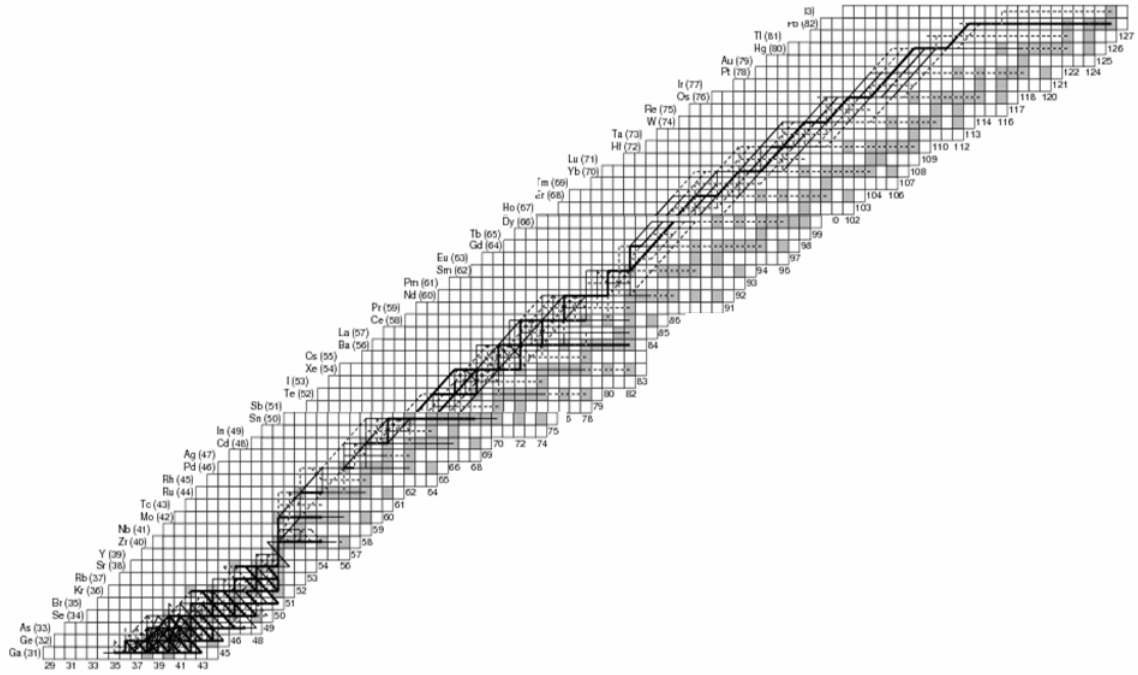


Figure 1.3 P-Process abundance evolution for a 25 solar mass star considering 14 different mass layers of the O-Ne burning zone [19].

## CHAPTER 2

### ASTROPHYSICAL FRAMEWORK

Nuclear reactions explain the bulk of the solar-system abundance distribution; however it is important to understand which measurements have an astrophysical relevance. To transform from the pure nuclear physics regime to the astrophysical realm, in particular to model the abundance distribution, a framework must be established.

#### 2.1 The S-factor

In a nuclear reaction, a projectile will penetrate a target nucleus (by tunneling through the Coulomb barrier) in order to form a compound nucleus. The probability that the particle penetrates the barrier is:

$$P = \exp(-2\pi\eta) \quad (2.1)$$

The quantity  $\eta$  is the Sommerfeld parameter and is defined by:

$$\eta = \frac{Z_p Z_T e^2}{\hbar v} \approx 0.1575 Z_p Z_T \sqrt{\frac{\mu \cdot \text{MeV}}{E}} \quad (2.2)$$

where  $Z_p \cdot e$  and  $Z_T \cdot e$  are the charges of the projectile and target;  $v$  is the relative velocity between projectile and target,  $\mu$  is the reduced mass and  $E$  is the center-of-mass energy (in MeV).

The cross section  $\sigma(E)$  for charged-particle-induced reactions, which is proportional to the tunneling probability  $P$ , is usually expressed in terms of the astrophysical S-factor:

$$S(E) = \sigma(E) E \exp(2\pi\eta) \quad (2.3)$$

This expression is valid for nonresonant reactions only.

## 2.2 Reaction rates and the Gamow window

The reaction rate  $\langle\sigma v\rangle$  per particle pair under astrophysical conditions involves the Maxwell-Boltzmann velocity distribution of the particles  $\phi(v)$ , the relative particle velocity  $v$  and the corresponding reaction cross section  $\sigma(v)$ :

$$\langle\sigma v\rangle = \int \phi(v) \cdot \sigma(v) \cdot v dv \quad (2.4)$$

Using the center-of-mass energy  $E = \frac{1}{2} \mu v^2$  and the Maxwell-Boltzmann transformed

distribution  $\phi(v) = 4\pi v^2 \left(\frac{\mu}{2\pi kT}\right)^2 \exp\left(-\frac{\mu v^2}{2kT}\right)$ , the reaction rate per particle pair can be

written in the form:

$$\langle\sigma v\rangle = \left(\frac{8}{\pi\mu}\right)^{1/2} \frac{1}{(kT)^{3/2}} \int_0^\infty \sigma(E) \cdot E \cdot \exp\left(-\frac{E}{kT}\right) dE \quad (2.5)$$

By inserting the definition of the S-factor (equation 2.3) into equation 2.5 it is possible to express the reaction rate per particle pair as:

$$\langle \sigma v \rangle = \left( \frac{8}{\pi \mu} \right)^{1/2} \frac{1}{(kT)^{3/2}} \int_0^{\infty} S(E) \exp\left(-\frac{E}{kT} - \frac{b}{E^{1/2}}\right) dE \quad (2.6)$$

where the quantity  $b$  arises from barrier penetrability. The quantity  $b^2$  is also called the Gamow energy,  $E_G$ , and is given by the expression:

$$E_G = 2\mu \left( \frac{\pi Z_P Z_T e^2}{\hbar} \right)^2 \approx 0.978 Z_P^2 Z_T^2 \mu \text{ MeV} \quad (2.7)$$

The total reaction rate  $r_{xy}$  can be obtained by multiplying the term  $\langle \sigma v \rangle$  by the absolute number of nuclei  $N_x$  and  $N_y$ :

$$R_{xy} = N_x \cdot N_y \cdot \langle \sigma v \rangle \cdot (1 + \delta_{xy})^{-1} \quad (2.8)$$

$\delta_{xy}$  is a function that accounts for the case when the reaction is between identical particles  $x = y$ .

For a given stellar temperature  $T$ , nuclear reactions take place within a narrow energy region around the effective burning temperature  $E_0$ . Often,  $S(E)$  is nearly constant over the window  $S(E) = S(E_0) = \text{constant}$ . Taking the derivative of the integrand in equation 2.6:

$$E_0 = \left( \frac{bkT}{2} \right)^{2/3} = 1.22 (Z_1^2 Z_2^2 \mu T_6^2)^{1/3} \quad (2.9)$$

$E_0$  is the effective mean energy for thermonuclear fusion reactions at a given temperature  $T$ . The width of the energy window is given as:

$$\Delta = 0.749 (Z_1^2 Z_2^2 \mu T_6^5)^{1/6} \quad (2.10)$$

Nuclear burning reactions take place predominantly over the energy window

$E = E_0 \pm \frac{\Delta}{2}$  also known as the Gamow window. For p-process temperatures of 2-3 GK,

assuming  $\alpha$ -capture on a target nucleus of  $^{120}\text{Te}$ , the Gamow window is from 5.2 to 10 MeV. Laboratory measurements would then be made within this energy range.

### 2.3 Detailed Balance theorem

Consider the reaction  $A + a \rightarrow B + b$ , where  $A$  and  $a$  denote the target and projectile, respectively, and  $B$  and  $b$  are the reaction products. Since these processes are invariant under time reversal, the cross section of the forward reaction is related to that of the reverse. At a given total energy, the corresponding cross sections are not equal but are related as:

$$\frac{\sigma_{Bb \rightarrow Aa}}{\sigma_{Aa \rightarrow Bb}} = \frac{(2j_A + 1)(2j_a + 1)k_{Aa}^2(1 + \delta_{Bb})}{(2j_B + 1)(2j_b + 1)k_{Bb}^2(1 + \delta_{Aa})} \quad (2.11)$$

where  $j_i$  denotes the spin of the respective particle ( $\delta$  is defined in the same way as in equation 2.8). The cross section  $\sigma_{Bb \rightarrow Aa}$  can be calculated independently from any assumptions regarding the reaction mechanism, if the quantity  $\sigma_{Aa \rightarrow Bb}$  is known.

In the lab, all cross section measurements assume a target nucleus in the ground state. In the stellar plasma, the nuclei are in thermal equilibrium and hence the target can be in an excited state. Before using the measured cross section for network simulations, it is necessary to transform it to a stellar cross section ( $\sigma^*$ ):

$$\sigma^*(E_{ij}) = \frac{\sum_{\mu} (2J_i^{\mu} + 1) \exp\left(\frac{-E_i^{\mu}}{kT^*}\right) \sum_{\nu} \sigma^{\mu\nu}(E_{ij})}{\sum_{\mu} (2J_i^{\mu} + 1) \exp(-E_i^{\mu} / kT^*)} \quad (2.12)$$

where  $T^*$  is the plasma temperature,  $\mu$  is the target state,  $\nu$  is the final nucleus state and  $J_{\mu}$

are the spins of the target nuclei. Oftentimes, the cross section measured in the lab can differ significantly from the stellar cross section.

For astrophysical applications, it is often most convenient to calculate the laboratory reaction rate (equation 2.5) which can then be multiplied by a correction factor (known as the stellar enhancement factor) [23] that accounts for the influence of the excited target states:

$$f^* = \frac{\langle \sigma^* \nu \rangle}{\langle \sigma^{lab} \nu \rangle} \quad (2.13)$$

Since both capture and photodissociation reactions are necessary inputs into a network simulation (Section 2.4) [19], the stellar reaction rate of the reverse reaction can then be obtained:

$$N_A \langle \sigma_m \nu \rangle^* = \left( \frac{A_i A_j}{A_o A_m} \right)^{3/2} \frac{(2J_i + 1)(2J_j + 1)G_i(T^*)}{(2J_o + 1)(2J_m + 1)G_m(T^*)} e^{-\frac{Q}{kT^*}} N_A \langle \sigma_i \nu \rangle^* \quad (2.14)$$

where i and j are the entrance channels and o and m the exit channels, G is the partition function, F is a numerical factor and

$$T^* = T_9^{3/2} 9.8685 \times 10^9 \text{ mol} \cdot \text{cm}^{-3} \quad (2.15)$$

## 2.4 Input for Network Calculations

Nuclear reaction network calculations are necessary to follow the time evolution of the isotopic abundances to determine the amount of energy released by nuclear reactions and to find the reaction path. The reaction network is defined as a set of differential equations for the various isotopic abundances. The time derivative of the

abundance for each isotope is expressed in terms of the reaction rates of the different production and depletion reactions [24]:

$$\frac{dY_i}{dt} = \sum_j N_j^i \lambda_j Y_j + \sum_{j,k} N_{j,k}^i \rho N_A \langle \sigma v \rangle_{(j+k)} Y_j Y_k + \sum_{j,k,l} N_{j,k,l}^i \rho^2 N_A^2 \langle \sigma v \rangle_{(j+k+l)} Y_j Y_k Y_l \quad (2.16)$$

where  $Y_i = \frac{X_i}{A_i}$  ( $X_i$  = mass fraction and  $A_i$  = mass #),  $\lambda_j$  = decay and photodisintegration

rates,  $\rho N_A \langle \sigma v \rangle_{(j+k)}$  = particle capture rates,  $\rho^2 N_A^2 \langle \sigma v \rangle_{(j+k+l)}$  = particle interaction rates.

The  $N^i$ 's are given by:

$$N_j^i = N_i \quad N_{j,k}^i = \frac{N_i}{(N_j! N_k!)} \quad N_{j,k,l}^i = \frac{N_i}{(N_j! N_k! N_l!)} \quad (2.17)$$

The  $N_i$ 's represent positive or negative numbers which specify how many particles of species i are created or destroyed in the reaction. The time integrated net reaction flow between two isotopes i and j is defined by:

$$F_{i,j} = \int \left[ \frac{dY_i}{dt_{(i \rightarrow j)}} - \frac{dY_j}{dt_{(j \rightarrow i)}} \right] dt \quad (2.18)$$

This quantity provides information about the main reaction path during the nucleosynthesis event and serves as a tool for monitoring the effects of nuclear structure parameters such as shell closures or deformation on reaction path and reaction branchings [19].

Network calculations for p-process nucleosynthesis consider about 20,000 reactions linking close to 2,000 nuclei with  $A \leq 210$  [13,25]. A recent p-process network simulation [19] considered the abundance evolution of about 1800 nuclei (from H to Bi)

in the framework of a parameterized Type II SN shock front model. Fig. 1.3 shows the reaction flux integrated over a 1s time interval.

The knowledge of  $(\gamma, \alpha)$  reaction rates is imperative for the accurate modeling of the p-process (both its path and abundance distribution). Under astrophysical conditions, the reaction rate for the photodisintegration reaction  $(\gamma, \alpha)$   $\lambda_{\gamma\alpha}$  is proportional to the reaction rate for the inverse  $(\alpha, \gamma)$  capture reaction  $\langle \sigma_{\alpha v} \rangle^*$  (i = target state and m = final nucleus) [23]:

$$\lambda_{\gamma} = \left( \frac{A_i A_{\alpha}}{A_m} \right)^{3/2} \frac{(2J_i + 1)(2J_{\alpha} + 1)}{(2J_m + 1)} \frac{G_i(T^*)}{G_m(T^*)} (T^*)^{3/2} F e^{-Q/kT^*} N_A \langle \sigma_{i v} \rangle^* \quad (2.19)$$

where  $G(T)$  is the temperature dependent partition function,  $J$  is the spin and  $F$  is a numerical factor (as defined in eq. 2.14) and  $T^*$  is defined in equation 2.15.

## CHAPTER 3

### THEORY

#### 3.1 Overview: One Piece of the Puzzle

For charged particle capture reactions on p-nuclei, the level density in the compound system is typically high. This is due in part to the large nucleon number (which intrinsically have a high density of excited states) and the particle energies involved for astrophysical applications are relatively high (measurements are made within the Gamow window). The cross section is then dominated by many resonances that appear nonresonant [26]. The cross sections can then be approximated using the Hauser-Feshbach (HF) approach, a statistical model of compound nuclear reactions.

Many nuclear ingredients go into the calculation of the statistical model: level densities, masses, energies and widths of the giant dipole resonances (GDR), isospin effects, and optical potentials; however, the most important quantities of the Hauser-Feshbach (HF) model are the particle and  $\gamma$ -transmission coefficients and the level density of excited states [23]. While all of the inputs present some uncertainties, it is generally the optical model potentials (OMP) and the nuclear level densities (NLD) that have been the most problematic [27,28,29].

The NLD generally doesn't show itself to be problematic for  $\alpha$ -capture reactions. Not only is this due to the higher bombarding energies involved (the number of states increases exponentially with excitation energy) but it is also due to an improved treatment of the NLD where its superiority at higher energies has been noted [28,30,31]. Instead, the theoretical overestimation in cross section when compared to  $\alpha$ -capture data on p-nuclei is mainly due to an uncertainty in the optical  $\alpha$ -nucleus potential at energies of astrophysical relevance [23].

While the model has been able to reproduce most of the measured  $(\alpha,\gamma)$  reactions on p-nuclei to within a factor of 2, much larger deviations have occurred [32]. In order to increase the accuracy of the model, the goal is to probe it at the local level. This can be achieved in two ways: direct measurement of  $\alpha$ -capture cross sections (within the effective burning regime of the astrophysical environment) which tests the validity of the model and the accuracy of the global  $\alpha$ -nucleus potentials or by determination of the  $\alpha$ -nucleus potential itself. For either case, more experimental data is required (this is particularly true in the heavier mass regions where the deviations are seen more strongly [32]).

### **3.2 HF formalism**

The vast majority of the reaction rates that are inputs into the p-process network simulation are derived from theoretically calculated HF cross sections. The model can be applied provided that the level density in the contributing energy window

(generally 5-10 levels  $\text{MeV}^{-1}$ ) around the peak of the projectile energy distribution is sufficiently high enough to justify a statistical treatment [23]. In essence, it can be applied when the average resonance width ( $\langle\Gamma\rangle$ ) is larger than the average level spacing ( $D = 1/\rho$ ) [30].

The HF model is based on the Bohr assumption. The formation and disintegration of the compound system into the products of the reaction can be treated as independent processes [33]. The cross section can be factored into two terms:

$$\sigma(\alpha, \beta) = \sigma_c(\alpha)G_c(\beta) \quad (3.1)$$

where  $\sigma_c(\alpha)$  is the cross section for the formation of C through channel  $\alpha$  and  $G_c(\beta)$  is the probability that C decays through channel  $\beta$ . The branching probability can be expressed as:

$$G_c(\beta) = \frac{\Gamma_\beta}{\Gamma} \quad (3.2)$$

where  $\Gamma_\beta$  is the partial width for the decay into channel  $\beta$  and  $\Gamma$  is the total decay rate. In the HF theory, the formation cross section is calculated in the same way as in the optical model but using averaged transmission coefficients  $\langle T \rangle$  [30]. These averaged transmission coefficients are related to the average widths by  $\langle T \rangle = 2\pi\rho\langle\Gamma\rangle$  where  $\rho$  is the average level density. The compound nucleus cross section can be derived from the Breit-Wigner formula by substituting the resonance parameters with average parameters [30]. The Breit-Wigner expression is (for n individual resonances):

$$\sigma_{BW}^{\alpha\beta} = \frac{\pi^2}{k_j^2} \frac{1 + \delta_{ij}}{(2I_i + 1)(I_j + 1)} \sum_{k=1}^n (2J_k + 1) \frac{\Gamma_k^\alpha \Gamma_k^\beta}{(E - E_k)^2 + (\Gamma_k^{tot}/2)^2} \quad (3.3)$$

The indices  $i$  refer to the target,  $j$  to the projectile,  $\alpha$  to the entrance channel, and  $\beta$  to the exit channel. The CN cross section is:

$$\sigma_{CN}^{\alpha\beta} = \frac{\pi}{k_j^2} \frac{I + \delta_{ij}}{(2I_i + 1)(2I_j + 1)} \sum_{J\pi ij i'} (2J + 1) \frac{\langle T_{Jj}^\alpha \rangle \langle T_{Jj'}^\alpha \rangle}{\sum_{\alpha j} \langle T_{Jj} \rangle} W^{\alpha\beta} \quad (3.4)$$

where  $W^{\alpha\beta}$  are the width fluctuation coefficients which correlate the incoming and outgoing channels and account for nonstatistical fluctuations by rearranging the flux into different channels. The width fluctuation coefficients ( $W^{\alpha\beta}$ ) are given as:

$$W^{\alpha\beta}(E, J, \pi) = \left\langle \frac{\Gamma_{J,\pi}^\alpha(E) \Gamma_{J,\pi}^\beta(E)}{\Gamma_{J,\pi}^{tot}(E)} \right\rangle \frac{\langle \Gamma_{J,\pi}^{tot}(E) \rangle}{\langle \Gamma_{J,\pi}^\alpha(E) \rangle \langle \Gamma_{J,\pi}^\beta(E) \rangle} \quad (3.5)$$

In particular, the elastic channel is enhanced. The HF cross section is an averaged Breit-Wigner cross section when  $W^{\alpha\beta} = 1$  [30].

In the statistical Hauser-Feshbach model [34], the cross section for the reaction  $i^\mu(\alpha, \gamma)l^\nu$  in which an incoming  $\alpha$  particle is captured by the target nucleus  $i$  in its state  $\mu$ , leaving the residual nucleus  $l$  and a photon is given by the expression:

$$\sigma_{\alpha\gamma}^\mu = \frac{\lambda_\alpha^2}{4\pi} \frac{1}{(2J_i^\mu + 1)} \sum_{J^\pi} (2J + 1) \frac{T_\alpha^\mu(J^\pi) T_\gamma(J^\pi)}{T_{tot}(J^\pi)} \quad (3.6)$$

where  $J_i$  is the spin of the target. The variable  $\lambda_\alpha$  describes the wavelength of the system  $\alpha+i$ . The transmission coefficient  $T_\alpha^\mu(J^\pi)$  measures the probability for forming the compound nucleus in its state  $J^\pi$ . Similarly,  $T_\gamma(J^\pi) = \sum_\nu T_\gamma^\nu(J^\pi)$  is the transmission coefficient for the decay of the compound nuclear state into the pair  $l + \gamma$ , considering all possible states  $\nu$  of  $l$  which can be populated in the decay.  $T_{tot}(J^\pi) = \sum_{i,j} T_i^\lambda(J^\pi)$

corresponds to the total transmission coefficient for the decay of the compound state into any combination  $i$  of nucleus and particles  $j$  which can be formed from all its possible decay modes  $\lambda$ .

The transition from an excited state in the compound nucleus to a state in nucleus  $i$  via the emission of an  $\alpha$  particle is given by the summation over all quantum mechanically allowed partial waves:

$$T_{\alpha}^{\mu} = \sum_{l=|J-s|}^{J+s} \sum_{s=|J_i^{\mu}-J_{\alpha}|}^{J_i^{\mu}+J_{\alpha}} T_{\alpha ls} (E_{i\alpha}^{\mu}) \quad (3.7)$$

where  $l$  is the angular momentum and  $s$  is the channel spin. When calculating the radiative transmission coefficients ( $T_{\gamma}$ ), the dominant  $\gamma$ -transitions are the electric and magnetic dipole transitions (E1 and M1); hence, the total photon width:

$$T_{\gamma} = T_{E1} + T_{M1} \quad (3.8)$$

The M1 transitions are treated in the simple single particle approach ( $T_{M1} \propto E^3$ ) [33]. The E1 transitions are calculated on the basis of the Lorentzian representation of the giant dipole resonance (GDR). Within this model, the E1 transmission coefficient for the transition emitting a photon of energy  $E_{\gamma}$  in a compound nucleus  ${}^A_Z$  is given by

$$T_{E1}(E_{\gamma}) = \frac{8NZe^2(1+\chi)}{3A\hbar cMc^2} \sum_{i=1}^2 \frac{i\Gamma_{G,i}E_{\gamma}^4}{3[(E_{\gamma}^2 - E_{G,i}^2)^2 + \Gamma_{G,i}^2E_{\gamma}^2]} \quad (3.9)$$

where  $M$  is the proton mass,  $\chi$  ( $= 0.2$ ), and  $\Gamma$ ,  $E$  are the width and energy of the GDR [23].

### 3.2.1 The potential dependence of the HF transmission coefficients

The transmission coefficients for the  $(\alpha, \gamma)$  reaction channel must be known in order to perform a correct calculation of the reaction cross section. In a nuclear reaction, a projectile will penetrate a target nucleus (by tunneling through the Coulomb barrier) in order to form a compound nucleus. This penetration factor (transmission coefficient) can be determined by solving the Schrödinger equation for a certain optical nuclear potential  $U(r)$ . This is solved numerically via the radial equation:

$$\left[ \frac{\hbar^2}{2\mu} \left( \frac{d^2}{dr^2} + \frac{l(l+1)}{r^2} \right) + \frac{Z_1 Z_2 e^2}{r} + U(r) \right] \phi_l(r) = E \phi_l(r) \quad (3.10)$$

The transmission coefficients can be calculated by

$$T = \left| \frac{J_{trans}}{J_{inc}} \right| \quad (3.11)$$

where  $J$  is the current density  $(= \frac{\hbar}{2mi} (\phi^* \vec{\nabla} \phi - \phi \vec{\nabla} \phi^*))$  of the transmitted and incident waves. For the scattering of finite nuclei, the potential  $U(r)$  consists of a Coulomb part:  $V_C(r)$  and a nuclear part:  $V(r) + iW(r)$ . The result of the short ranged nuclear potential on the total wave function when  $r < R_N$  ( $R_N$  is the nuclear radius) is an extra scattered wave besides the wave provided by the Coulomb potential. When  $r > R_N$ , the only potential is the Coulomb potential (Sections 3.4.1 and 3.4.2).

### 3.3 Optical Potential

The interaction of two nuclei is a complicated many body problem which can be simplified in the case of elastic scattering through the use of an optical potential. For such a model both particles are considered to be structureless bodies interacting via a simple potential. This potential only depends on the distance between the center of mass of both particles  $U = U(r)$ .

The analysis of the experimental scattering data presented in this work is performed within the optical model framework. The optical potential is made up of three terms:

- The Coulomb potential  $V_C$
- The real part of the nuclear potential  $V$
- The imaginary part of the potential  $W$

$$U(r) = V_C(r) + V(r) + iW(r) \quad (3.12)$$

#### 3.3.1 Coulomb potential

The Coulomb potential is taken to be the potential of a homogeneously charged sphere:

$$V_C(r) = Z_P Z_T e^2 \frac{3 - \left(\frac{r}{R_C}\right)^2}{2R_C} \quad \text{for } r \leq R_C$$

$$V_C(r) = Z_P Z_T \frac{e^2}{r} \quad \text{for } r > R_C \quad (3.13)$$

where  $R_C$  represents the radius of the sphere. The value adopted for  $R_C$  has been chosen identically with the root-mean-square radius  $r_{\text{rms}}$  of the double folding potential  $V_F$ .

### 3.3.2 Nuclear Potential

The nuclear potential is responsible for the description of the strong interaction between two nuclei. It is written in a complex form, where a central potential is usually considered in the real part. An imaginary part is needed, as soon as inelastic channels (inelastic scattering, particle absorption or transfer reactions) open and might affect the elastic interaction channel. Different parameterizations are usually considered for both components of the nuclear potential:

- Volume Woods-Saxon:  $V(r) = V_0 f_V(r) = V_0 \left(1 + \exp\left(\frac{r - R_V}{a_V}\right)\right)^{-1}$
- Surface Woods-Saxon:  $V(r) = a_S V_0 \frac{df_S(r)}{dr} = V_0 \exp\left(\frac{r - R_S}{a_S}\right) \left(1 + \exp\left(\frac{r - R_S}{a_S}\right)\right)^{-2}$
- Gauss:  $V(r) = V_0 \exp\left(-\frac{r^2}{R^2}\right)$
- Fourier-Bessel:  $V(r) = \sum_k a_k \frac{\sin(k\pi r / R)}{(k\pi r / R)}$

where  $f_i(r) = (1 + \exp((r - R_i)/a_i))^{-1}$  are the Woods-Saxon form factors, with  $R_i = r_i \cdot A_T^{1/3}$

and  $i = V, S$ .

For the description of elastic scattering, the different parameters in the Woods-Saxon, Gauss or Fourier-Bessel potentials are adjusted to the experimental data. In this work, volume and surface Woods-Saxon forms were used for the imaginary part of the nuclear potential. While the Fourier-Bessel gives very good agreement at higher energies, the oscillatory nature makes the extrapolation down to lower energies useless (no diffraction pattern is present in the scattering data). Ambiguities arise and it's necessary to consider:

1. Continuous ambiguities: Variations in the geometry parameters of the potentials are followed automatically by adjustments in the rest of the geometry parameters, resulting in potentials that produce similar scattering phases and an equal description of the scattering data [10].

It is possible to reduce continuous ambiguities to a great extent by using a double folding parameterization for the real nuclear potential. The shape of the folding potential is fixed while the standard potentials of the Woods-Saxon (WS) type require normalization to its geometry form factors.

2. Singular ambiguities: Potentials with similar geometry but different depths produce very close results in the description of the elastic scattering data [10].

The scattering at the lowest energies is determined by the phase shifts, and the pattern of phase shifts is largely unchanged if the potential is changed in depth so that the nearest bound or resonant state in a given partial wave remains the same distance from threshold.

If the potential is made deeper, then a bound state would have an extra node. These singular (or discrete) ambiguities give rise to the "family problem". This effect was previously studied on p-nuclei at low energies [35,36] where the normalization of the depth of the real part of the nuclear potential (the strength parameter  $\lambda$ ) was systematically varied. The width parameter  $w$  and the imaginary geometry terms are

adjusted for each fixed value of  $\lambda$  for the best fit. What results is a continuous variation of  $\chi^2/F$  with respect to  $J_R$  (the strength of the real potential). The strength is obtained by the integral of the potential through the whole space and is usually normalized to the number of interacting nucleons  $A_P \cdot A_T$  [10]. Another characteristic of the potential is described by its mean square radius  $r_{rms}$ . These two quantities are derived for the real and imaginary part of the nuclear potential through the expressions:

$$J_R = \frac{1}{A_P \cdot A_T} \int V(r) d^3 r \quad J_I = \frac{1}{A_P \cdot A_T} \int W(r) d^3 r \quad (3.14)$$

$$r_{rms,R} = \sqrt{\frac{\int V(r) r^2 d^3 r}{\int V(r) d^3 r}} \quad r_{rms,I} = \sqrt{\frac{\int W(r) r^2 d^3 r}{\int W(r) d^3 r}} \quad (3.15)$$

The volume integrals of the different components of the nuclear potential are negative quantities (the absolute values of  $J_R$  and  $J_I$  are used). Each (local) minimum in  $\chi^2/F$  corresponds to one family of the optical potential. Figure 3.1 shows such a study done on  $^{89}\text{Y}(\alpha,\alpha)^{89}\text{Y}$  [10,37]. The deepest minimum in the  $\chi^2/F$  landscape should correspond to the correct family. In this case, the deepest minima occur for families number 3,4, and 5. The solution to which of these is the correct family can be solved by considering elastic scattering data at higher energies ( $E \approx 100$  MeV [38]) where a linear extrapolation of  $J_R$  is expected (including energies below the Coulomb barrier). Volume integrals of about  $J_R \approx 330\text{-}340$  MeV fm<sup>3</sup> were obtained for the case of  $^{144}\text{Sm}(\alpha,\alpha)^{144}\text{Sm}$  [35],  $J_R \approx 340$  MeV fm<sup>3</sup> for the case of  $^{92}\text{Mo}(\alpha,\alpha)^{92}\text{Mo}$  [36], and  $J_R \approx 340\text{-}350$  MeV fm<sup>3</sup> for  $^{112,124}\text{Sn}$  [39]. Further confirmation comes from considering the cluster model. By adjusting the  $\alpha$ -nucleus potential to the bound state properties of the nucleus  $(A+4) = A$

⊗  $\alpha$  [40,41,42], the potential at energies of astrophysical relevance was determined by considering the energy gap between the bound state and scattering potentials (5-12 MeV) [43]. This confirmed that the correct description of the strength potential led to values of  $J_R \approx 320\text{-}350 \text{ MeV fm}^3$ . The volume integrals considered in this study were chosen to fall within this range.

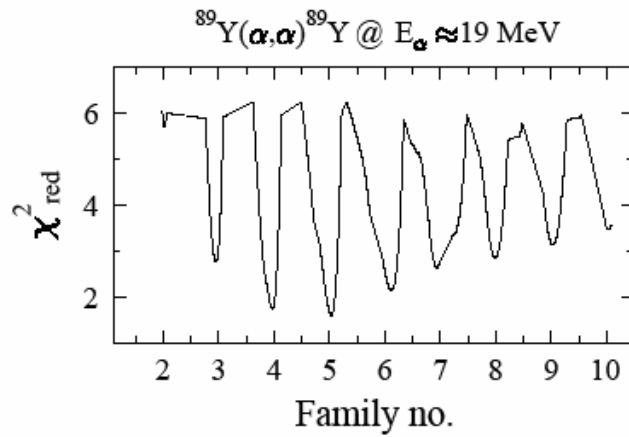


Figure 3.1  $\chi_{red}^2$  in the study of the different potential families for the reaction  $^{89}\text{Y}(\alpha, \alpha)^{89}\text{Y}$  at  $E \approx 19 \text{ MeV}$ . The best description of the experimental cross sections is observed for the families 3, 4, and 5 [10].

### 3.3.3 Double Folding Potential

The double folding potential expresses the potential in terms of an effective nucleon-nucleon interaction (NN) between the nucleons of the interacting nuclei integrated over both their densities. The folding of the densities of both nuclei and their interaction via an effective nucleon-nucleon interaction can be written as:

$$V_f(r) = \iint \rho_a(r_a) \rho_A(r_A) v_{eff}(E, \rho, s) d^3 r_a d^3 r_A \quad (3.16)$$

The geometry of this parameterization is shown schematically in Figure 3.2.  $\rho_a(r_a)$  and  $\rho_A(r_A)$  represent the charge densities of the projectile  $a$  and the target nucleus  $A$ .

The charge densities were obtained from electron scattering experiments [44]. In the situation where data was unavailable (e.g.,  $^{120}\text{Te}$ ), a linear extrapolation using the muonic + isotopic data of the other Te isotopes was performed and the density parameters thus

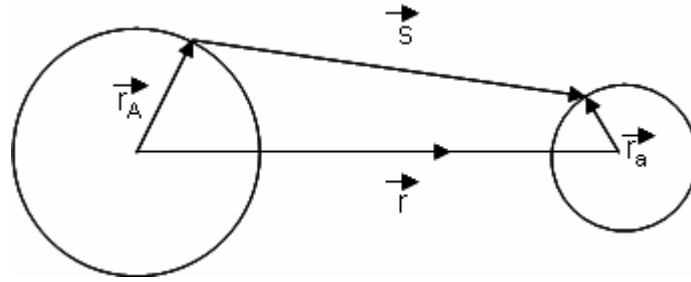


Figure 3.2 Schematic representation of the double folding parameterization [10].

derived. In cases where no data was available, a reasonable estimate can be obtained by a simple scaling of the radius parameter  $\sim A^{1/3}$  [43]. For all isotopes in this current study, a two parameter Fermi (2pF) form was used for the density distribution [44,45]. This form follows the relation of the volume WS term. It has been shown to reproduce the constant central region and the diffused edge of the density distribution well.

The effective nucleon-nucleon interaction chosen in this work is that developed by Satchler and Kobos [46,47] based on a combination of three Yukawa potentials folded with the density of both projectile and target nuclei, also called the DDM3Y

parameterization. This description can be separated into two terms, one dependent on the distance between both nuclei, the other is a function of density, for a given energy E:

$$v_{eff}(s, \rho_a, \rho_A, E) = f(s, E) \cdot g(\rho_a, \rho_A, E) \quad (3.17)$$

where

$$f(s, E) = 7999 \frac{e^{-4s}}{4s} - 2134 \frac{e^{-2.5s}}{2.5s} + \hat{J}_{00}(E) \quad (3.18)$$

is denoted as the Reid-interaction [48], and the weak energy dependence is given by

$$\hat{J}_{00}(E) = -276(1 - 0.005 \cdot E)\delta(s) \quad (3.19)$$

The density dependence of the double folding potential can be parameterized as:

$$g(\rho_a, \rho_A, E) = C(E) \cdot (1 + \alpha(E)e^{-\beta(E)\rho}) \quad (3.20)$$

The variable s in the above equations represents the absolute value of the vector

$\vec{s} = \vec{r}_a + \vec{r} - \vec{r}_A$  (Figure 3.2). E is the energy per nucleon, and  $\rho$  is the sum of the densities

of both nuclei at rest  $\rho = \rho_a + \rho_A$ . The energy dependence of the coefficients C(E),  $\alpha(E)$ ,

$\beta(E)$  can be determined by adjusting the volume integral of the effective nucleon-nucleon

(NN) interaction  $v_{eff}$  with realistic calculations of the G-matrix [49]. The G-matrix is a

scattering operator that allows the transformation of the bare interaction potential into an

effective one (higher order contributions are now considered – not just one or two body

terms). The double folding potential is parameterized as:

$$V(\mathbf{r}) = \lambda V_f(\mathbf{r}/w) \quad (3.21)$$

where  $\lambda$  is a normalization for the strength of the potential. Typical range of values for  $\lambda$

= 1.1-1.4 [40,50,51].

The parameter  $w$  modifies the width of the potential. This accounts for deviations between the proton and neutron density distribution within the nucleus. For stable light nuclei with  $Z = N$  this parameter is usually not necessary [52]. In the medium and heavy mass region, where  $N/Z \approx 1.2$  for stable nuclei, it is necessary to take this correction into consideration [10]. The value of  $w$  should remain very close to 1. A large deviation from unity for the stable nuclei, where the neutron and proton densities are very similar, would indicate that the nucleon-nucleon interaction is not well chosen [39]. In a first order approximation, the protons and neutrons are considered to be equally distributed around the nucleus. In this work, the double folding potential has been calculated [53].

### **3.4 Scattering Theory**

Elastic scattering is one of the simplest nuclear reactions between a projectile and a target. Despite this, elastic scattering has been an important source of information on nuclear properties. This information comes primarily through the interaction potential. The many body problem that exists is simplified through the introduction of a potential. Such a potential is the complex optical model. The real part accounts for the elastic scattering and the imaginary part accounts for the sum of all contributions of non-elastic channels (reaction cross section). Below the threshold energy of the lowest non-elastic channel the flux is absorbed into compound-elastic scattering and at higher energies, the absorption goes into non-elastic reaction channels. The following derivation is from [10, 54].

The elastic scattering process between a projectile  $a$  and a target nucleus  $A$  can be described by finding a solution of the Schrödinger equation:

$$\left[ -\frac{\hbar^2}{2\mu} \cdot \nabla^2 + V(\vec{r}) \right] \Psi(\vec{r}) = E\Psi(\vec{r}) \quad (3.22)$$

where  $\mu$  represents the reduced mass of the system. The potential  $V(\vec{r})$  is composed of a Coulomb and a complex nuclear potential. The wave function  $\Psi(\vec{r})$  is a sum of the incoming plane wave and the outgoing spherical wave

$$\Psi(\vec{r}) = A_0 \left( \exp(i\vec{k} \cdot \vec{r}) + f(\theta, \phi) \frac{\exp(ikr)}{r} \right) \quad (3.23)$$

where  $f(\theta, \phi)$  is the scattering amplitude and  $\vec{k}$  the wave number of the incoming wave.

The density of the emitted particles is given by the square of the wave function in equation 3.23, integrated over all internal degrees of freedom:

$$\rho = \frac{A_0^2}{r^2} |f(\theta, \phi)|^2 \quad (3.24)$$

An expression for the differential scattering cross section, defined as the number of particles emitted per solid angle  $d\Omega$  divided by the incident flux of particles per unit time, is given as:

$$\frac{d\sigma}{d\Omega} = |f(\theta, \phi)|^2 \quad (3.25)$$

### 3.4.1 Elastic scattering on a nuclear potential

When considering a spherically symmetric potential, the angular momentum of the system is a constant of the motion. In this way the wave function can be factored into

a radial and angular part:

$$\chi_{lm}(\vec{r}) = u_l(r)Y_l^m(\theta, \phi) \quad (3.26)$$

Likewise, the Schrödinger equation can be separated into a radial and angular form.

The radial equation takes the form:

$$-\frac{\hbar^2}{2\mu} \frac{d^2}{dr^2} w_l + \left[ V(r) + \frac{\hbar^2}{2\mu} \cdot \frac{l(l+1)}{r^2} \right] w_l = E w_l \quad (3.27)$$

where the term  $\frac{\hbar^2}{2\mu} \cdot \frac{l(l+1)}{r^2}$  represents the centrifugal barrier of a particle moving in an orbit with angular momentum  $l\hbar$ .

The scattering process can be understood as the interaction of several partial wave functions with angular momentum  $l$  with the central potential. Only those particles with angular momentum  $l\hbar$  relative to the target less than a maximum value will interact effectively with the target nucleus.

For the elastic scattering case, the asymptotic limit leads to an approximation of equation 3.26

$$\chi(r, \theta, \phi) \rightarrow \exp(i\vec{k}\vec{r}) + f(\theta, \phi) \exp\left(\frac{ikr}{r}\right) \quad (3.28)$$

Assume that the particles do not have any intrinsic spins, so that the total angular momentum is just the orbital angular momentum  $l$ . Adopting  $k$  along the z axis, it is possible to express the scattering amplitude of a nuclear potential as follows:

$$f(\theta, \phi) = \frac{1}{2ik} \sum_l (2l+1) [S^l - 1] P_l(\cos \theta) \quad (3.29)$$

where  $P_l(\cos\theta)$  are the Legendre polynomials, and  $S$  represents the unitary scattering matrix which is expressed in terms of the reflection coefficients  $\eta_l$  and the scattering phase shifts  $\delta_l$ .

$$S^l = \eta_l \exp(2i\delta_l) \quad (3.30)$$

The reflection coefficients  $\eta_l$  represent the amplitude attenuation of the  $l$ -th partial wave. For a real potential, no attenuation is expected, since  $\eta_l = 1$  (for complex potentials,  $\eta_l < 1$ ). The scattering phase shifts  $\delta_l$  correspond to the angular shift experienced by the  $l$ -th partial wave compared to an undisturbed wave. An attractive potential ( $V < 0$ ) leads to a positive phase shift, whereas a repulsive potential ( $V > 0$ ) produces a negative phase shift. In the absence of a nuclear potential, all phase shifts vanish.

### 3.4.2 Elastic scattering on a Coulomb field

The existence of an electromagnetic interaction between two interacting particles requires the adoption of an extra term for the wave function, which asymptotically takes the form:

$$\chi_C(\vec{k}\vec{r}) \rightarrow \frac{1}{r} \exp[ikr - \eta \ln(2kr)] \quad (3.31)$$

with a phase shift relative to an undisturbed wave which depends logarithmically on the distance  $r$ , the Sommerfeld parameter  $\eta$ , defined in equation 2.2. Taking into account the above correction, the wave function of equation 3.26 has the form:

$$\chi(r, \theta, \phi) \rightarrow \chi_C(r, \theta) + \chi_N(r, \theta, \phi)$$

$$\rightarrow (f_C(\theta) + f_N(\theta, \phi)) \frac{1}{r} \exp[i(kr - n \ln(2kr))] \quad (3.32)$$

The amplitude  $f_N$  incorporates all possible interactions but the electromagnetic. The Rutherford scattering amplitude is written as:

$$f_C = -\frac{n}{2k \sin^2(\theta/2)} \exp[-i(n \ln(\sin^2(\theta/2)) + 2\sigma_0)] \quad (3.33)$$

whereas the scattering amplitude of the nuclear interaction is given by

$$f_N(\theta, \phi) = \frac{1}{2ik} \sum_l (2l+1) \exp(2i\sigma_l) [S^l - 1] P_l(\cos \theta) \quad (3.34)$$

The Coulomb phase shift  $\sigma_l$ , which contains the effect of the electromagnetic interaction on the scattering amplitude  $f_N(\theta, \phi)$ , is given by the expression

$$\sigma_l = |\Gamma(l+1+i\eta)| \quad (3.35)$$

Considering both the effects of the electromagnetic and nuclear interactions, the total scattering amplitude of a projectile on a target nucleus A is expressed in the form

$$\frac{d\sigma}{d\Omega}(\theta, \phi) = |f_C(\theta) + f_N(\theta, \phi)|^2 \quad (3.36)$$

## CHAPTER 4

### ACTIVATION EXPERIMENTS

#### 4.1 Overview

In some cases, the cross section of  $\gamma$ -induced reactions can be measured by photodissociation experiments; however, reproduction of the thermal photon bath is experimentally challenging [55,56,57]. Generally, it is the inverse capture reaction that is measured. Detecting the prompt  $\gamma$ 's of the capture reaction is exceedingly difficult due to the low cross sections at energies of astrophysical interest. The beam induced background usually swamps the  $\gamma$ -ray of interest; hence, for capture reactions on p-nuclei, the cross section is generally determined via the activation technique. This involves bombarding a stable target with a charged particle beam (in the case of  $\alpha$ - or p-) thereby producing a radioactive species. If the lifetime of the residual radioactivity is long enough (between minutes and hours), the radioactive product can then be measured offline.

Due to the very low natural abundances of p-nuclei, enriched targets are generally necessary for p-process measurements. While several (p, $\gamma$ ) measurements have

been made using natural targets [58,59,60,61,62], the situation for  $\alpha$ -capture is different (due to the very low cross sections). The degree of enrichment needed depends greatly on the cross section (how small it is) and also on the decay scheme of the radioactive nucleus produced (how complicated it is). Competing reactions can produce  $\gamma$ -transitions very close in energy to or with cross sections of the same order of (or greater than) the one of interest. In these cases, a very high enrichment is needed to improve the peak-to-background ratio.

The aim of this experiment was the measurement of the  $\alpha$ -capture cross section on  $^{106}\text{Cd}$ . Based on Hauser-Feshbach predictions for the reaction rate, the  $p$ -process branching point at which the  $(\gamma,\alpha)$  and  $(\gamma,p)$  reactions become competitive with the  $(\gamma,n)$  process along the  $Z=50$  chain is located at mass number 110-112 (Figure 4.1) [64].

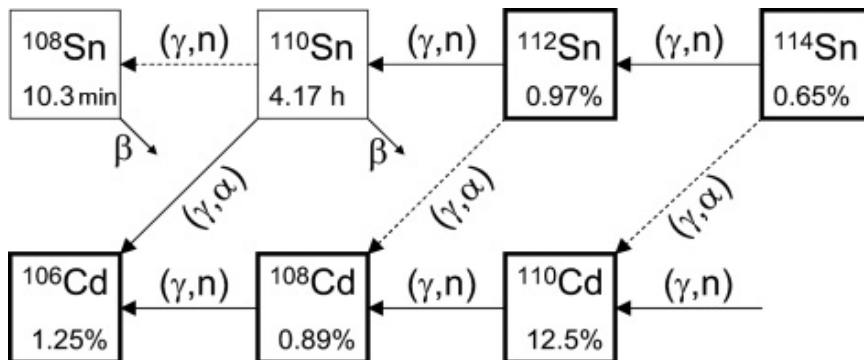


Figure 4.1 The  $p$ -process reaction flow in the Cd-Sn region. For simplicity, only even-even isotopes are shown, hence the  $(\gamma,n)$  arrow indicates two subsequent neutron emissions. Stable isotopes are indicated by bold squares. The solid arrows show the main reaction flow path, whereas dashed arrows indicate weaker branchings [63,64].

This reaction is particularly important because it focuses on the photodisintegration of a closed proton shell ( $Z=50$ ). Near closed shells the level density is reduced and the statistical model may not be fully applicable (this is particularly true for neutron magic numbers due to their wider level spacing) [64]. In addition to  $^{110}\text{Sn}$ , the reaction products of  $^{106}\text{Cd}(\alpha,n)^{109}\text{Sn}$  and  $^{106}\text{Cd}(\alpha,p)^{109}\text{In}$  are also radioactive. The reaction product of  $^{106}\text{Cd}(\alpha,p)^{109}\text{In}$  is the same as the daughter of  $^{109}\text{Sn}$  from the  $^{106}\text{Cd}(\alpha,n)^{109}\text{Sn}$  reaction (Figure 4.2).

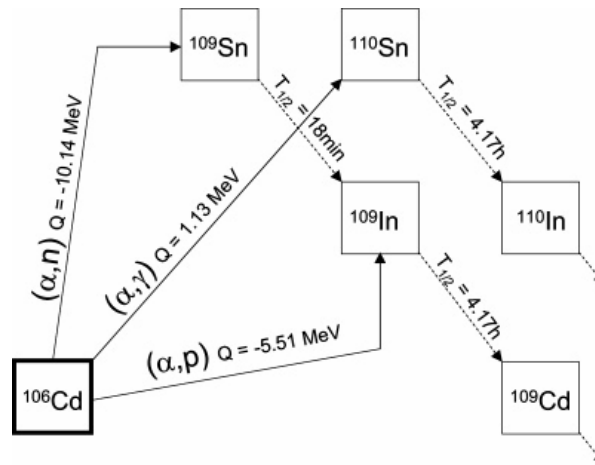


Figure 4.2: The  $\alpha$ -induced reactions on  $^{106}\text{Cd}$  and the decay of the reaction products [64].

Above the  $(\alpha,n)$  threshold ( $E_\alpha = 10.53$  MeV), the  $(\alpha,n)$  channel rapidly becomes stronger than the  $(\alpha,p)$  reaction; therefore, the  $^{106}\text{Cd}(\alpha,p)^{109}\text{In}$  cross section is determined only below the  $(\alpha,n)$  threshold.

The experiment was performed independently at Notre Dame and at Atomki, Hungary [64]. The experiments overlapped at certain energies and therefore allow for the detection of any hidden systematic error. Since there is little  $\alpha$ -capture data on p-nuclei,

this increases the reliability of the measurements. The experiment performed at Notre Dame will be presented [64].

For the  $^{106}\text{Cd}(\alpha,n)^{109}\text{Sn}$  reaction, no results were obtained from the Notre Dame data. Due to the very complicated decay scheme and the absence of dominant  $\gamma$ -ray transitions, the close geometry of the counting set-up (Section 4.1.5) would have required significant summing corrections leading to large uncertainties [64].

In addition to the  $\alpha$ -capture cross section of  $^{106}\text{Cd}$ ,  $^{120}\text{Te}(\alpha,n)^{123}\text{Xe}$  was also measured (at Notre Dame only). Since  $^{120}\text{Te}(\alpha,\gamma)$  produces  $^{124}\text{Xe}$  (a stable product), it is not possible to measure this reaction via the activation technique. Information about the behavior of the  $\alpha$ -optical potential can also be obtained by measuring the  $(\alpha,n)$  and  $(\alpha,p)$  channels. While  $^{120}\text{Te}(\alpha,p)$  produces a radioactive species ( $^{123}\text{I}$ ), the main  $\gamma$ -ray transition (159 keV) has feeding from the  $(\alpha,n)$  reaction.

#### 4.1.1 Beamline set-up

Figure 4.3 shows the experimental set-up for the irradiations. The first figure shows the target chamber for the  $^{106}\text{Cd}$  activations while the second is that of  $^{120}\text{Te}$ . The entire target chamber was isolated from the beam line and acted as a Faraday cup. Secondary electrons from the target were suppressed by a bias voltage of -300 V.

Due to the relatively low melting point of the  $^{106}\text{Cd}$  targets (321°C), they were placed in a brass holder which was air cooled. A thick carbon disc was placed directly behind the target to stop the beam. The beam spot for the  $^{106}\text{Cd}$  and the  $^{120}\text{Te}$

irradiations was defined by using a 5 mm collimator at the target position.

For the  $^{106}\text{Cd}+\alpha$  activations, the beam current was recorded in real time with a current integrator in time steps of 32s, allowing fluctuations in the beam to be monitored.

For the  $^{120}\text{Te}(\alpha,n)$  irradiations, the current was recorded in time steps of 10s.

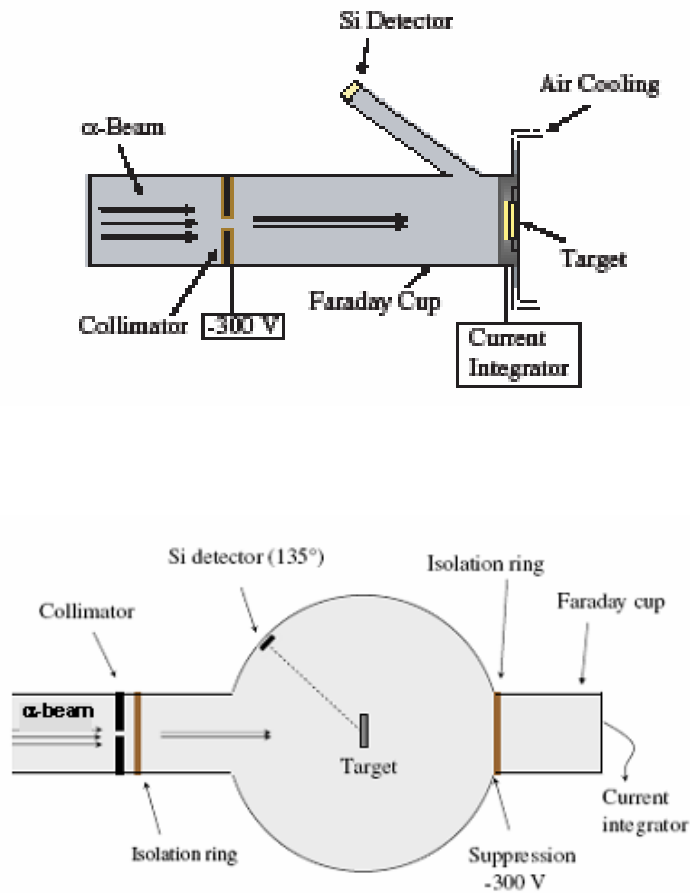


Figure 4.3 A collimated Si surface barrier detector was mounted at  $135^\circ$  with respect to the beam axis to monitor the stability of the target [65,66].

#### 4.1.2 Enriched $^{106}\text{Cd}$ and $^{120}\text{Te}$ targets

Highly enriched (86.4%)  $^{106}\text{Cd}$  targets were prepared via mechanical rolling at Argonne National Laboratory. They were self supporting targets with thicknesses of 2.3  $\text{mg}/\text{cm}^2$  (determined by weighing). The thicknesses were also measured by the Rutherford backscattered (RBS) approach and turned out to be  $2.1 \pm 0.2 \text{ mg}/\text{cm}^2$ . The Cd foils were mounted on Ta frames with apertures of diameters of 12.5 mm.

Highly enriched  $^{120}\text{Te}$  oxide targets (99.4%) were prepared by resistive heating at the University of Notre Dame. The material was evaporated onto 1.5  $\text{mg}/\text{cm}^2$  thick Al foil and then placed on 1 cm diameter hole Ta target frames. The target thicknesses were on the order of 1  $\text{mg}/\text{cm}^2$ .

The target thicknesses were continuously monitored during the experiments by RBS (Figure 4.3). The measurements showed the targets were stable. Tests done with natural targets prior to the experiment showed that there was no deterioration with  $\alpha$ -beams up to 250eV.

#### 4.1.3 Counting Set-up

The irradiated targets were measured using a pair of Clover detectors placed face to face in close geometry (5 mm distance from face to face). The set-up is shown in Figure 4.4. Each clover detector consists of four individual crystals with a relative efficiency of 20%. The detectors were shielded by 5 cm of lead against room background and an inner Cu lining of 3 mm (Figure 4.5). A plastic holder joined the faces of the two detectors such that the target could slide into the exact center.

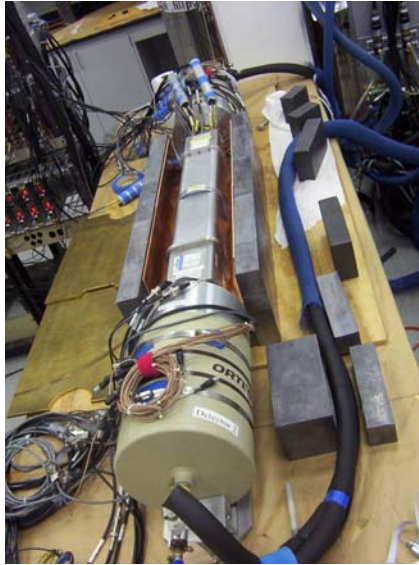


Figure 4.4 Two clover detectors placed in close geometry to measure offline  $\gamma$ -activity

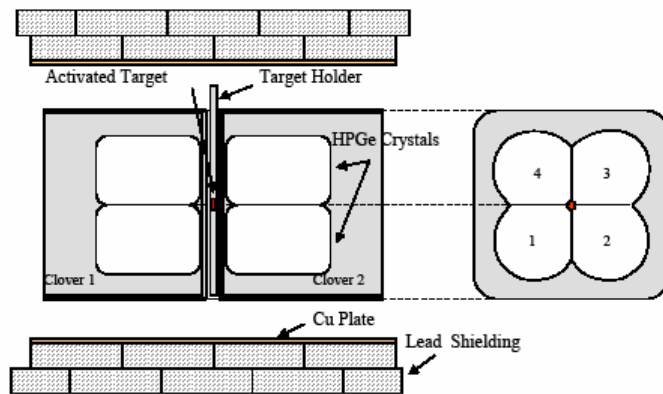


Figure 4.5 Schematic view of the inside of the clover counting set-up. The Pb is lined with 3 mm Cu plates [65].

#### 4.1.4 Electronics

In addition to detecting the produced radioactivity offline for cross section calculations, the half-life of  $^{110}\text{Sn}$  was also measured. This necessitates an accurate dead time estimate. This is complicated at higher energies where the count rates are high and varying; therefore, in addition to the acquisition dead time, the dead time in the electronics chain must be taken into account. Since each of the eight crystals was considered as one “detector” operated in direct mode [67], the  $\gamma$ -ray energy is detected in each crystal event-by-event.

The real time was produced by a fixed frequency generator (“oscillator” in Fig. 4.6). Two signals are produced. One sends a pulse every 8s for real time and the other is fed into one of the Ge amplifiers for dead time monitoring. Since the detector output contains both the actual detected signal and the produced pulse signal, one bit of the register module (NIM interrupt) was used every time a pulser signal was created [68]. Separate spectra can then be created for real and pulser events. The ratio of these gives the total live time of the system:

$$\text{Pulser in Live Trigger} / \text{Pulser} = 1 - \tau$$

where  $\tau$  is the total dead time of the detection system [68] (Figure 4.6).

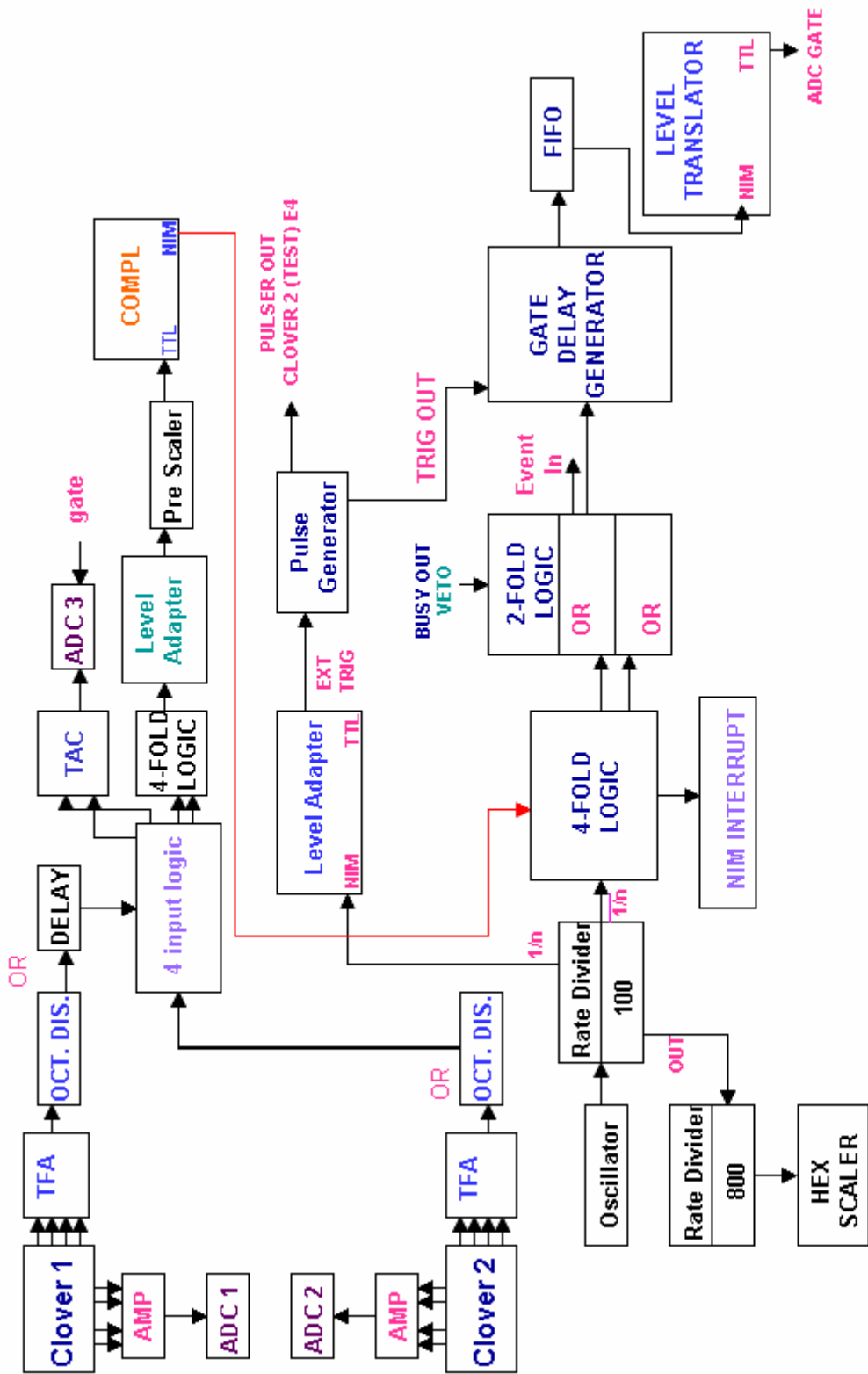


Figure 4.6 Electronics set-up for activation measurements

#### 4.1.5 Efficiency Determination

The absolute photopeak efficiencies of the detectors were determined using calibrated  $^{54}\text{Mn}$ ,  $^{60}\text{Co}$  and  $^{133}\text{Ba}$  sources and the energy range extended by also using an uncalibrated  $^{152}\text{Eu}$  source of unknown activity. Two separate methods were used to calculate the efficiency. The first was the standard method involving the decay branching ratios and the activities of the sources. Due to the high counting efficiency, summing corrections had to be taken into account. When defining efficiency, a distinction must be made between the total efficiency  $\varepsilon_t$  and the photopeak efficiency  $\varepsilon$ . The photopeak efficiency is defined as the count rate (number of counts in the peak divided by the measuring time) in the peak corresponding to the energy  $E$  divided by the rate at which photons are emitted from the source. The total efficiency, on the other hand, is the ratio of the number of pulses recorded in the spectrum and the number of photons emitted from the source [69]. Both follow the same mathematical relation:

$$\varepsilon = \frac{N_t}{A \cdot B_\gamma} \quad (4.7)$$

where  $N_t$  is the counting rate,  $A$  is the activity of the source and  $B_\gamma$  is the branching ratio of the particular gamma cascade of interest. If the source-detector distance is small (as was in our set-up), then  $N_t$  is significantly affected by coincidence summing. This effect occurs when the source emits two or more photons in sequence within the resolving time of the detector [69]. The 8 crystals were operated in “direct-mode” (each crystal is considered independently as a single detector). If two coincident photons are detected in the same crystal, then a sum pulse is seen which leads to the loss of events in the

photopeak of interest. This is referred to as “summing-out”. Summing corrections can be calculated by considering the probability of detecting other photons, emitted simultaneously by the decaying nucleus. A detailed calculation is given in Appendix B. Tables currently exist for calculating cascade-summing corrections in gamma-ray spectroscopy [70] for standard radioactive sources.  $N_t$  is then multiplied by this correction to obtain the counting rate without summing (see Appendix B). The corrections used in the tables given by [70] also include the total efficiency as an input. The total efficiency was obtained numerically by considering the source-detector distance, the thickness of any absorbers between source and crystal face, and the dimensions of the crystal. It was obtained from 50 keV to 2 MeV. The monoenergetic source  $^{54}\text{Mn}$  was used as a calibration to normalize the calculated total efficiency curve to our particular set-up. By using this and the photopeak efficiencies of  $^{133}\text{Ba}$  and  $^{60}\text{Co}$ , the correction factors were calculated from the equations in Appendix B and the photopeak efficiency from 100 keV to 1.5 MeV was obtained.

A second method was used to obtain the photopeak efficiencies [71]. This method has the advantage of allowing the efficiency to be determined without knowledge of the activity of the source. A  $^{152}\text{Eu}$  source of unknown activity was used as a check of the previous method.  $^{152}\text{Eu}$  has a complicated decay scheme (see Appendix B); however, 73% of the time  $^{152}\text{Eu}$   $\beta^-$  decays to  $^{152}\text{Gd}$ . For the 779-344 keV transition, the efficiency at 779 keV can be determined by:

$$\varepsilon(779) = \frac{(779 - 344)\text{coin}}{344(\text{all}) \cdot B.R.} \quad (4.8)$$

A gate is made on one crystal in clover #1 around the 344 keV region and the 4 crystals in clover #2 are checked for the 779 keV coincidences. This then is divided by the singles spectra of 344 keV of all 8 crystals times the branching ratio (B.R.) of this particular cascade. The photopeak efficiency of 779 keV is then the sum of the result from clover 1 and clover 2. In this particular method, the photopeak efficiency of 779 keV was computed to be  $9.51\% \pm 0.036\%$ . If we compare it to the value obtained by the first method, we get  $9.55\% \pm 0.18\%$ . Both methods agree within the uncertainties (see Appendix B). For 280.5 keV (the gamma ray of interest for the  $^{106}\text{Cd}(\alpha,\gamma)^{112}\text{Sn}$  reaction), the photopeak efficiency had a value of  $22.3 \pm 0.5\%$ . Figure 4.7 shows the photopeak efficiency obtained from  $^{152}\text{Eu}$  plotted on a log-log scale.

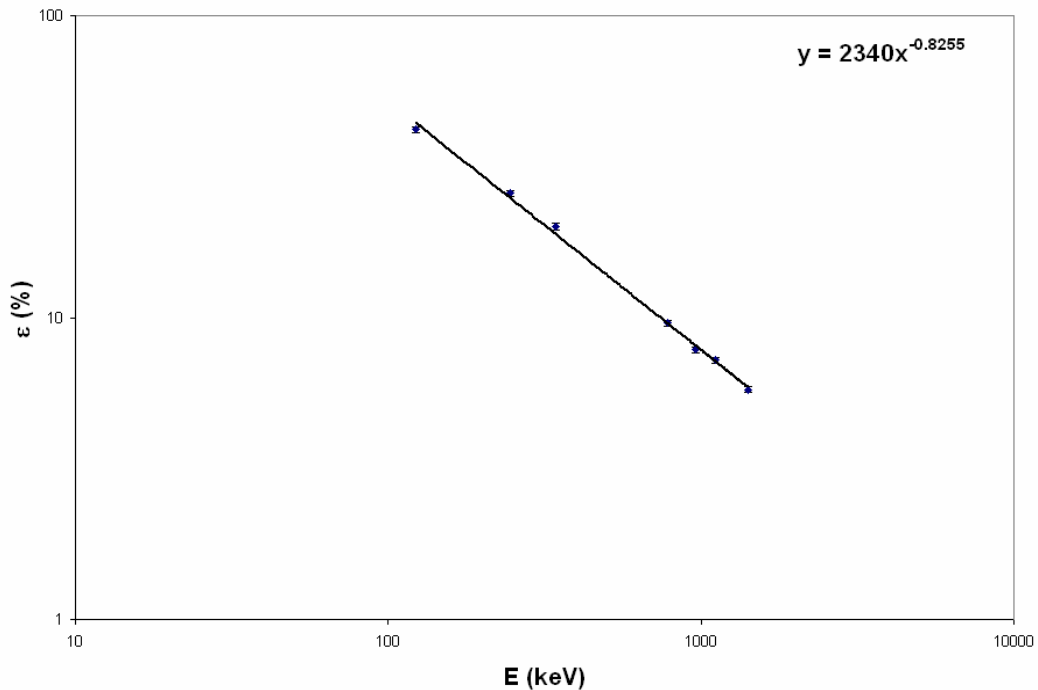


Figure 4.7 Photopeak efficiency determined from  $^{152}\text{Eu}$ .

## 4.2 Activations

The peak of the Gamow window for  $^{106}\text{Cd}(\alpha,\gamma)^{110}\text{Sn}$  at a p-process temperature of  $T_9 = 3.0$  is located at 7.21 MeV; its width is about 4 MeV. The lowest energy reached in the experiment was  $E_{\text{c.m.}} = 7.56$  (well within the Gamow window). The measurements extended up to 12.06 MeV to probe the reliability of the Hauser-Feshbach predictions over a wider energy range [64]. The activations at Notre Dame were carried out at beam energies between 7.0 and 12.0 MeV. Data below 8 MeV couldn't be obtained because of a strong Compton background caused by a  $\gamma$  line ( $E_\gamma = 373$  keV) from the reaction of  $^{40}\text{Ca}(\alpha,p)^{43}\text{Sc}$  that overwhelmed the 280.5 keV  $\gamma$ -line of interest (see Figure 4.8) [64].

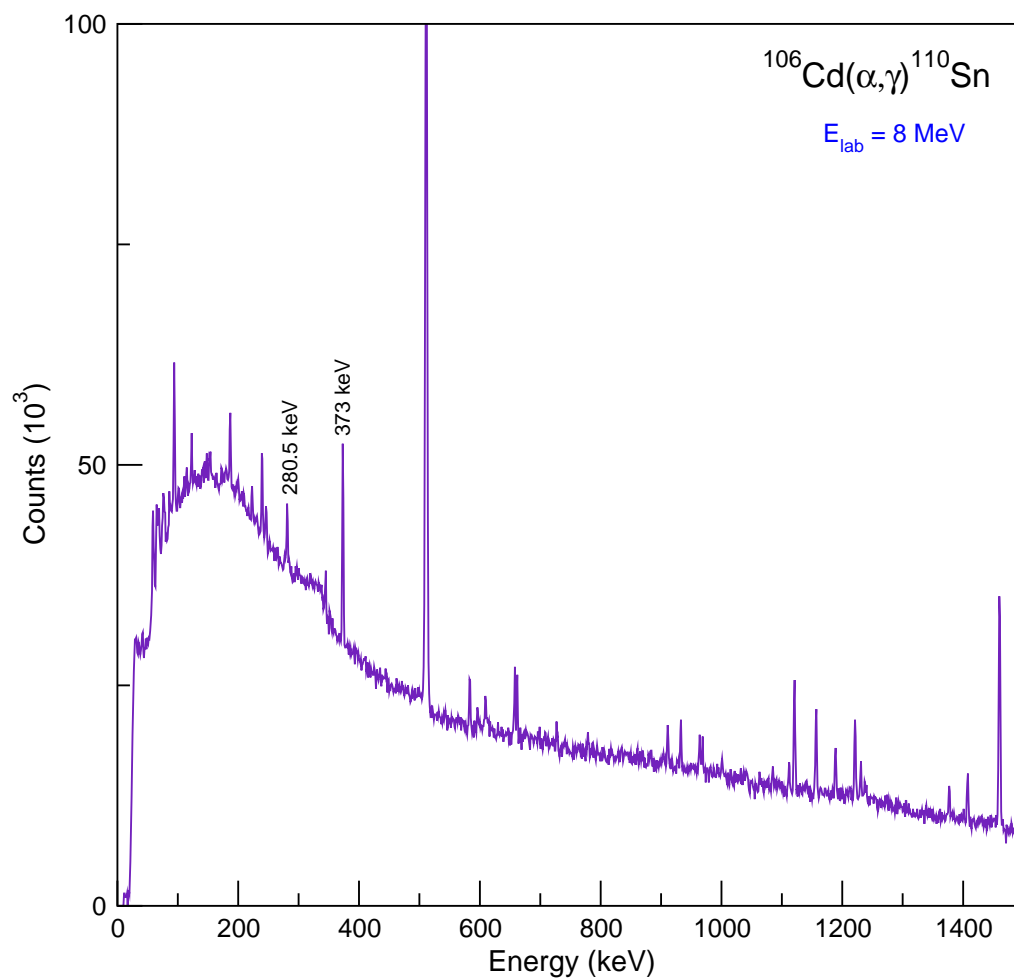


Figure 4.8 The  $^{106}\text{Cd}(\alpha,\gamma)^{110}\text{Sn}$  reaction at the lowest measured energy.

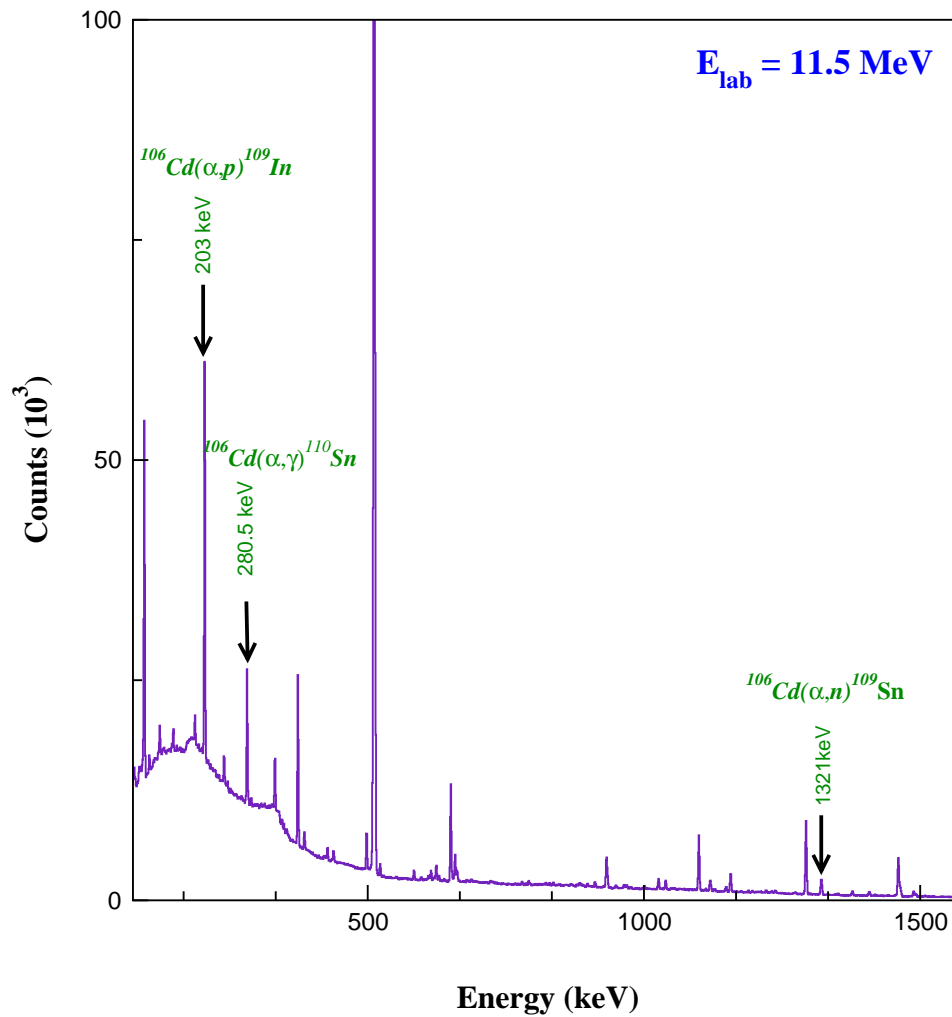


Figure 4.9 The  $^{106}\text{Cd} + \alpha$  reactions that are open at  $E_{\text{lab}} = 11.5 \text{ MeV}$ .

$^{40}\text{Ca}$  is a common contaminant that has a much lower Coulomb barrier than that of  $^{106}\text{Cd}$  and the half-life of  $^{43}\text{Sc}$  is comparable to that of  $^{110}\text{In}$  [64]. Due to the larger Coulomb barrier, the  $^{106}\text{Cd} + \alpha$  cross sections drop much faster than that of the  $^{40}\text{Ca} + \alpha$  reaction at lower beam energies (Figure 4.9) [64].

The  $^{120}\text{Te}(\alpha,n)^{123}\text{Xe}$  reaction channel opens above 10 MeV; therefore, the cross section was measured at a lab energy of 10.5 and 11 MeV. Figure 4.10 shows the activation spectrum of  $^{120}\text{Te}(\alpha,n)^{123}\text{Xe}$  at  $E_{\text{lab}} = 10.5$  MeV. During an activation, the optimum production rate is reached at about 2-3 half-lives, therefore, the counting time for the decay of the produced radioactivity was 2 half-lives (Table 4.1).

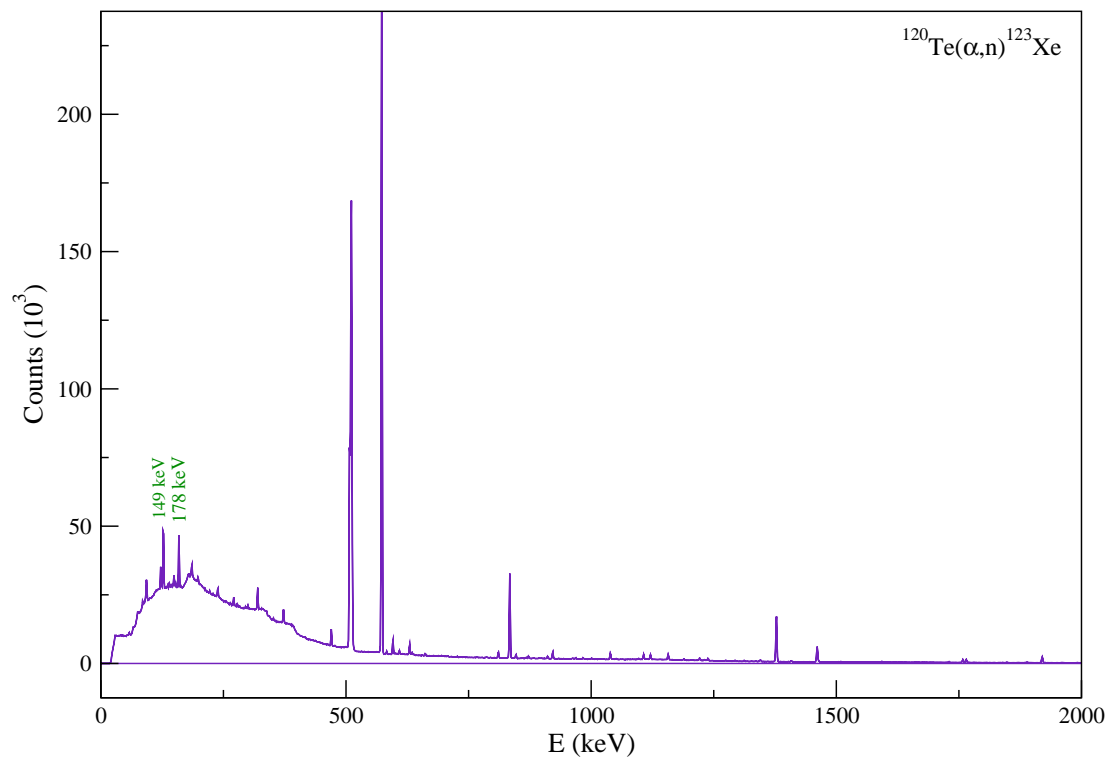


Figure 4.10 Activation spectrum of  $^{120}\text{Te}(\alpha,n)^{123}\text{Xe}$  at  $E_{\text{lab}} = 10.5$  MeV.

TABLE 4.1  
 DECAY PARAMETERS OF  $^{106}\text{Cd}+\alpha$  REACTION PRODUCTS AND OF  
 $^{120}\text{Te}(\alpha,n)^{123}\text{Xe}$

Product nucleus	Half-life (h)	Gamma energy (keV)	Relative $\gamma$ Intensity per decay (%)	Ref.
$^{110}\text{Sn}$	$4.173 \pm 0.023$	280.5	97	[72]
	$(4.11 \pm 0.1)$			[73]
$^{109}\text{Sn}$	$(18.0 \pm 0.2)\text{m}$	1099.2	30.1 3.0	[74]
		1321.3	11.9 1.4	
$^{109}\text{In}$	$4.167 \pm 0.018$	203.5	73.5 0.5	[74]
$^{123}\text{Xe}$	2.08	148.9	48.9	[75]
		178.1	14.99	[75]

The new half-life of  $^{110}\text{Sn}$  [72] was used in the determination of the cross section.

#### 4.2.1 Cross Section calculation

In addition to allowing for the removal of beam induced background, measuring the radioactive target offline allows for an optimization of the detector set-up. Figure 4.11 shows the decay scheme of the radioactive product from the reaction of  $^{106}\text{Cd}(\alpha,\gamma)^{110}\text{Sn}$ . In this case, the scheme is simple and there is only one  $\gamma$ -ray (no summing corrections need to be considered).

The decay scheme for  $^{120}\text{Te}(\alpha,n)^{123}\text{Xe}$  is much more complicated.  $^{123}\text{Xe}$  decays 100% of the time to  $^{123}\text{I}$ . Although  $^{123}\text{I}$  produces many  $\gamma$ -lines, there are two dominant ones at 149 keV (48.9%) and at 178 keV (14.9%) (Figure 4.12)

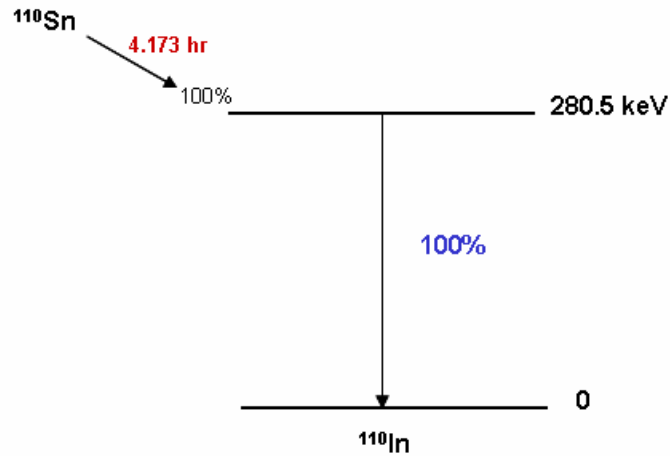


Figure 4.11 Decay scheme for  $^{106}\text{Cd}(\alpha,\gamma)^{110}\text{Sn}$

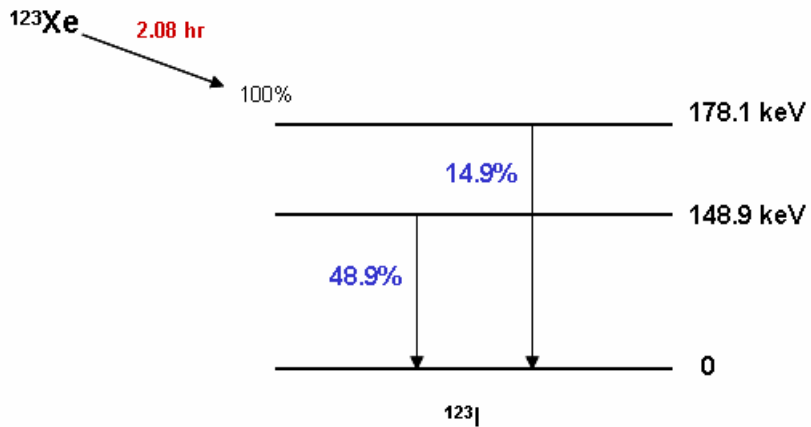


Figure 4.12 Simplified decay scheme of the  $^{120}\text{Te}(\alpha,n)^{123}\text{Xe}$  reaction (the two dominant  $\gamma$ -transitions used in the analysis are shown).

The number of radioactive nuclei (after the irradiation),  $N_{irr}$ , is:

$$N_{irr} = n_t \sigma(E) \int_0^{t_{irr}} I(t) e^{-(t_{irr}-t)/\tau} dt \quad (4.1)$$

where  $I(t)$  is the particle current of the incident beam,  $n_t$  is the target density in nuclei/cm<sup>2</sup>,  $\tau$  is the lifetime of the nuclei created, and  $t_{irr}$  is the duration of the irradiation.

The counting time happens from a period starting at  $t_1$  after the irradiation until a time  $t_2$ .

The above integral can be expressed as

$$N_{irr} = n_t \sigma(E) \sum_{i=1}^{N_{ch}} \frac{Q_i \exp\left[-\frac{(N_{ch} - i)}{\tau} \Delta t\right]}{ne} \quad (4.2)$$

where  $\Delta t$  represents the time duration of each channel,  $i$  is a summing index,  $ne$  is the charge state,  $Q_i$  is the integrated charge (per channel) and  $N_{ch}$  is the number of channels of the beam collection (each lasting  $\Delta t$  seconds). The number of decays that will occur during this counting time,  $N_{decay}$ , including those possible from  $N_{left}$  undecayed nuclei from previous irradiations that remain at the end of the new irradiation, will be

$$N_{decay} = (N_{irr} + N_{left}) \exp\left(\frac{-t_1}{\tau}\right) \left(1 - \exp\left[\frac{-(t_2 - t_1)}{\tau}\right]\right) \quad (4.3)$$

Assuming a previously irradiated target has no residual radioactivity before being irradiated again, then  $N_{left} = 0$  and the above equation becomes:

$$N_{decay} = N_{irr} \exp\left(\frac{-t_1}{\tau}\right) \left(1 - \exp\left[\frac{-(t_2 - t_1)}{\tau}\right]\right) \quad (4.4)$$

The photopeaks observed in the resulting spectra ( $N_{decay}$ ) are a function of the detection efficiency ( $\epsilon$ ), the number of counts per  $\gamma$ -line ( $N_\gamma$ ), summing corrections ( $S_c$ ), correction

for  $\gamma$ -self absorption in target ( $K_{abs}$ ), and the branching ratio of the particular  $\gamma$ -line of interest ( $I_\gamma$ ):

$$N_{decay} = \frac{N_\gamma S_C K_{abs}}{I_\gamma \epsilon_\gamma} \quad (4.5)$$

Combining equations 4.2, 4.4, and 4.5, allows for the determination of the cross section:

$$\sigma(E) = \frac{N_\gamma S_C K_{abs} n e}{I_\gamma \epsilon \exp\left(\frac{-t_1}{\tau}\right) \left(1 - \exp\left[\frac{-(t_2 - t_1)}{\tau}\right]\right) \sum_{i=1}^{N_{ch}} Q_i \exp\left[\frac{-(N_{ch} - i)\Delta t}{\tau}\right]} \quad (4.6)$$

where the units are  $\text{cm}^2$ .

The correction for  $\gamma$ -self absorption ( $K_{abs}$ ) in the target is negligible for our target thicknesses.  $S_C$  is equal to one for the  $^{106}\text{Cd}(\alpha, \gamma)^{110}\text{Sn}$  reaction since only one  $\gamma$ -transition occurs (see Figure 4.11). Summing corrections had to be taken into account for the decay of the radioactive product of  $^{106}\text{Cd}(\alpha, p)$  and  $^{120}\text{Xe}(\alpha, n)$  since several  $\gamma$ 's were emitted in that decay (Figures 4.12 and 4.13). The branching ratio ( $I_\gamma$ ) is taken from literature [75] and the rest are experimentally determined quantities to be discussed in the following sections.

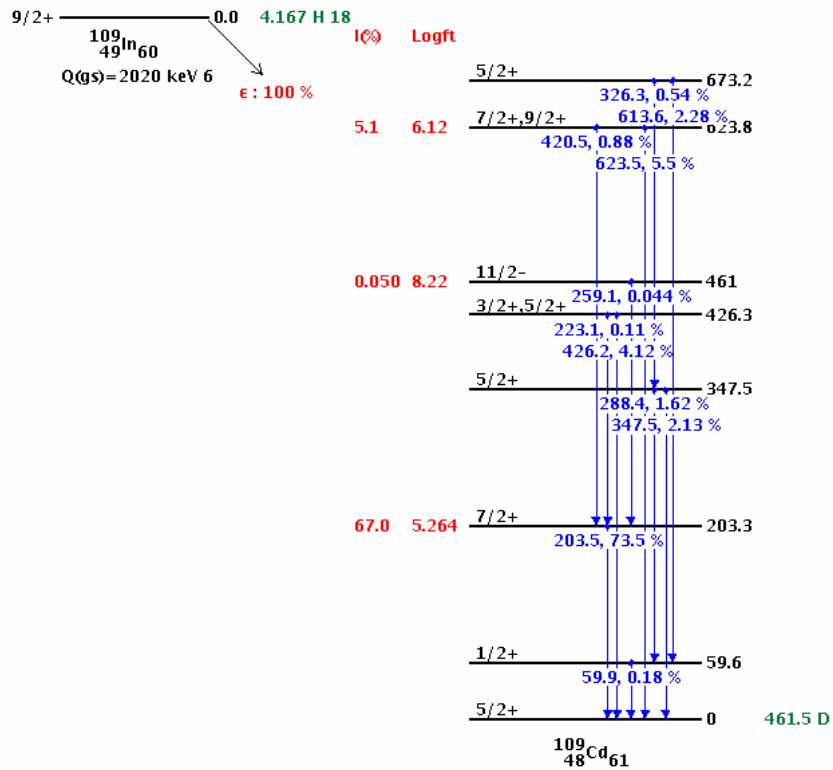


Figure 4.13 Simplified decay scheme of  $^{106}\text{Cd}(\alpha, p)^{109}\text{In}$ .

### 4.3 Results

The cross sections and S-factors for the reactions  $^{106}\text{Cd}(\alpha, \gamma)^{110}\text{Sn}$ ,  $^{106}\text{Cd}(\alpha, p)^{109}\text{In}$ , and  $^{120}\text{Te}(\alpha, n)^{123}\text{Xe}$  are listed in Tables 4.2, 4.3, and 4.4. The second column shows the effective center-of-mass energies. The error associated with this arises from the uncertainty in the calculation. The error of the Notre Dame cross section (S-factor) values is the quadratic sum of the following partial errors: detector efficiency (2.3%), number of target atoms (target thickness) (9%), current measurements (3%), uncertainty of the level parameters found in literature ( $\leq 12\%$ ), and counting statistics

(0.17-14%) [64]. For the ATOMKI measurement, the quoted errors of the energies include the energy loss in the targets calculated with the SRIM code [76], the energy stability of the cyclotron and the energy straggling in the degrader foil where it was applied [64].

TABLE 4.2

CROSS SECTION AND S-FACTOR OF  $^{106}\text{Cd}(\alpha,\gamma)^{110}\text{Sn}$ 

$E_{\text{beam}}$ (MeV)	$E_{\text{c.m.}}^{\text{eff}}$ (MeV)	Cross Section ( $\mu\text{b}$ )	S factor ( $10^{21}$ MeV b)
Notre Dame			
8	7.566 +/- 0.01	0.078 +/- 0.014	164 +/- 29
8.5	8.040 +/- 0.01	0.480 +/- 0.0148	141 +/- 14
9	8.513 +/- 0.011	2.59 +/- 0.26	126 +/- 13
9.5	8.992 +/- 0.012	11.8 +/- 1.2	108 +/- 11
10	9.466 +/- 0.012	46.4 +/- 4.6	92.7 +/- 9.3
10	9.470 +/- 0.012	48.3 +/- 4.8	95.3 +/- 9.5
10*	9.599 +/- 0.012	75.1 +/- 5.4	99.9 +/- 7.7
11	10.429 +/- 0.014	244 +/- 24	30.6 +/- 3.6
11.5	10.909 +/- 0.014	434 +/- 43	15.8 +/- 1.6
12	11.385 +/- 0.015	596 +/- 61	6.85 +/- 0.70
Atomki			
8.5	8.123 +/- 0.029	0.85 +/- 0.37	180 +/- 78
9.008	8.632 +/- 0.026	4.87 +/- 0.55	155 +/- 18
11.300*	9.108 +/- 0.049	22.8 +/- 2.9	143 +/- 18
10	9.599 +/- 0.030	79.1 +/- 8.2	105 +/- 11
11.2 <sup>a</sup>	9.909 +/- 0.036	147 +/- 15	78.4 +/- 8.1
10.8	10.371 +/- 0.033	234 +/- 24	34.3 +/- 3.5
11.2	10.775 +/- 0.033	298 +/- 31	15.1 +/- 1.6
11.6	11.167 +/- 0.034	507 +/- 53	9.8 +/- 1.0
12.4 <sup>a</sup>	11.167 +/- 0.037	471 +/- 49	9.08 +/- 0.94
11.998	11.544 +/- 0.035	601 +/- 62	4.78 +/- 0.50
12.523 <sup>b</sup>	12.050 +/- 0.036	1270 +/- 150	3.28 +/- 0.39
12.523	12.057 +/- 0.036	1280 +/- 133	3.26 +/- 0.34

a: energy degrader foil, b: natural Cd target, \*: Atomki target [64].

TABLE 4.3

CROSS SECTION AND S-FACTOR OF  $^{106}\text{Cd}(\alpha,p)^{109}\text{In}$ 

$E_{beam}$ (MeV)	$E_{c.m.}^{eff}$ (MeV)	Cross Section ( $\mu\text{b}$ )	S factor ( $10^{21}$ MeV b)
<b>Notre Dame Results</b>			
9.500	$8.992 \pm 0.012$	$0.24 \pm 0.04$	$2.23 \pm 0.35$
10.000	$9.470 \pm 0.012$	$2.76 \pm 0.28$	$5.45 \pm 0.55$
10.000*	$9.599 \pm 0.010$	$5.70 \pm 0.67$	$7.85 \pm 0.89$
<b>Atomki</b>			
10.000	$9.599 \pm 0.030$	$6.0 \pm 0.8$	$8.0 \pm 1.1$
11.200 <sup>a</sup>	$9.909 \pm 0.036$	$39.6 \pm 4.2$	$21.1 \pm 2.2$

a: energy degrader foil, \*:Atomki target [64].

TABLE 4.4

CROSS SECTION AND S-FACTOR OF  $^{120}\text{Te}(\alpha,n)^{123}\text{Xe}$ 

$E_{beam}$ (MeV)	$E_{c.m.}^{eff}$ (MeV)	Cross Section ( $\mu\text{b}$ )	S factor ( $10^{24}$ MeV b)
<b>Notre Dame Results</b>			
10.5	10.16	$56.28 \pm 6.3$	$2.69 \pm 0.30$
10.5	10.16	$47.15 \pm 7.2$	$2.25 \pm 0.34$
11.0	10.64	$114.4 \pm 1.1$	$1.32 \pm 0.1$
11.0	10.64	$116.8 \pm 1.3$	$1.35 \pm 0.2$

The first set of values is that obtained using the 149 keV  $\gamma$ -transition while the second is from the 178 keV transition.

To test for systematic uncertainties, the  $^{106}\text{Cd}(\alpha,\gamma)^{110}\text{Sn}$  cross section was measured at Notre Dame at the same beam energy (10 MeV) using an ATOMKI target. The value obtained for the cross section of the ATOMKI target at Notre Dame at a beam energy of 10 MeV is  $75.1 \pm 5.4 \mu\text{b}$ . In comparison, the value obtained at the same beam energy with an identical target thickness at the ATMOKI set-up yields a value of  $79.1 \pm 8.2 \mu\text{b}$ . The results agree within the errors.

Figures 4.13, 4.14, and 4.15 show a comparison of the experimental results to the Hauser-Feshbach statistical model cross sections [77] obtained with the standard settings of NON-SMOKER [77,78,79]. The predicted cross sections are too low in the case of the  $(\alpha,p)$  reaction. In the case of the  $(\alpha,\gamma)$  data, there is a discrepancy of a factor of 5 in cross section at the lowest energy while at the higher energies the discrepancy is on the order of 2.2. For the  $^{120}\text{Te}(\alpha,n)^{123}\text{Xe}$  data, there is a 1.4 overestimation of theory to data in cross section for the lowest energy point; however, there is a three order of magnitude overestimation in S-factor. The comparison of data to theory will be further addressed in Chapter 6.

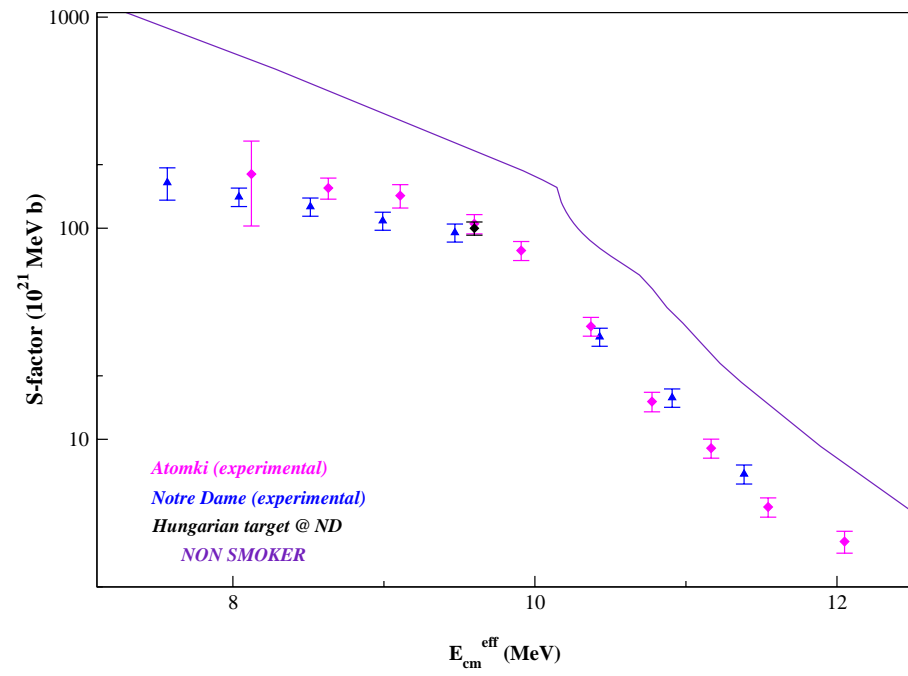
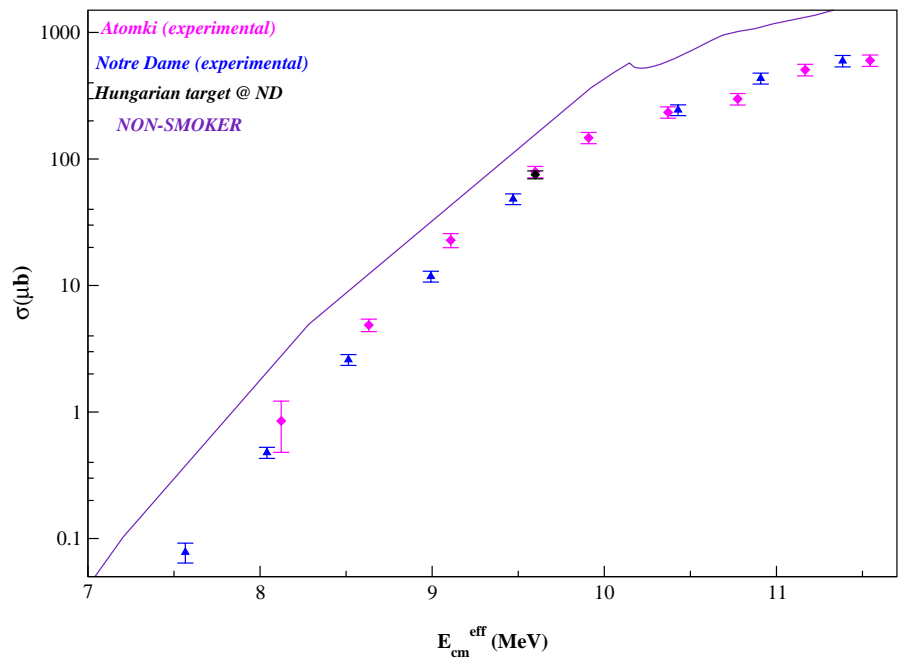


Figure 4.14 Cross Section and S-factor of  $^{106}\text{Cd}(\alpha,\gamma)^{110}\text{Sn}$

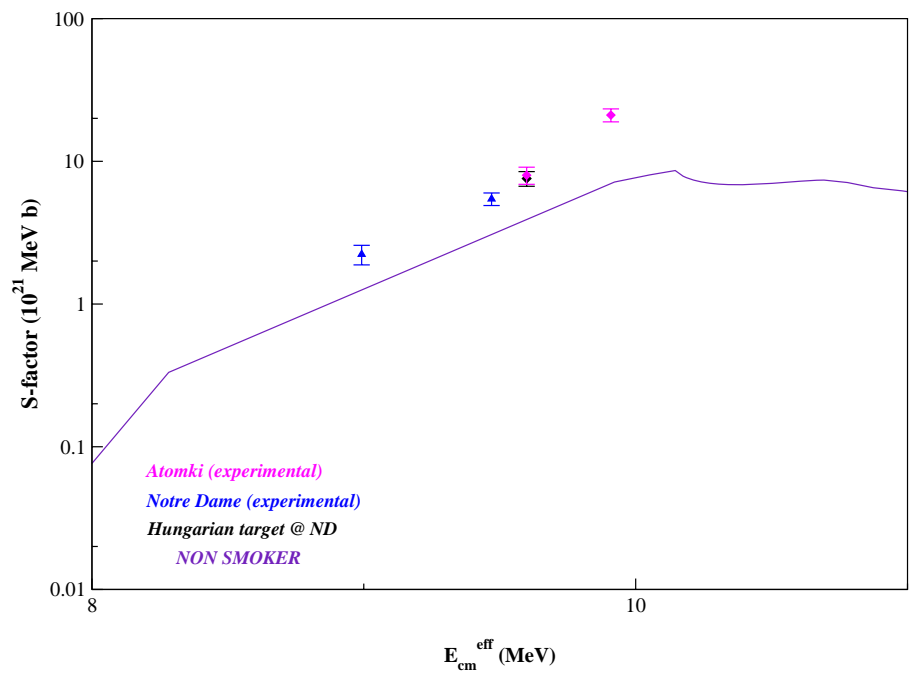
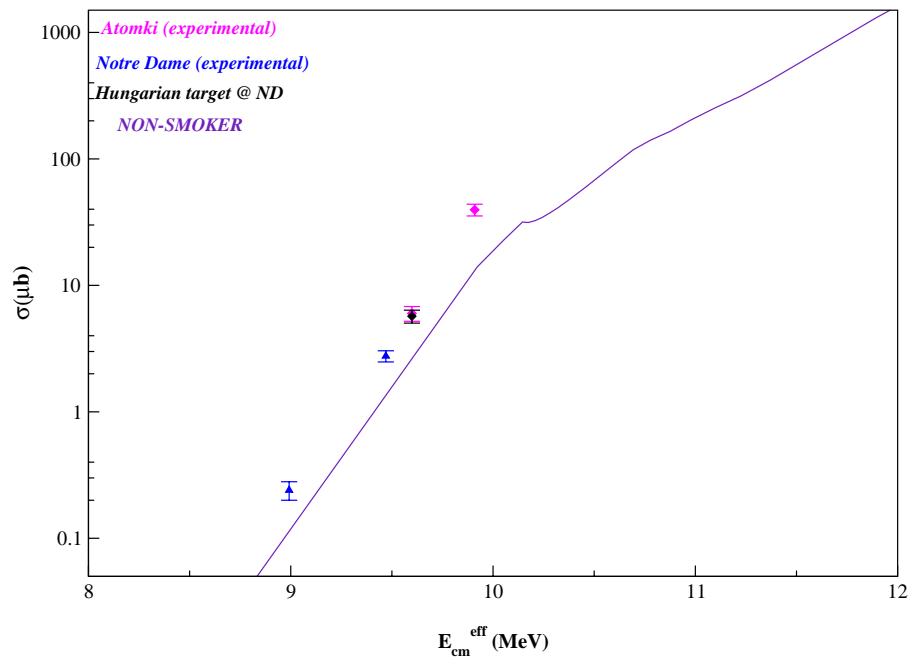


Figure 4.15 Cross Section and S-factor of  $^{106}\text{Cd}(\alpha,p)^{109}\text{In}$

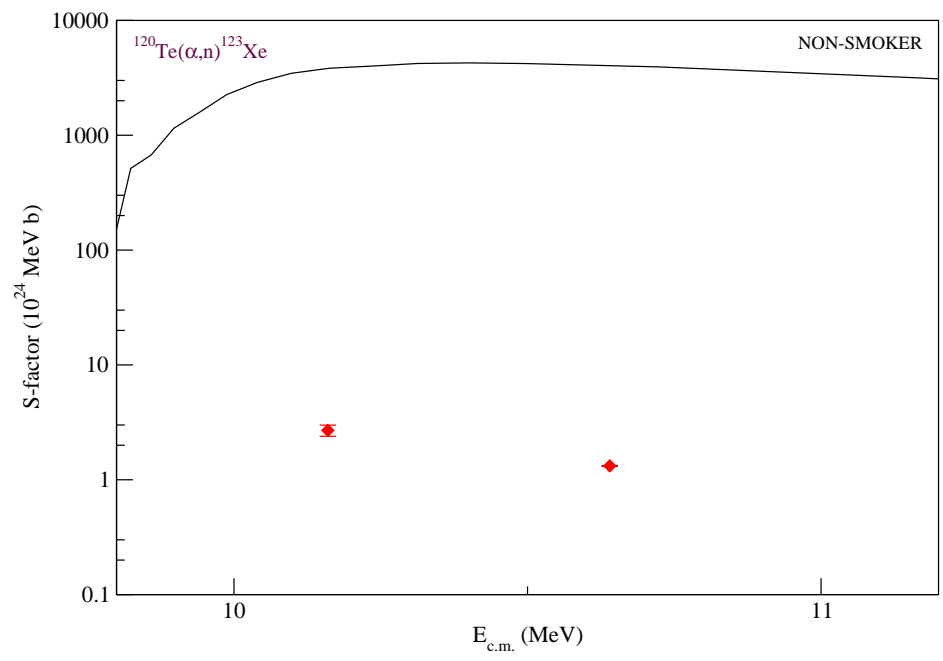
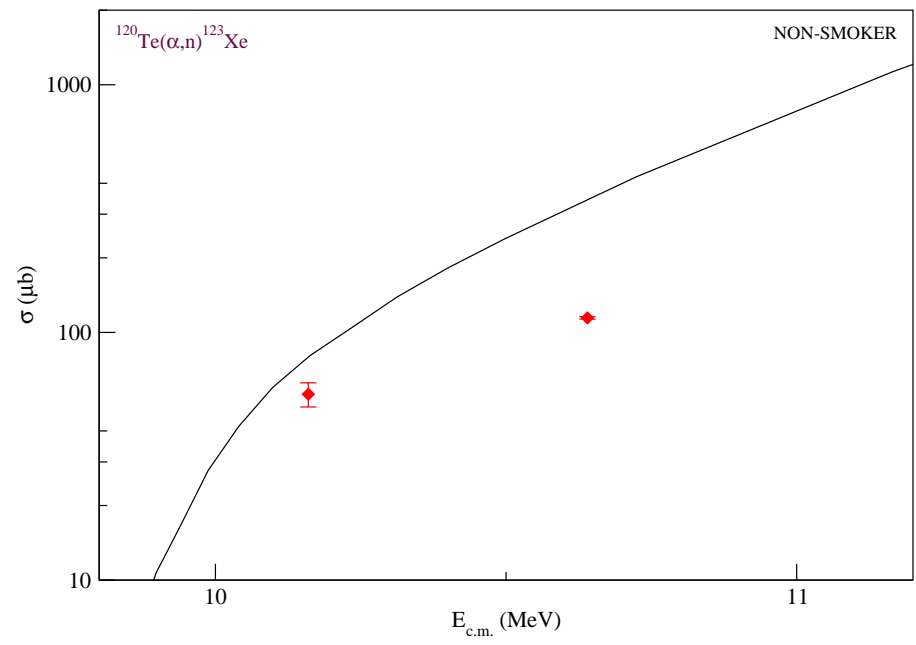


Figure 4.16 Cross Section and S-factor of  $^{120}\text{Te}(\alpha,n)^{123}\text{Xe}$ . Results using the 149 keV  $\gamma$ -transition are shown.

## CHAPTER 5

### ELASTIC SCATTERING EXPERIMENTS

#### 5.1 $\alpha$ -scattering on p-nuclei

In addition to measuring  $\alpha$ -capture cross sections of p-nuclei (which allow a direct comparison of theory to experiment), a sensitive probe of the global parameterizations used within the statistical model, namely the global  $\alpha$ -nucleus potentials, can be achieved via elastic scattering experiments.

To date, the behavior of the  $\alpha$ -nucleus potential at energies below the Coulomb barrier is not well understood. While elastic scattering allows the determination of local potentials, certain constraints must be taken into account. One large experimental deterrent is the enrichment of the p-nucleus. While  $\alpha$ -capture experiments can sometimes be achieved with lower enrichment, an enrichment of 90% is needed for elastic scattering experiments (for the closeness in masses of the scattered particles). Table 5.1 shows the natural abundances of the isotopes used in the measurement and their percent enrichment ( $^{106}\text{Cd}$  and  $^{120}\text{Te}$  are the p-nuclei).

TABLE 5.1  
ENRICHMENT

Isotope	Abundance	Enrichment
<sup>106</sup> Cd	1.25%	86.4%
<sup>118</sup> Sn	24.23%	97.0%
<sup>120</sup> Te	0.096%	99.4%
<sup>124</sup> Te	4.82%	99.5%
<sup>126</sup> Te	18.95%	99.0%
<sup>128</sup> Te	31.69%	98.8%
<sup>130</sup> Te	33.80%	99.8%

The isotopes with their corresponding natural abundance and the degree of enrichment used. Note the very low natural abundance of <sup>120</sup>Te.

In addition, the angular distribution in the full angular range with high precision has to be determined in order to reliably extract the nuclear potentials. Below the Coulomb barrier, the cross section is dominated by the electromagnetic interaction and it is difficult to derive the potential unambiguously. While the potential can be uniquely determined at high energies ( $\geq 100$  MeV [38]), we are interested in astrophysical energies which are well below the barrier.

The real part of the nuclear potential can be fairly well determined (below the barrier) [43,80] but there is a very strong energy dependence of the imaginary part of the nuclear potential below the barrier [43]. In fact, it has been shown that transmission coefficients in statistical model calculations depend sensitively on the volume integral  $J_I$  and also on the shape of the imaginary part of the potential [80]. All of these issues must be considered when performing experiments on p-nuclei. In this case, a compromise has

to be reached. It is necessary to go above the barrier in order to extract nuclear properties but it is necessary to also measure below in order to ensure that the extrapolation down to sub-barrier energies (in particular within the Gamow window) will be as accurate as possible.

In the current study, the mass and energy dependence of the  $\alpha$ -nucleus potential is probed by elastic scattering on the p-nucleus  $^{120}\text{Te}$  and its neutron richer counterparts  $^{124,126,128,130}\text{Te}$  at 17, 19 (Coulomb barrier), 22, 24.5 ( $^{120,124,128}\text{Te}$  only) and 27 MeV ( $^{120,124,128,130}\text{Te}$ ). In addition, the charge dependence is also tested via scattering on  $^{118}\text{Sn}$ . To test for any hidden systematic errors of different experimental set-ups,  $^{106}\text{Cd}$  was remeasured [81] and extended to higher energies.

### 5.1.1 Enriched $^{120,124,126,128,130}\text{Te}$ , $^{118}\text{Sn}$ and $^{106}\text{Cd}$ targets

In order to ensure a clear identification of the elastically scattered  $\alpha$ -particles, relatively thin targets (between 100-300  $\mu\text{g}/\text{cm}^2$ ) are used; however, a too thin target decreases the yield so it is important to balance the two. Another problem that can arise is if the material has a low melting point. Both metallic Te (450° C) and Te oxide (733° C) targets were used. When exposed to particle beam, self-supporting metallic Te targets degrade quickly [82]. Hence, the targets are evaporated onto C backings to help with heat conduction. Evaporated metallic and oxide Te targets were prepared at Argonne National Lab by vacuum deposition from a resistively heated source boat [83]. The  $^{106}\text{Cd}$  targets (metallic) were prepared by electron gun by Micromatter and the thicknesses were

270  $\mu\text{g}/\text{cm}^2$ . The  $^{118}\text{Sn}$  oxide targets were also evaporated onto C backings and were prepared at Notre Dame by resistive heating. The thicknesses of the Sn oxide targets were 145 and 170  $\mu\text{g}/\text{cm}^2$  (see Appendix A). Target tests prior to experiment showed that the oxide targets could withstand currents of up to 300 enA without deterioration while for the metallic targets it was up to 150enA.

### 5.1.2 Detection System

Thirty two Si pin diode detectors (500  $\mu\text{m}$  thicknesses and an active area of 9x9 mm) were placed in the 1.6 m diameter scattering chamber. The detectors were mounted on a rotatable table that consisted of 100° arcs attached to a supporting frame (see Figure 5.1). Thirty detectors were placed on the rotatable table allowing for the complete angular range from 22° to 168° in 2.5° increments. The detectors were placed at a distance of 25.3'' from the target while two monitor detectors were fixed at a distance of 25.71'' and placed at 15° on either side of the beam axis. In order to avoid very high counting rates and to achieve a high angular resolution, different collimators were placed in front of the detectors. The solid angle covered by the monitor detectors was  $\Delta\Omega_M \approx 1 \times 10^{-5}$  sr each while for the other rotatable detectors it was  $\Delta\Omega_{\text{all}} \approx 8 \times 10^{-5}$  sr each.

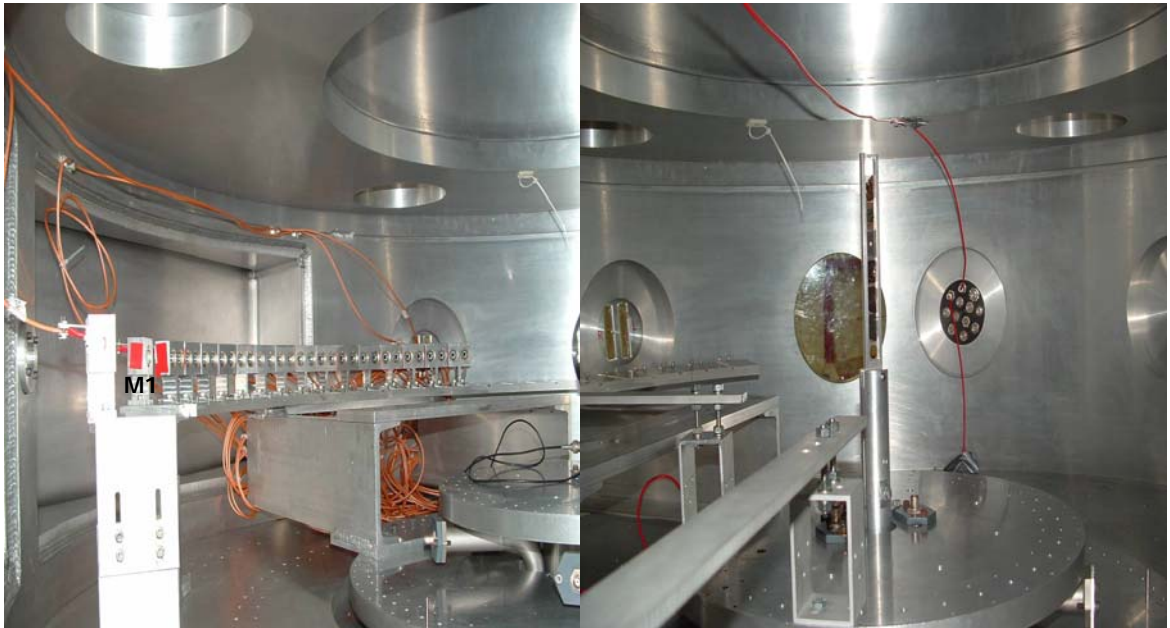


Figure 5.1 Inside view of the scattering chamber. The left view shows the Si pin diode detectors mounted on a rotatable table and the two fixed monitor detectors. The right view shows the moveable (both transitional and rotational) target ladder.

Three different angular spans were used for each isotope for each energy. The most forward orientation covered the angular range from  $22.5^\circ$  to  $95^\circ$  while the second spanned from  $32.5^\circ$  to  $105^\circ$  and the backward range covered from  $95^\circ$  to  $167.5^\circ$  in  $2.5^\circ$  increments (Figure 5.2). The angular position of each detector was known to  $0.01^\circ$  accuracy. The angles were determined by aligning the left and right edge of each collimator with a telescope placed at  $0^\circ$  outside the chamber. The exact center of the detector was determined in this way. An electronic and mechanical reading outside of

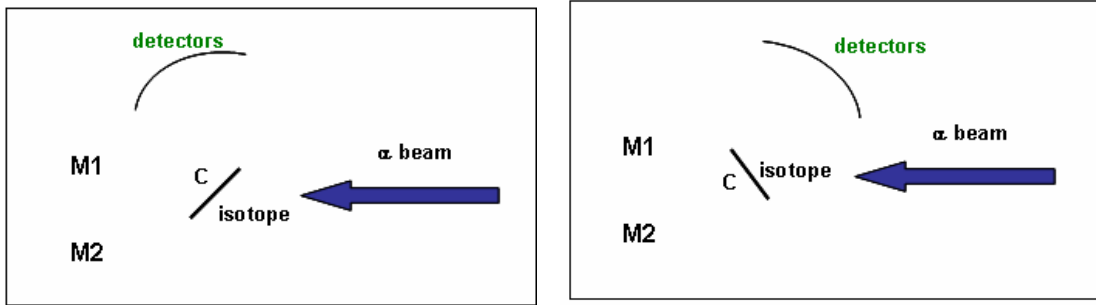


Figure 5.2 Forward (left) and Backward (right) orientations of the detectors and targets.

the chamber verified that the position of the exact center of each detector could be reproduced to an accuracy of  $0.01^\circ$ .

The charge was integrated via a Faraday cup that was located on the beamline after the scattering chamber that was electrically insulated from the chamber itself. Prior to each energy change, the beam was tuned through a 2 mm diameter collimator on the target position to ensure a small and well tuned beam spot.

### 5.1.3 Electronics

Thirty-two Si pin diode detectors were biased at +90V. Two high density charge sensitive preamplifier boxes (each capable of taking 16 channels) were supplied with +/-12V in addition to the bias voltage input (supplied by a Tennelec 953 dual HVPS). The preamp signals were then fed into Caen (model N568 LC) amplifiers. From here, the shaped energy signals are readout by the Camac (v785) ADC and the timing signals are sent to the Oct. CF discriminator for further processing and trigger construction. The deadtime was constructed by taking the ratio of the livetrigger over the

trigger (any event from the 32 detectors). Beam current was limited so that the two monitor detectors had countrates not exceeding 3K. Figure 5.3 shows the electronics set-up in detail.

#### **5.1.4 Solid Angle Determination**

High precision solid angle determination is one of the most important ways to reduce systematic error. In the very forward angles ( $50^\circ$  and below for 17 MeV and  $35^\circ$  and below for 27 MeV), the largest source of error comes from systematic error due to the solid angle determination. Three independent methods were used to measure the solid angle. An error of only 1% was achieved. The first method was done previous to the start of the experiment. Each of the 32 collimators were placed directly in front of a Si barrier detector and a calibrated alpha source was positioned at a distance of 3.432'' from the detector in a small chamber. The solid angle is given by:

$$\Omega = \text{Area}/d^2 \quad (5.3)$$

The solid angle ( $\Omega$ ) can be determined by dividing the observed number of decays/sec from the  $\alpha$ -source by its activity. Since  $d$  is known (the distance of the source to the collimator), the exact dimension of the collimator can be obtained.

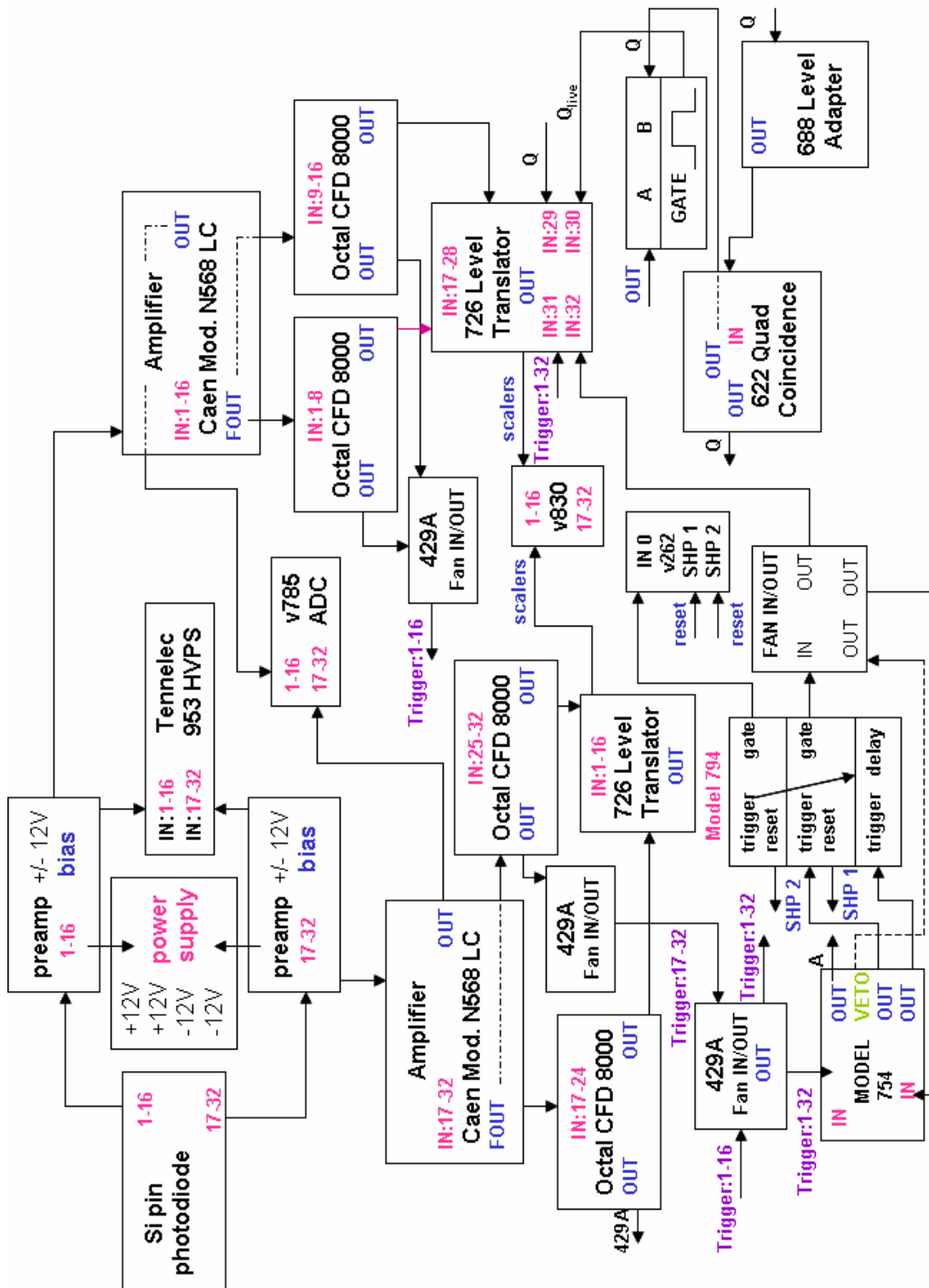


Figure 5.3 Electronics set-up for elastic scattering measurements

A second method was done post experiment in the scattering chamber by placing an alpha source in the target ladder position and by the same method as above (and positioning the detectors in the forward running position), the solid angle was again measured. A comparison of the two previous methods shows a 1% error arising from the collimator diameter (Figure 5.4)

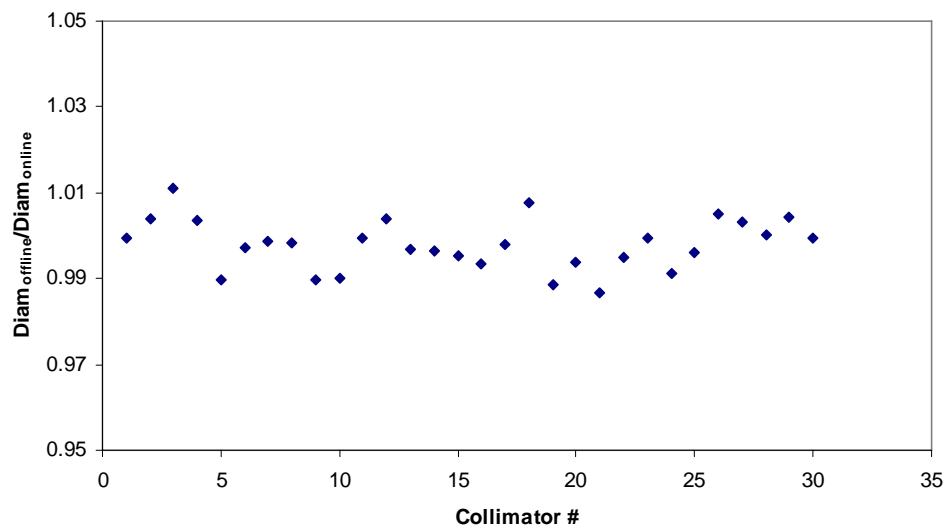


Figure 5.4 Ratio of the diameters of the collimators obtained from the offline method versus the online method (1<sup>st</sup> two methods). A deviation of 1% is obtained.

The solid angle obtained from the measurement post experiment in the scattering chamber was used in the cross section calculation.

The last method was performed during the experiment by overlapping angles. That is, in different orientations, the same angle is measured twice for certain detectors.

This is a way to double check the solid angle determination for specific detectors during the experiment.

## 5.2 Data Analysis

The experimental quantity of interest in the calculation of the cross section is the elastic  $\alpha$ -peak. Figure 5.5 shows the most forward ( $22.59^\circ$ ) angle and lowest energy (17 MeV) and the most backward angle ( $165.8^\circ$ ) and highest energy (27 MeV) for the  $\alpha$ -particles scattered from  $^{120}\text{Te}$ . At the highest energy, the first two excited states of  $^{120}\text{Te}$  are reached.

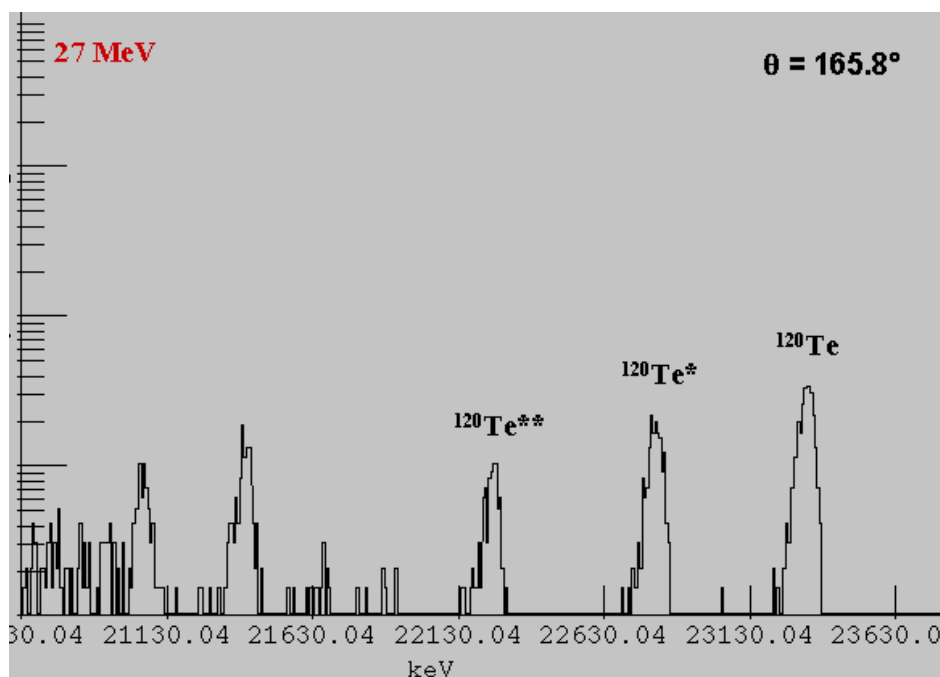
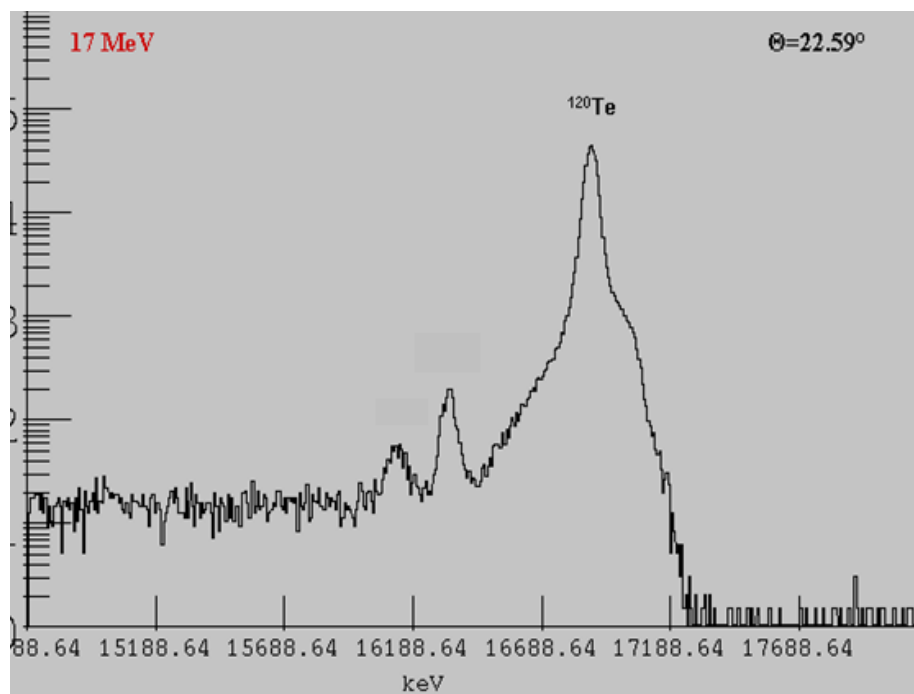


Figure 5.5 Spectra of  $^{120}\text{Te}$  at the highest energy and most backward angle and lowest energy and most forward angle.

The experimental elastic cross section can be calculated via:

$$\left(\frac{d\sigma}{d\Omega}\right)(\mathcal{G}) = \frac{N(\mathcal{G})}{N_{Proj}\Delta x\Delta\Omega} \quad (5.1)$$

where  $N(\mathcal{G})$  represents the number of elastically scattered  $\alpha$  particles at the angle  $\mathcal{G}$  in the lab frame. The number of incoming  $\alpha$  particles is denoted by  $N_{Proj}$ , whereas  $\Delta x$  is the total number of target atoms per unit area. The solid angle covered by the detector is  $\Delta\Omega$ .

In order to achieve accuracy in the cross section measurement, the factors of equation 5.1 must be measured precisely. Possible inhomogeneities of the target thickness may result in large uncertainties for the quantity  $\Delta x$ . A way to avoid this problem is to normalize the cross section relative to the cross section measured by the monitor detectors at  $\mathcal{G}_{lab} = 15^\circ$ , which is described by the Rutherford scattering formula [10,36,51]:

$$\left(\frac{d\sigma}{d\Omega}\right)(\mathcal{G}) = \left(\frac{d\sigma}{d\Omega}\right)_M(\mathcal{G} = 15^\circ) \frac{N(\mathcal{G})}{N_M(\mathcal{G} = 15^\circ)} \frac{\Delta\Omega_M}{\Delta\Omega} \quad (5.2)$$

$N_M(\mathcal{G} = 15^\circ)$  corresponds in this case to the number of elastically scattered  $\alpha$  particles at  $15^\circ$  and  $\Delta\Omega_M$  represents the solid angle of the monitor detectors. The cross section can then be calculated from the experimental data without systematic uncertainties arising from the target. A precise determination of the angles at which the detectors are placed with respect to the target position is essential for an accurate calculation of the cross section (described in section 5.1.2). The error in the cross section is a sum in quadrature of two sources of error: statistical error that dominates at larger angles and higher energies while systematic error in the form of the solid angle of a value of 1% that dominates in most cases at the very forward angles. The total error in cross section at the

most backward angle at the highest energies for most isotopes was on the order of 6-8 % (due to statistical error) while at the very forward angles it was 1% (systematic error). Since there were three different angular running orientations, it was at times necessary to combine cross sections from different runs. Each run had to be normalized to the monitor detectors to take into account deviations (Section 5.2.2). It was therefore necessary to combine cross sections by normalizing each data set to its own monitor detectors and combining cross sections of overlapping angles thusly. Figure 5.6 shows the normalized cross sections of  $^{106}\text{Cd}$  and  $^{120}\text{Te}$  (p-nuclei) at all measured energies. Appendix C lists the normalized experimental cross sections of all the isotopes from this study.

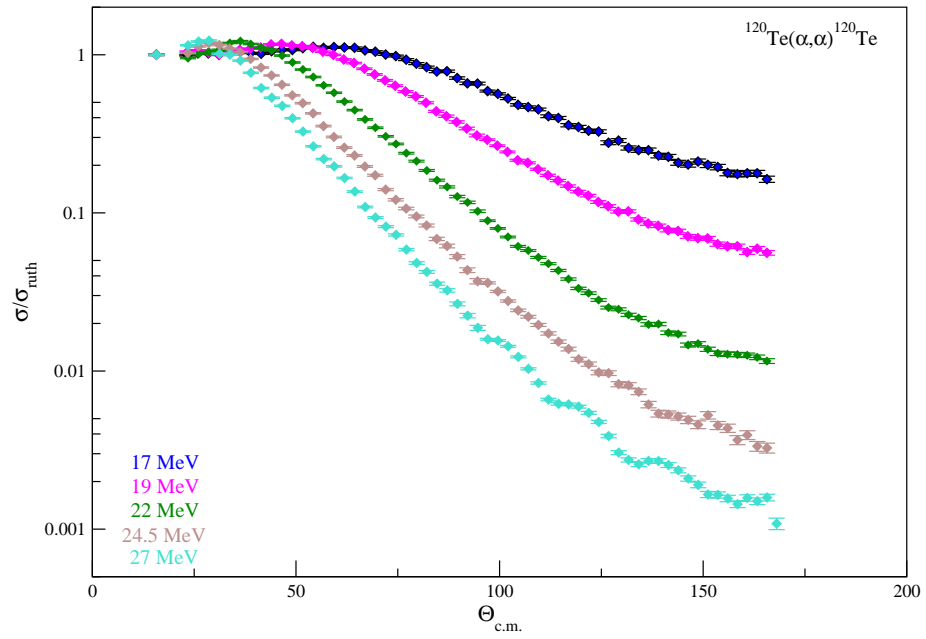
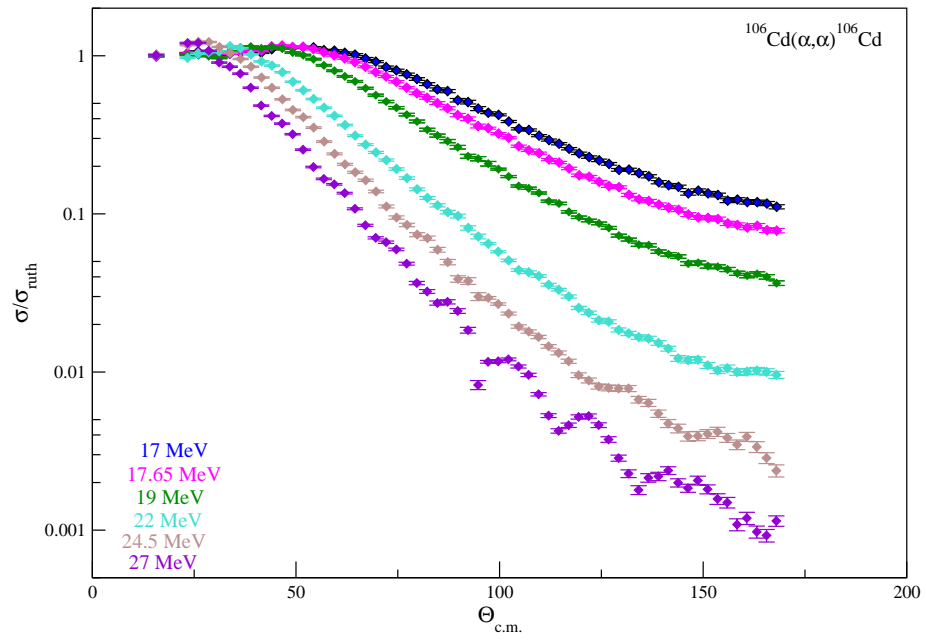


Figure 5.6 Normalized cross sections of  $^{106}\text{Cd}(\alpha, \alpha)^{106}\text{Cd}$  and  $^{120}\text{Te}(\alpha, \alpha)^{120}\text{Te}$  at all measured energies.

## CHAPTER 6

### RESULTS AND CONCLUSIONS

#### 6.1 $\alpha$ -nucleus potentials

A global  $\alpha$ -nucleus potential is one calculated from  $\alpha$ -elastic scattering data over a very wide range of energies and masses. It should be able to provide a general description of the elastic scattering processes (at all energies and masses). A local potential is derived from  $\alpha$ -elastic scattering data off of one isotope (and over a much narrower energy range).

This current study aims to test the mass (both neutron number and charge) and energy dependence of the  $\alpha$ -nucleus potential by  $\alpha$ -elastic scattering on  $^{106}\text{Cd}$  (p-nucleus),  $^{118}\text{Sn}$ ,  $^{120}\text{Te}$  (p-nucleus),  $^{124}\text{Te}$ ,  $^{126}\text{Te}$ ,  $^{128}\text{Te}$ , and  $^{130}\text{Te}$ . Of particular importance is  $^{106}\text{Cd}$  since it is a remeasurement [10,81] to test for any systematic error arising from the different experimental set-ups. Table 6.1 shows the nuclear properties of the nuclei considered in this investigation.

TABLE 6.1

## NUCLEAR PROPERTIES OF THE NUCLEI FROM THIS STUDY

Nucleus	Z	N	Shell	Subshell	Ground State
$^{106}\text{Cd}$	48	58		Closed (N)	Deformed [84]
$^{118}\text{Sn}$	50	68	Magic (Z)	Closed (N)	
$^{120}\text{Te}$	52	68		Closed (N)	Deformed [85]
$^{124}\text{Te}$	52	72			Deformed [85]
$^{126}\text{Te}$	52	74			
$^{128}\text{Te}$	52	76			
$^{130}\text{Te}$	52	78			

In order to correctly predict cross sections and reaction rates for particle capture and emission reactions involving  $\alpha$ -particles in the framework of the HF model, it is necessary to construct a reliable  $\alpha$ -nucleus potential. The following global models were used in comparison to the scattering data from this work:

- In the middle of the sixties, McFadden and Satchler [86] analyzed the angular distribution of elastically scattered 24.7 MeV  $\alpha$ -particles on several elements from Oxygen to Uranium, and proposed a global parameterization based on a four-parameter volume Woods–Saxon (WS) potential. It includes a volume WS form in the real and imaginary part where the (real and imaginary) radius and surface diffuseness are identical. In addition, there is no energy or mass dependence to the WS geometry parameters. This global potential is considered the standard potential.
- M.Avrigeanu et al. [87] extended a previous study by Nolte et al. [88] ( $\alpha$ -elastic scattering on  $^{12}\text{C}$ ,  $^{40}\text{Ca}$ ,  $^{50}\text{Ti}$ ,  $^{58}\text{Ni}$ ,  $^{90}\text{Zr}$  and  $^{208}\text{Pb}$ ) at energies above 80 MeV to the lower energy region ( $E \leq 32$ ) for the description of ( $\alpha$ ,n) reactions (from  $^{89}\text{Y}$  to  $^{124}\text{Sn}$ ), and its possible application to astrophysical scenarios. A volume Woods-Saxon (WS) form adopted in the real part of the nuclear potential is accompanied by a sum of volume and surface WS parameterizations in the imaginary nuclear potential [89,90].

- C. Fröhlich and T. Rauscher [91,92] proposed a modification of the potential from [86], in which the form of the real nuclear potential was varied and a potential strength between 360 and 390 MeV·fm<sup>3</sup> was obtained. This modification was introduced to more accurately describe ( $\alpha$ ,n) and ( $\alpha$ , $\gamma$ ) reaction data.
- Most recently, Kumar and Kailas [94] have obtained a global potential by studying elastic scattering data over a wide mass ( $A = 12 - 209$ ) and energy range (Coulomb barrier to about 140 MeV). A volume WS form is used in both the real and imaginary part. The geometry form factors have been obtained by considering the systematics of volume integrals ( $J_R$ ).

Although it was not used in comparison to the data from this work, an additional global potential is that of Demetriou [95].

- This global potential uses a double folding parameterization whose goal it was to mainly reproduce ( $\alpha$ , $\alpha$ ), ( $\alpha$ , $\gamma$ ), ( $\alpha$ ,n), (n, $\alpha$ ) and ( $\alpha$ ,p) reaction cross sections at low energies in medium mass nuclei. The double folding parameterization in the real part was tested with three different potentials for the imaginary nuclear potential with different mass and energy dependences resulting from a microscopic study of the experimental data.

Considering the astrophysical interest in explosive scenarios, the global parameterizations should describe the existing ( $\gamma$ , $\alpha$ ) [96] and ( $\alpha$ , $\gamma$ ) [32, 65, 97, 98, 99] cross sections for medium and heavy mass nuclei. These potentials have been derived by adjusting the potential parameters to elastic scattering data at medium and high energies (between 20 and 100 MeV), with the exception of [91,92] (only particle capture reaction data was considered).

### 6.1.1 Comparison to current Models

One such recent comparison of experimental data to global parameterizations has been done by D. Galaviz [10,39] via  $\alpha$ -elastic scattering on <sup>112,124</sup>Sn. Fig. 6.1 shows the experimental cross section obtained by Galaviz [10,39] to the cross section obtained

using the geometry parameters of the different global potentials [86,90,91,92,95]. By dividing the Rutherford normalized cross sections of the two isotopes, the variation is due to the effect of the difference in neutron number. None of the global parameterizations are able to accurately match the experimental data.

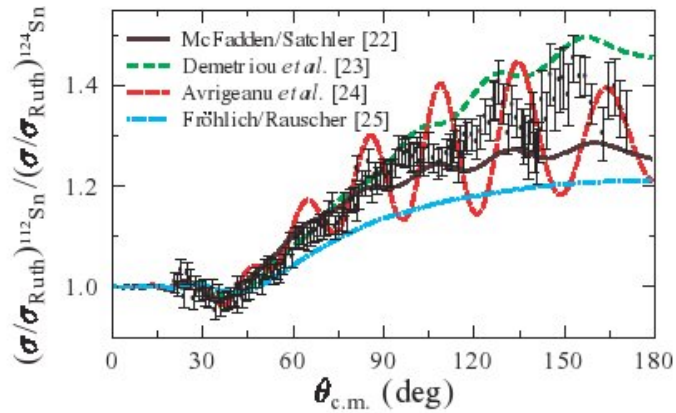


Figure 6.1 Mass dependence (arising from the difference in neutron number) of experimental cross section of  $^{112}\text{Sn}$  (p-nucleus) versus  $^{124}\text{Sn}$  compared to the cross section obtained using standard global potentials [39]. The Rutherford normalized cross sections are shown as a function of center-of-mass angle.

The same comparison has been obtained in this study (Figure 6.2 and Figure 6.3). Here, the Rutherford normalized cross section of  $^{120}\text{Te}$  to  $^{130}\text{Te}$  at all measured energies is compared to the cross section obtained from standard global potentials [86,89,90,91,92,94]. It is difficult to say which potential is the best reproduction of the data. The trend exhibited is that below the barrier (19 MeV), the Avrigeanu potential gives the most accurate representation while above it is the McFadden/Satchler potential.

If we examine the geometry properties of the potentials, we see that all four potentials use WS forms in the real and volume parts of the imaginary potential; however, the Avrigeanu potential adds a surface WS contribution in the imaginary part. In addition, the Fröhlich potential and McFadden/Satchler potential are identical in the imaginary geometry terms. They differ only in the values for the real part of the potential (both employing WS forms). Unambiguous determination of the real part of the optical potential is known at a particular distance [41] while the imaginary term has a very strong energy dependence at sub-barrier energies and its behavior is largely unknown [42]. In addition, the elastic scattering at low energies is very sensitive to the surface region of the potential. The family problem was discussed in Section 3.3.2. All the potential families should cross at a particular radius,  $R_S$ , which is usually referred to as the sensitivity radius [100] (it is called the strong absorption radius in the case of higher-energy elastic scattering). At energies close to the barrier, the sensitivity radius is situated in the surface region [41]. It has been suggested by [41] that the surface region of the potential ( $R \geq R_1 + R_2$ ) is much more sensitive to small changes of the density parameters than the inner region.

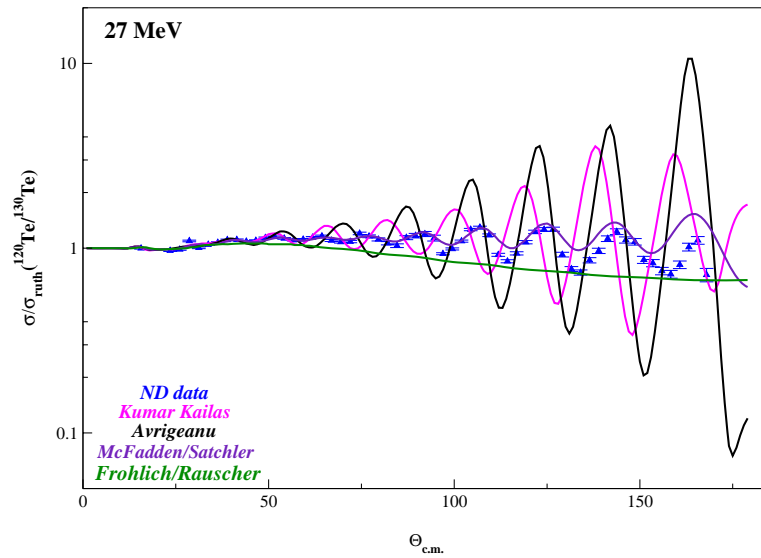
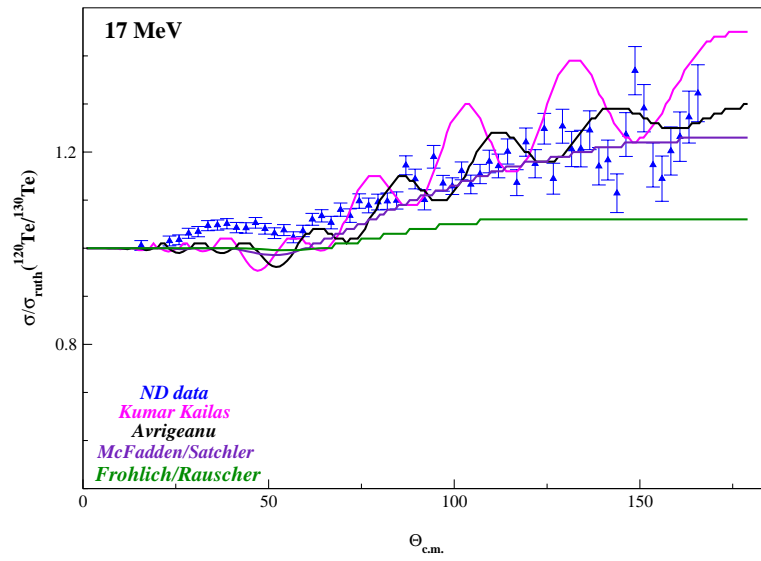


Figure 6.2 Mass dependence (due to neutron number) of  $^{120}\text{Te}/^{130}\text{Te}$  at 17 MeV (above) and 27 MeV (bottom) compared to the cross section obtained from standard potentials [86,89,90,91,92,94].

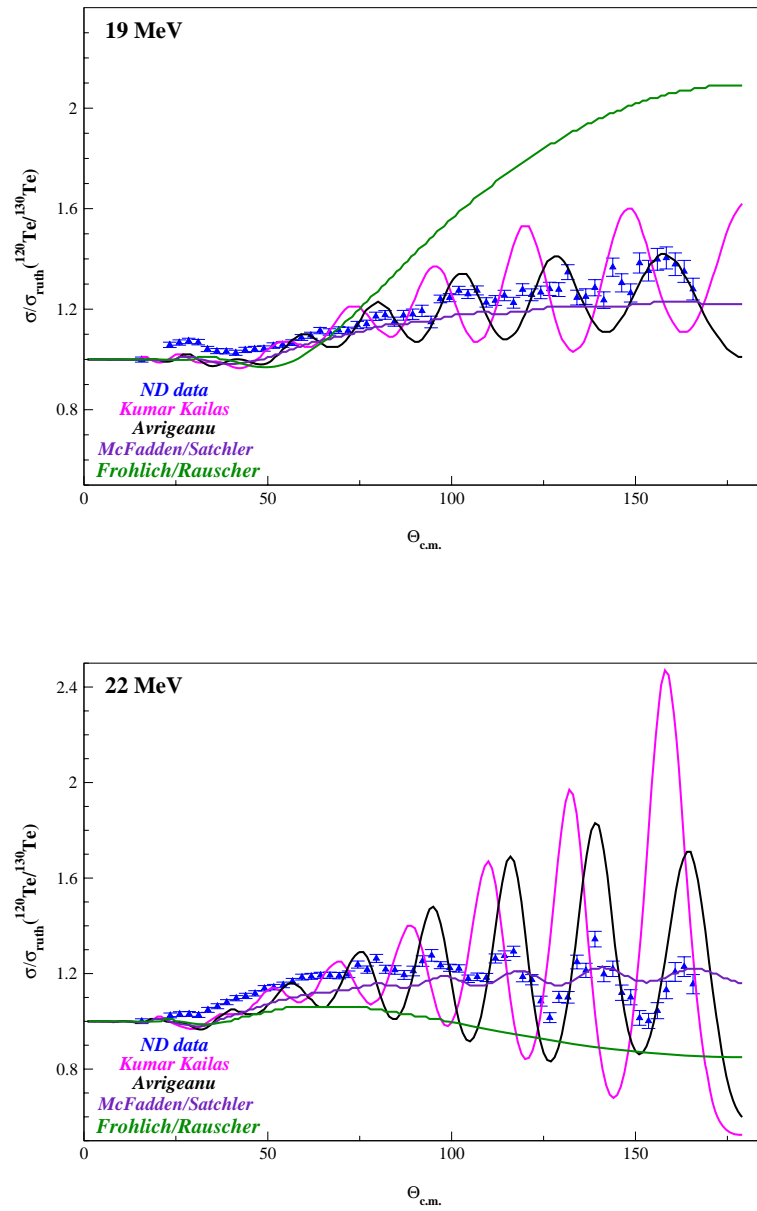


Figure 6.3 Mass dependence (due to neutron number) of  $^{120}\text{Te}/^{130}\text{Te}$  at 19 MeV (above) and 22 MeV (bottom) compared to the cross section obtained from standard potentials [86,89,90,91,92,94].

They conclude that as a result of such structure effects, the strength of the nuclear potential in the region near the barrier radius may vary by about 20%, and the major part of this variation is connected to the diffuseness parameter ( $a$ ). They also suggest a value of 0.62 fm for the diffuseness (for the real nuclear potential). This could explain why the McFadden/Satchler potential describes the data better than the Fröhlich potential since the only difference between them is in the real part. In the case of the former, the diffuseness value for the real part is 0.52 fm versus 0.48 fm for the latter.

The energy dependence of the potential was also tested in this study. Figure 6.4 shows the potential for  $^{120}\text{Te}$  and  $^{130}\text{Te}$  compared to standard global potentials [86,89,90,91,92,94] obtained from the current study. The Avrigeanu potential gives an accurate representation of the data for the p-nucleus  $^{120}\text{Te}$  and its neutron rich counterpart  $^{130}\text{Te}$  at 17 MeV. It greatly overestimates the data at 27 MeV.

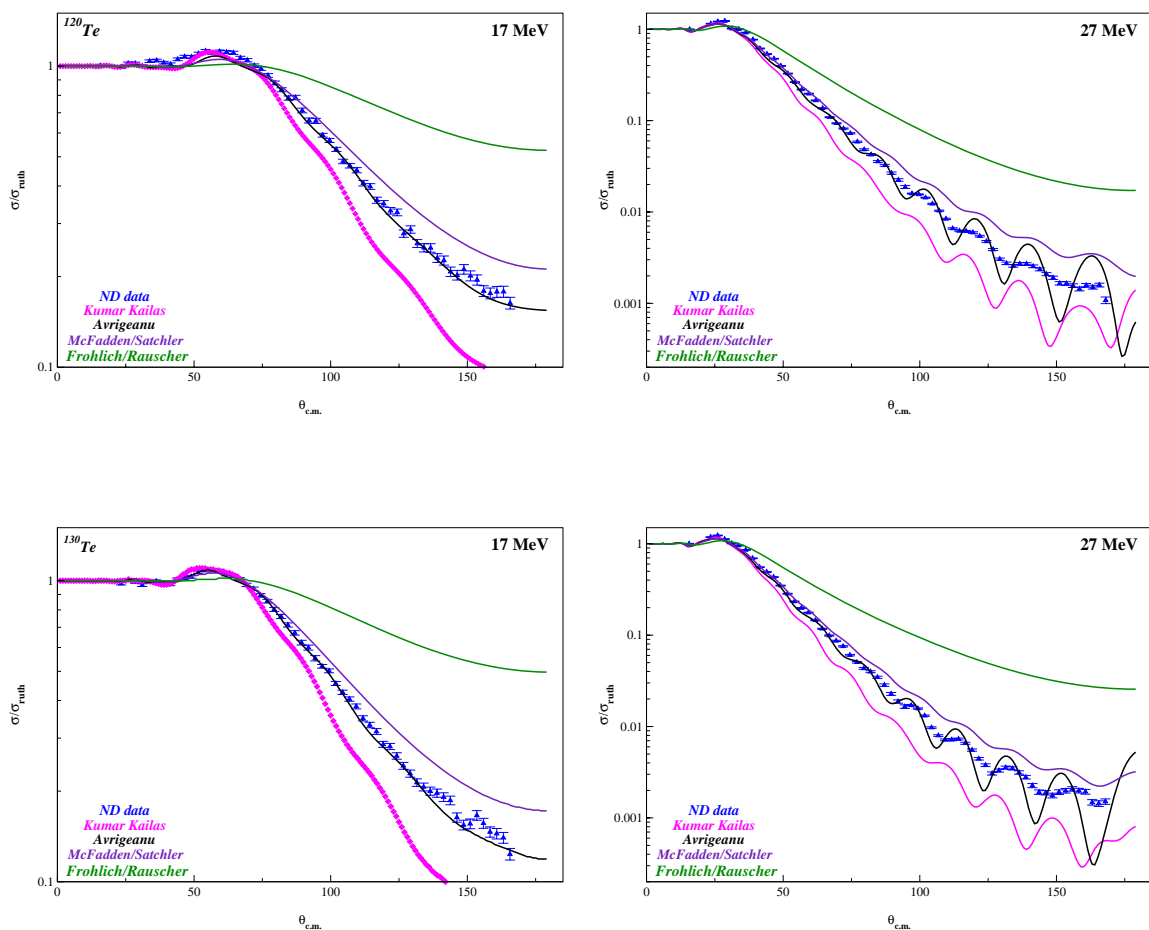


Figure 6.4 The Rutherford normalized cross section of  $^{120}\text{Te}$  (top) and  $^{130}\text{Te}$  (bottom) is compared to the global potentials of [86,89,90,91,92,94]. The Avriganu potential gives a very accurate representation at low energies but at the high energy it overestimates the diffraction pattern.

To explicitly see the effect (if any) of the potential to a variation in charge,  $^{118}\text{Sn}$  was included in the list of measured nuclei (Table 6.1). Figure 6.5 illustrates the region of the chart of nuclides that has been tested in the current and previous studies. Nuclei in pink in addition to  $^{106}\text{Cd}$  have been tested in this study while those in blue have been

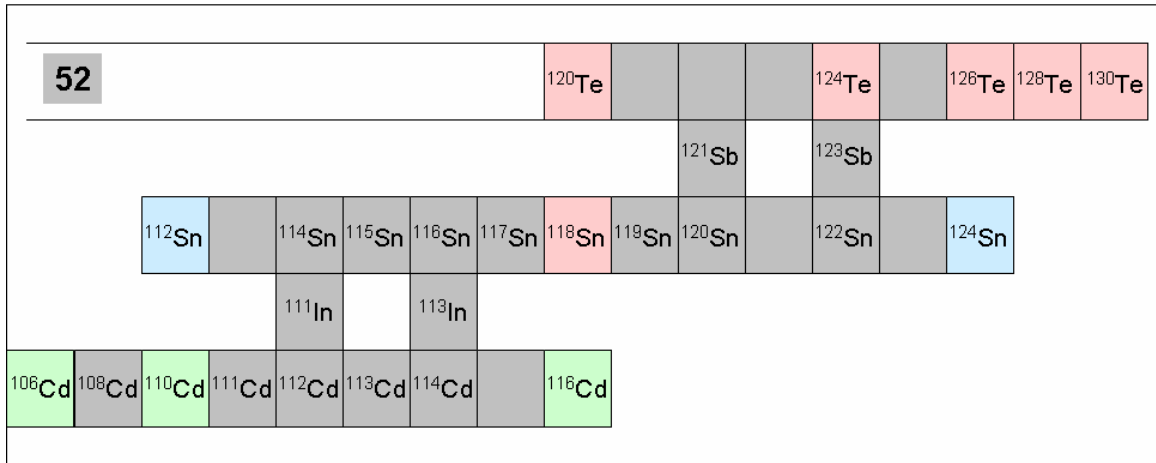


Figure 6.5 Nuclei in pink have been measured in this work in addition to a remeasurement on  $^{106}\text{Cd}(\alpha, \alpha)^{106}\text{Cd}$  [10,81]. Nuclei in blue have been measured by Galaviz [39] and the nuclei in green have been measured by Kiss [81] ( $^{110,116}\text{Cd}$  are yet unpublished).

tested by Galaviz [39] and those in green by Kiss [81]. This collaborative effort has focused on the  $Z = 50$  region since this is a closed shell. Near closed shells the level density is reduced and hence the statistical model may not be fully applicable.

$^{106}\text{Cd}$  and  $^{118}\text{Sn}$  at the two extreme energies (17 and 27 MeV) are compared to standard model predictions (Figure 6.6). The same trend for the energy dependence exhibited for the p-nucleus  $^{120}\text{Te}$  and its neutron rich counterpart  $^{130}\text{Te}$  is seen for all isotopes [Appendix D].

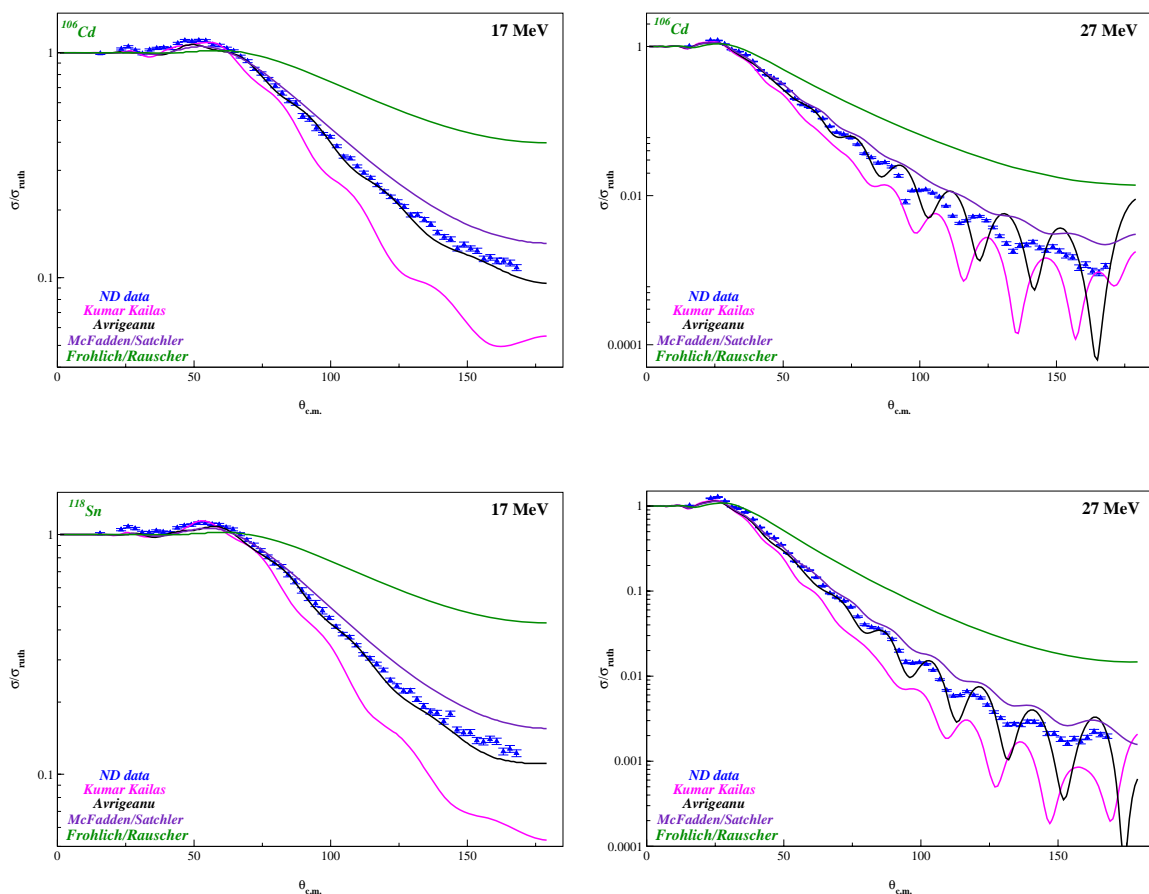


Figure 6.6 The Rutherford normalized cross section of  $^{106}\text{Cd}$  and  $^{118}\text{Sn}$  is compared to the global potentials of [86,89,90,91,92,94]. The Avrigeanu potential reproduces the scattering data at 17 MeV but it clearly overestimates it at 27 MeV.

Let us revisit this overestimation in diffraction pattern that we have seen from the Avrigeanu potential above the Coulomb barrier (19 MeV) in both the mass and energy dependence (Figures 6.1-6.4; 6.6). Figure 5.7 gives the Rutherford normalized cross section of  $^{106}\text{Cd}(\alpha,\alpha)^{106}\text{Cd}$  at all measured energies. In comparison to the other nuclei (Appendix C), there is a more pronounced minimum that occurs at 27 MeV. Recall that the Avrigeanu potential (Section 6.1) was obtained from considering elastic scattering data off of nuclei in the  $A \approx 100$  mass region.

Although we are at a higher energy (27 MeV), still at this mass range the level density is reduced. The HF theory assumes that there exists many resonances such that the transmission coefficients become averaged quantities. If, however, we are at a reduced level density, then individual resonances become important. The elastic cross section is composed of two parts: the nonresonant part and the compound elastic part [101]. The nonresonant part (often called the shape elastic or potential scattering) offers a smooth background. This is what is seen below the barrier (the scattering is not probing the nuclear interior) since it is the dominating part of the cross section. At higher energies, in the vicinity of a resonance (at resonance energies), this becomes the dominating factor in the elastic cross section. This would account for the increased diffraction patterns seen in both the Avrigeanu potential at 27 MeV and that of  $^{106}\text{Cd}(\alpha,\alpha)^{106}\text{Cd}$ .

### **6.1.2 An improved $\alpha$ -nucleus global potential?**

Of the global potentials considered in this work, the Avrigeanu potential and the McFadden/Satchler potential seemed to offer the best reproduction (Section 6.1.1). A very rough attempt has been made to constrain the potential parameters. Keeping the imaginary parts of the Avrigeanu potential fixed, the diffuseness parameter for the real part has been changed to that of the McFadden/Satchler value of 0.52. Figures 6.7 and 6.8 show the calculated Rutherford normalized cross section using this “modified” Avrigeanu potential in comparison to the  $^{106}\text{Cd}$  experimental data (taken above the Coulomb barrier only).

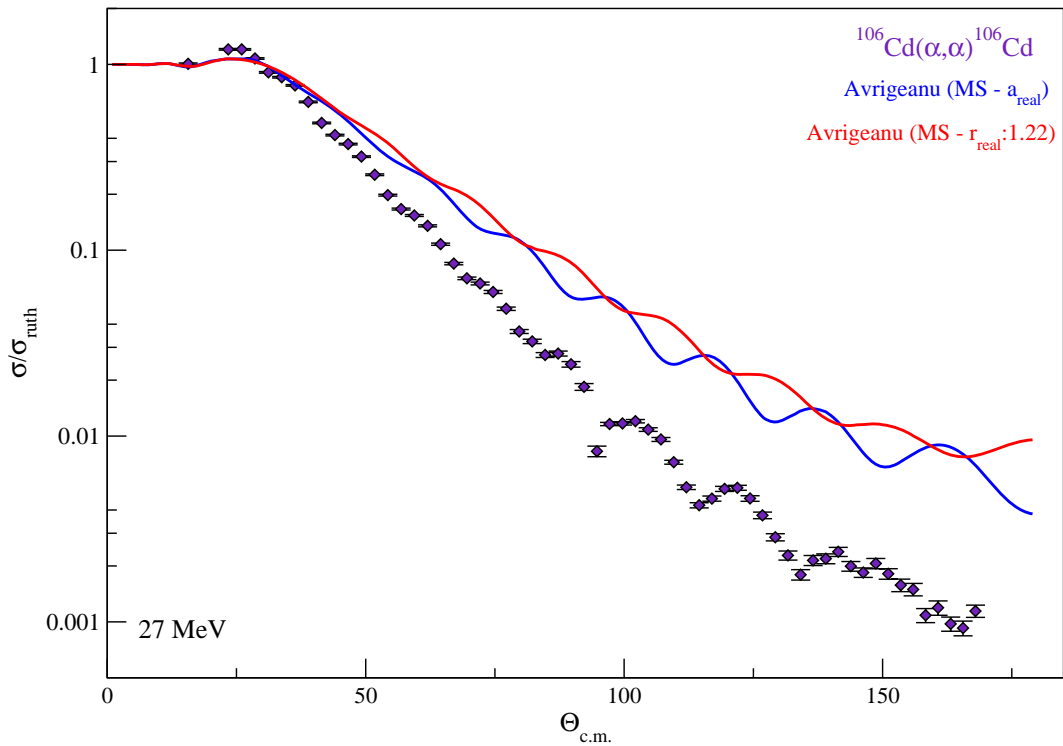


Figure 6.7 Rutherford normalized cross section of  $^{106}\text{Cd}(\alpha,\alpha)^{106}\text{Cd}$  at 27 MeV compared to a modified Avriganu potential. The potential with the matching McFadden/Satchler diffuseness parameter in the real part (0.52) matches the amplitude of the diffraction pattern. The red line shows a modification of the Avriganu potential by assuming a value of 1.22 for the real radius. Here the diffraction pattern is damped. Both overestimate the cross section in magnitude.

Perhaps more accuracy can be achieved from the Avriganu potential over the entire energy range by changing the diffuseness parameter in the real part at the higher energies and refitting to the data. Perhaps even greater results could be achieved by repeating the method used by Avriganu in deriving the global potential on medium mass nuclei where the level density is higher.

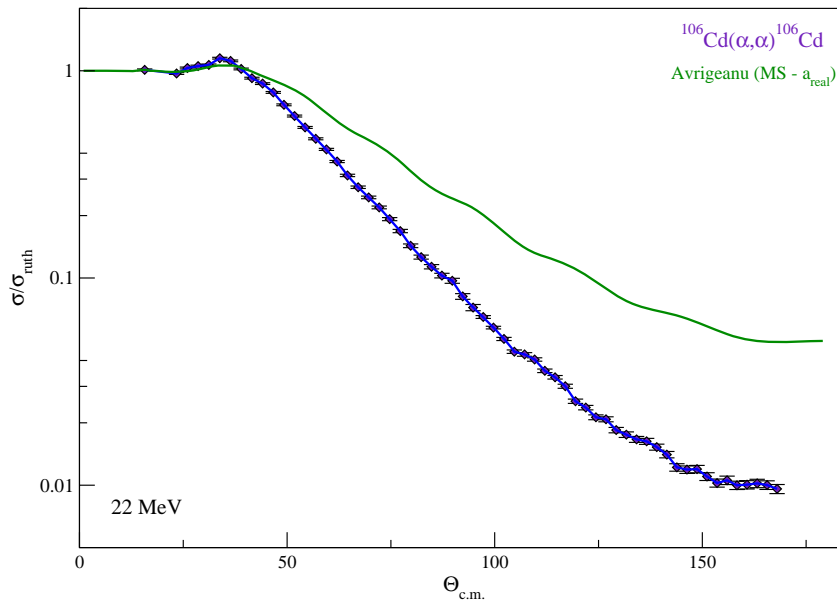
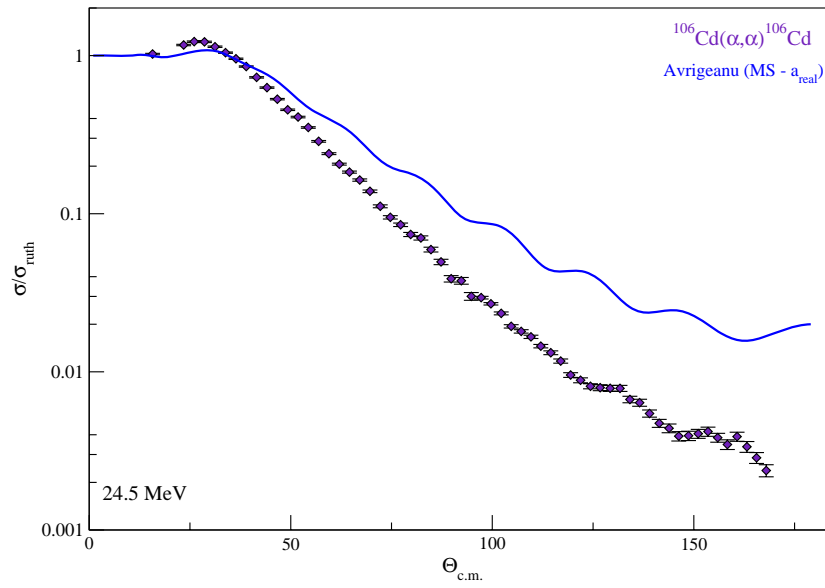


Figure 6.8 Rutherford normalized cross section of  $^{106}\text{Cd}(\alpha,\alpha)^{106}\text{Cd}$  at 22 and 24.5 MeV compared to a modified Avrigeanu potential (diffuseness parameter in the real part (0.52)).

## 6.2 Optical Model Analysis

The analysis of the experimental absolute cross sections proceeds by performing a  $\chi_{red}^2$  minimization, and adjusting the different parameters of the potential systematically [102].

For the inputs into the model, the following values were used:

- The Coulomb potential radius (equation 3.13) is chosen to be equal to the mean square radius of the double folding potential:  $R_C = r_{rms,df}$ .
- The parameters  $C(E)$ ,  $\alpha(E)$ , and  $\beta(E)$  (eq.3.20) are chosen to be equal to the corresponding values derived at an energy  $E_\alpha = 20$  MeV

[48]. The adopted values are:

$$C = 0.460 \quad \alpha = 3.962 \quad \beta = 10.785$$

- For the imaginary potential, only surface and volume WS parameterizations are used.

### 6.2.1 Cross Section Calculation

The analysis and calculation of the theoretical cross section has been performed [102]. The code calculates the solution of the scattering matrix  $S$  for a certain nuclear potential. Only those terms which contribute to the elastic scattering are taken into account [10]. A sufficient number of partial waves are taken, and the corresponding values for the scattering phase shift  $\delta_l$  and the reflection coefficients  $\eta_l$  are derived [10]. Figure 6.9 shows the values for  $\eta_l$  and  $\delta_l$  derived in one calculation of the scattering matrix  $S$  corresponding to the elastic scattering of  $\alpha$  particles on  $^{120}\text{Te}$  at a lab energy of

27 MeV. The number of partial waves considered is sufficient ( $\approx 30$ ) to completely describe the elastic scattering process (partial waves with  $\eta_l=1$  and  $\delta_l=0$  don't contribute to the nuclear scattering process). Once the matrix elements of the scattering matrix are calculated, it is possible to derive the scattering cross section induced by the initial optical potential [10].

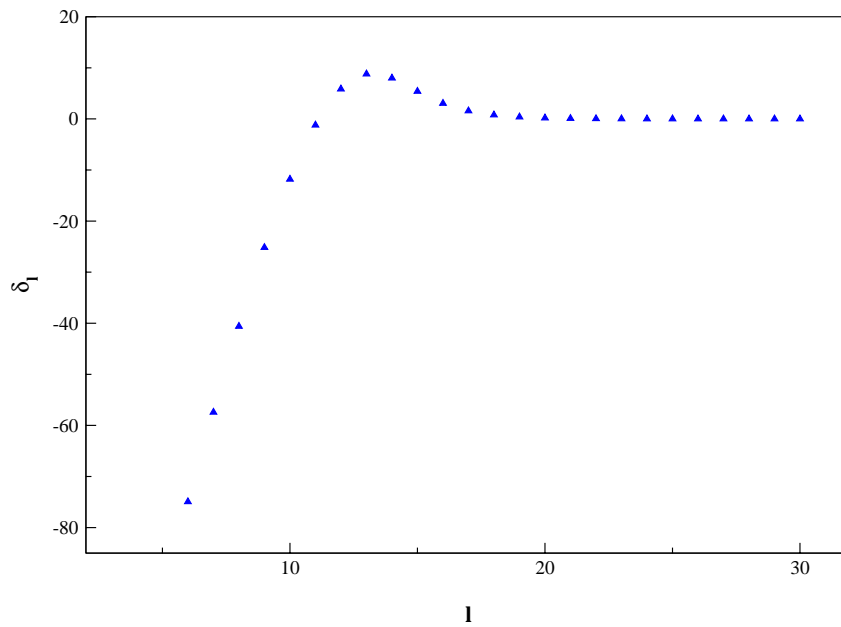
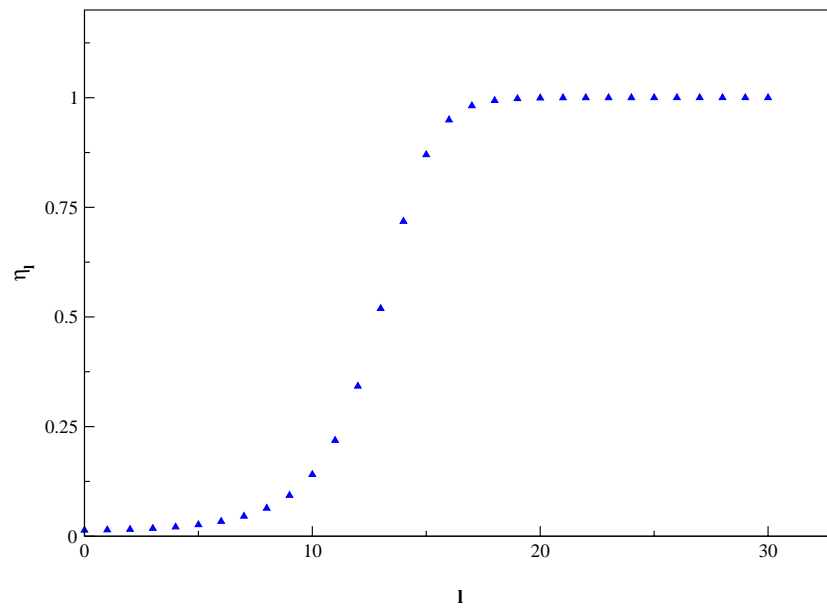


Figure 6.9 Amplitude and phase shift (as a function of the number of partial waves) derived in an S matrix calculation performed for  $^{120}\text{Te}$  at a bombarding energy of 27 MeV.

## 6.2.2 Local Potentials

Figures 6.10, 6.11 and Appendix E show the Rutherford normalized cross section calculated from the derived local potentials compared to the experimental data.

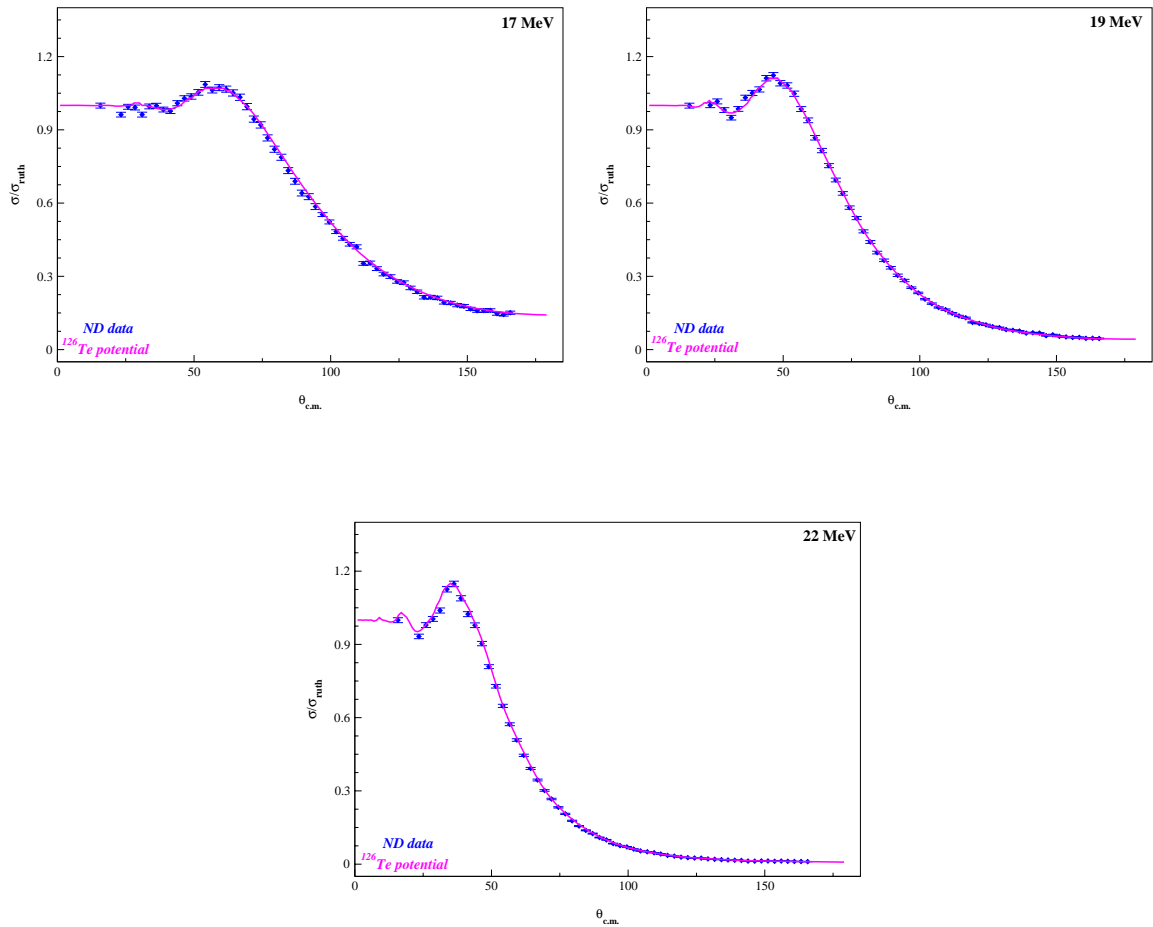


Figure 6.10 Comparison of the Rutherford normalized cross section calculated from the local potential of  $^{126}\text{Te}$  at all energies to the experimental data (no normalization has been applied).

In some cases, it was necessary to apply a normalization factor to the potential. The fitting routine assumes that the first point (of the monitor detectors) is 1 [102, 103].

Since the monitor detectors could not be set to this value (Section 5.2), there is a slight offset that occurs. The value of this normalization was not applied to the potential parameters. It is only used to see the accuracy of the Rutherford normalized cross section calculated from the potential parameters to the experimental cross section [103]. It shows how the cross section calculated from the derived potential parameters would look had the cross section calculated from the monitor detectors been equal to 1. Where necessary, in the case of the Te isotopes, this normalization was applied (again for illustrative effects only). This normalization was too great in the case of Sn and Cd. In those instances where needed, a 4% normalization was applied to the calculated cross section (Figure 6.11).

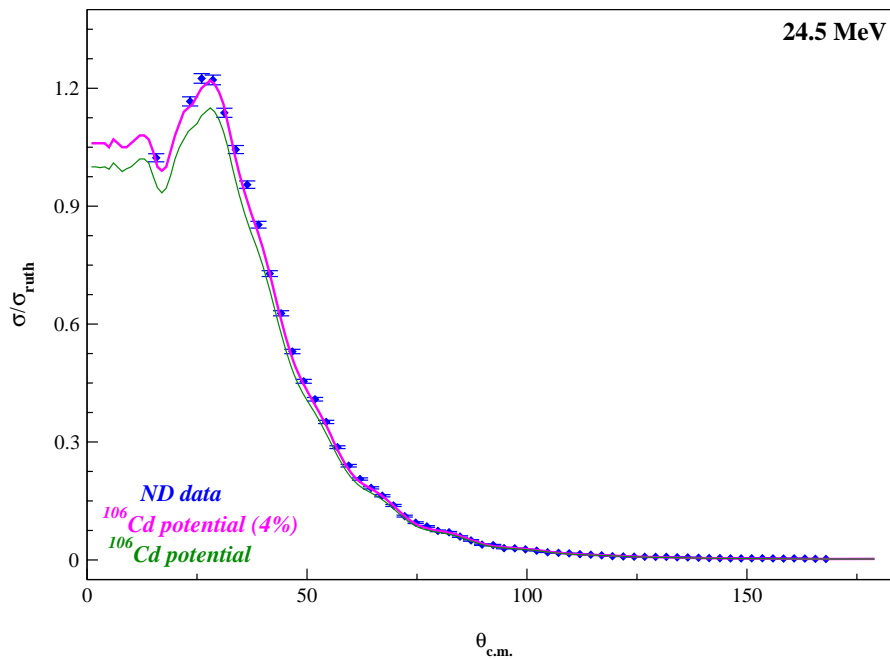


Figure 6.11 Rutherford normalized cross section calculated from the local potential of  $^{106}\text{Cd}$  at 24.5 MeV. Shown is the 4% normalization applied to the cross section derived from the local potential (illustrative purposes only). The first few points fall off of the unnormalized curve but the rest are unaffected.

### 6.2.3 Real part

Using a double folding parameterization for the real part of the potential allows for the removal of certain uncertainties (continuous ambiguities) by fixing the shape. In this way, there are only two parameters to consider, the strength of the potential ( $\lambda$ ) and the width ( $w$ ). The real part can be characterized by its strength ( $J_R$ ) (defined in equation 3.14). This allows for the normalization between different results (from different experiments). Table 6.2 lists the values for the real strength of the potential for all isotopes at all energies. The first column represents the value of the real strength potential. The second column is the rms radius with the corresponding  $\chi^2$  for that particular fit (this is the total  $\chi^2$  -including geometry parameters of the imaginary part). The width of the double folding parameterization  $w$  has been adjusted locally for each nucleus. The adopted corrections produced by the deviation of the charge density are always less than 2%. It was suggested by [36] that a value close to unity for this parameter ( $w$ ) should be kept otherwise the results would not yield a correct description of the scattering data. The strength of the potential has been varied making use of the parameter  $\lambda$ , which has been parameterized linearly with the energy:

$$\lambda = \frac{a^* + b^* \cdot E_{c.m.}}{J_{R,0}} \quad (6.1)$$

Figure 6.12 shows the parameterization of  $\lambda J_{R,0}$  as a function of center-of-mass energy for

$^{120}\text{Te}$ .  $J_{R,0}$  is defined as  $J_R$  with  $\lambda = 1$ .

TABLE 6.2

DOUBLE FOLDING PARAMETERIZATION RESULTS FROM FITS FOR ALL ISOTOPES.

Reaction	$E_{c.m.}$ (MeV)	$J_R$ (MeV·fm <sup>3</sup> )	$r_{rms,R}$ (fm)	$\chi^2_{red}$
$^{106}\text{Cd}(\alpha,\alpha)^{106}\text{Cd}$	16.38	329.47	5.22	1.7
$^{106}\text{Cd}(\alpha,\alpha)^{106}\text{Cd}$	17.01	328.81	5.22	1.8
$^{106}\text{Cd}(\alpha,\alpha)^{106}\text{Cd}$	18.31	328.00	5.22	1.9
$^{106}\text{Cd}(\alpha,\alpha)^{106}\text{Cd}$	21.20	327.01	5.24	2.5
$^{106}\text{Cd}(\alpha,\alpha)^{106}\text{Cd}$	23.61	326.00	5.26	4.3
$^{106}\text{Cd}(\alpha,\alpha)^{106}\text{Cd}$	26.02	324.99	5.27	14.5
$^{118}\text{Sn}(\alpha,\alpha)^{118}\text{Sn}$	16.44	350.52	5.30	1.3
$^{118}\text{Sn}(\alpha,\alpha)^{118}\text{Sn}$	18.38	348.31	5.30	1.2
$^{118}\text{Sn}(\alpha,\alpha)^{118}\text{Sn}$	21.28	346.71	5.30	1.5
$^{118}\text{Sn}(\alpha,\alpha)^{118}\text{Sn}$	23.70	343.22	5.30	1.8
$^{118}\text{Sn}(\alpha,\alpha)^{118}\text{Sn}$	26.12	341.28	5.30	3.9
$^{120}\text{Te}(\alpha,\alpha)^{120}\text{Te}$	16.45	353.33	5.32	2.3
$^{120}\text{Te}(\alpha,\alpha)^{120}\text{Te}$	18.39	350.78	5.32	2.6
$^{120}\text{Te}(\alpha,\alpha)^{120}\text{Te}$	21.29	348.18	5.32	3.1
$^{120}\text{Te}(\alpha,\alpha)^{120}\text{Te}$	23.71	345.51	5.32	3.0
$^{120}\text{Te}(\alpha,\alpha)^{120}\text{Te}$	26.13	343.13	5.32	4.8
$^{124}\text{Te}(\alpha,\alpha)^{124}\text{Te}$	16.47	349.04	5.31	2.0
$^{124}\text{Te}(\alpha,\alpha)^{124}\text{Te}$	18.41	346.63	5.31	2.5
$^{124}\text{Te}(\alpha,\alpha)^{124}\text{Te}$	21.31	343.29	5.31	2.1
$^{124}\text{Te}(\alpha,\alpha)^{124}\text{Te}$	23.72	339.20	5.31	3.0
$^{124}\text{Te}(\alpha,\alpha)^{124}\text{Te}$	26.16	337.84	5.31	6.4
$^{126}\text{Te}(\alpha,\alpha)^{126}\text{Te}$	16.48	344.47	5.36	1.5
$^{126}\text{Te}(\alpha,\alpha)^{126}\text{Te}$	18.42	343.53	5.36	1.2
$^{126}\text{Te}(\alpha,\alpha)^{126}\text{Te}$	21.32	342.93	5.36	1.2
$^{128}\text{Te}(\alpha,\alpha)^{128}\text{Te}$	16.48	344.61	5.42	2.2
$^{128}\text{Te}(\alpha,\alpha)^{128}\text{Te}$	18.42	342.41	5.42	1.8
$^{128}\text{Te}(\alpha,\alpha)^{128}\text{Te}$	21.33	340.21	5.42	2.5
$^{128}\text{Te}(\alpha,\alpha)^{128}\text{Te}$	23.76	339.55	5.42	2.5
$^{128}\text{Te}(\alpha,\alpha)^{128}\text{Te}$	26.18	337.48	5.42	5.8
$^{130}\text{Te}(\alpha,\alpha)^{130}\text{Te}$	16.49	347.20	5.45	1.1
$^{130}\text{Te}(\alpha,\alpha)^{130}\text{Te}$	18.43	344.77	5.45	1.1
$^{130}\text{Te}(\alpha,\alpha)^{130}\text{Te}$	21.34	341.68	5.45	1.4
$^{130}\text{Te}(\alpha,\alpha)^{130}\text{Te}$	26.19	338.03	5.45	2.6

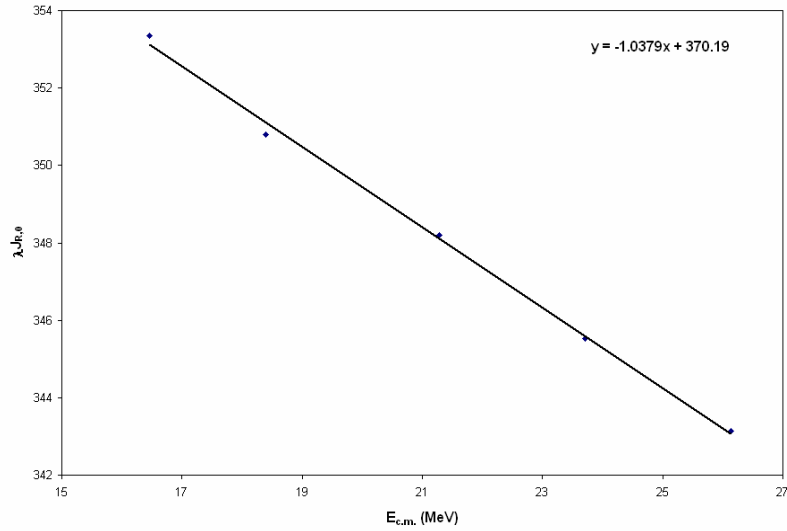


Figure 6.12  $\lambda_{J_{R,0}}$  parameterized as a function of center-of-mass energy for  $^{120}\text{Te}$ .

The coefficients  $a^*$  and  $b^*$  and the strength of the potential ( $J_{R,0}$ ) are listed in Table 6.3.

TABLE 6.3

VALUES FOR THE PARAMETERIZATION OF  $\lambda$

Isotope	$a^*$ (MeV·fm <sup>3</sup> )	$b^*$ (fm <sup>3</sup> )	$J_{R,0}$ (MeV·fm <sup>3</sup> )
$^{106}\text{Cd}^*$	341.49	-0.7381	275.94
$^{118}\text{Sn}$	366.18	-0.9524	263.15
$^{120}\text{Te}$	370.19	-1.0379	263.52
$^{124}\text{Te}$	368.83	-1.2083	258.93
$^{126}\text{Te}$	349.43	-0.3087	264.93
$^{128}\text{Te}$	355.48	-0.6886	272.50
$^{130}\text{Te}$	362.16	-0.9336	276.21

$^{106}\text{Cd}$  has only been parameterized at 19 MeV and below using this method. A separate parameterization for  $^{106}\text{Cd}$  had to be taken at the higher energies (equation 6.2).

For the case of  $^{106}\text{Cd}$ , the value of  $w$  could not be fixed at all energies (the value listed in Table 6.3 is valid for the energy range of 17 – 19 MeV). Instead, a linear parameterization of  $w$  with energy was obtained from 22 -27 MeV (Table 6.4):

$$w = -0.0014E_{c.m.} + 0.9715 \quad \text{and} \quad \lambda = -4.4525w + 5.6325 \quad (6.2)$$

TABLE 6.4  
VALUES OF THE PARAMETERIZATION OF THE REAL PART FOR  $^{106}\text{Cd}$  FROM  
22 - 27 MeV

$a^*(w)$	$b^*(w)$	$a^*$	$b^*$
0.9715	0.0014	5.6325	-4.4525

$a^*(w)$  and  $b^*(w)$  correspond to the coefficients obtained from the equation on the left (6.2) while  $a^*$  and  $b^*$  are those derived from  $\lambda$  (equation on the right of 6.2)

To see any possible trend of  $J_R$  as a function of mass, the values of  $J_R$  (equation 3.14) for  $\lambda = w = 1$  were also obtained (Table 6.5). Factoring out the strength ( $\lambda$ ) and width ( $w$ ) from the potential thusly allows the effect of  $N$  on the real nuclear potential to be clearly seen (in the case of the Te isotopic chain). The trend of  $J_R$  is one of decreasing value with increasing mass number. In actuality, it is one of increasing neutron number since there

is a large deviation in value from  $^{106}\text{Cd}$  to  $^{118}\text{Sn}$  ( $Z = 48$  and  $50$ , respectively but  $N = 58$  and  $68$ , respectively). In particular, the value of  $J_R$  for  $^{118}\text{Sn}$  and  $^{120}\text{Te}$  are practically

TABLE 6.5

VALUE OF  $J_R$  FOR  $\lambda = w = 1$

Isotope	$J_R$ (MeV·fm <sup>3</sup> )
$^{106}\text{Cd}$	277.59
$^{118}\text{Sn}$	269.57
$^{120}\text{Te}$	269.12
$^{124}\text{Te}$	266.86
$^{126}\text{Te}$	265.72
$^{128}\text{Te}$	264.48
$^{130}\text{Te}$	263.37

identical. Both have a closed neutron subshell of 68 ( $Z = 50$  for  $^{118}\text{Sn}$ - magic number and  $Z = 52$  for  $^{120}\text{Te}$ ). Consider the value of  $J_R$  (for  $\lambda = w = 1$ ) for previous studies done of  $\alpha$ -elastic scattering on p-nuclei and nuclei from this study (with the exception of  $^{112}\text{Sn}$ ) (Table 6.6).  $^{106}\text{Cd}$  has a larger value than the other isotopes. In fact, after this isotope there is a decrease in the strength with increasing mass number. There is some sort of enhancement that happens at  $^{106}\text{Cd}$ .

TABLE 6.6

VALUES OF  $J_R$  ( $\lambda = w = 1$ ) FOR ALL PREVIOUS STUDIED NUCLEI (WITH EXCEPTION OF  $^{112}\text{Sn}$  WHICH WAS UNLISTED).

Isotope	$J_R$ (MeV·fm <sup>3</sup> )	N	Z
$^{92}\text{Mo}$	267.88	50	42
$^{106}\text{Cd}$	277.59	58	48
$^{118}\text{Sn}$	269.57	68	50
$^{120}\text{Te}$	269.12	68	52
$^{124}\text{Te}$	266.86	72	52
$^{126}\text{Te}$	265.72	74	52
$^{128}\text{Te}$	264.48	76	52
$^{130}\text{Te}$	263.37	78	52
$^{144}\text{Sm}$	260.41	82	62

#### 6.2.4 Imaginary Part

The parameterizations used to describe the imaginary part of the nuclear potential consist of WS potentials (both volume and surface). It was shown [36] that this particular combination delivered the most precise description of the scattering cross sections. Since this shape is not fixed, a normalization of the geometry parameters to the experimental data is required. Like the real strength ( $J_R$ ), the imaginary geometry terms can be defined by an imaginary strength ( $J_I$  – equation 3.14). Table 6.7 shows the contribution of the surface to volume terms of the imaginary potential for all isotopes. Not all of the geometry parameters for all nuclei could be fixed at all energies. Instead, a

linear parameterization as a function of the center-of-mass energy was applied in several cases. Figure 6.13 shows such a parameterization taken for the volume depth ( $W_V$ ) and diffuseness ( $a_V$ ) for  $^{130}\text{Te}$ .

TABLE 6.7  
THE SURFACE TO VOLUME CONTRIBUTION OF THE IMAGINARY  
POTENTIAL FOR ALL ISOTOPES.

Isotope	Surface to Volume
$^{106}\text{Cd}$	$J_{I,\text{vol}} \approx 0.22 \cdot J_{I,\text{surf}}$
$^{118}\text{Sn}$	$J_{I,\text{vol}} \approx 0.39 \cdot J_{I,\text{surf}}$
$^{120}\text{Te}$	$J_{I,\text{vol}} \approx 0.30 \cdot J_{I,\text{surf}}$
$^{124}\text{Te}$ (17 MeV)	$J_{I,\text{vol}} \approx 0.11 \cdot J_{I,\text{surf}}$
$^{124}\text{Te}$ (19 MeV)	$J_{I,\text{vol}} \approx 0.15 \cdot J_{I,\text{surf}}$
$^{124}\text{Te}$ (22 MeV)	$J_{I,\text{vol}} \approx 0.21 \cdot J_{I,\text{surf}}$
$^{124}\text{Te}$ (24.5 MeV)	$J_{I,\text{vol}} \approx 0.27 \cdot J_{I,\text{surf}}$
$^{124}\text{Te}$ (27 MeV)	$J_{I,\text{vol}} \approx 0.34 \cdot J_{I,\text{surf}}$
$^{126}\text{Te}$	$J_{I,\text{vol}} \approx 0.16 \cdot J_{I,\text{surf}}$
$^{128}\text{Te}$ (17 MeV)	$J_{I,\text{vol}} \approx 0.22 \cdot J_{I,\text{surf}}$
$^{128}\text{Te}$ (19 MeV)	$J_{I,\text{vol}} \approx 0.23 \cdot J_{I,\text{surf}}$
$^{128}\text{Te}$ (22 MeV)	$J_{I,\text{vol}} \approx 0.24 \cdot J_{I,\text{surf}}$
$^{128}\text{Te}$ (24.5 MeV)	$J_{I,\text{vol}} \approx 0.25 \cdot J_{I,\text{surf}}$
$^{128}\text{Te}$ (27 MeV)	$J_{I,\text{vol}} \approx 0.26 \cdot J_{I,\text{surf}}$
$^{130}\text{Te}$ (17MeV)	$J_{I,\text{vol}} \approx 0.35 \cdot J_{I,\text{surf}}$
$^{130}\text{Te}$ (19MeV)	$J_{I,\text{vol}} \approx 0.36 \cdot J_{I,\text{surf}}$
$^{130}\text{Te}$ (22MeV)	$J_{I,\text{vol}} \approx 0.37 \cdot J_{I,\text{surf}}$
$^{130}\text{Te}$ (27MeV)	$J_{I,\text{vol}} \approx 0.40 \cdot J_{I,\text{surf}}$

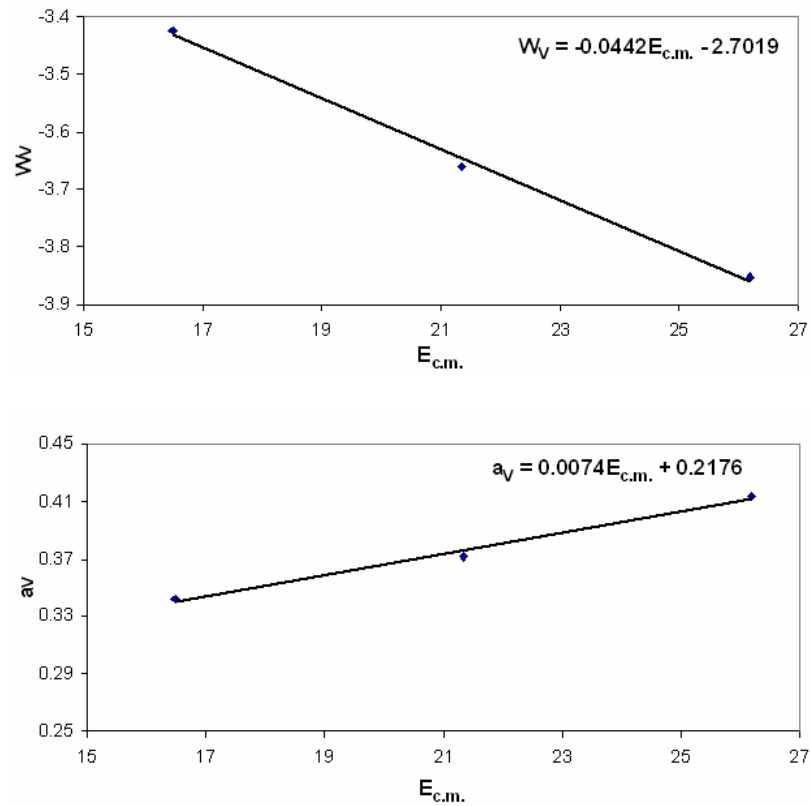


Figure 6.13  $W_V$  and  $a_V$  parameterized as a function of center-of-mass energy for  $^{130}\text{Te}$ .

In the previous work done on  $^{92}\text{Mo}$  [36] and  $^{112,124}\text{Sn}$  [39], the contribution of the volume term to surface term was  $J_{I,\text{vol}} \approx 0.22 J_{I,\text{surf}}$ . The dominance of the surface term at lower energies has been mentioned [104], whereas an enhancement of the contribution of the volume Woods-Saxon potential with the energy above the Coulomb barrier may be necessary [78]. The increase of the volume contribution with increasing energy is observed for the case of  $^{124,128,130}\text{Te}$  (Table 6.7).

Tables 6.8 and 6.9 give the imaginary geometry parameters of the derived local potentials of all isotopes considered in the study. Perhaps due to its ground state deformation [85],  $^{124}\text{Te}$  could not be parameterized at 27 MeV and an extra dependence in energy was necessary in the volume diffuseness ( $a_v$ ).

TABLE 6.8  
IMAGINARY PARAMETERS FOR  $^{106}\text{Cd}$ ,  $^{120}\text{Te}$ ,  $^{126}\text{Te}$

<b>Reaction</b>	<b><math>W_V</math></b>	<b><math>r_V</math></b>	<b><math>a_V</math></b>	<b><math>W_S</math></b>	<b><math>r_S</math></b>	<b><math>a_S</math></b>
$^{106}\text{Cd}(\alpha, \alpha)^{106}\text{Cd}$	-2.964	1.783	0.382	334.35	1.238	0.234
$^{120}\text{Te}(\alpha, \alpha)^{120}\text{Te}$	-3.932	1.745	0.397	312.13	1.179	0.264
$^{126}\text{Te}(\alpha, \alpha)^{126}\text{Te}$	-2.33	1.704	0.445	333.66	1.229	0.251

Imaginary geometry parameters where a fixed value at all energies was possible (with the exception of  $w$  for  $^{106}\text{Cd}$  at the higher energies – 22, 24.5 and 27 MeV).

TABLE 6.9

IMAGINARY GEOMETRY TERMS PARAMETERIZED AS A FUNCTION OF ENERGY.

Reaction	$E_{c.m.}$	$W_V$	$r_V$	$a_V$	$W_S$	$r_S$	$a_S$
$^{118}\text{Sn}(\alpha, \alpha)^{118}\text{Sn}$	26.11	-3.923	1.77	0.429	244.96	1.182	0.27
	23.70			0.411			
	21.28			0.394			
	18.38			0.373			
	16.44			0.359			
$^{124}\text{Te}(\alpha, \alpha)^{124}\text{Te}$	26.16	-3.918	1.712	0.592*	300.3	1.119	0.265
	23.73	-3.342		0.373			
	21.31	-2.767		0.400			
	18.41	-2.077		0.433			
	16.47	-1.617		0.455			
$^{128}\text{Te}(\alpha, \alpha)^{128}\text{Te}$	26.18	-3.108	1.76	0.356	298.92	1.183	0.265
	23.76	-2.990		0.342			
	21.33	-2.873		0.328			
	18.42	-2.732		0.311			
	16.48	-2.638		0.300			
$^{130}\text{Te}(\alpha, \alpha)^{130}\text{Te}$	26.19	-3.860	1.74	0.411	227.3	1.188	0.274
	21.34	-3.645		0.376			
	18.43	-3.517		0.354			
	16.49	-3.431		0.340			

The previous study by Galaviz of the mass dependence of the  $\alpha$ -nucleus potential [39] (Table 6.10) was limited to the energy range of the Coulomb barrier and below ( $E = 14.4$  and  $19.5$  MeV for  $^{112}\text{Sn}$  and  $E = 19.5$  MeV for  $^{124}\text{Sn}$ ).

TABLE 6.10

IMAGINARY GEOMETRY PARAMETERS AND WIDTH (w) FOR  $^{112,124}\text{Sn}$  [39]

Reaction	$W_V$	$r_V$	$a_V$	$W_S$	$r_S$	$a_S$	w
$^{112}\text{Sn}(\alpha, \alpha)^{112}\text{Sn}$	-3.137	1.737	0.341	356.36	1.252	0.218	1.004
$^{124}\text{Sn}(\alpha, \alpha)^{124}\text{Sn}$	-2.467	1.723	0.296	212.22	1.23	0.299	1.006

Comparing the results from Galaviz [39] with the current ones of  $^{118}\text{Sn}$  at 16.44 and 18.38 MeV, a trend emerges. Parameterizing the depth ( $W_S$ ) and diffuseness ( $a_S$ ) of the surface terms as a function of neutron number gives:

$$W_S = -12.012*N + 1088 \quad a_S = 0.0067*N - 0.1967 \quad (6.3)$$

TABLE 6.11

PARAMETERIZATION OF THE DEPTH AND DIFFUSENESS OF THE SURFACE TERMS AS A FUNCTION OF NEUTRON NUMBER

Reaction	$W_{S_{meas}}$	$W_{S_{par}}$	%	$a_{S_{meas}}$	$a_{S_{par}}$	%
$^{112}\text{Sn}(\alpha, \alpha)^{112}\text{Sn}$	356.36	343.26	3.68	0.218	0.219	0.3
$^{118}\text{Sn}(\alpha, \alpha)^{118}\text{Sn}$	244.96	271.18	9.67	0.27	0.259	4
$^{124}\text{Sn}(\alpha, \alpha)^{124}\text{Sn}$	212.22	199.11	6.18	0.299	0.299	0.3

From this study and that of Galaviz [39]

The difference in the imaginary depth and diffuseness between [39] and the current study is less than 10% in all cases (Table 6.11). This linear parameterization of the surface terms that arises could be because the previous study [39] was limited to the low energy regime where the surface is most sensitive to the scattering. The higher energy range in the current study should account for the difference observed in the volume terms (since at higher energies there may be an enhancement of the volume contribution).

### 6.2.5 Parameterizations

Atzrott et al. [50] computed the  $\alpha$ -nucleus potentials for a number of semi- and doubly magic nuclei over a large energy range (140 to 27 MeV). Their analysis included the DF parameterization in the real part. Different parameterizations for the imaginary part were chosen including Fourier-Bessel and WS volume and surface terms. Considering also the study done on  $^{92}\text{Mo}(\alpha,\alpha)^{92}\text{Mo}$  and  $^{112}\text{Sn}(\alpha,\alpha)^{112}\text{Sn}$  [36,39], the general trend of  $J_R$  has been linear such that it increases with decreasing energy (Figure 6.14).

The total strength of the real potential normalized to the number of interacting nucleons, defined in equation 3.14 as the volume integral  $J_R$ , is a way to normalize between different results. Figure 6.15 shows the trend of  $J_R$  of all nuclei obtained from this study. Notice that the values of  $^{106}\text{Cd}$  fall within the bottom range for this family of potentials (320-350 MeV fm<sup>3</sup>). Referring back to Table 6.6, this is expected since there seems to be an enhancement in  $J_R$  ( $\lambda = w = 1$ ). Previous results of  $^{106}\text{Cd}$  by [81] list a value of 266.91 for  $J_{R,0}(\lambda = 1 \text{ and } w = 0.987)$  which at  $E_{\text{lab}} = 17.65$  MeV would give a

result of  $J_R = 367 \text{ MeV fm}^3$ . This value corresponds to a different family of potentials than the one considered here.

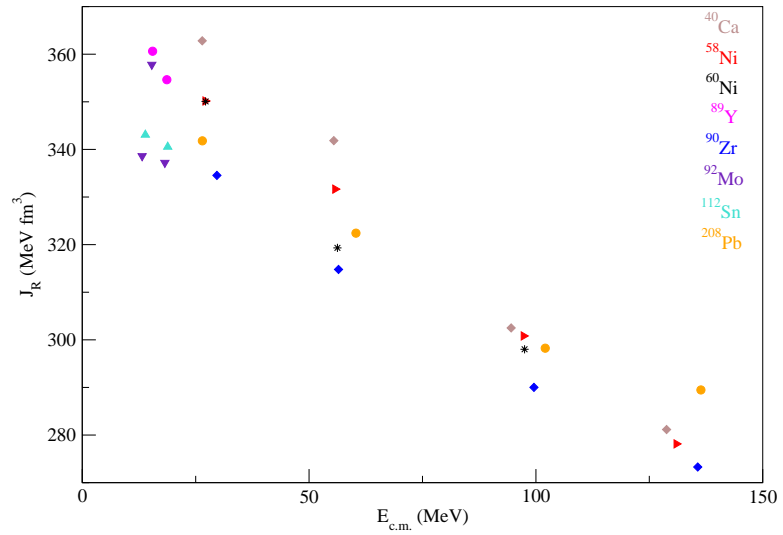


Figure 6.14 Volume integral values ( $J_R$ ) from previous studies on semi-magic and doubly magic nuclei

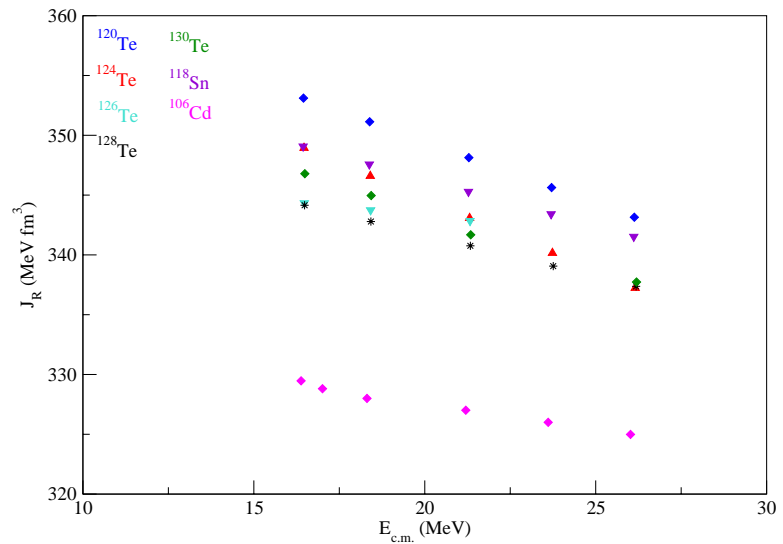


Figure 6.15 Strength of the real potential for all isotopes of this study.

Since the shape of the real potential is given by the folding procedure, this means that the real part of the  $\alpha$ -nucleus optical potential can be determined at energies below the Coulomb barrier with relatively small uncertainties (discrete ambiguities can be resolved from the systematic behavior of  $\alpha$ -nucleus potentials). The situation for the imaginary part of the potential is different. The volume integral  $J_I$  of the imaginary part depends strongly on the energy because many reaction channels open at energies around the Coulomb barrier. Different parametrizations have been proposed [33,105,106]. As an example, the Brown-Rho (BR) parametrization [105] is applied to  $^{128,130}\text{Te}$ . It takes the form of:

$$\begin{aligned}
 J_I(E_{c.m.}) &= 0 && \text{for } E_{c.m.} \leq E_0 \\
 J_I(E_{c.m.}) &= J_0 \frac{(E_{c.m.} - E_0)^2}{(E_{c.m.} - E_0)^2 + \Delta^2} && \text{for } E_{c.m.} > E_0
 \end{aligned} \tag{6.4}$$

with the excitation energy  $E_0$  of the first excited state. The saturation parameter  $J_0$  and the rise parameter  $\Delta$  are adjusted to the experimentally derived values (Table 6.12).

TABLE 6.12  
VALUES FOR THE BR PARAMETERIZATION APPLIED TO  $^{128,130}\text{Te}$

Isotope	Saturation Value	Rise parameter	Threshold energy
$^{128}\text{Te}$	$J_0 = 89.1 \text{ MeV fm}^3$	$\Delta = 3.58 \text{ MeV}$	$E_0 = 0.743 \text{ MeV}$
$^{130}\text{Te}$	$J_0 = 78.1 \text{ MeV fm}^3$	$\Delta = 3.69 \text{ MeV}$	$E_0 = 0.839 \text{ MeV}$

Figure 6.16 shows the values of the imaginary strength of the potential at the different energies. The data points fall nicely on the curve. Unlike the real part, the shape of the imaginary potential remains undetermined. The noted ambiguities (arising from the inability to fix the geometry form factors) reduce the reliability of extrapolation to lower energies.

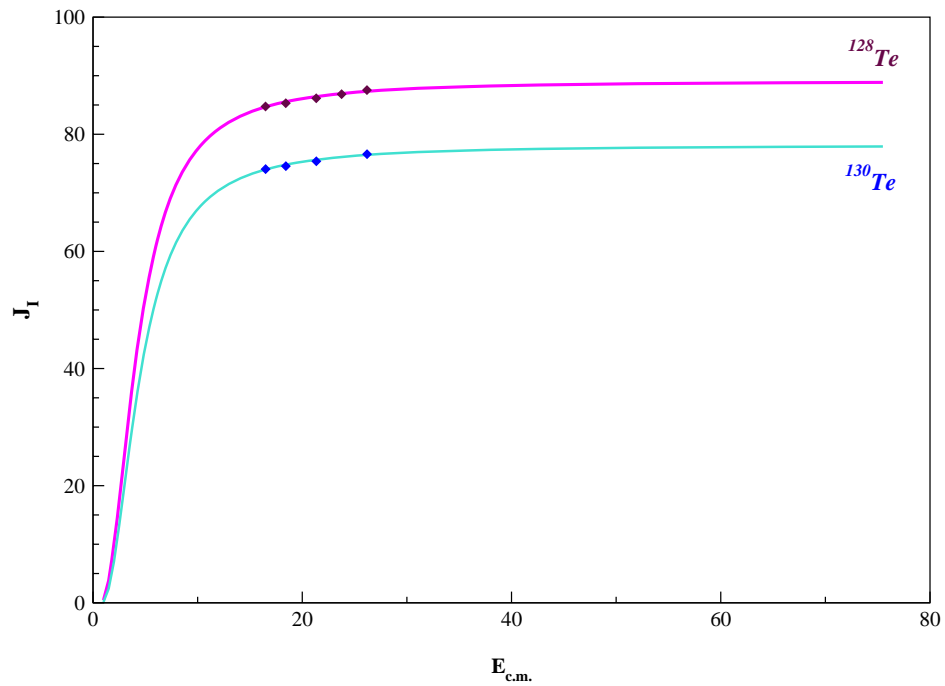


Figure 6.16 The BR parameterization applied to  $^{128,130}\text{Te}$ .

Table 6.1 listed the nuclear properties of the nuclei considered in the current study. In particular, several of the nuclei had ground state deformation. This effect (in particular in the case of  $^{124}\text{Te}$ ) perhaps shows itself in the inability of fixing all of the

geometry terms in the imaginary part. It has previously been suggested by Rauscher [78] that deformation effects should be included in the statistical model. While  $^{124,128,130}\text{Te}$  and  $^{118}\text{Sn}$  required some parameterization of the imaginary terms as a function of energy,  $^{124}\text{Te}$  required an extra parameterization in the surface contribution. This also seems to support the idea that for deformed nuclei, a stronger absorption is present at lower energies [103]. When taking a global look at the local potentials derived in this study, there doesn't seem to be any pattern arising with charge (at least not at such a close vicinity  $Z = 48, 50$  and  $52$ ); however, a possible predictive link was observed when looking at the depth of the imaginary volume term ( $W_V$ ) at low energies as a function of neutron number.

TABLE 6.13  
RELATIONSHIP OF VOLUME DEPTH ( $W_V$ ) TO NEUTRON NUMBER (\* IS A  
CLOSED SUBSHELL).

Isotope	Z	N	$W_V$
$^{106}\text{Cd}$	48	58*	-2.964
$^{118}\text{Sn}$	50	68*	-3.923
$^{120}\text{Te}$	52	68*	-3.932
$^{124}\text{Te}$	52	72	-1.617
$^{126}\text{Te}$	52	74	-2.330
$^{128}\text{Te}$	52	76	-2.638
$^{130}\text{Te}$	52	78	-3.431

The volume depth of the imaginary term for each of the isotopes studied is listed in Table 6.13.  $^{106}\text{Cd}$ ,  $^{118}\text{Sn}$ , and  $^{120}\text{Te}$  all have a closed neutron subshell.  $^{118}\text{Sn}$  also has a magic

proton shell ( $Z=50$ ). The other Te isotopes are unfilled subshells and shells; however, a linear trend of  $W_V$  with  $N$  exists for both sets of data. Parameterizing both, the following relationships ensue:

$$\text{Closed subshell: } W_V = -0.0963*N + 2.6243$$

$$\text{Unfilled subshell: } W_V = -0.2875*N + 19.061 \quad (6.5)$$

The value for  $W_V$  obtained by Galaviz for  $^{112}\text{Sn}$  and  $^{124}\text{Sn}$  was -3.137 and -2.467, respectively [39]. Using the unfilled subshell equation, a value of -2.214 is obtained for the case of  $^{124}\text{Sn}$ . This is a difference of about 10%. Although not a closed  $N$  subshell, if we parameterize  $^{112}\text{Sn}$  using the closed subshell equation (6.5), a value of -3.346 is obtained. This is a 6% difference. More  $\alpha$ -elastic scattering data within this current energy and mass regime may provide some insight as to whether the relationships of equations 6.3 and 6.5 could be generalized.

### 6.2.6 Comparison of Local Potentials

Due to the very small number of  $\alpha$ -elastic scattering experiments performed on p-nuclei [35,36,39,81] and the difficulties previously outlined in determining potentials below the Coulomb barrier,  $^{106}\text{Cd}(\alpha,\alpha)^{106}\text{Cd}$  was remeasured [10,81] and extended to the higher energy regime. Table 6.14 shows the geometry parameters of the result obtained in this study along with the parameters resulting from the study done by [81]. The energy range for the Atomki run was 16.13, 17.65 and 19.61 MeV (lab frame). Note that in this current study an energy value of 17.65 MeV was chosen to exactly match with the

Atomki results. Although a comparison cannot be made at one energy point since the potential parameters are obtained from considering all energy values; nevertheless, it makes for a more effective comparison. Note the difference in the  $b^*$  parameter (slope)

TABLE 6.14

SOLUTIONS OF  $^{106}\text{Cd}(\alpha,\alpha)^{106}\text{Cd}$  OBTAINED FROM THIS STUDY AND [81]

Solution	$W_V(\text{MeV})$	$R_V(\text{fm})$	$a_V(\text{fm})$	$W_S(\text{MeV})$	$R_S(\text{fm})$	$a_S(\text{fm})$
ND	-2.964	1.783	0.382	334.35	1.238	0.234
Atomki	-2.879	1.744	0.347	339.01	1.262	0.206

Solution	$a^*(\text{MeV fm}^3)$	$b^*(\text{fm}^3)$	$J_{R,0}$	$w$
ND	341.49	-0.7381	275.94	0.998
Atomki	377.99	-0.6519	266.91	0.987

from the two solutions. For all previous studies done on p-nuclei [36,39,81], this weak value for  $b^*$  was chosen so as to reduce the uncertainties of the extrapolation to the relevant energy region. Due to the much larger energy regime considered in this study, maintaining this value for the slope for all isotopes was not possible. It should be emphasized that the parameters of the DF potential (excluding  $\lambda$  and  $w$ ) were identical. That is, using 0.987 for  $w$  obtained from [81], a value of  $J_{R,0} = 266.91$  (an exact match) results when doing the calculation; therefore, the variation in the real part of the potential from the separate local potentials doesn't come from any variation in the target or projectile densities but it arises only from the strength ( $\lambda$ ) and width ( $w$ ) of the real

potential. The relation between these two quantities has been previously studied [36].

TABLE 6.15  
PARAMETERS OF THE REAL AND IMAGINARY PART OF THE LOCAL  
POTENTIALS DERIVED FROM THIS STUDY AND [81]

Solution	$\lambda$	w	$J_R$	$V_V$	$r_V$	$a_V$	$V_S$	$R_S$	$a_S$
ND	1.1916	0.998	328.81	-2.964	1.783	0.382	334.35	1.238	0.234
Atomki	1.3746	0.987	366.9	-2.879	1.744	0.347	339.01	1.262	0.206
%				3	2.2	9.2	1.4	2.1	12

Table 6.15 lists the values of the real and imaginary parts of the two solution sets (at the same energy  $E_{lab} = 17.65$  MeV). Here two different minima are presented for  $^{106}\text{Cd}$ . According to the Atomki measurement, the correct family doesn't correspond to the one suggested by [43]. The third row shows the difference in percentage of the imaginary geometry terms. Giving a conservative estimate of 5% for the errors, with the exception of the volume and surface diffuseness ( $a_V$  and  $a_S$ ), all other geometry parameters would fall within the range. In addition, when comparing the surface to volume ratio of the imaginary terms, one finds for both data sets that:

$$J_{I,V} = 0.22 J_{I,S}$$

It has been suggested [107] that the relative weight between the volume and surface terms of the imaginary part of the nuclear potential should be  $J_{I,V} = 0.22 J_{I,S}$ . Although the variation in diffuseness cannot be discounted, if for the moment any sensitivity in the geometry parameters individually is ignored and the relative weight is considered, then

the difference between the two arises from the real part only. Although the shape of the real part of the potential is fixed below the barrier, it has been suggested that at low  $\alpha$ -energies, there is a strong energy dependence of the real part of the  $\alpha$ -nucleus interaction [108]. This has been confirmed by  $\alpha$ -scattering on  $^{16}\text{O}$  and  $^{15}\text{N}$  [41]. This seems to suggest [43] that the correct family is the one that falls within the range of 320-350 and not the one offered by [81].

### 6.3 Astrophysical Implications

Cross sections and reaction rates for astrophysical applications are in the low energy regime (thermal energies up to a few MeV). In addition, most of the rates are experimentally undetermined and a reliable model must be developed to predict these properties with an acceptable degree of accuracy across the nuclear landscape. The challenge then is to try and provide all the necessary inputs into the model in a reliable way.

This study focused on the determination of local  $\alpha$ -nucleus potentials in order to try and remove some of the discrepancy observed between experimental data and theoretical predictions (as in the case of  $\alpha + ^{106}\text{Cd}$  and  $^{120}\text{Te}(\alpha, n)$ ). The correct modeling of the p-nuclei abundances requires an accurate global  $\alpha$ -nucleus potential. Remember that the experimental database for  $(\alpha, \gamma)$  reactions on p-nuclei is not a large one [32,64,65,109]. In addition, almost all reactions have been limited to under  $A \approx 140$ . The p-process simulation done by W. Rapp [19] showed the increased sensitivity of the

reaction rates above this mass region. This was verified in a previous study done on  $^{144}\text{Sm}(\alpha,\gamma)$  [32] where not only was there a large overestimation in cross section from the model predictions but in addition the local  $\alpha$ -nucleus optical potential derived [35] also failed to reproduce the experimental data at the lowest energies (a deviation of 3.5 at the lowest measured energy of 10.19 MeV).

### 6.3.1 Extrapolation of the potentials

The real part of the nuclear potential can be extrapolated linearly to within the Gamow window. Table 6.16 lists the value for the strength of the real potential for the p-nuclei  $^{106}\text{Cd}+\alpha$  and  $^{120}\text{Te}+\alpha$  assuming the approximate energy regime for these p-process reactions in the temperature range of  $T_9 = 2-3$  K.

TABLE 6.16

VALUES OF THE STRENGTH POTENTIAL OF THE REAL PART AT THE APPROXIMATE EFFECTIVE BURNING TEMPERATURES OF THE GAMOW WINDOW FOR THE  $^{106}\text{Cd}+\alpha$  AND  $^{120}\text{Te}+\alpha$  SYSTEMS

Isotope	$J_R(E)$	E (MeV)	$J_R$
$^{106}\text{Cd}$	$341.49-0.7381*E_{c.m.}$	7	336.5
		11	333.66
$^{120}\text{Te}$	$370.19-1.0379*E_{c.m.}$	7	362.92
		11	359.6

Although the Brown-Rho parameterization was used to parameterize the imaginary strength potential for  $^{128,130}\text{Te}$ , it was not possible to do so for other isotopes. A variation in  $J_I$  is required and for  $^{106}\text{Cd}$  and  $^{120}\text{Te}$ , the value of  $J_I$  was the same at all energies (the imaginary geometry parameters were fixed at all energies).

### 6.3.2 The S-factor of $^{106}\text{Cd}(\alpha,\gamma)^{110}\text{Sn}$

The calculation of the S-factor was performed by using the web based NON-SMOKER [110]. The only parameter that was changed was the  $\alpha$ -optical potential, all other inputs were kept at the standard settings. The values used were taken from the local potential at 17 MeV. Since it was not possible to parameterize the imaginary term, it was therefore not possible to use an extrapolation down to the Gamow window in the calculation of the S-factor. The real part of the potential is the result from the calculation

of eq. (3.14) and was input as 800 data points in radial step sizes of 0.025. The imaginary part was taken as a sum of volume and surface WS potential with the corresponding geometry form factors obtained from the fits to the data.

Figure 6.17 shows the results of the S-factor calculated from the local  $^{106}\text{Cd}$  potential. In addition, the S-factor using the standard settings of NON-SMOKER is shown. In that case, the  $\alpha$ -potential is the global one of McFadden/Satchler. The experimental data points for the S-factor of the  $\alpha$ -capture reaction are those of the Notre Dame experiment. When looking at Figure 6.17, note that as we go farther within the Gamow window (towards decreasing energy) the data to calculated S-factor value from the local potential seems to deviate more and more. The exception to this is at 11 MeV but here the  $(\alpha, n)$  channel opens which is stronger than the  $(\alpha, \gamma)$  and suppresses it. Remember that the potential was taken at 17 MeV. No extrapolation was used. It seems to indicate that an energy extrapolation within the Gamow window may produce better agreement. While it is possible to extrapolate the real part within the window, it is unclear how such an extrapolation should occur for the imaginary part. Even if we keep the same relative weight of 0.22 of surface to volume, how to effectively weight the individual imaginary geometry terms is unclear. Any conclusive results are difficult to draw since there are several unknowns. These include the effect of the real part of the potential on the S-factor (even for a small deviation) and how well an extrapolation of the local potential down to the Gamow window would reproduce the data (in particular of the imaginary part which varies strongly below the barrier).

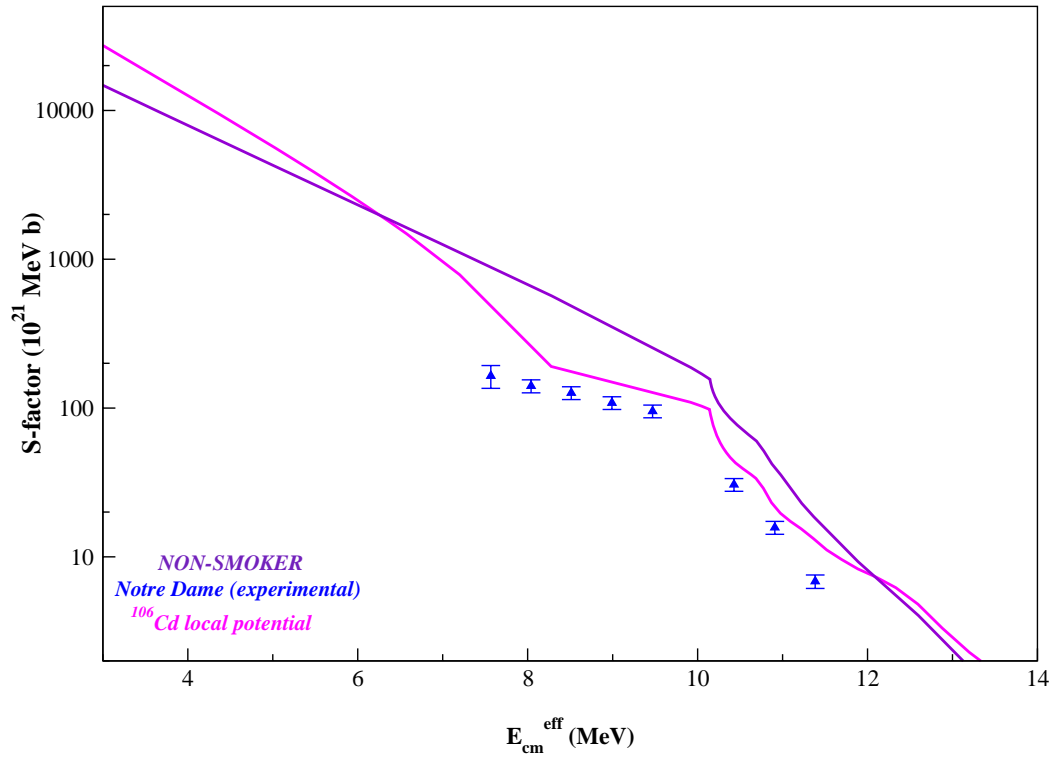


Figure 6.17 S-factor of  $^{106}\text{Cd}(\alpha,\gamma)$  using the local potentials of  $^{106}\text{Cd}$  obtained in this study along with the values obtained from the standard settings of NON-SMOKER [77,78,79,110,111].

### 6.3.3 The S-factor of $^{106}\text{Cd}(\alpha,n)^{109}\text{Sn}$ and $^{106}\text{Cd}(\alpha,p)^{109}\text{In}$

The local potential of  $^{106}\text{Cd}$  obtained from this study was also compared to the experimental results obtained from [64] for the  $(\alpha,p)$  and  $(\alpha,n)$  channels. When comparing the local potential to the results obtained from the standard settings of NON-SMOKER [77,78,79,110,111], we see that the shape of the  $(\alpha,n)$  is very similar in both cases (Figure 6.18). The local potential reproduces the lower energy points better while the standard potential better matches the higher energy data.

When comparing the potentials to the ( $\alpha$ ,p) case, a different trend arises.

The shape of the two potentials is exactly reproduced until about 11 MeV where the local potential deviates much more strongly. The lowest energy point crosses the local potential while the second data point falls on the standard potential curve. In fact, the local potential places the peak of the S-factor at a much higher energy.

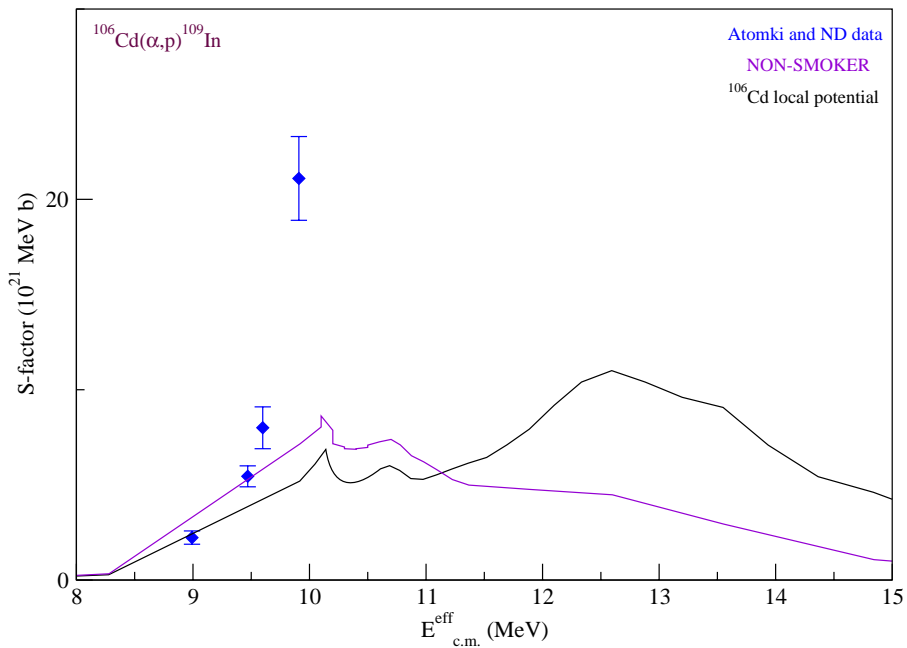
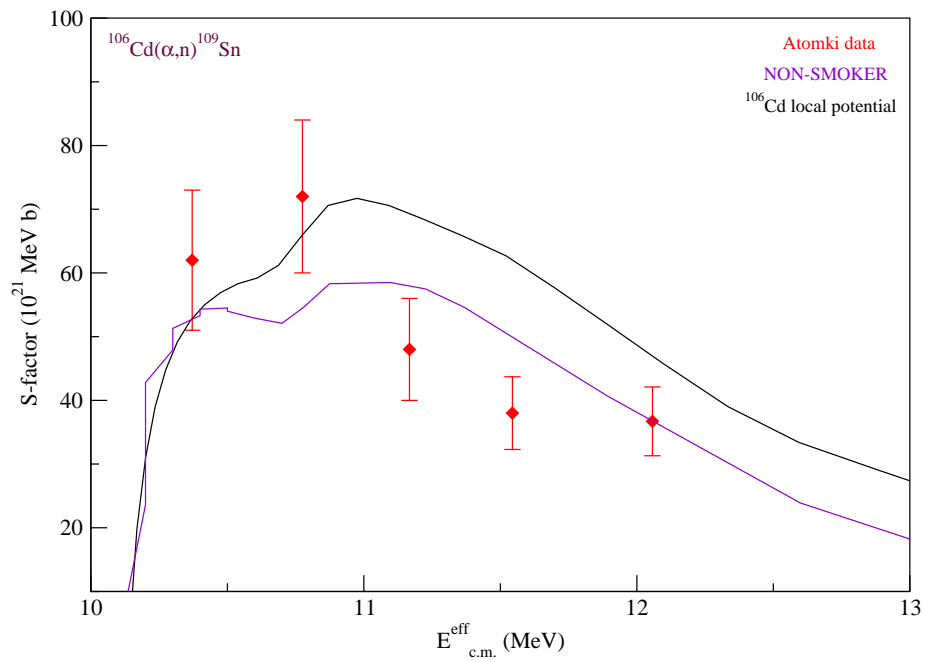


Figure 6.18 Experimental S-factors of  $^{106}\text{Cd}(\alpha,n)^{109}\text{Sn}$  and  $^{106}\text{Cd}(\alpha,p)^{109}\text{In}$  compared to the S-factor values obtained from the local potential and NON-SMOKER [77,78,79,110,111].

#### 6.3.4 The S-factor of $^{120}\text{Te}(\alpha, n)^{123}\text{Xe}$

Further confirmation of the very strong sensitivity of the S-factor to the  $\alpha$ -nucleus potential comes from the case of  $^{120}\text{Te}(\alpha, n)^{123}\text{Xe}$ .

As was done for the  $^{106}\text{Cd}(\alpha, \gamma)^{110}\text{Sn}$  reaction, the S-factor was calculated using the web based NON-SMOKER [110]. All of the standard settings were kept fixed with the exception of the  $\alpha$ -nucleus potential. In that case, the local potential of  $^{120}\text{Te}$  derived from this study was used. Figure 6.19 shows the experimental S-factor values in comparison to the S-factor derived from the local potential of  $^{120}\text{Te}$  and the theoretical S-factor values obtained from the standard settings of NON-SMOKER [77,78,79,111]. Although the same flat trend of the S-factor is reproduced, the values derived considering the local potential underestimate it while the values obtained using the standard global potential [86] grossly overestimate it (Table 6.17).

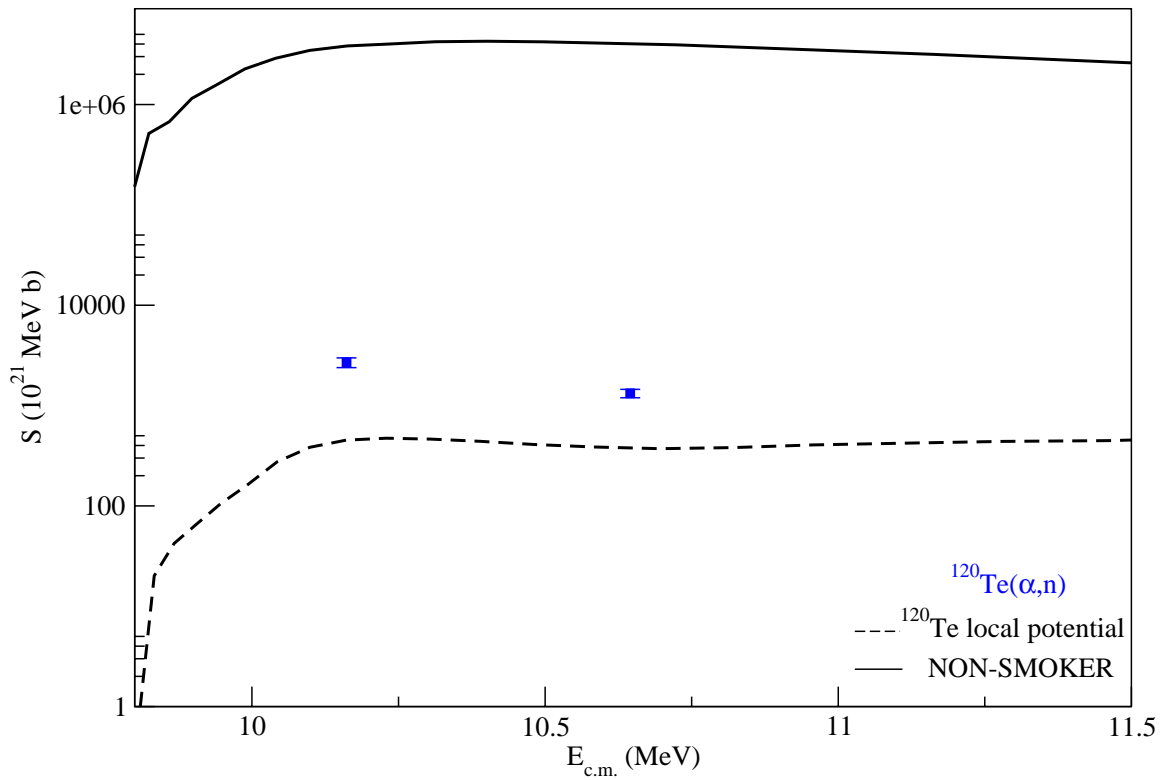


Figure 6.19 S-factor of  $^{120}\text{Te}(\alpha,n)^{123}\text{Xe}$  experimental values compared to the theoretical S-factors values derived from the  $^{120}\text{Te}$  local potential considered in this study and the global potential of McFadden/Satchler (standard settings of NON-SMOKER). The values are those of the 149 keV  $\gamma$ -line [77,78,79,86,110,111].

TABLE 6.17

 $^{120}\text{Te}(\alpha,n)^{123}\text{I}$ : EXPERIMENTAL S-FACTOR COMPARED TO NON-SMOKER

$E_{\text{cm}}$ (MeV)	$S$ ( $10^{21}$ MeV b)	factor
10.16	$2688.7 \pm 300.97$	
10.16	452	6
10.16	$3.83 \times 10^6$	$1.4 \times 10^3$
10.64	$1323.09 \pm 127.2$	
10.69	372	3.5
10.72	$3.93 \times 10^6$	$3 \times 10^3$

Comparison of data (1<sup>st</sup> row) to theory (2<sup>nd</sup> row: local potential; 3<sup>rd</sup> row: NS values) of the S-factor for  $^{120}\text{Te}(\alpha,n)$ . NON-SMOKER (NS) greatly overestimates the values.

Avrigeanu [89] has compared (n, $\alpha$ ) data of  $^{92,95,98,100}\text{Mo}$  with the potential obtained by [87,90] and that of [86]. At low energies (within the Gamow window), the potentials fail to match the experimental data. In fact, the same trend is observed. That is, the potential underestimates the data points. It has been suggested [89] that there is a need for an increased diffuseness parameter to correctly describe ( $\alpha,n$ ) and (n, $\alpha$ ) data. This would seem to support the suggestion that [89] the temperature dependence of the nuclear density distribution function would have to be included. The failure of the local potential of  $^{120}\text{Te}$  to reproduce the capture data seems to suggest that some modification (to the potential for  $\alpha,n$  reactions) is needed. For the case of  $^{106}\text{Cd}(\alpha,n)$ , the local potential (and standard potential) reproduced the experimental data fairly well. Why is there a much larger deviation in the case of  $^{120}\text{Te}(\alpha,n)$ ? This effect could be due to the fact that we are at a higher mass region where the ( $\gamma,\alpha$ ) branchings are more dominant

and hence the ( $\alpha$ ,n) and ( $\alpha$ ,p) much more sensitive to the  $\alpha$ -optical potential (as in the case of  $^{144}\text{Sm}(\alpha,\gamma)^{148}\text{Gd}$  [32]).

#### **6.4 Local Potentials: A user's guide**

Table 6.18 lists all of the local potential parameters derived in this study. Although the real part of the potential can be extrapolated down (by use of the equation under the column “ $\lambda$ ”) past 17 MeV, the imaginary parameters cannot and are valid within the specified energy range.

TABLE 6.18

LOCAL POTENTIAL PARAMETERS

Isotope	E (MeV)	$V_V$	$r_V$	$a_V$
<sup>106</sup> Cd	27 - 17	-2.964	1.783	0.382
<sup>118</sup> Sn	27 - 17	-3.923	1.77	$a_V = 0.0072 * E_{c.m.} + 0.2405$
<sup>120</sup> Te	27 - 17	-3.932	1.745	0.397
<sup>124</sup> Te	24.5 - 17	$V_V = 2.2946 - 0.2375 * E_{c.m.}$	1.712	$a_V = 0.6391 - 0.0112 * E_{c.m.}$
<sup>124</sup> Te	27	$V_V = 2.2946 - 0.2375 * E_{c.m.}$	1.712	0.592
<sup>126</sup> Te	22 - 17	-2.33	1.704	0.445
<sup>128</sup> Te	27 - 17	$V_V = -(1.8405 + 0.0484 * E_{c.m.})$	1.76	$a_V = 0.2041 + 0.0058 * E_{c.m.}$
<sup>130</sup> Te	27 - 17	$V_V = -(2.7019 + 0.0442 * E_{c.m.})$	1.74	$a_V = 0.2176 + 0.0074 * E_{c.m.}$

Isotope	E (MeV)	$V_S$	$r_S$	$a_S$
<sup>106</sup> Cd	27 - 17	334.35	1.238	0.234
<sup>118</sup> Sn	27 - 17	244.96	1.182	0.27
<sup>120</sup> Te	27 - 17	312.13	1.179	0.264
<sup>124</sup> Te	24.5 - 17	300.3	$r_S = 1.4671 - 0.0133 * E_{c.m.}$	0.265
<sup>124</sup> Te	27	300.3	$r_S = 1.4671 - 0.0133 * E_{c.m.}$	0.265
<sup>126</sup> Te	22 - 17	333.66	1.229	0.251
<sup>128</sup> Te	27 - 17	298.92	1.183	0.265
<sup>130</sup> Te	27 - 17	227.3	1.188	0.274

Isotope	E (MeV)	$J_{R,0}$	$a^*$	$b^*$	$\lambda$	$w$
<sup>106</sup> Cd	$E \leq 19$	275.94	341.49	-0.7381	$\lambda = (a^* + b^* E_{c.m.}) / J_{R,0}$	0.998
<sup>106</sup> Cd	$E > 19 - 27$	**	**	**	$\lambda = 5.6325 - 4.4525w$	$w = 0.0014 * E_{c.m.} + 0.9715$
<sup>118</sup> Sn	$E \leq 27$	263.15	366.18	-0.9524	$\lambda = (a^* + b^* E_{c.m.}) / J_{R,0}$	0.992
<sup>120</sup> Te	$E \leq 27$	263.52	370.19	-1.0379	$\lambda = (a^* + b^* E_{c.m.}) / J_{R,0}$	0.993
<sup>124</sup> Te	$E \leq 27$	258.93	368.83	-1.2083	$\lambda = (a^* + b^* E_{c.m.}) / J_{R,0}$	0.99
<sup>126</sup> Te	$E \leq 22$	264.93	349.43	-0.3087	$\lambda = (a^* + b^* E_{c.m.}) / J_{R,0}$	0.999
<sup>128</sup> Te	$E \leq 27$	272.5	355.48	-0.6886	$\lambda = (a^* + b^* E_{c.m.}) / J_{R,0}$	1.01
<sup>130</sup> Te	$E \leq 27$	276.21	362.16	-0.9336	$\lambda = (a^* + b^* E_{c.m.}) / J_{R,0}$	1.016

## 6.5 Resonances

The pattern of phase shifts observed in Fig. 6.7 (for  $^{106}\text{Cd}$ ), the large overestimation in diffraction pattern of the Avrigeanu potential (especially in  $^{106}\text{Cd}$  – a deformed nucleus near a closed shell), and the huge overestimation in the last point of the S-factor of  $^{106}\text{Cd}(\alpha,p)$  (Fig. 6.18 – right below the neutron threshold) indicate the presence of isolated resonant components. This is also evidenced when looking at the cross section calculated from the Avrigeanu potential of  $^{128}\text{Te}$  versus  $^{130}\text{Te}$  at 27 MeV (Appendix D). In that case, we see an increased diffraction pattern in  $^{128}\text{Te}$ . This is most probably due to contaminants arising from the  $^{128}\text{Te}$  oxide (versus  $^{130}\text{Te}$  which is metallic). In addition, the large  $\chi^2$  obtained in the fitting (Table 6.2) indicate that the current model fails to include compound contributions [103]. It appears that in order to effectively extrapolate the nuclear potential down to within the relevant energy regime requires that the current global models address these resonant contributions.

## CHAPTER 7

### CONCLUSION AND OUTLOOK

The  $\alpha$ -nucleus potential, which is an essential component of the HF model for the simulation of the abundance distribution of p-nuclei, is inconsistent. The standard global  $\alpha$ -potential of McFadden/Satchler [86] and Avrigeanu [89,90] seemed to give the best reproduction for elastic scattering data but the standard potential [86] results in a large overestimation for  $^{120}\text{Te}(\alpha, n)^{123}\text{Xe}$ . The superiority of local to global potentials has been shown in the case of  $^{106}\text{Cd}(\alpha, \gamma)^{110}\text{Sn}$  and particularly for  $^{120}\text{Te}(\alpha, n)^{123}\text{Xe}$ . Local potentials for  $^{106}\text{Cd}$ ,  $^{118}\text{Sn}$ , and  $^{120,124,126,128,130}\text{Te}$  have been obtained. Unfortunately, due to the high enrichment needed ( $\approx 90\%$ ), further  $\alpha$ -elastic scattering experiments are currently limited to the case of  $^{144}\text{Sm}$ . Although this has been previously measured [51], it was obtained considering only one energy point. Due to the very large deviations seen at low energy when comparing  $^{144}\text{Sm}(\alpha, \gamma)^{148}\text{Gd}$  [32] to that obtained from the local potential of  $^{144}\text{Sm}$  [51], a remeasurement (extending to the higher energy regime) is warranted. The mass region above  $A \approx 140$  is particularly important to investigate since the p-process simulation by W. Rapp showed the sensitivity of the abundances to a global variation of the rates ( $\gamma, \alpha$  and  $\alpha, \gamma$ ) in this regime [19].

Further testing of the HF model can come through activation experiments. This is limited above  $A \approx 120$  to a handful of measurements (i.e.,  $\alpha$ -capture on  $^{130}\text{Ba}$ ,  $^{136}\text{Ce}$ , and  $^{162}\text{Er}$ ). In particular, the reaction  $^{130}\text{Ba}(\alpha, \gamma)^{134}\text{Ce}$  would be a good candidate to test the local potential of  $^{130}\text{Te}$ . Additional information could be made available by direct determination of photodisintegration rates. Current efforts for  $(\gamma, \alpha)$  reactions are underway at the Institut für Strahlenphysik in Dresden, Germany.

In addition, for those reactions producing long-lived radioisotopes or even for those that can be measured by the activation technique but which produce insufficient  $\gamma$ -rays or low energy x-rays, AMS provides another means.

While several of the nuclei had ground state deformation, the particular case of  $^{124}\text{Te}$  perhaps is indicative that deformation should be included in the current statistical model [78]. Using a double folding parameterization on deformed nuclei has been considered by [112]; however, including such effects in the imaginary part of the potential when the geometry form factors are not fixed remains unknown. Clearly, much more extensive investigation is necessary for a more accurate global  $\alpha$ -nucleus potential.

## APPENDIX A

## TARGET INVENTORY

#	isotope	backing ( $\mu\text{g}/\text{cm}^2$ )	thickness ( $\mu\text{g}/\text{cm}^2$ )
1	$^{130}\text{Te}$	C(20)	126 (metal)
2	$^{120}\text{Te}$	C(20)	204.5 (oxide)
3	$^{124}\text{Te}$	C(20)	225.4 (oxide)
4	$^{126}\text{Te}$	C(20)	145 (metal)
5	$^{128}\text{Te}$	C(20)	181 (oxide)
a	$^{128}\text{Te}$	C(20)	132 (oxide)
56	$^{128}\text{Te}$	C(20)	132 (oxide)
77	$^{124}\text{Te}$	C(20)	184(oxide)
64	$^{120}\text{Te}$	C(20)	124(oxide)
50	$^{130}\text{Te}$	C(20)	157 (metal)
55	$^{130}\text{Te}$	C(20)	124 (metal)
1A	$^{118}\text{Sn}$	C(20)	116(oxide)
1h	$^{118}\text{Sn}$	C(20)	136(oxide)
3D	$^{106}\text{Cd}$	C(20)	230(metal)

APPENDIX B  
SUMMING CORRECTIONS

Theory: Coincidence Summing [113]

Assume a radionuclide with the following decay scheme:

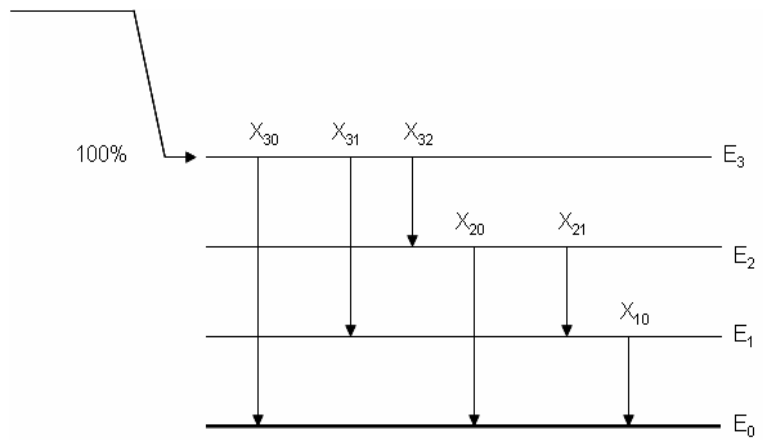


Figure B1 Decay scheme defining some of the parameters used in coincidence summing

The  $\gamma$ -ray abundances  $a_{ij}$  can be calculated from the branching ratios  $X_{ij}$  which are defined such that:

$$\sum_j X_{ij} = 1 \quad (\text{B1})$$

and the abundances as:

$$a_{10} = (X_{31} + X_{32}X_{21})X_{10} \frac{1}{1 + \alpha_{10}} \quad (\text{B2})$$

$$a_{30} = X_{30} \frac{1}{1 + \alpha_{30}} \quad (\text{B3})$$

In the absence of coincidence summing, the probability per disintegration of obtaining a count in a photopeak  $P_{ij}$  for any decay scheme is given by

$$P_{ij} = a_{ij} \varepsilon_{p_{ij}} \quad (\text{B4})$$

where  $\varepsilon_{p_{ij}}$  is the photopeak efficiency of the detector for photon energy  $E_\gamma = E_i - E_j$ . In the presence of coincidence summing, this basic probability has to be corrected for the probability of detecting other photons, emitted simultaneously by the decaying nucleus.

If this happens, even if the other photon deposits only part of its energy in the detector, the count will be lost from the photopeak (summing out). The resulting probability (considering only one cascade) is given as (B5):

$$P_{10} = X_{10} \frac{1}{1 + \alpha_{10}} \varepsilon_{p_{10}} X_{31} \left(1 - \frac{1}{1 + \alpha_{31}} \varepsilon_{t_{31}}\right) + X_{10} \frac{1}{1 + \alpha_{10}} \varepsilon_{p_{10}} X_{32} \left(1 - \frac{1}{1 + \alpha_{32}} \varepsilon_{t_{32}}\right) \cdot X_{21} \left(1 - \frac{1}{1 + \alpha_{21}} \varepsilon_{t_{21}}\right)$$

where  $\varepsilon_{t_{ij}}$  is the total detection efficiency for a photon with energy  $E_i - E_j$ .

Corrections for Cascade-Summing [70]

<sup>133</sup>Ba

Energy (keV)	Correction factor
81.0	[1.000-.789(KX)-0.030(79.6)-0.203(302.9)-0.004(223.0)-0.691(356.0)-0.071(276.4) -0.16(53.0)]
276.4	[1.000+0.005 {223.0} {53.0} / {276.4}] [1.000-1.520(KX)-.347(81.0)-0.079(160.8)-.337(79.6)]
302.9	[1.000+0.008 {79.6} {223.0} / {302.9}] [1.000-1.478(KX)-.386(81.0)-0.076(53.0)]
356.0	[1.000+0.038 {79.6} {276.4} / {356.0} +0.022 {302.9} {53.0} / {356.0}] [1.000-1.099(KX)-.386(81.0)]
384.0	[1.000+.793 {81.0} {302.9} / {384.0} +0.004 {161} {223.0} / {384.0}] [1.000-1.023(KX)-0.076(53.0)]

<sup>152</sup>Eu

Energy (keV)	Correction factor
121.8	[1.000-.772(KX)-.105(244.7)-.247(964.1)-.235(1112.1)-.073(867.4)-.364(1408.0)-0.005(719.4)-.029(444.0)-.008(295.9)-.009(1457.6)-.024(1212.9)]
244.7	[1.000-.772(KX)-.461(121.8)-.628(867.4)-.040(719.4)-.016(295.9).210(1212.9)]
344.3	[1.000-.003(KX)-0.081(411.1)-0.003(930.6)-.006(764.9)-.480(778.9)-.032(367.8)-.063(1089.7)-.017(678.6)-.001(324.8)-.060(1299.1)-.002(520.3)]
778.9	[1.000+.065 {411.1} {367.8} / {778.9}] [1.000-.028(KX)-.962(344.3)-.004(520.3)]
964.1	[1.000-1.064(KX)-.461(121.8)-.116(444.0)]

1085.9	$[1.000+.674\{121.8\}\{964.1\}/\{1085.9\}]$ $[1.000-.771(KX)-.116(444.0)]$
1112.1	$[1.000+.280\{244.7\}\{867.4\}/\{1112.1\}]$ $[1.000-1.063(KX)-.461(121.8)-.025(295.9)]$
1408.0	$[1.000+.011\{244.7\}\{719.4\}/\{1408.0\}+$ $0.079\{964.1\}\{444.0\}/\{1408.0\}+.016\{1112.1\}\{295.9\}/\{1408\}]$ $[1.000-1.046(KX)-.461(121.8)]$

\*\* [ ] represents the total efficiency and { } is the photopeak efficiency.

<sup>152</sup>Eu: all values are fit on a log-log scale and  $\epsilon = 22.688E-0.81991$

TABLE B1  
PHOTOPEAK EFFICIENCY DERIVED FROM <sup>152</sup>Eu

<b>E (keV)</b>	<b><math>\epsilon</math></b>
122	42% $\pm$ 0.98%
245	25.8% $\pm$ 0.60%
344	20% $\pm$ 0.47%
779	9.6% $\pm$ 0.22%
964	7.83% $\pm$ 0.18%
1112	7.22% $\pm$ 0.17%
1408	5.78% $\pm$ 0.13%

TABLE B2

PHOTOPEAK EFFICIENCY DERIVED FROM  $^{133}\text{Ba}$ 

<b>E (keV)</b>	<b><math>\epsilon</math></b>
276	22.4% $\pm$ 0.69%
303	21.6% $\pm$ 0.67%
356	18.89% $\pm$ 0.58%

The efficiency values obtained from  $^{133}\text{Ba}$  allow us to check the validity of the method used for the  $^{152}\text{Eu}$ . From the log-log fit:

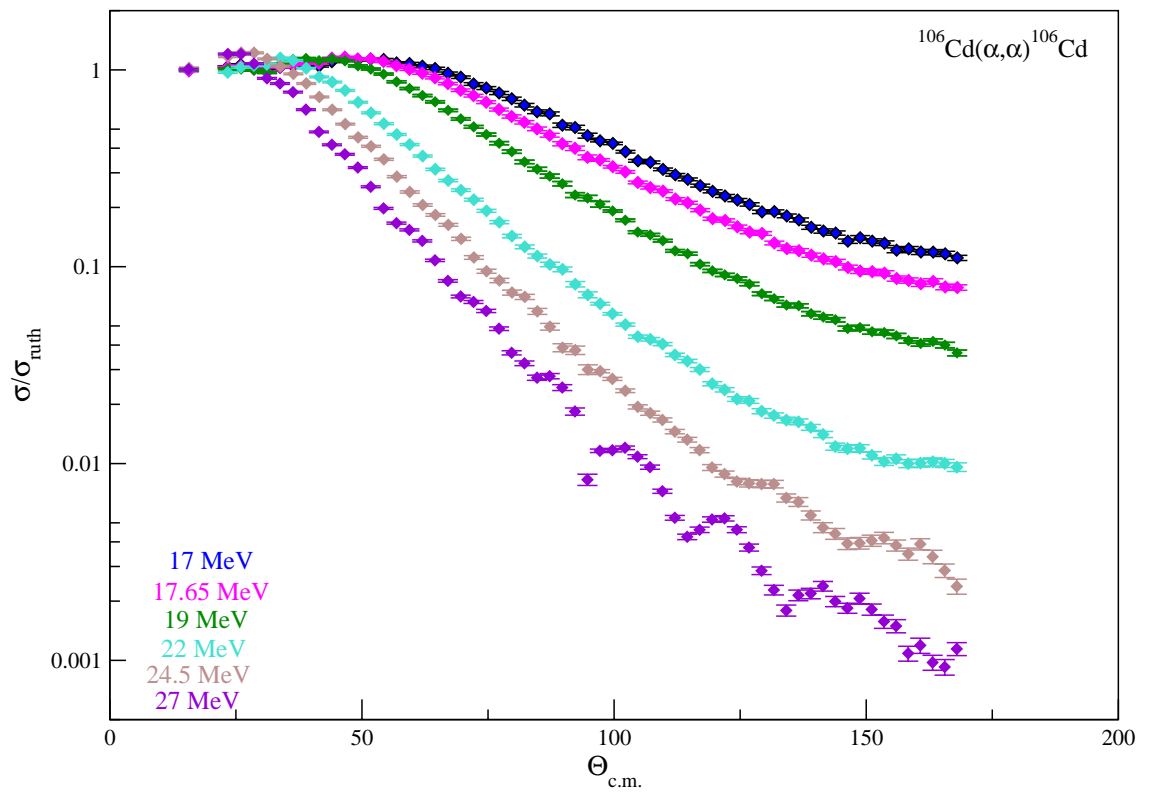
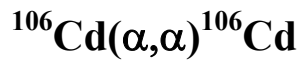
TABLE B3  
 PHOTOPEAK EFFICIENCY VALUES DERIVED FROM THE LOG-LOG FIT  
 USING  $^{152}\text{Eu}$

$E_{\gamma}$ (keV)	$\epsilon$	Reaction
203.5	29% $\pm$ 0.67%	$^{106}\text{Cd}(\alpha, p)^{109}\text{In}$
280.5	22.32% $\pm$ 0.51%	$^{106}\text{Cd}(\alpha, \gamma)^{110}\text{Sn}$
1321	6.26% $\pm$ 0.14%	$^{106}\text{Cd}(\alpha, n)^{109}\text{Sn}$

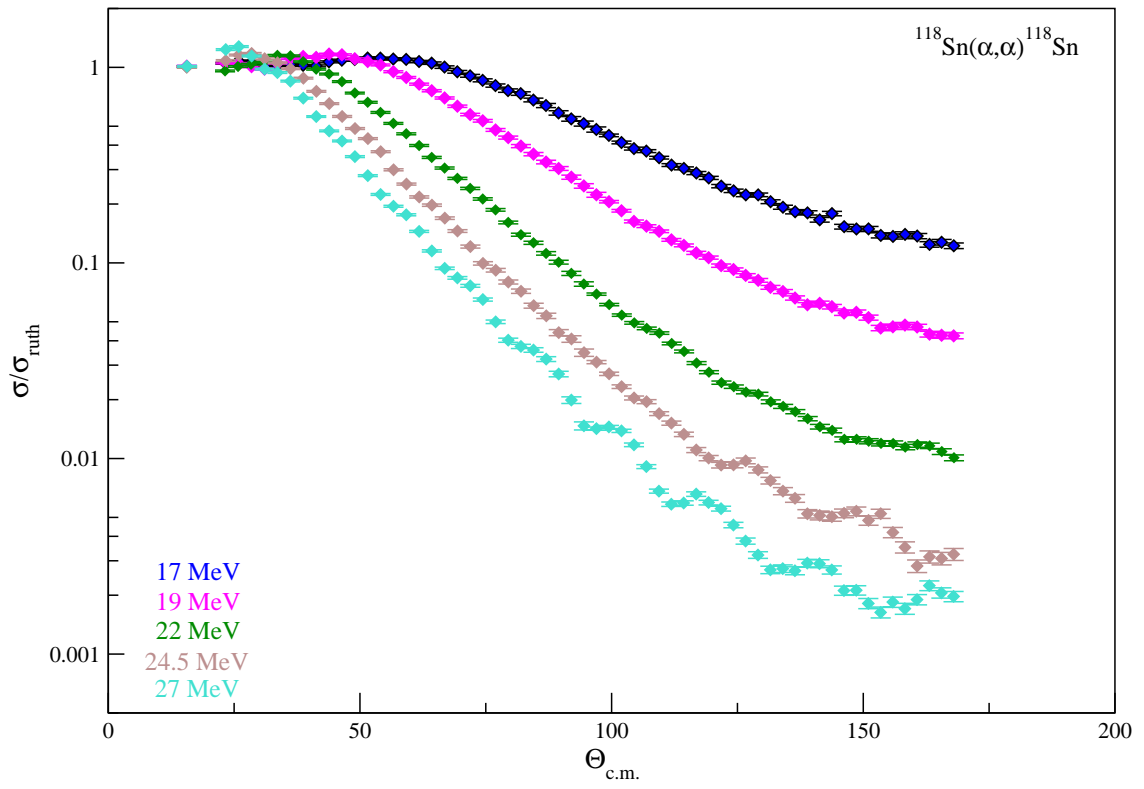
We see excellent agreement between the two methods.

APPENDIX C

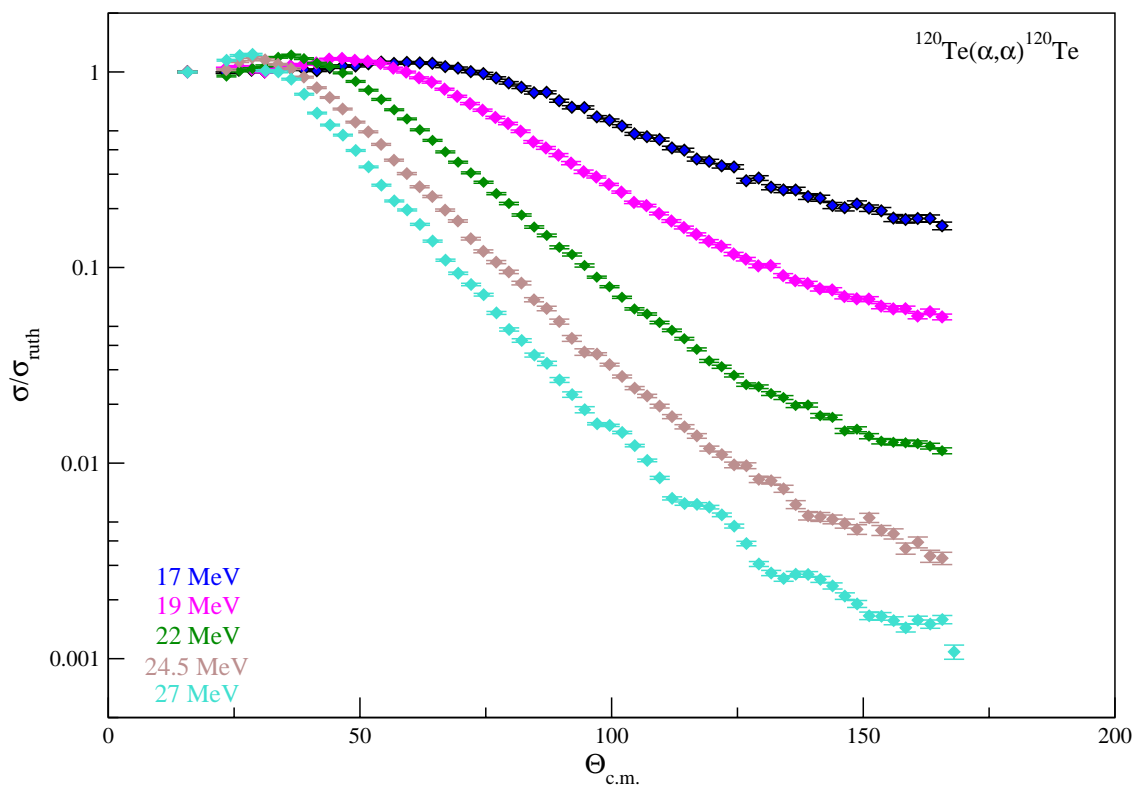
NORMALIZED CROSS SECTIONS



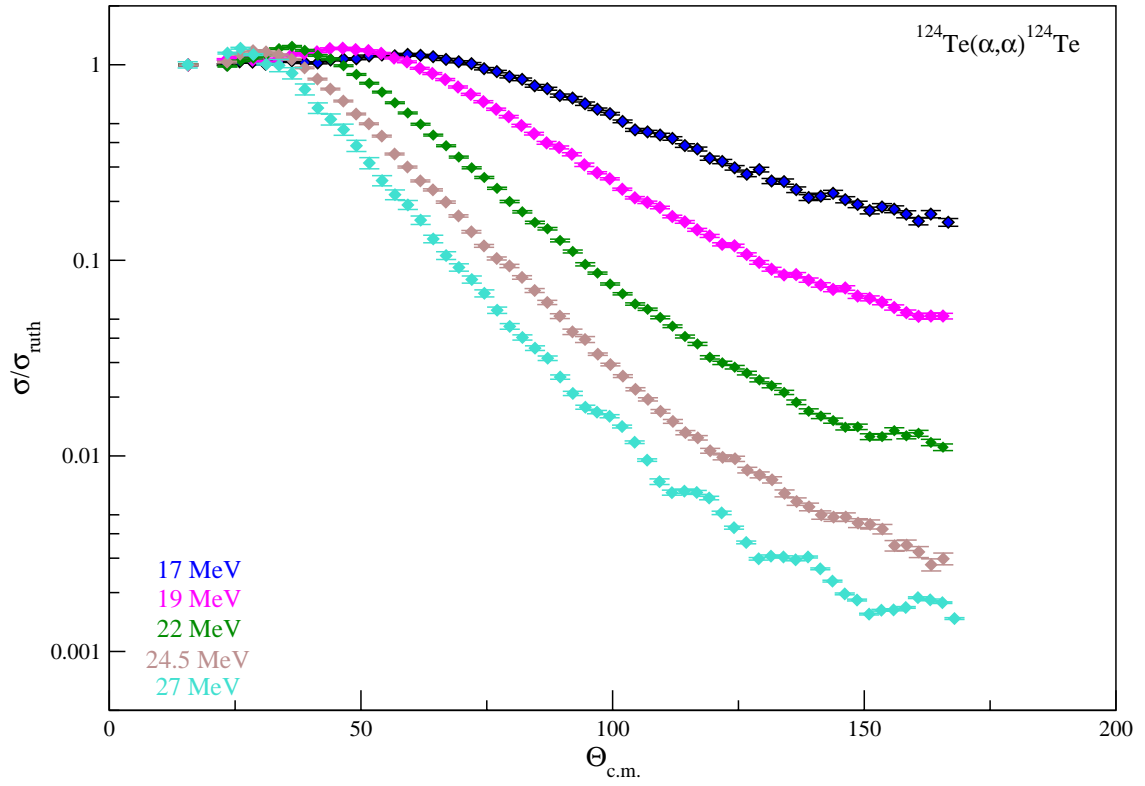
# $^{118}\text{Sn}(\alpha,\alpha)^{118}\text{Sn}$



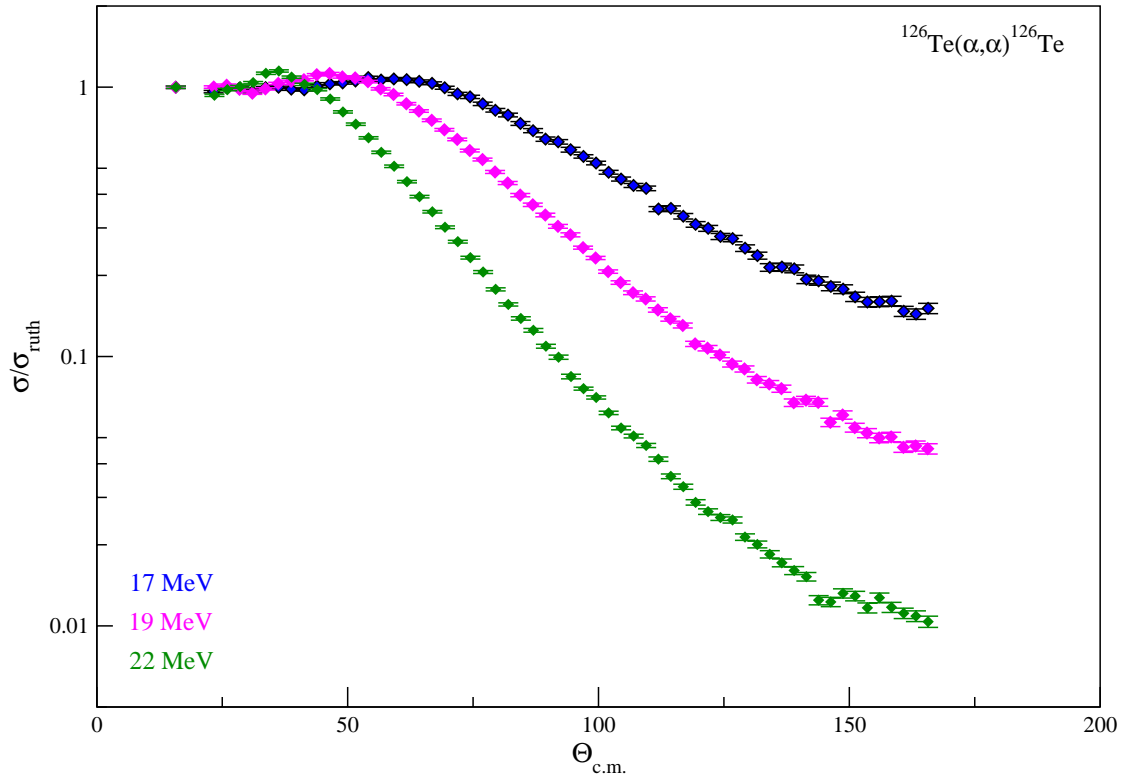
# $^{120}\text{Te}(\alpha,\alpha)^{120}\text{Te}$



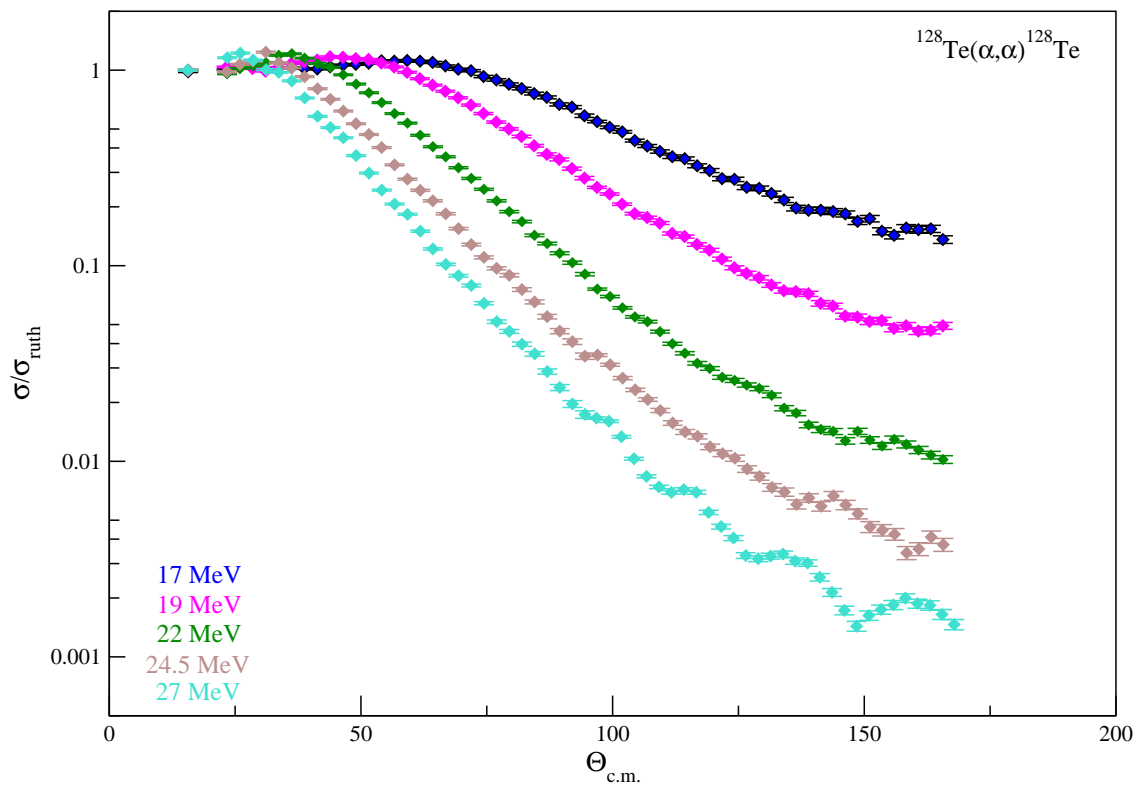
# $^{124}\text{Te}(\alpha,\alpha)^{124}\text{Te}$



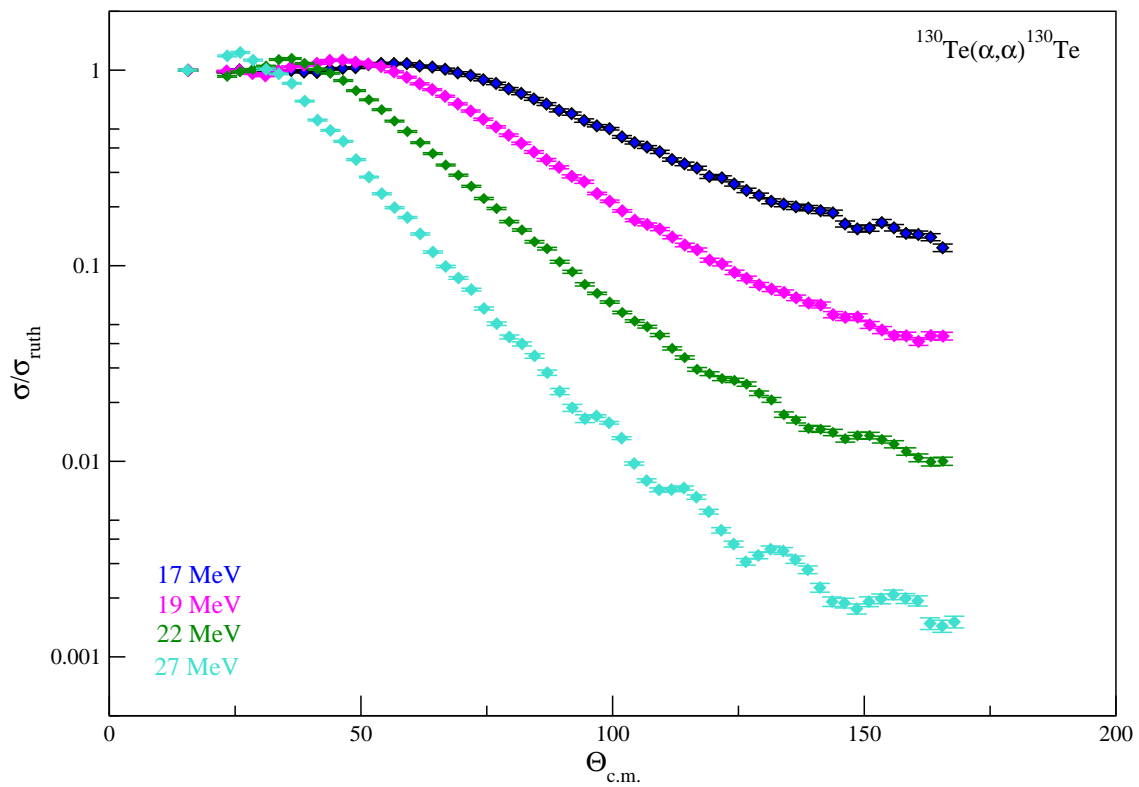
$^{126}\text{Te}(\alpha,\alpha)^{126}\text{Te}$



# $^{128}\text{Te}(\alpha,\alpha)^{128}\text{Te}$

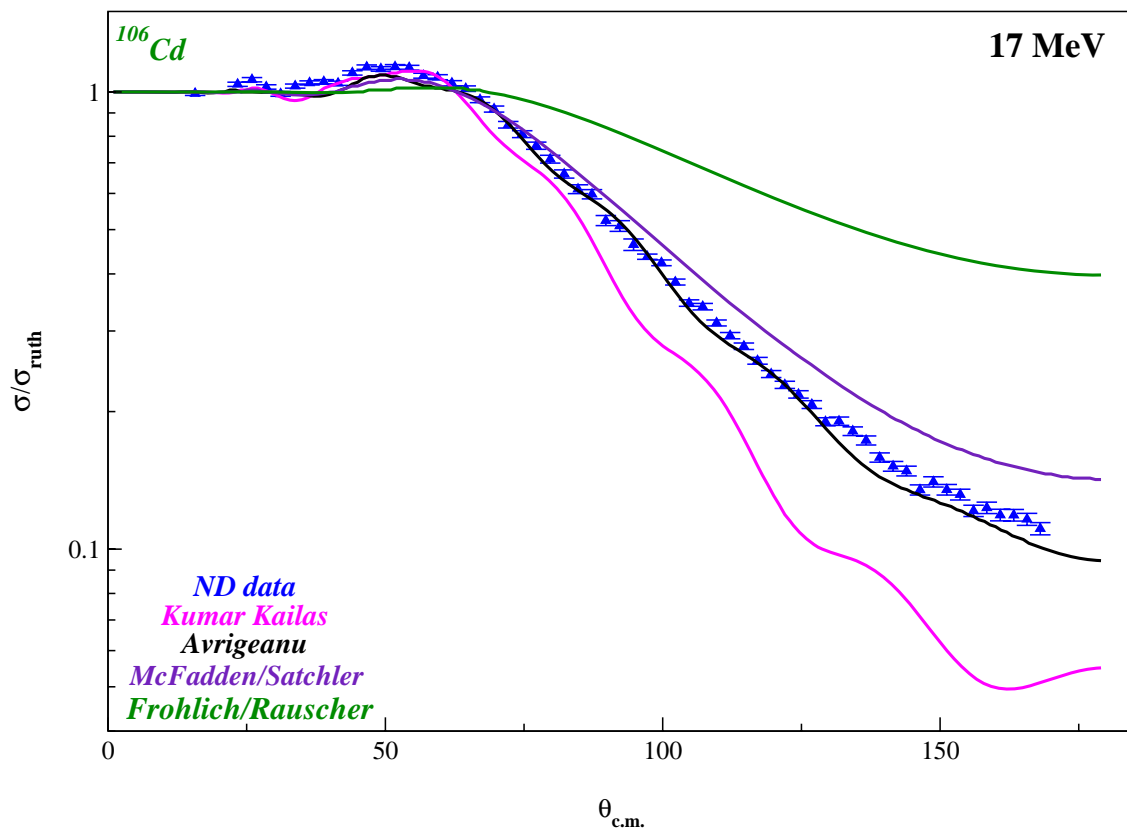


# $^{130}\text{Te}(\alpha,\alpha)^{130}\text{Te}$

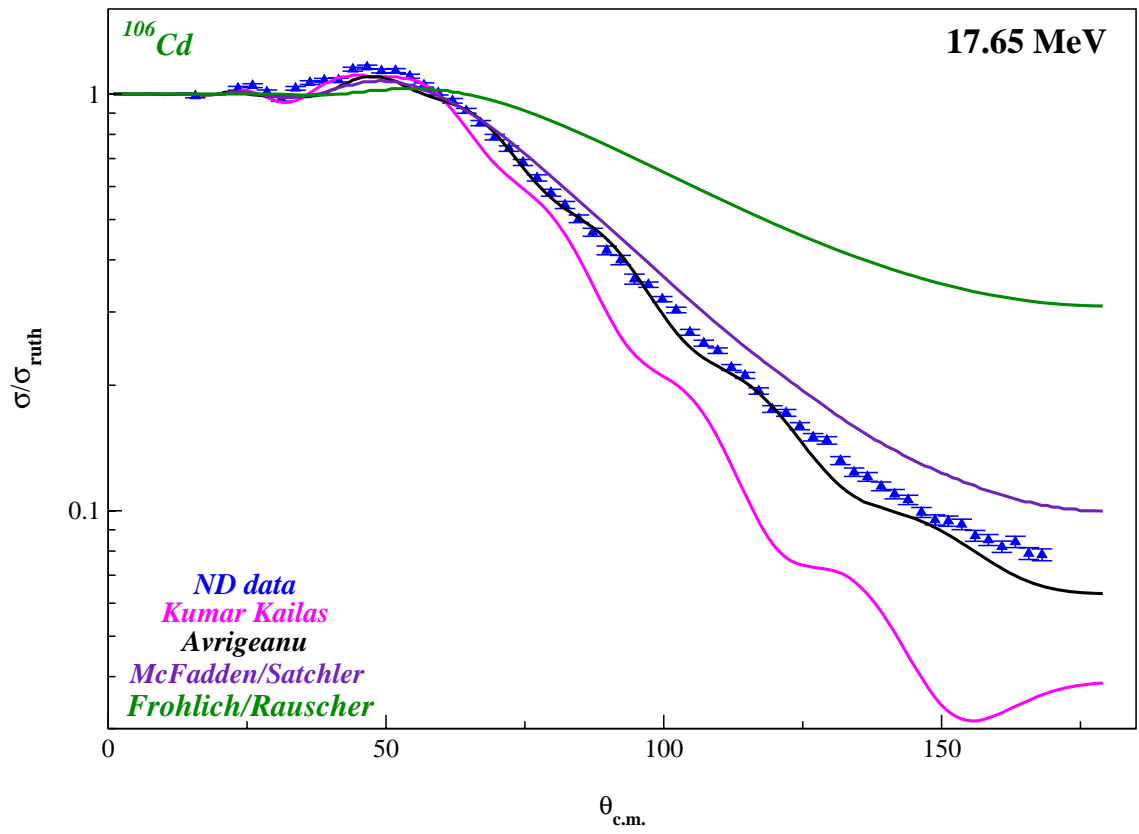


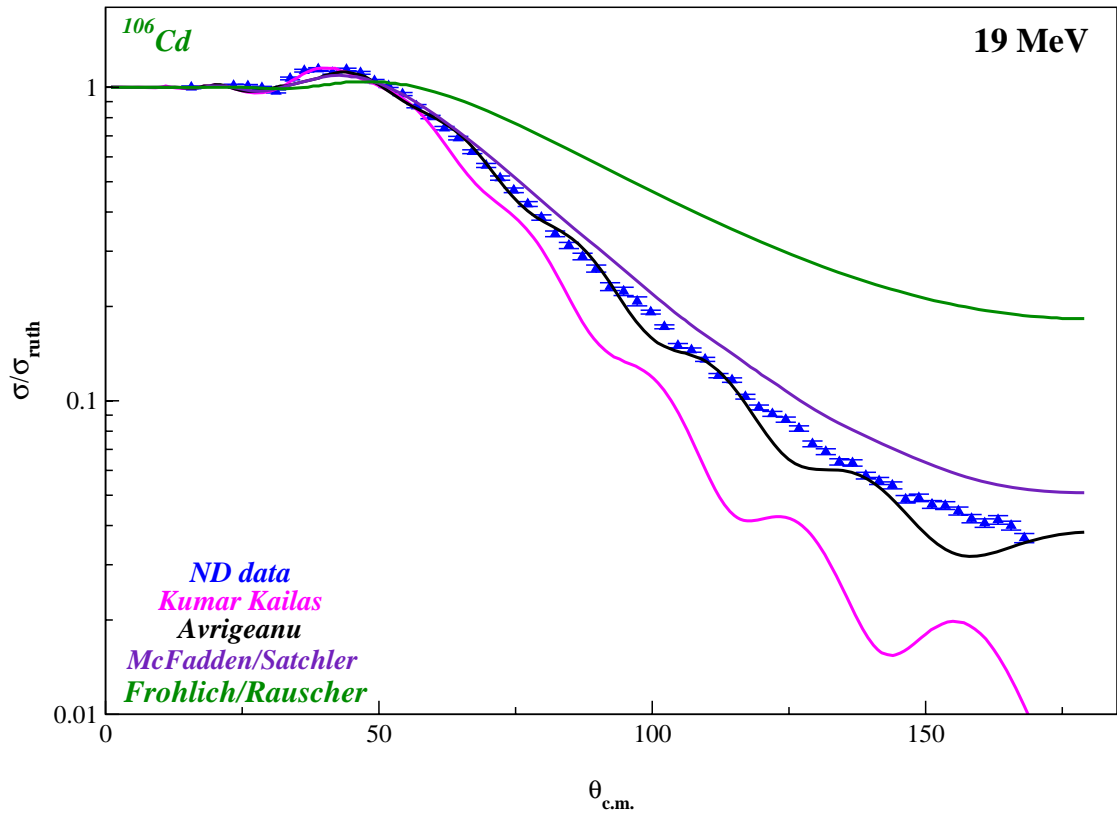
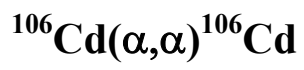
APPENDIX D  
GLOBAL POTENTIALS

$^{106}\text{Cd}(\alpha,\alpha)^{106}\text{Cd}$

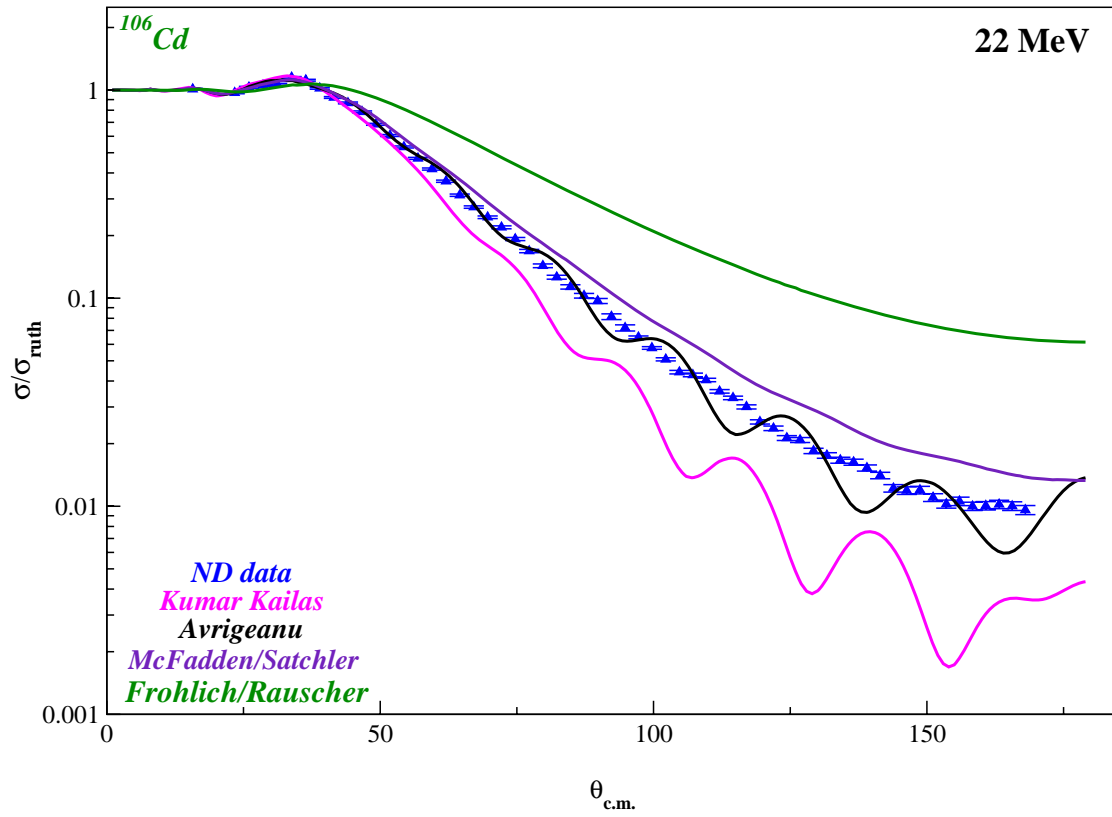


$^{106}\text{Cd}(\alpha,\alpha)^{106}\text{Cd}$

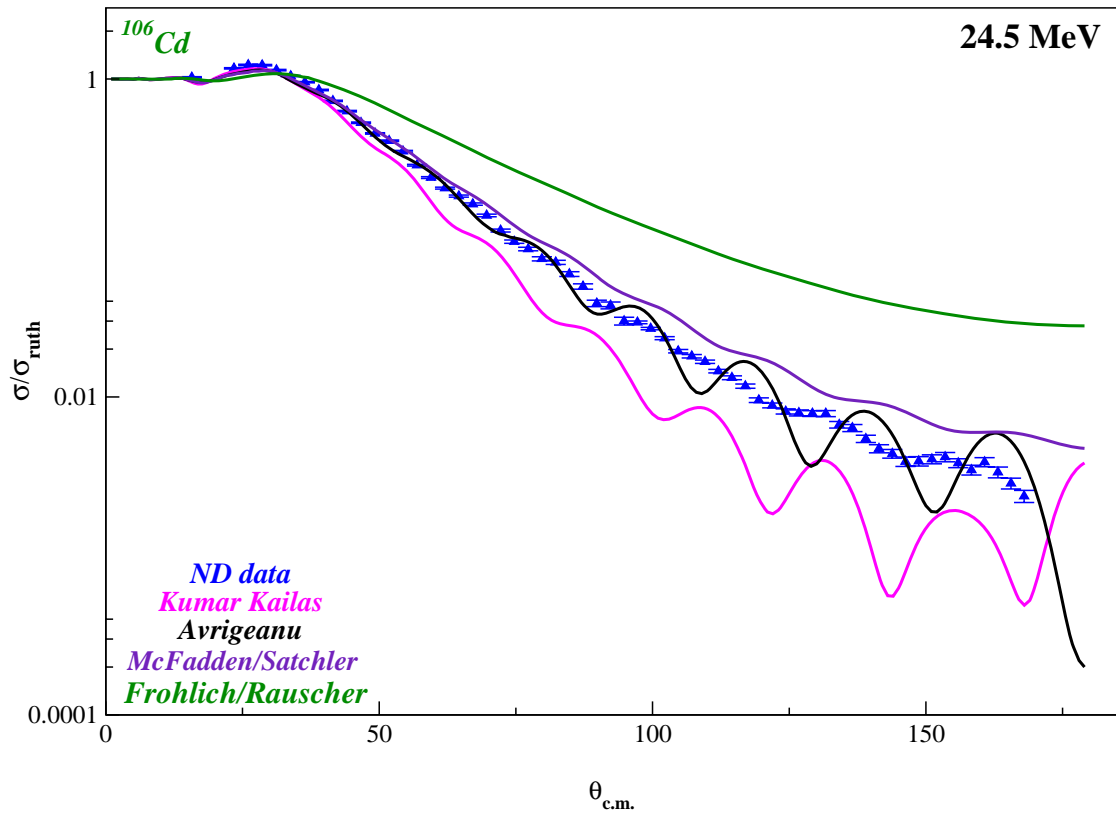




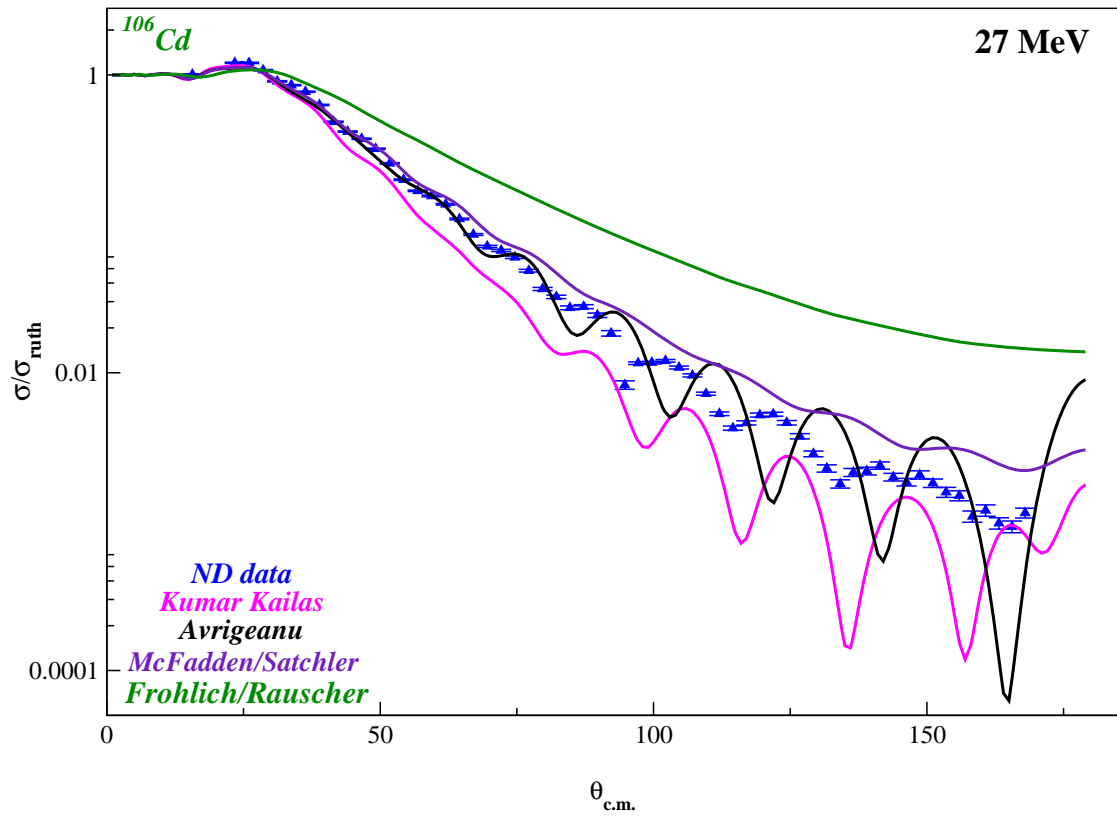
$^{106}\text{Cd}(\alpha,\alpha)^{106}\text{Cd}$



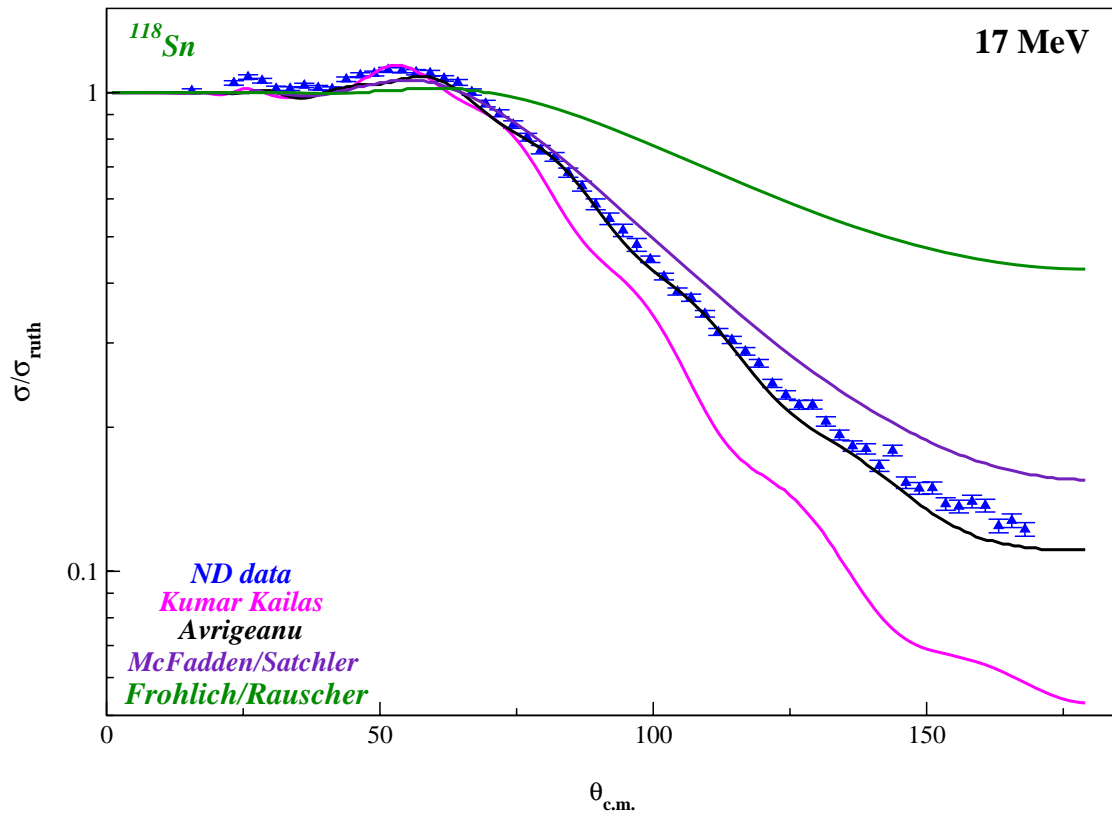
# $^{106}\text{Cd}(\alpha,\alpha)^{106}\text{Cd}$



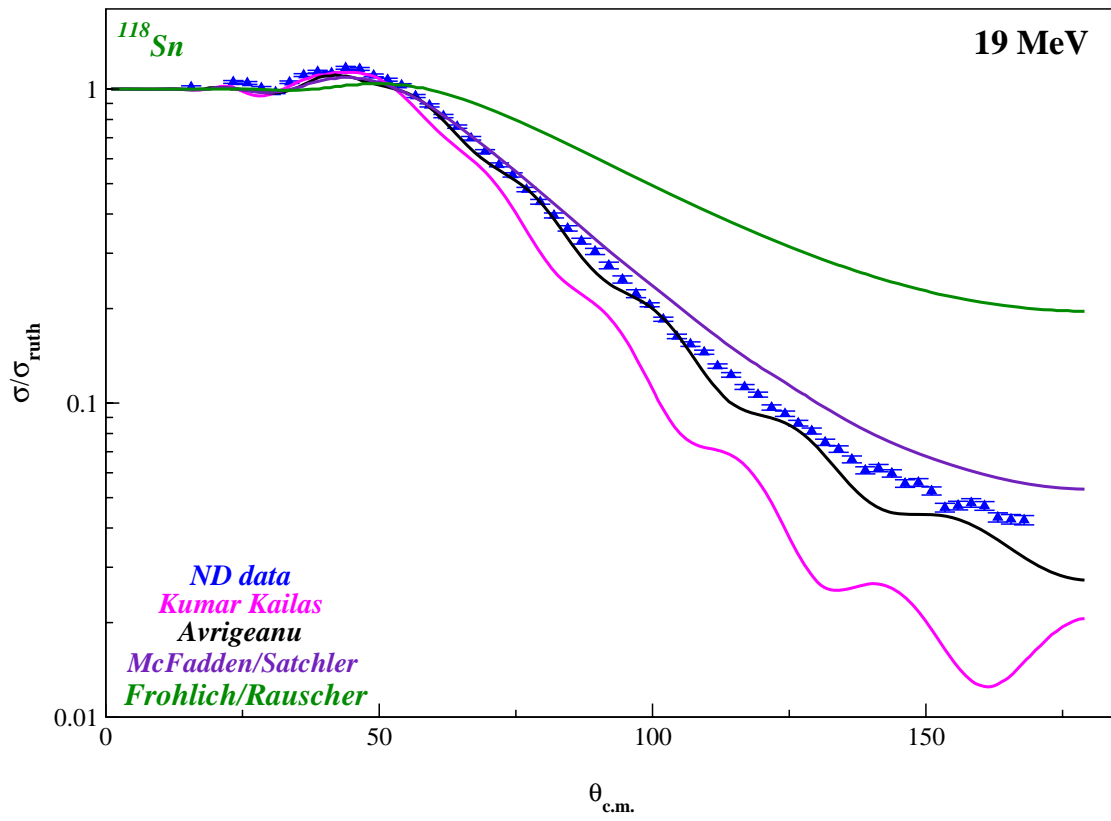
# $^{106}\text{Cd}(\alpha,\alpha)^{106}\text{Cd}$



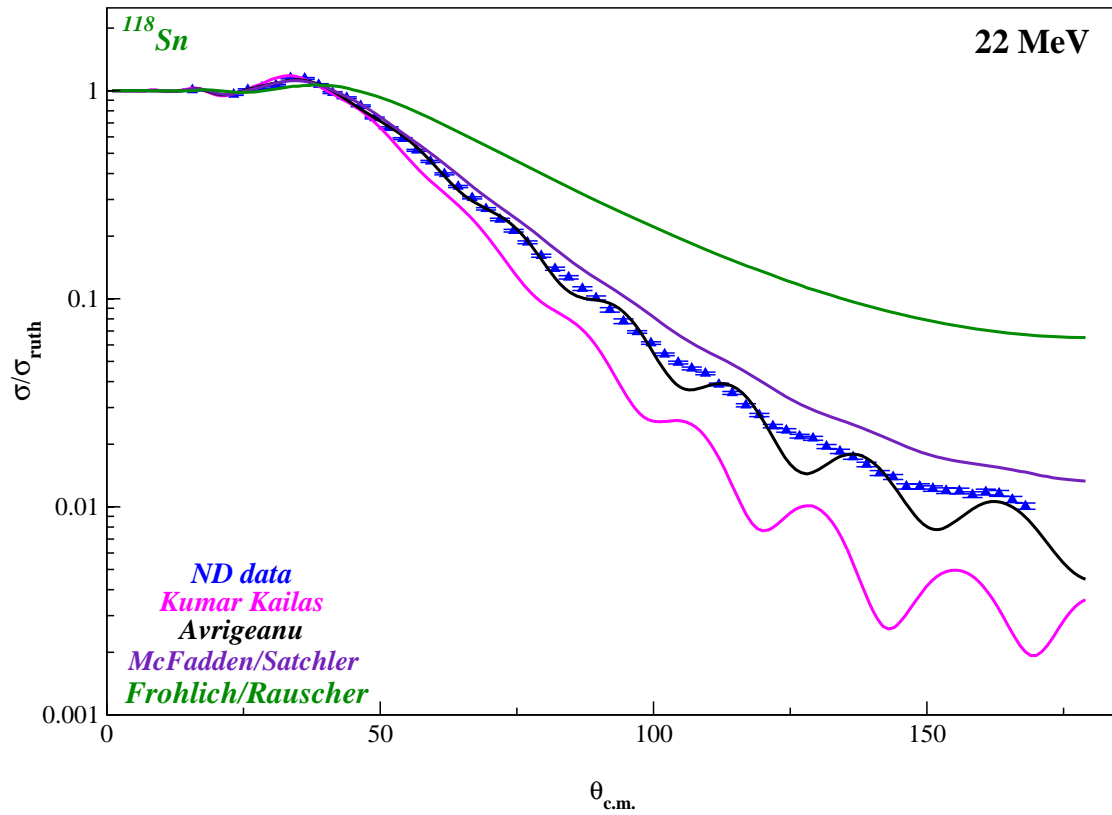
$^{118}\text{Sn}(\alpha,\alpha)^{118}\text{Sn}$



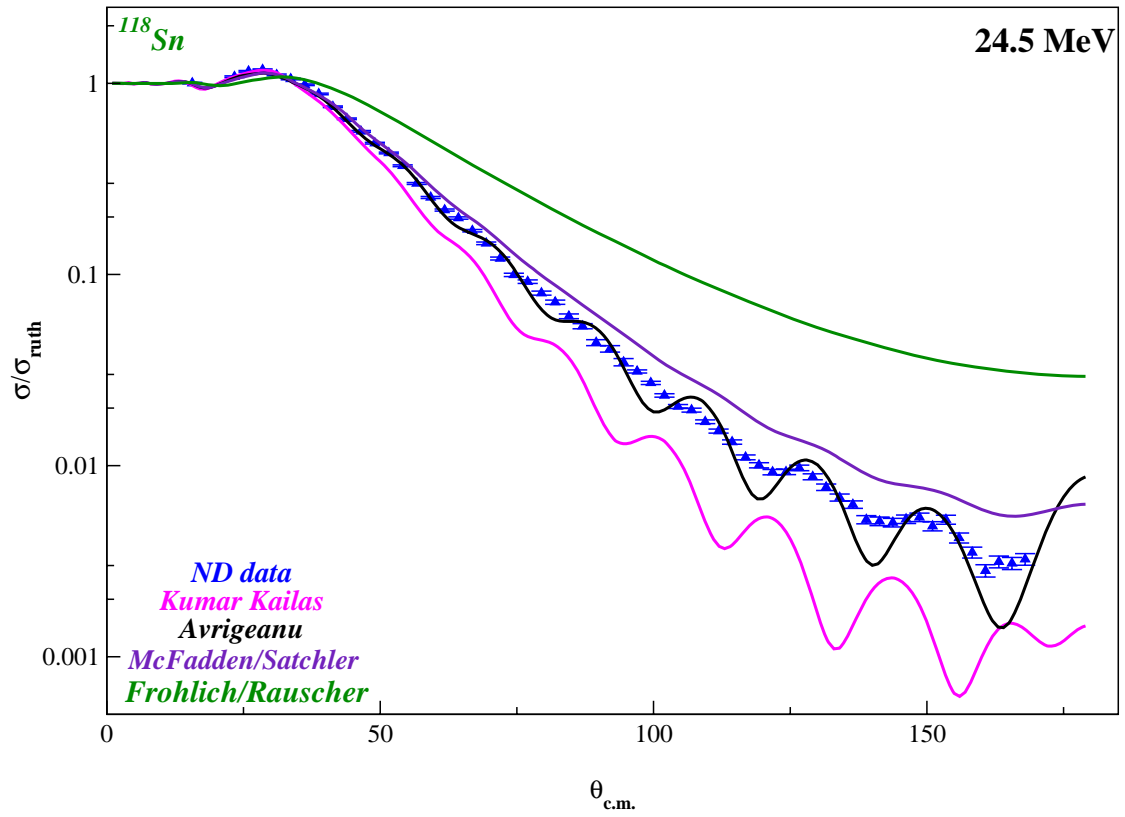
$^{118}\text{Sn}(\alpha,\alpha)^{118}\text{Sn}$



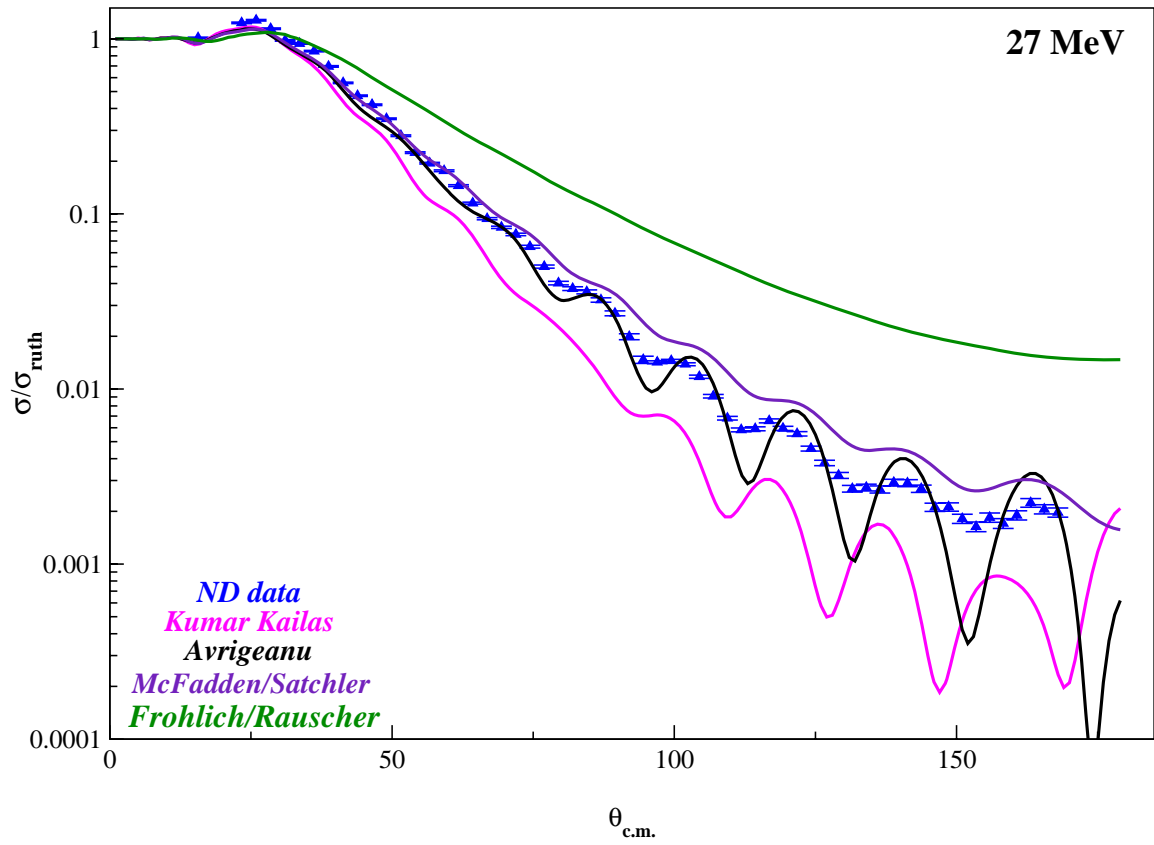
$^{118}\text{Sn}(\alpha,\alpha)^{118}\text{Sn}$

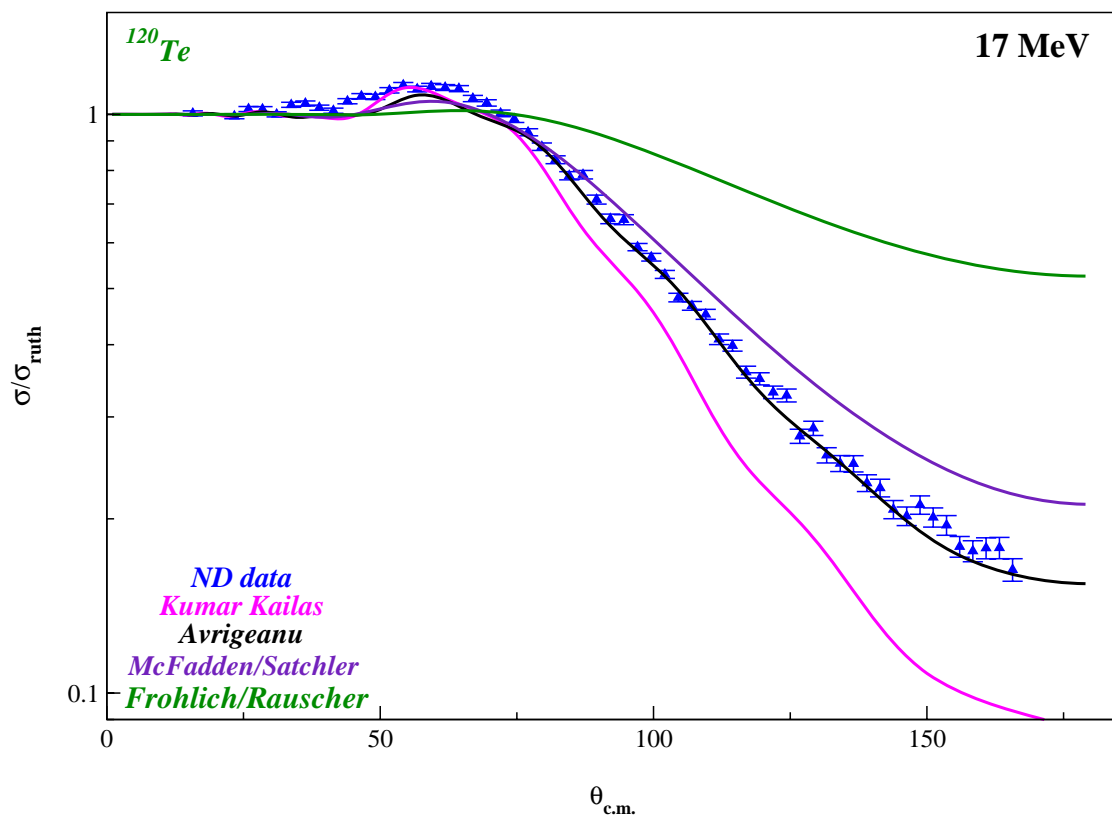
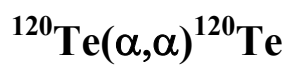


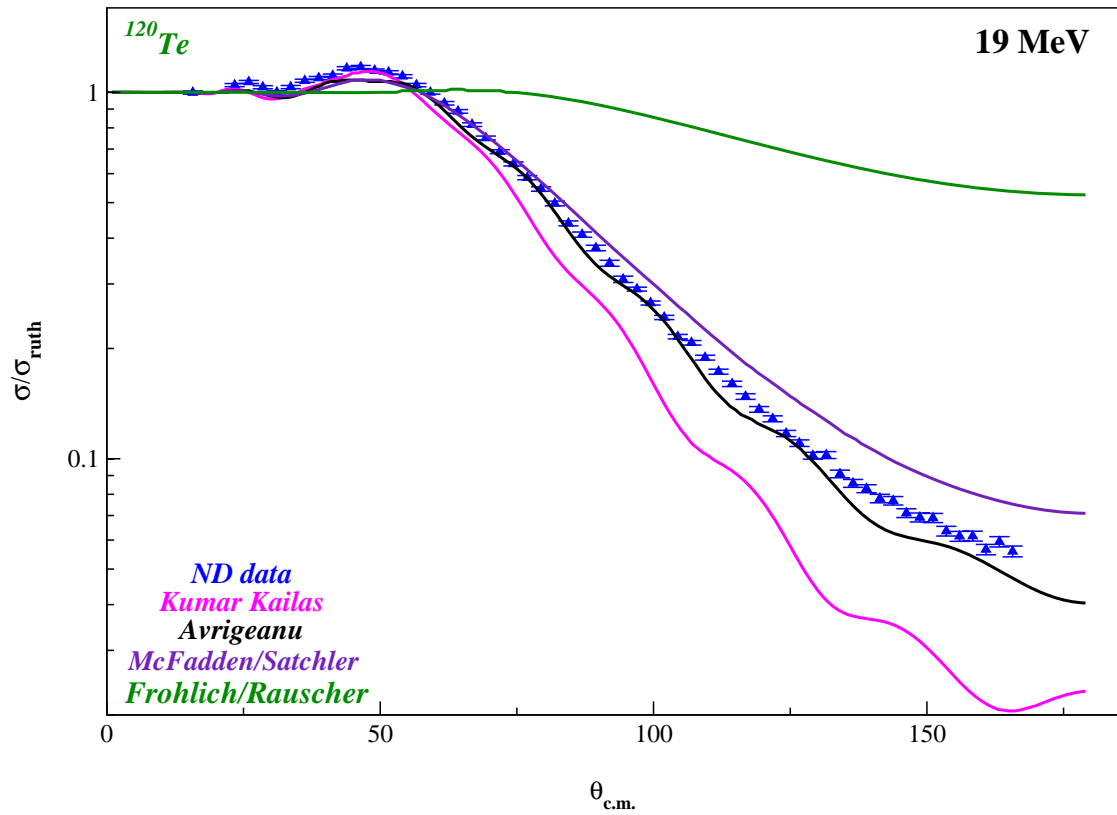
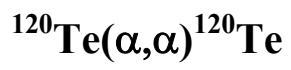
$^{118}\text{Sn}(\alpha,\alpha)^{118}\text{Sn}$



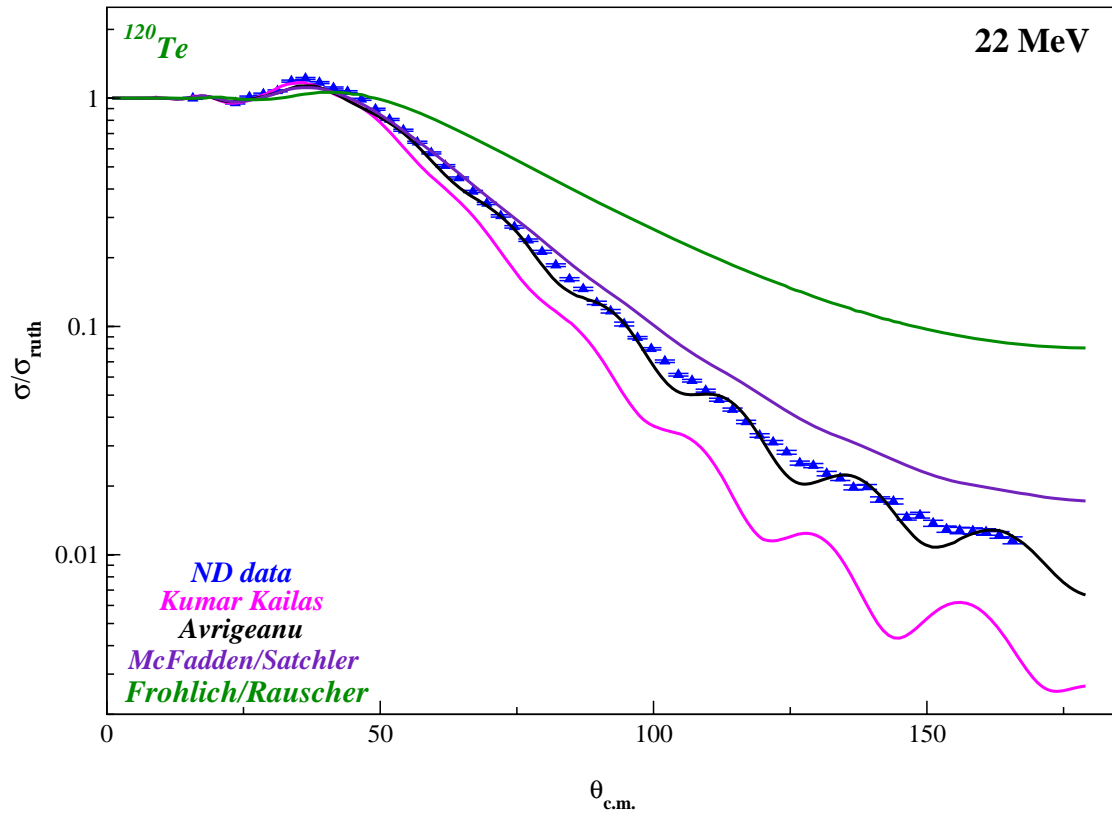
$^{118}\text{Sn}(\alpha,\alpha)^{118}\text{Sn}$

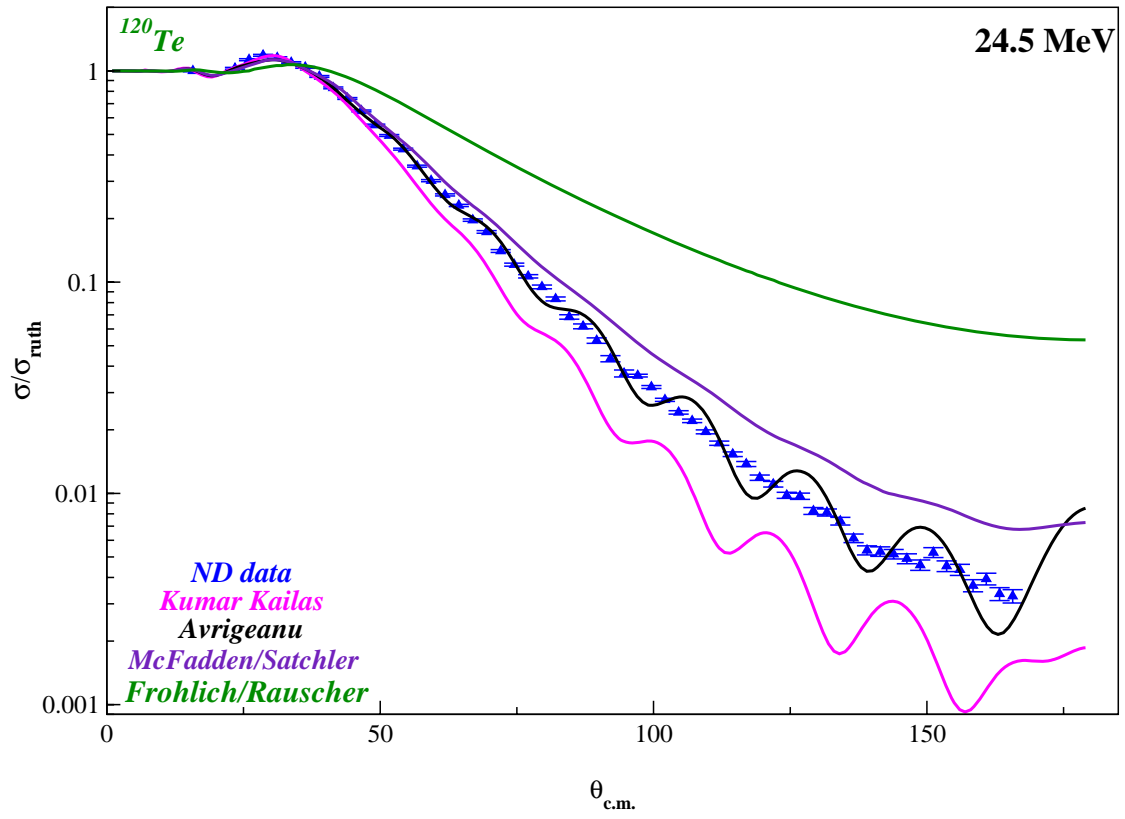
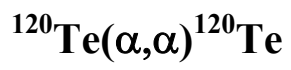


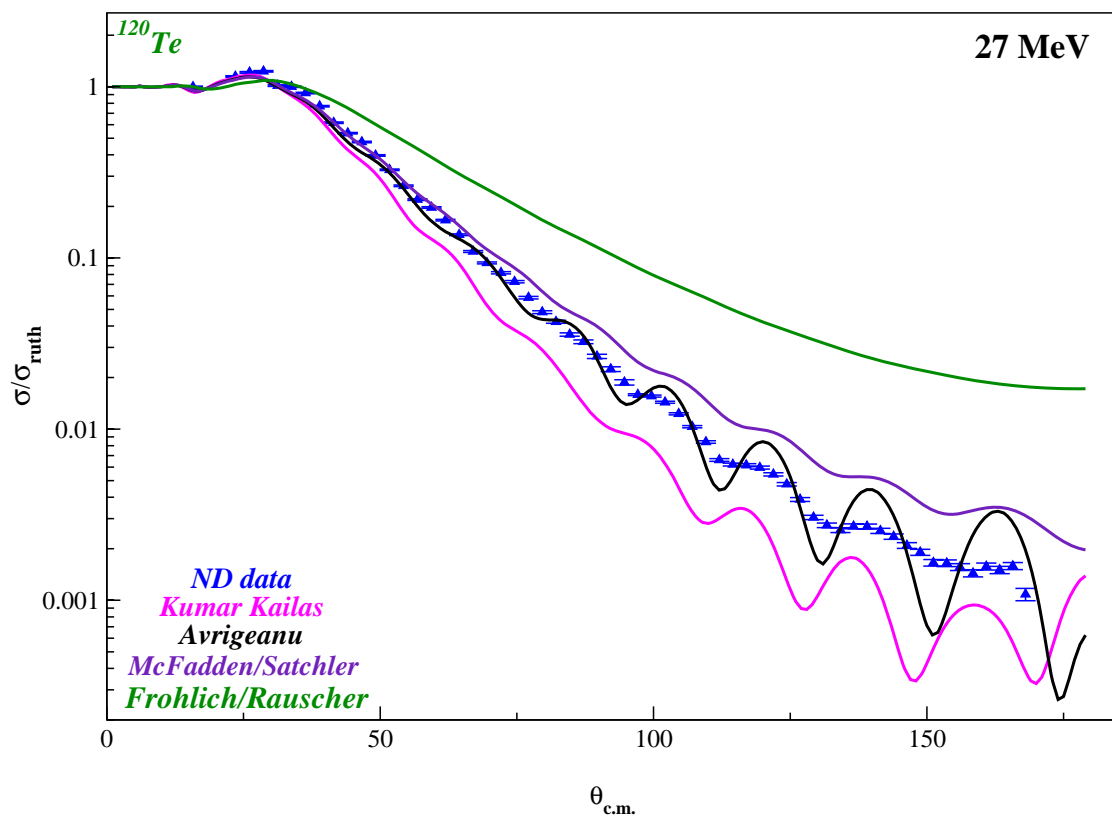
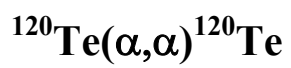


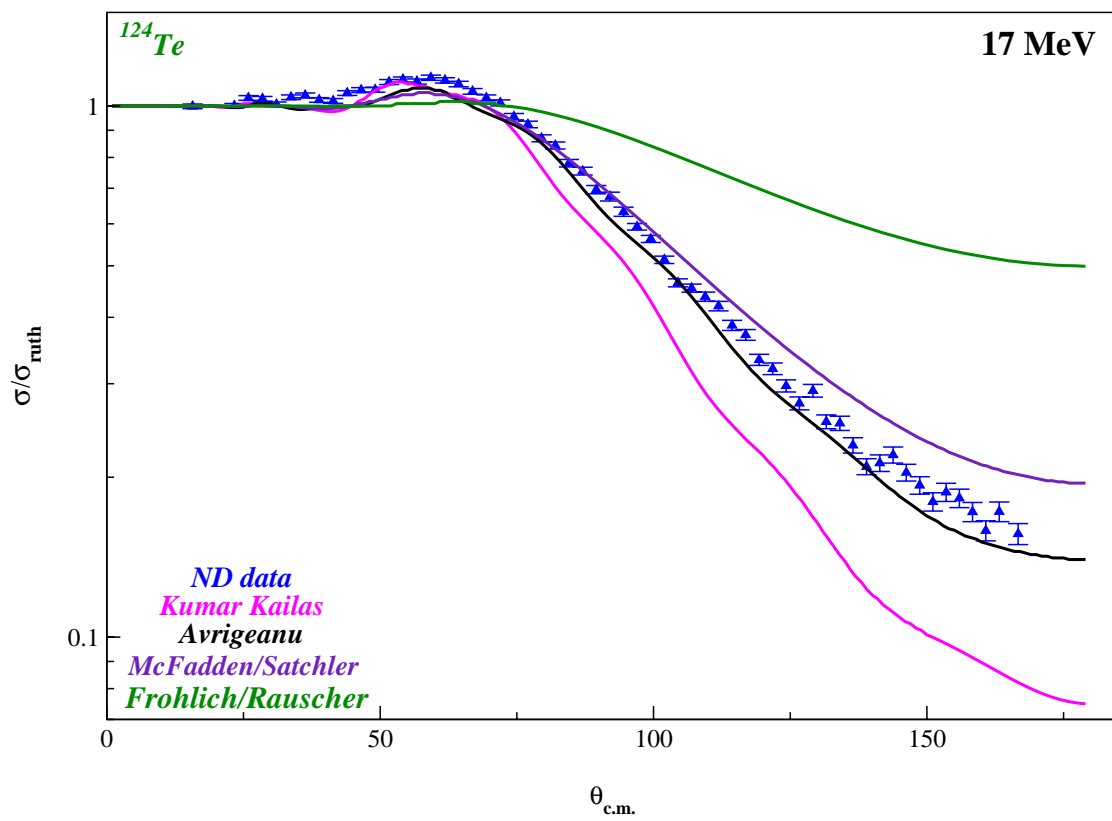
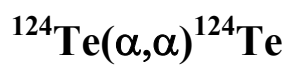


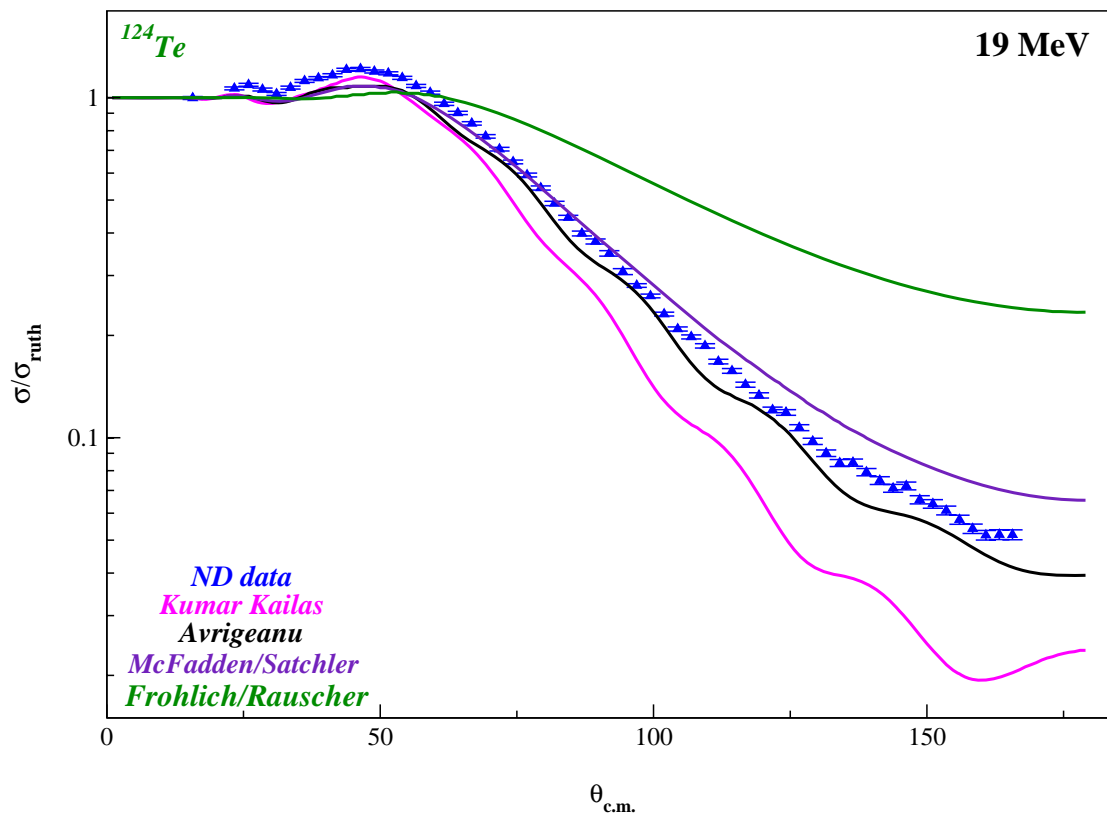
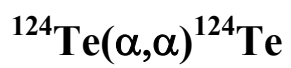
$^{120}\text{Te}(\alpha,\alpha)^{120}\text{Te}$



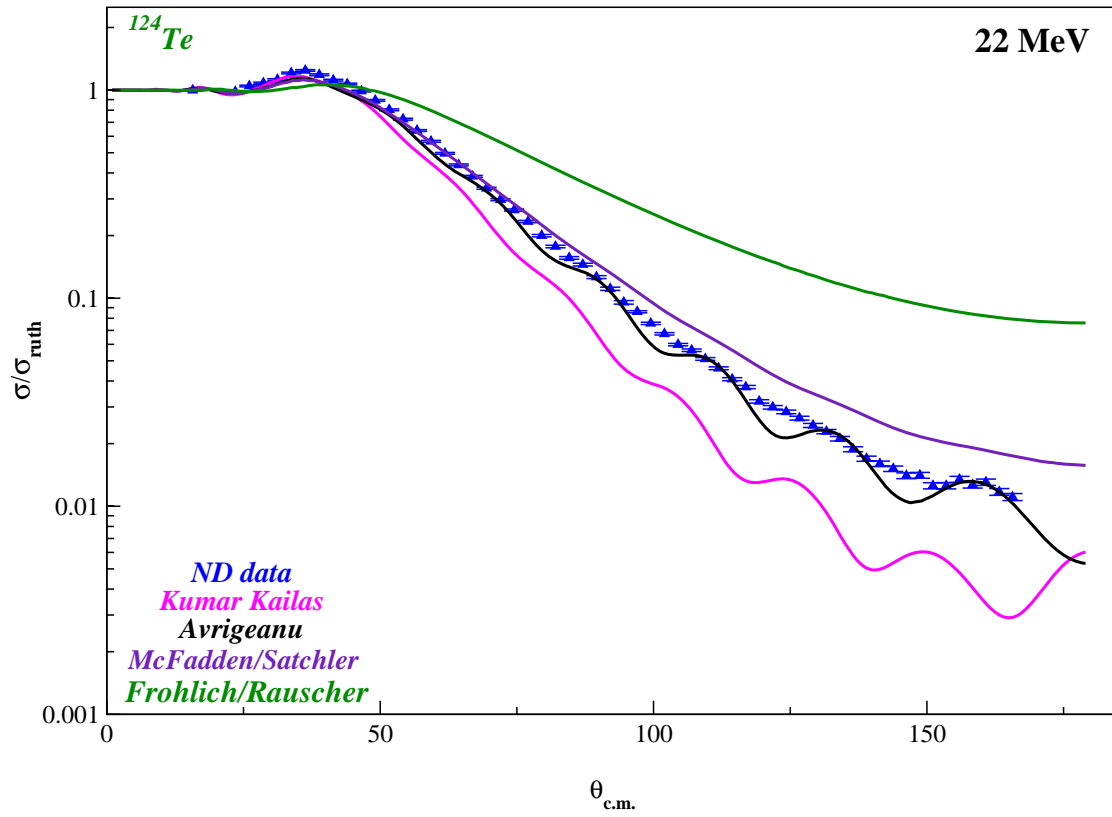




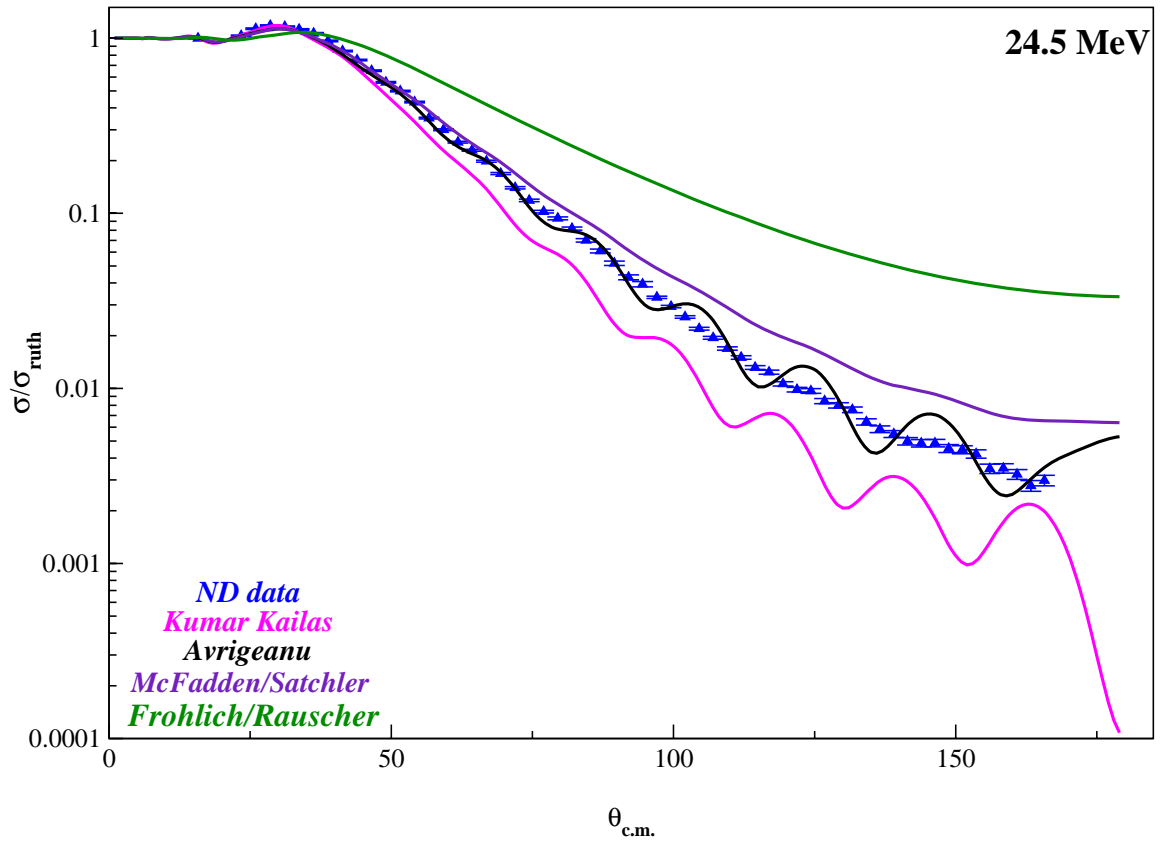




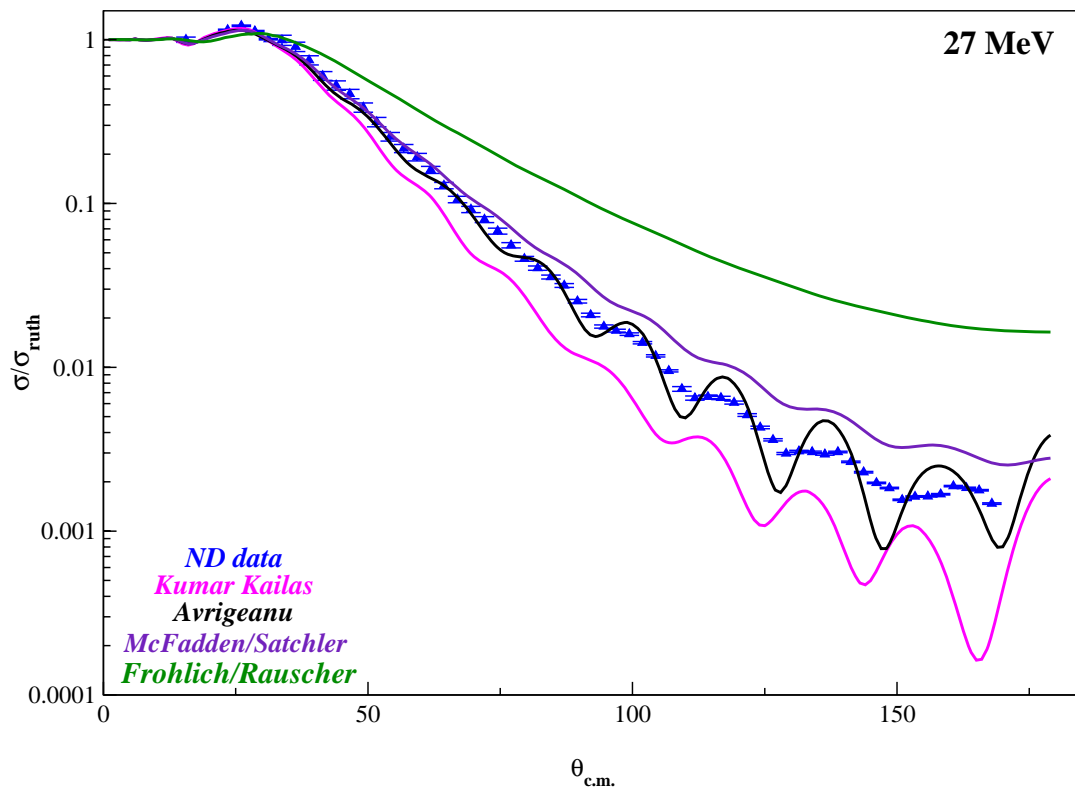
$^{124}\text{Te}(\alpha,\alpha)^{124}\text{Te}$



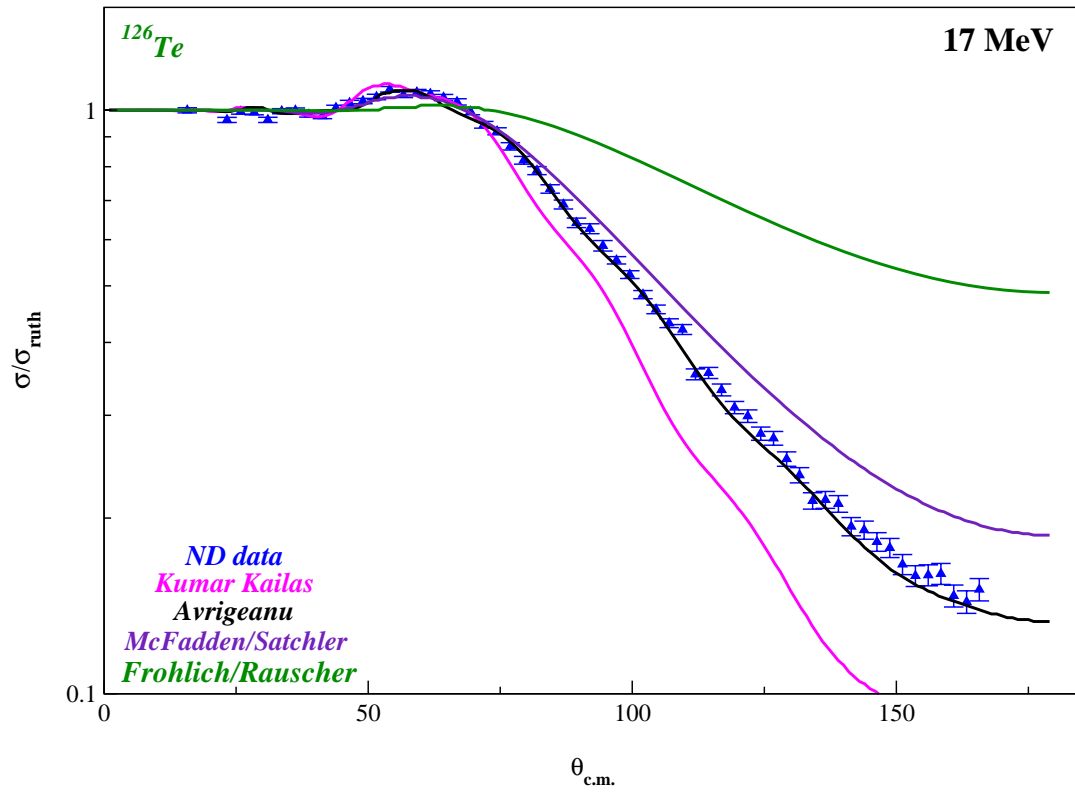
$^{124}\text{Te}(\alpha,\alpha)^{124}\text{Te}$



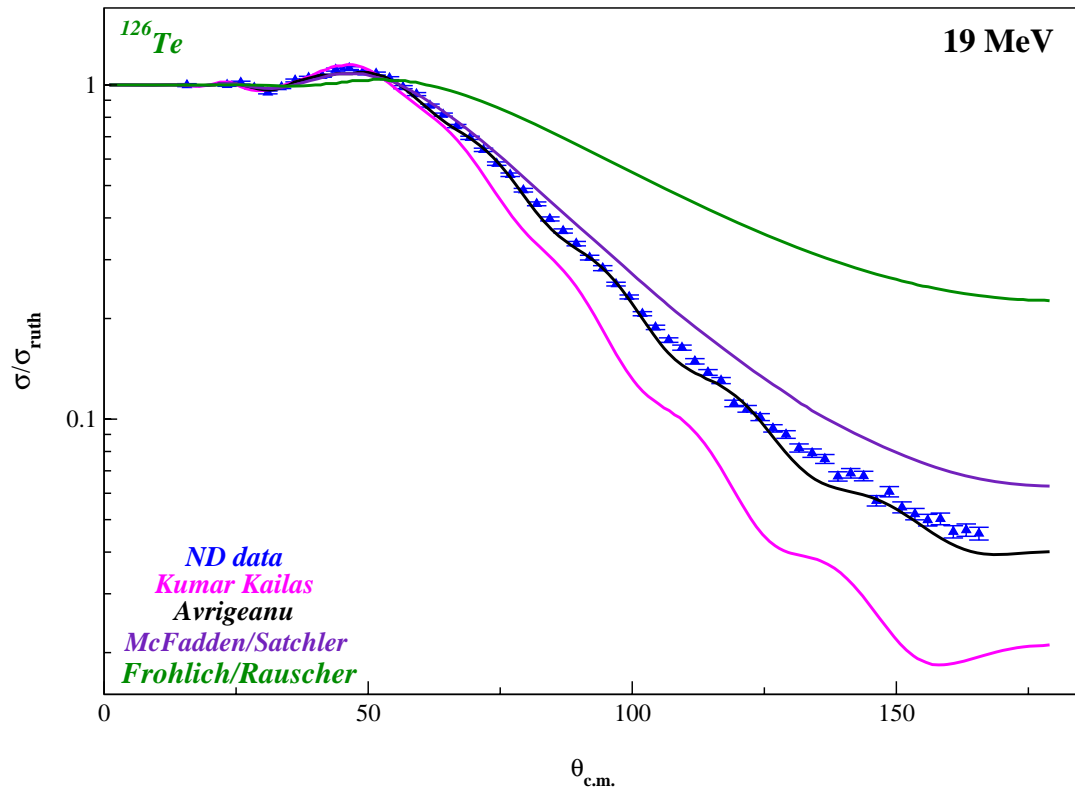
$^{124}\text{Te}(\alpha,\alpha)^{124}\text{Te}$



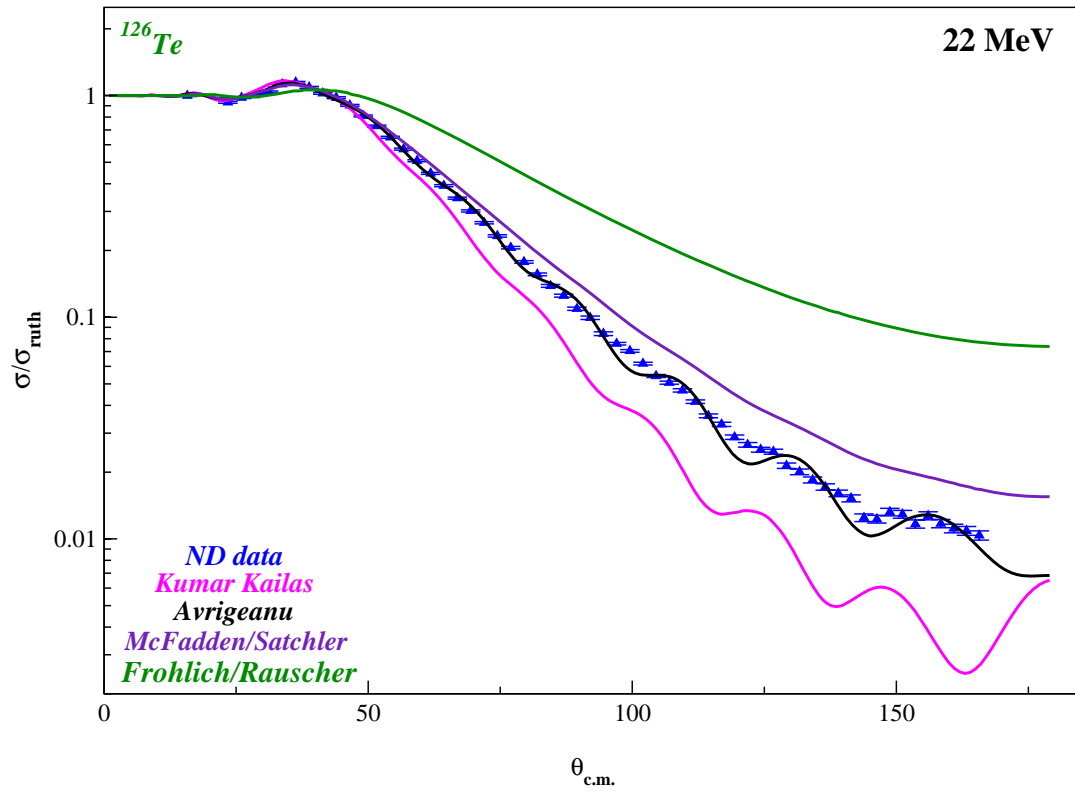
$^{126}\text{Te}(\alpha,\alpha)^{126}\text{Te}$



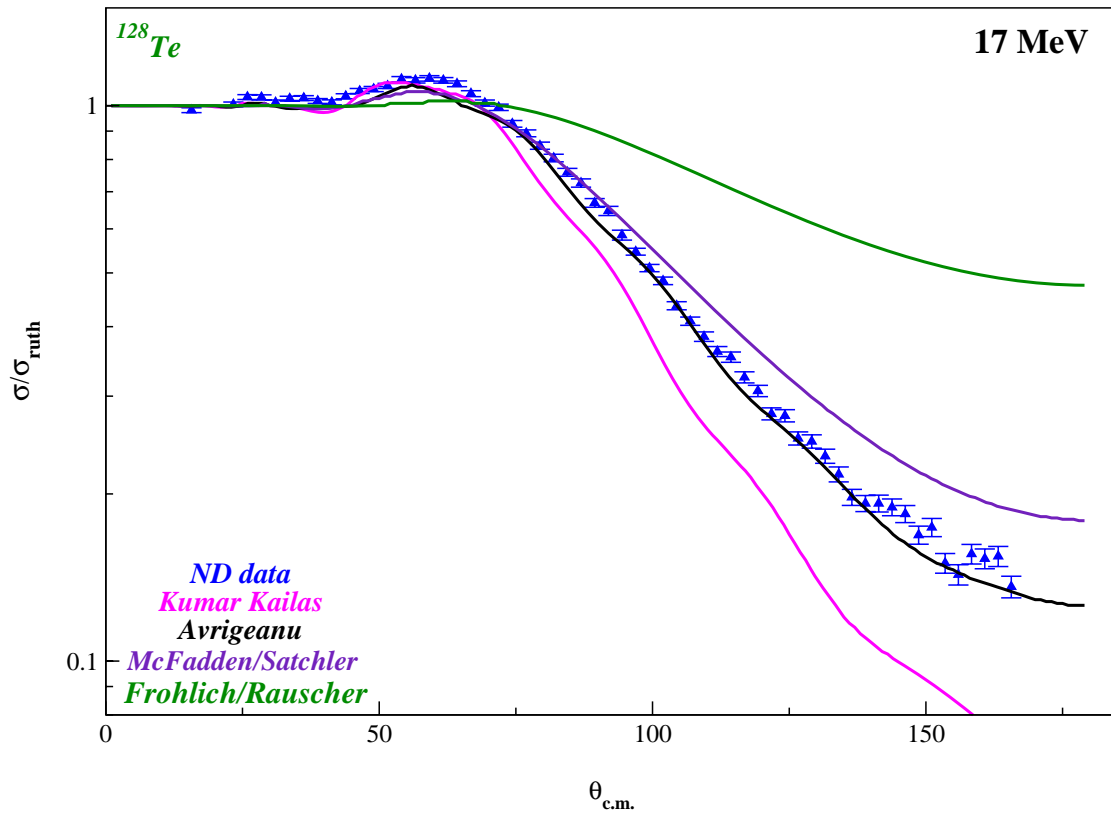
$^{126}\text{Te}(\alpha,\alpha)^{126}\text{Te}$

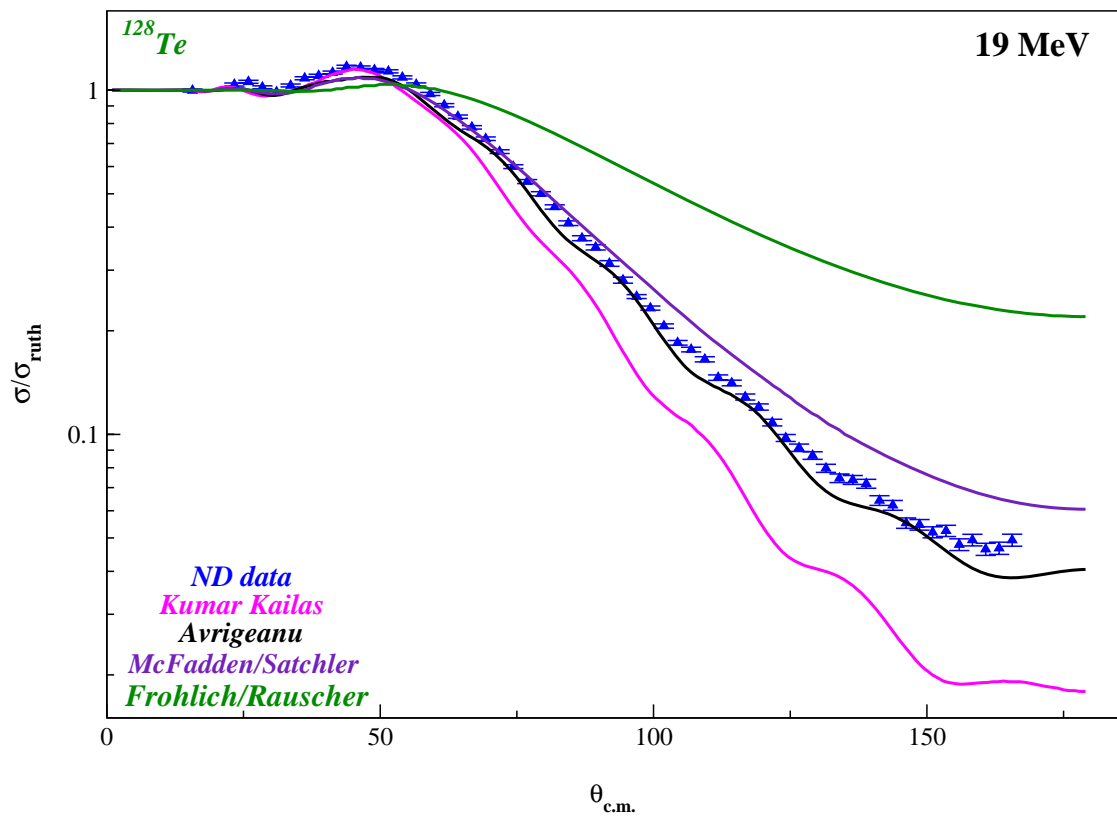
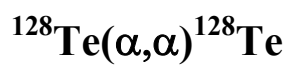


$^{126}\text{Te}(\alpha,\alpha)^{126}\text{Te}$

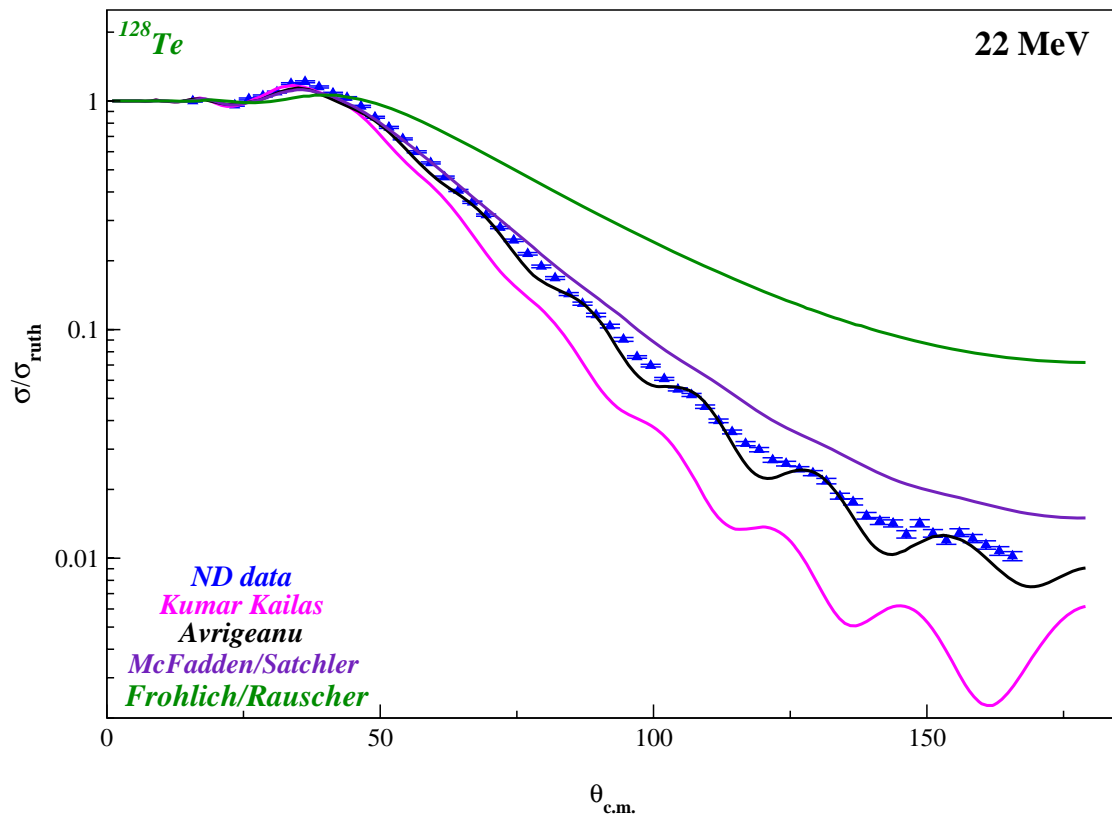


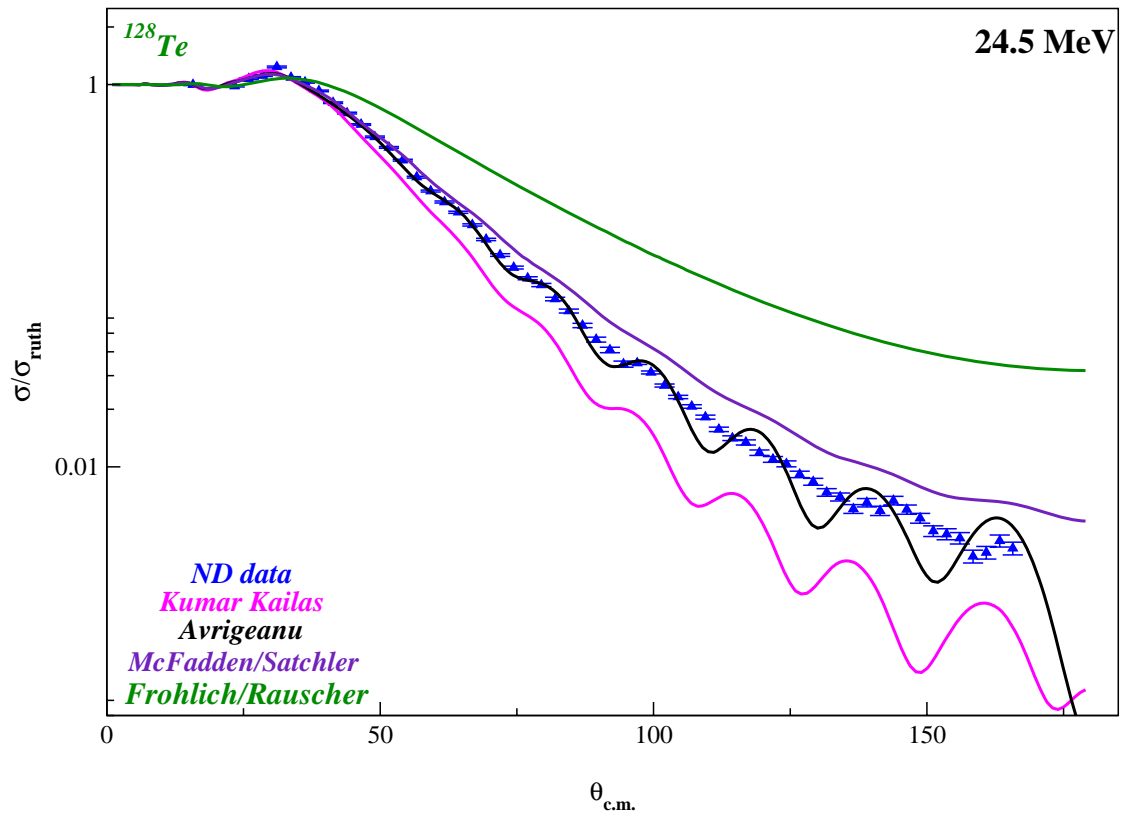
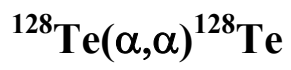
$^{128}\text{Te}(\alpha,\alpha)^{128}\text{Te}$



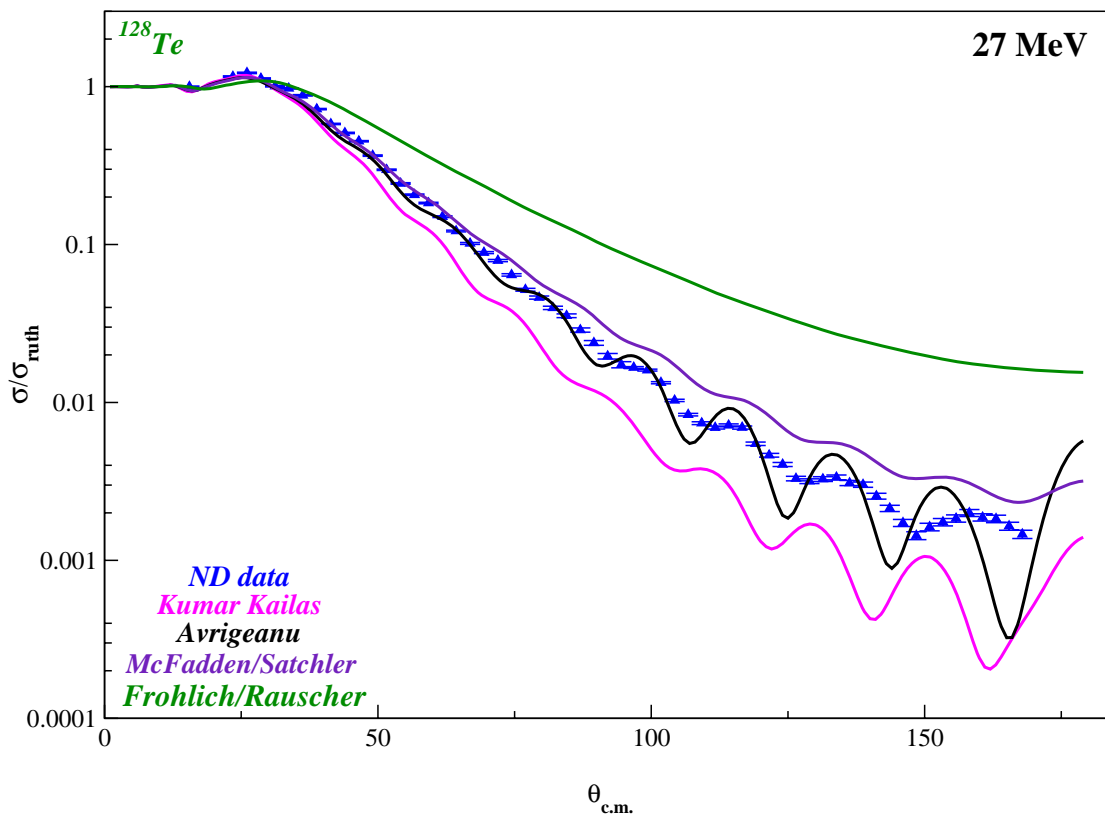


$^{128}\text{Te}(\alpha,\alpha)^{128}\text{Te}$

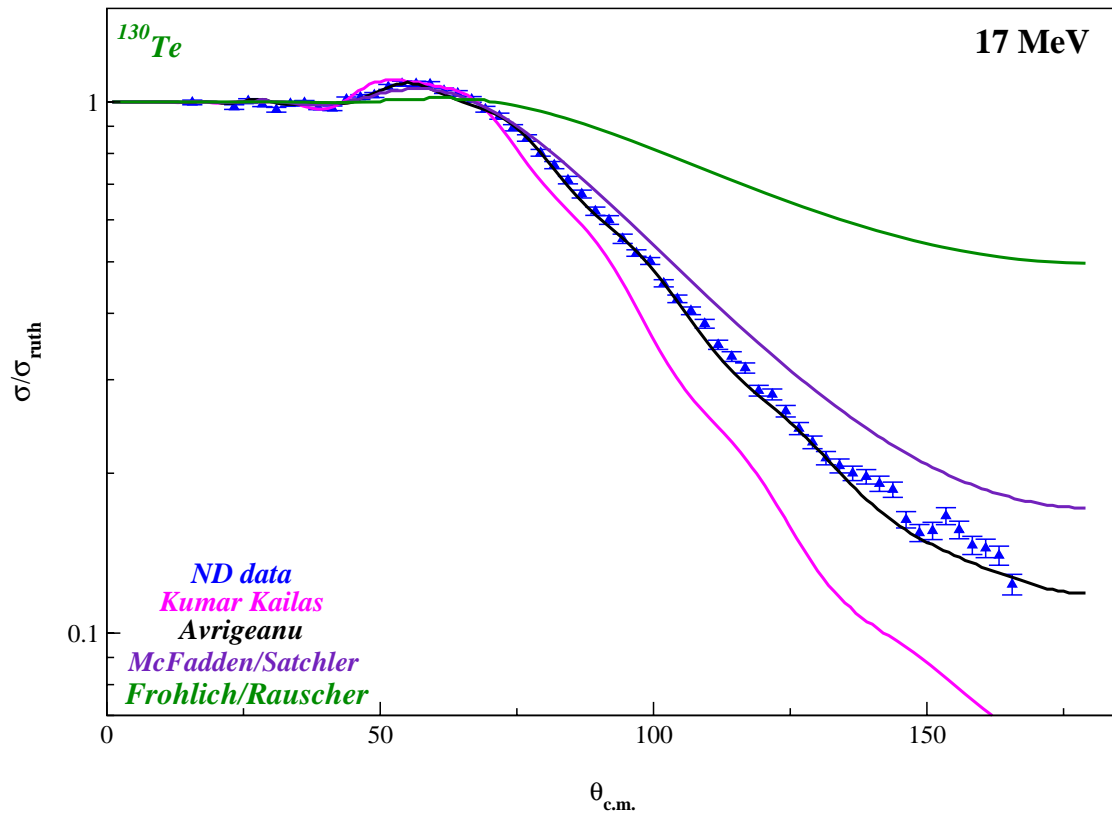


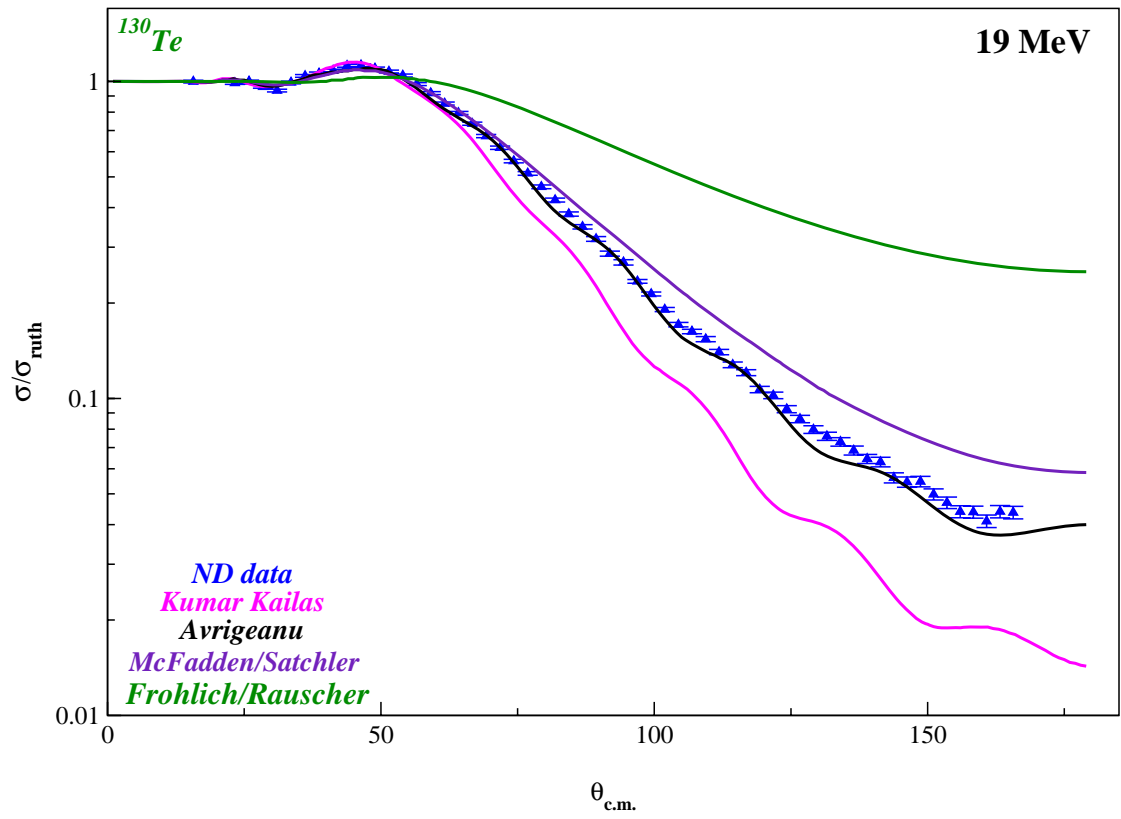
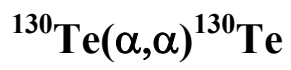


$^{128}\text{Te}(\alpha,\alpha)^{128}\text{Te}$

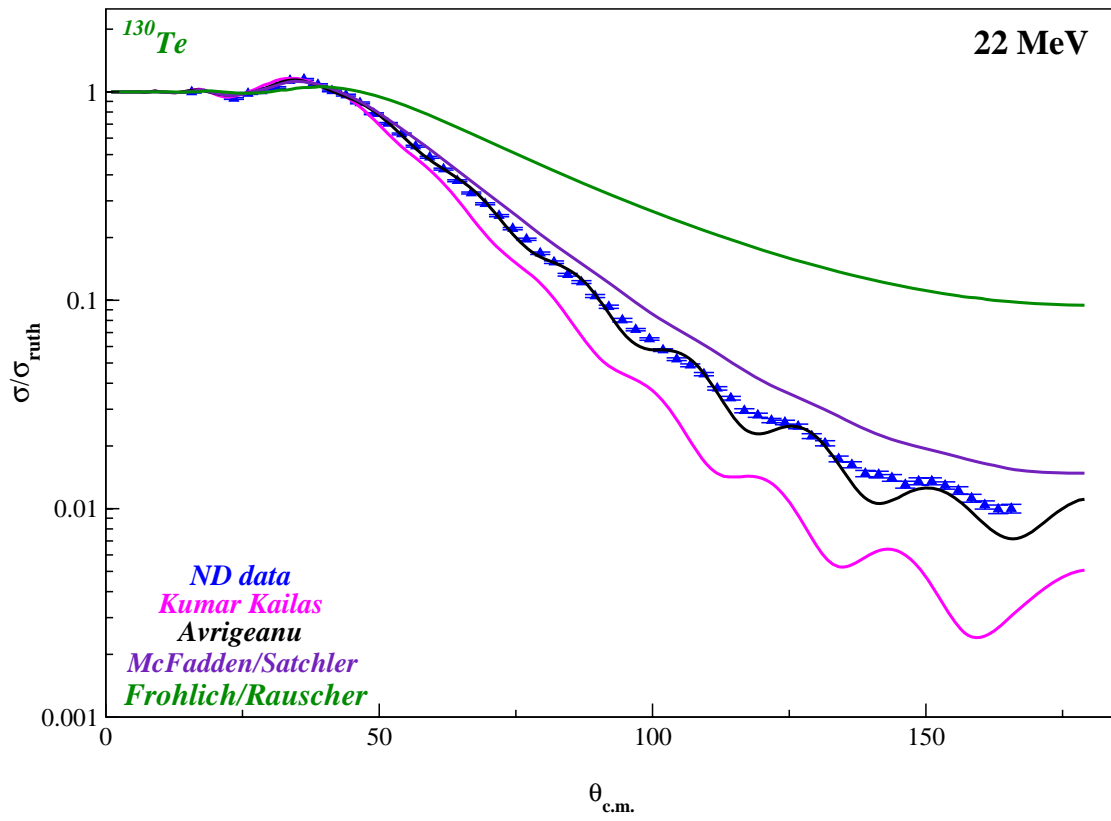


$^{130}\text{Te}(\alpha,\alpha)^{130}\text{Te}$

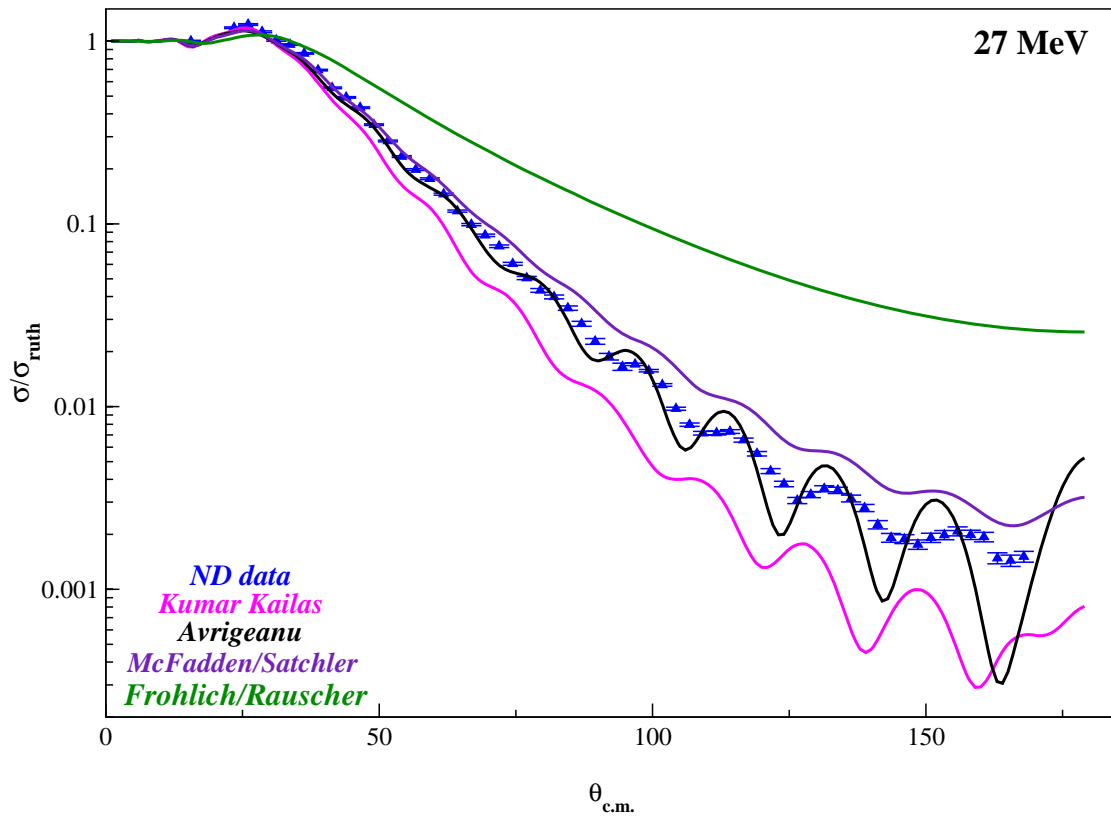




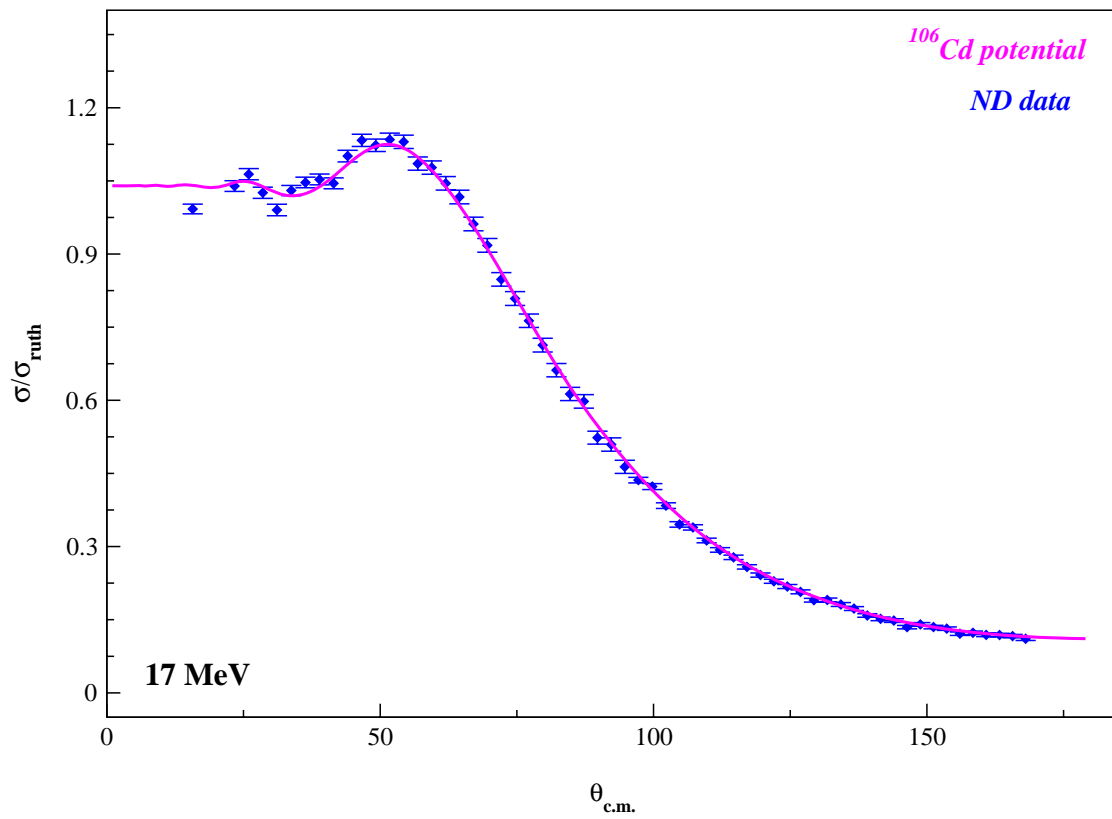
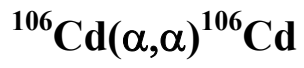
$^{130}\text{Te}(\alpha,\alpha)^{130}\text{Te}$

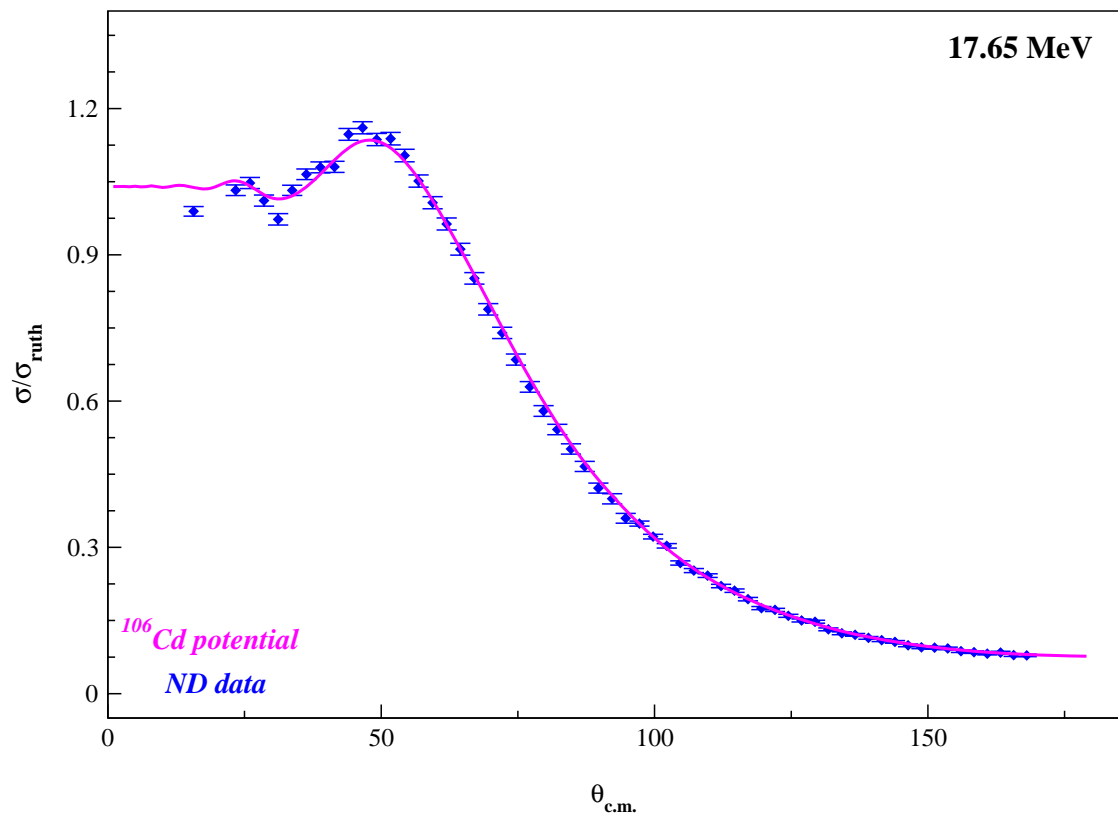
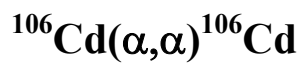


$^{130}\text{Te}(\alpha,\alpha)^{130}\text{Te}$

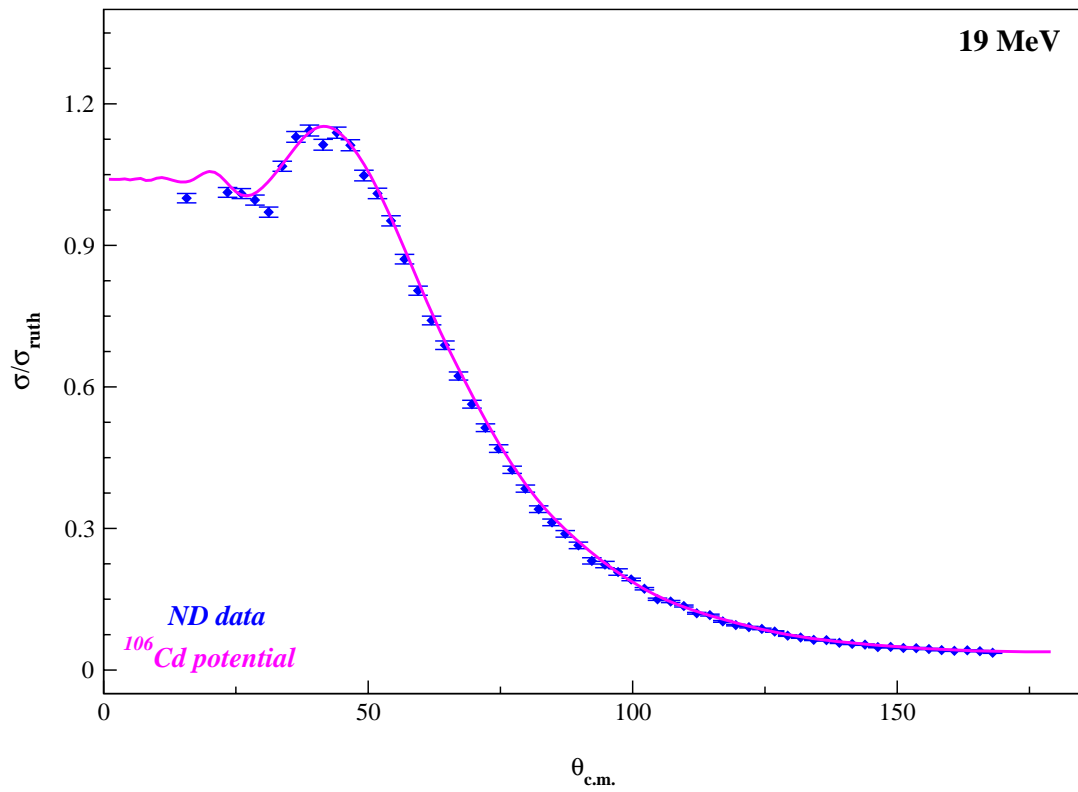


APPENDIX E  
LOCAL POTENTIALS

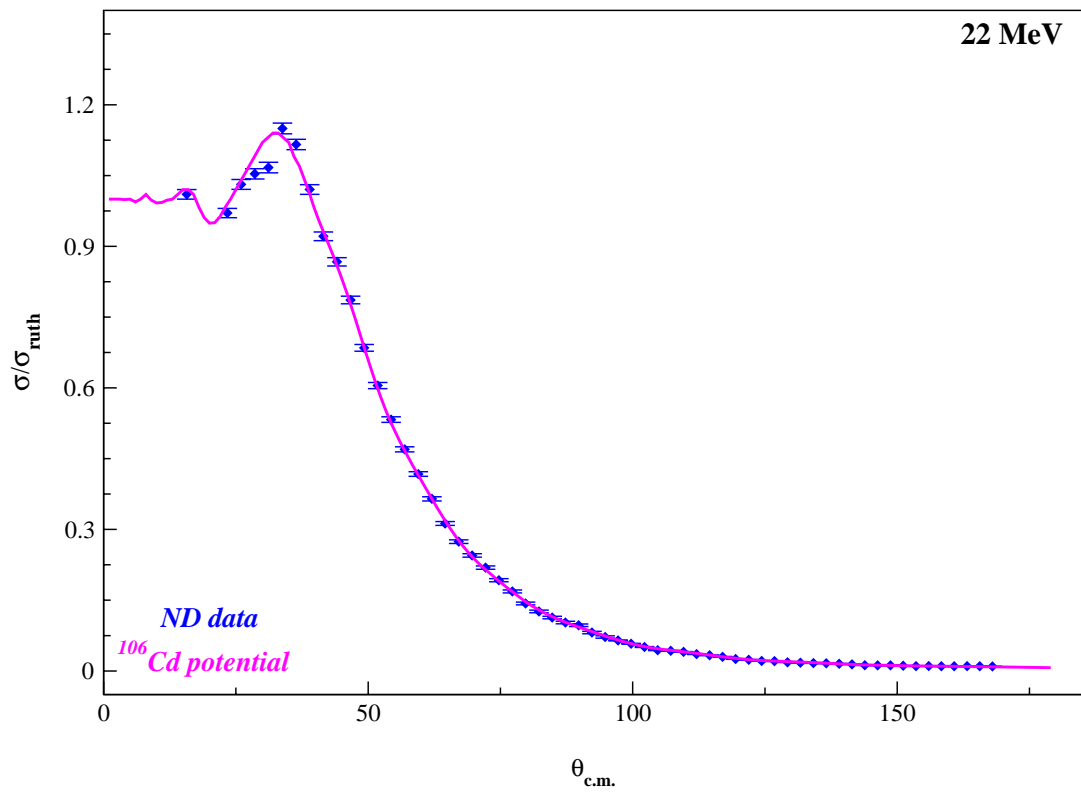




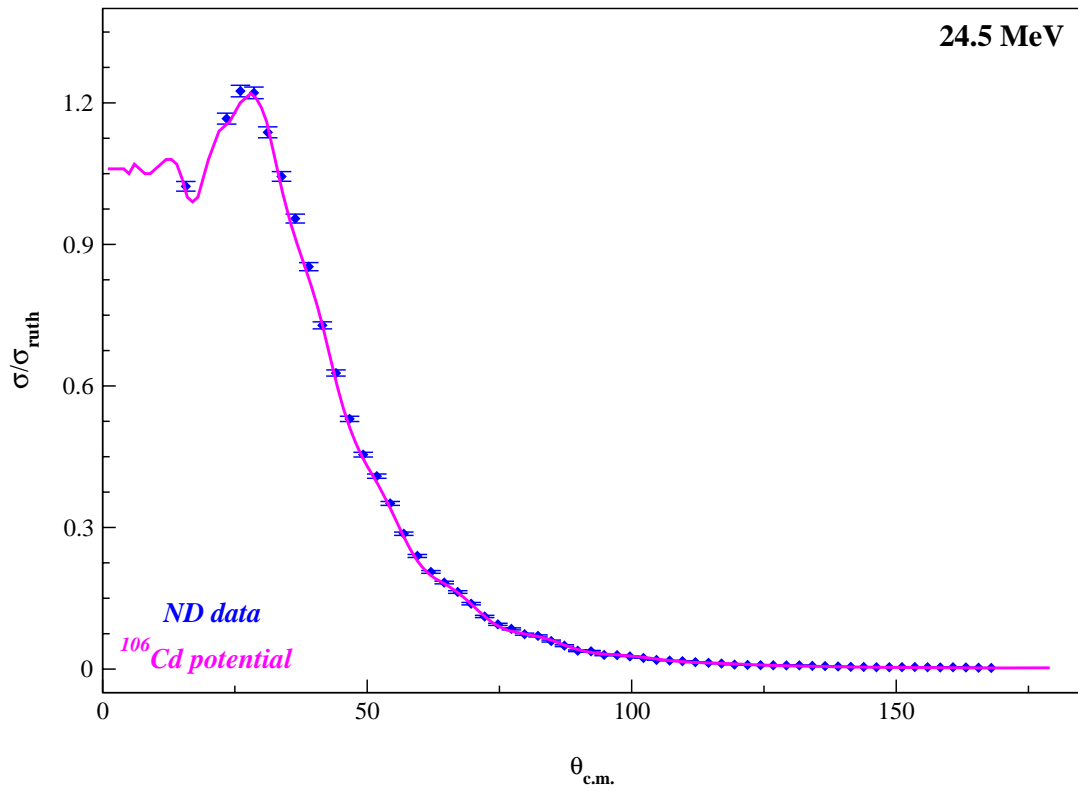
$^{106}\text{Cd}(\alpha,\alpha)^{106}\text{Cd}$

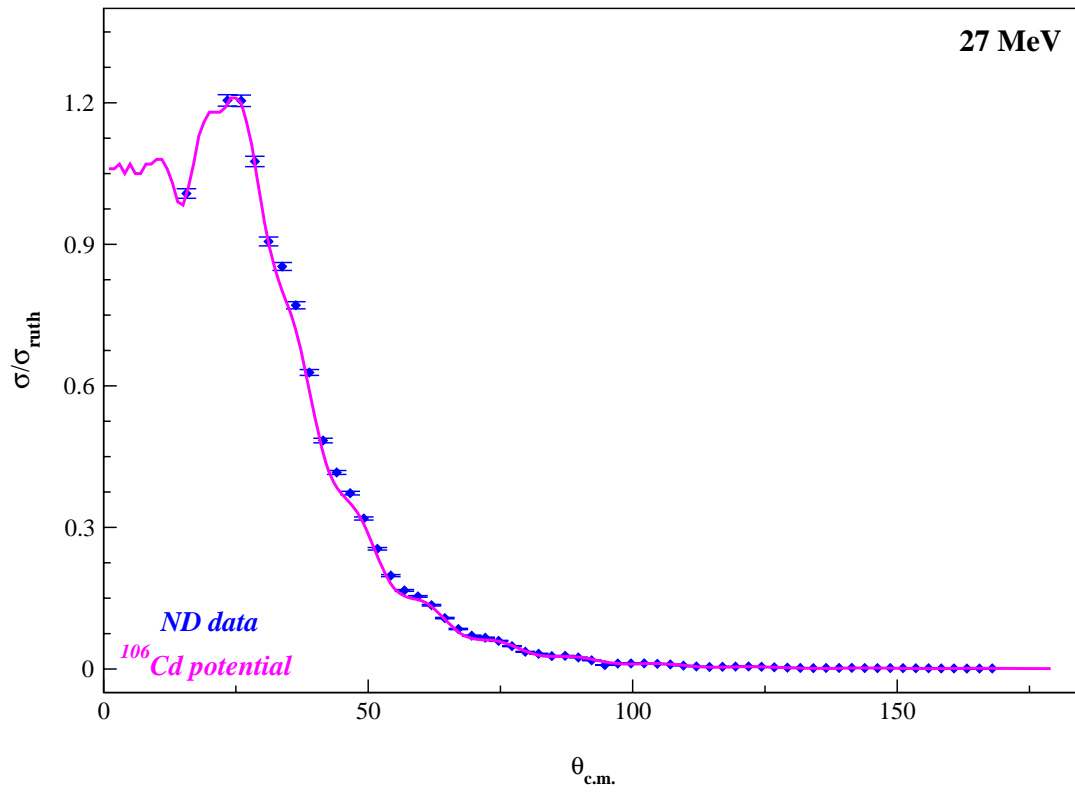
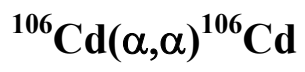


$^{106}\text{Cd}(\alpha,\alpha)^{106}\text{Cd}$

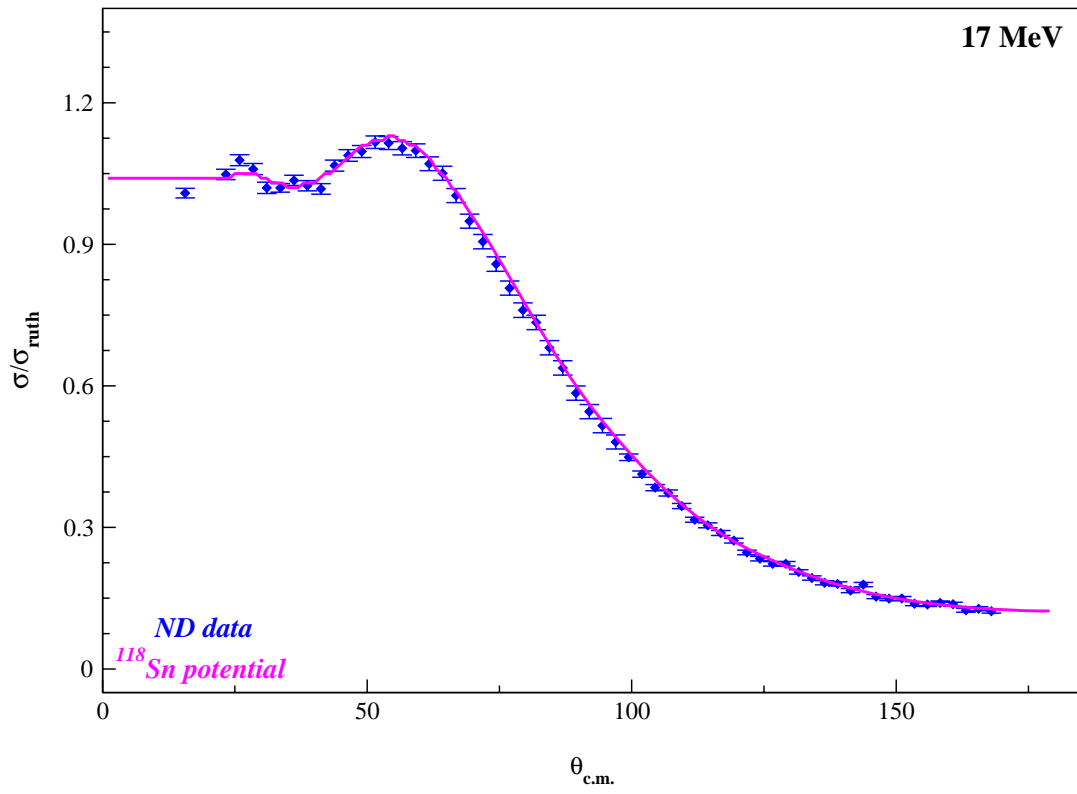


$^{106}\text{Cd}(\alpha,\alpha)^{106}\text{Cd}$

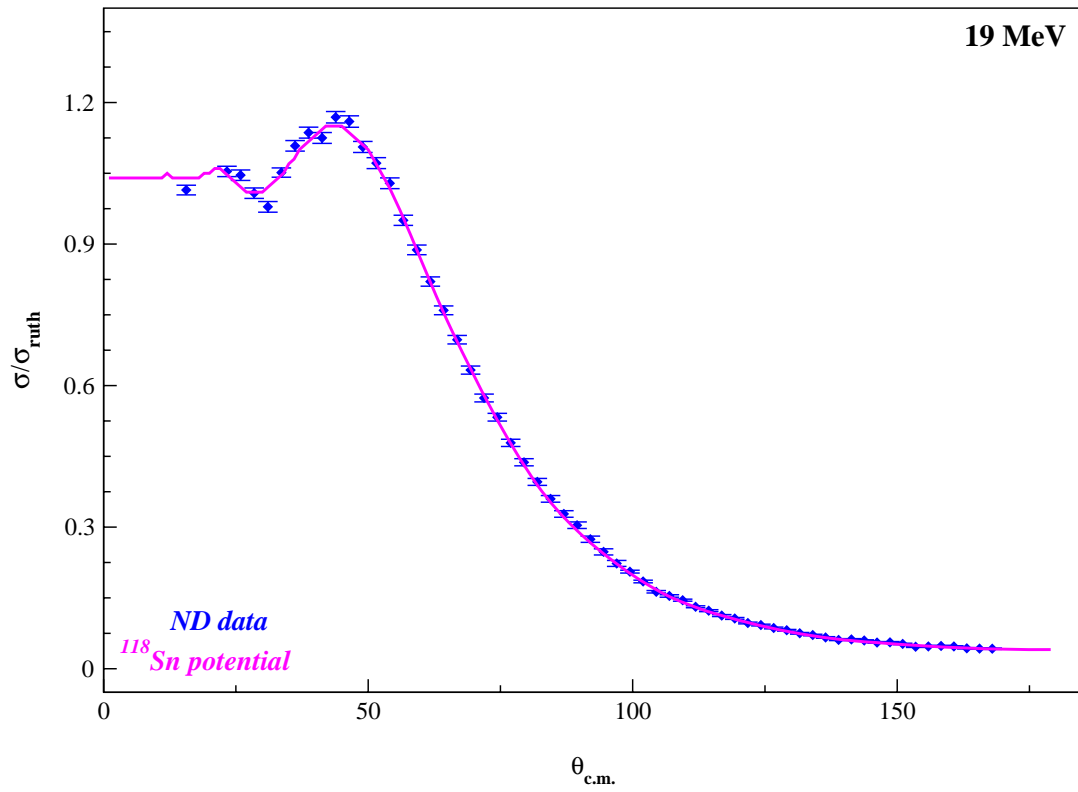




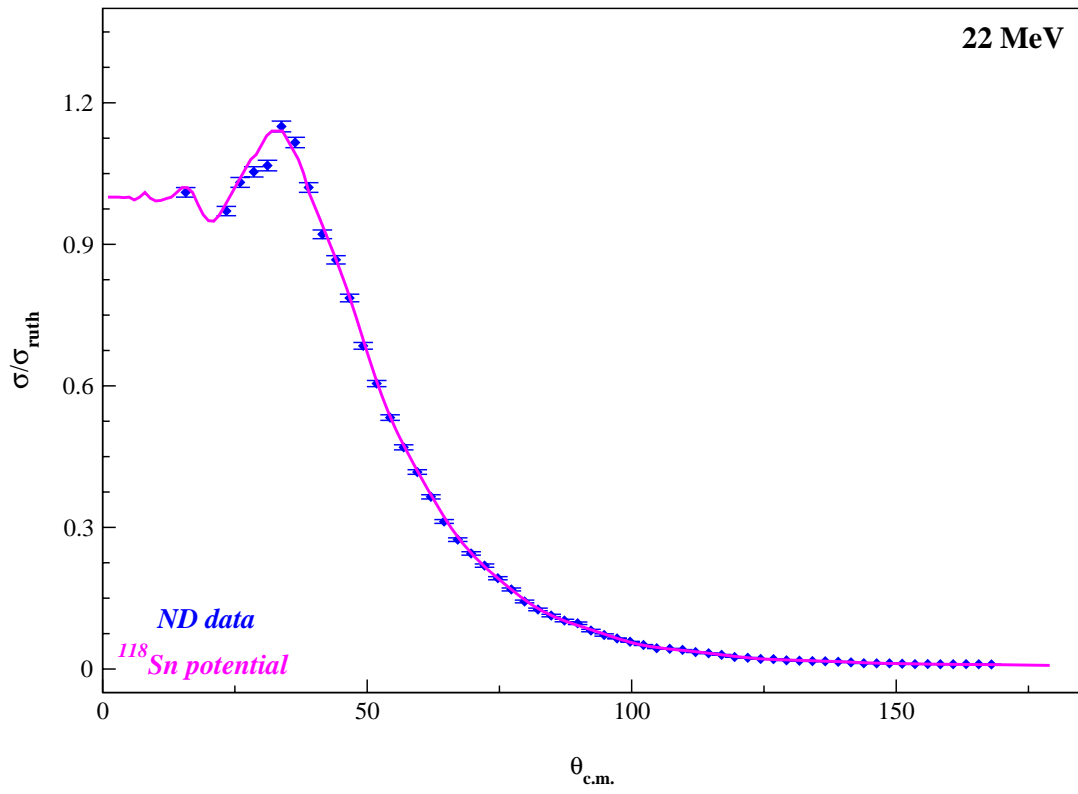
$^{118}\text{Sn}(\alpha,\alpha)^{118}\text{Sn}$



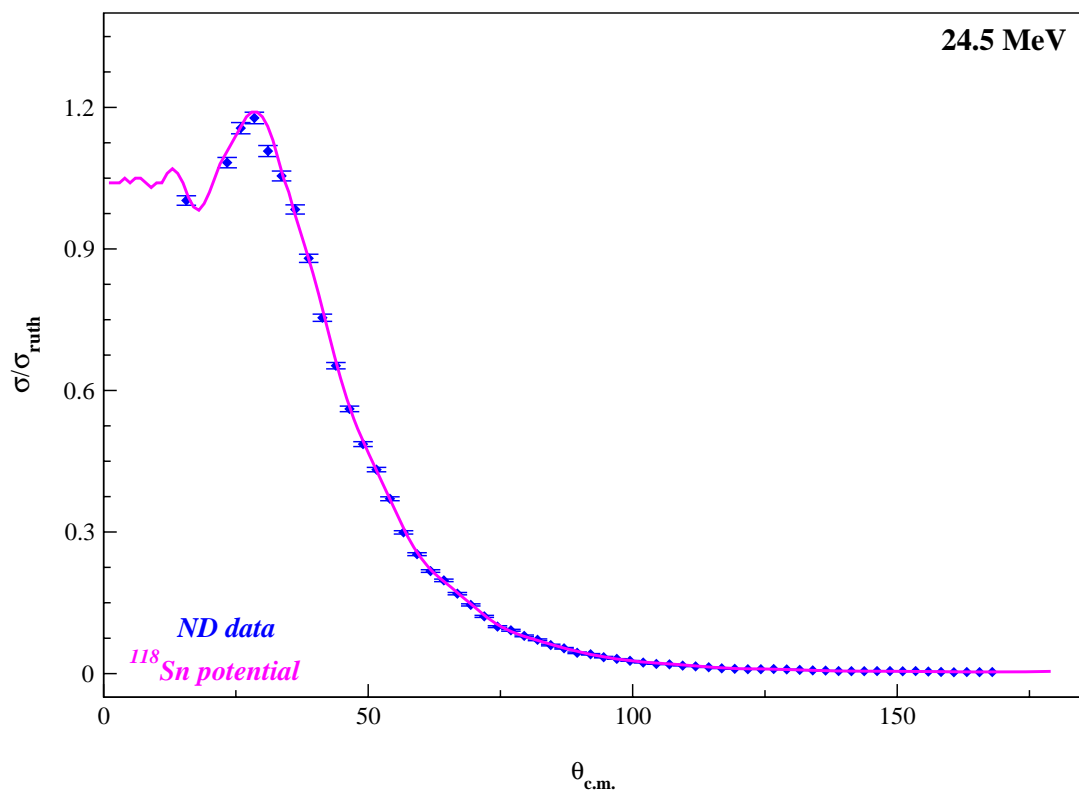
$^{118}\text{Sn}(\alpha,\alpha)^{118}\text{Sn}$



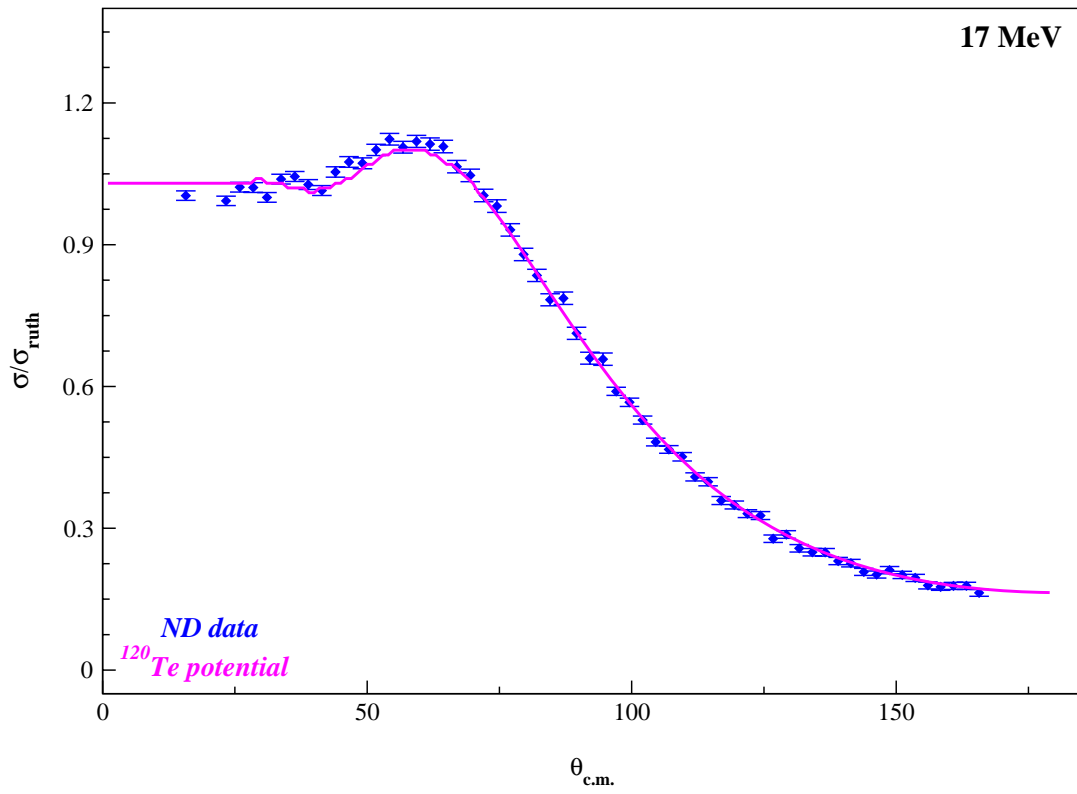
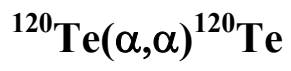
$^{118}\text{Sn}(\alpha,\alpha)^{118}\text{Sn}$



$^{118}\text{Sn}(\alpha,\alpha)^{118}\text{Sn}$



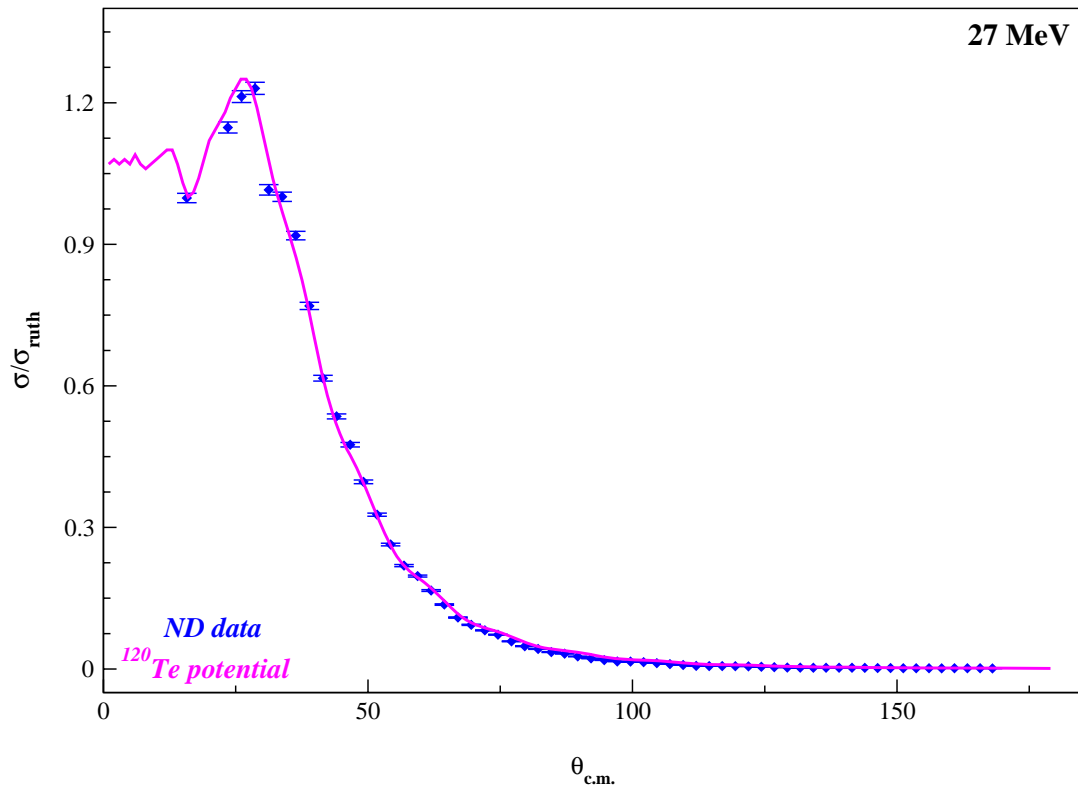
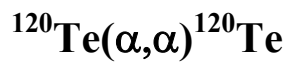




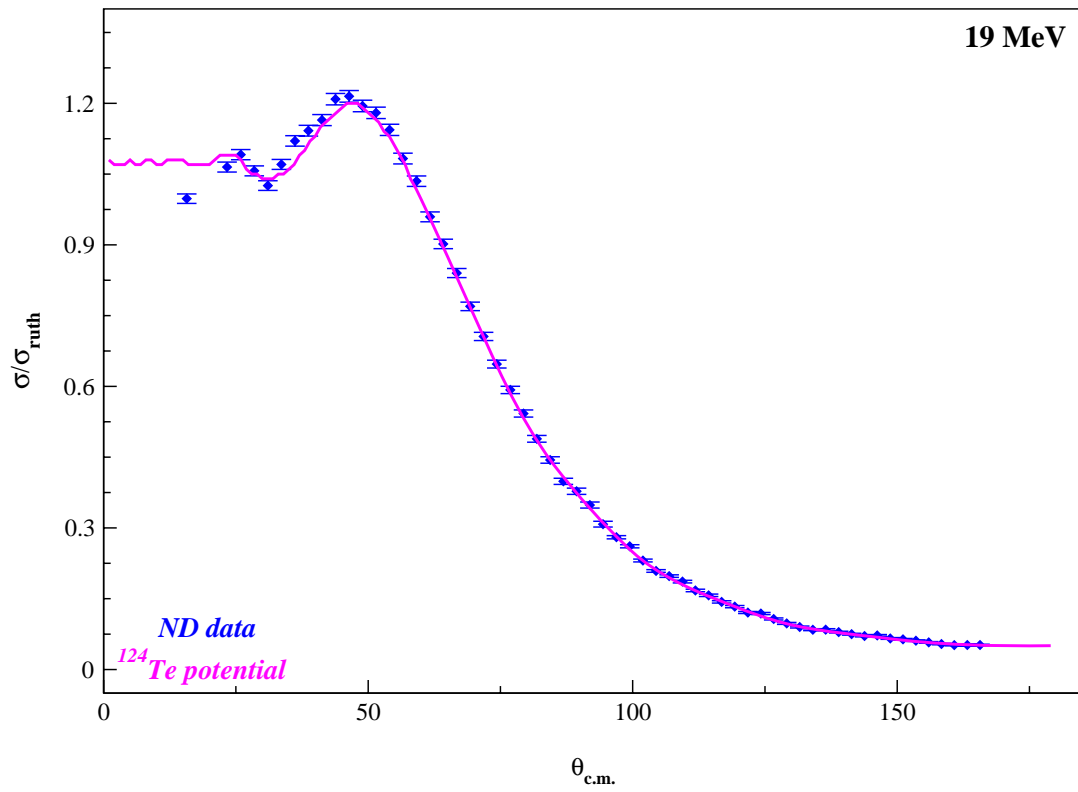
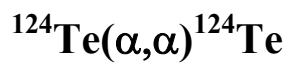


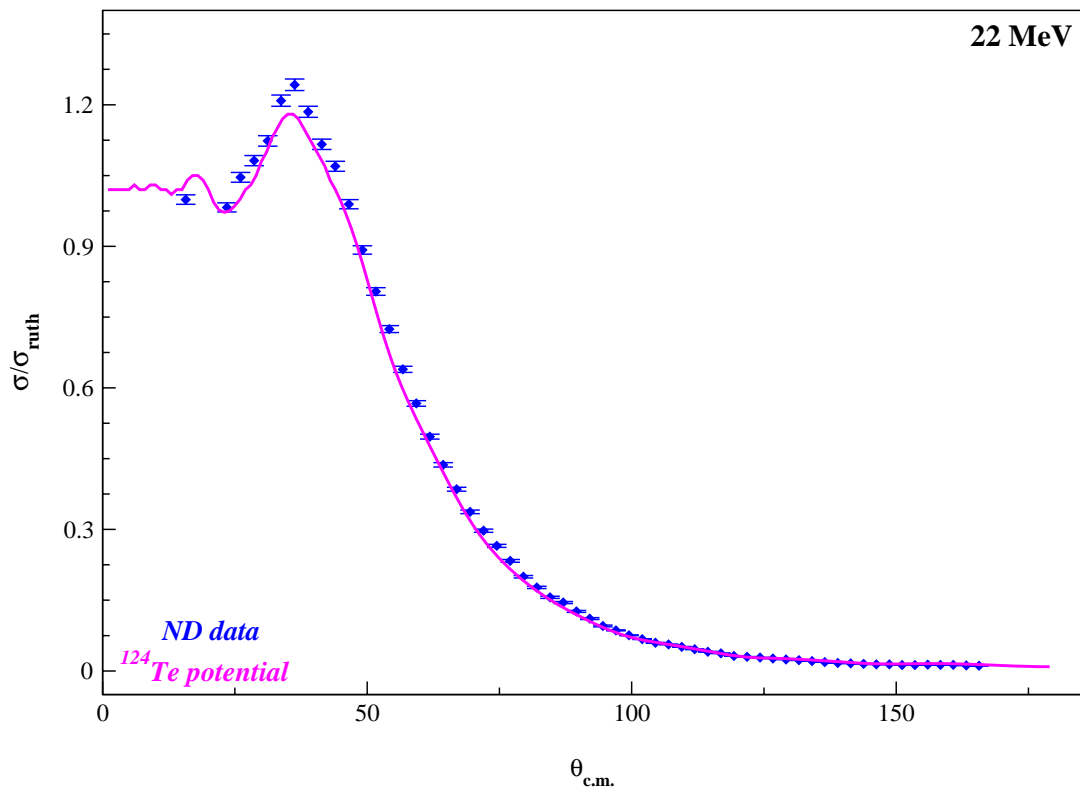
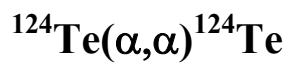


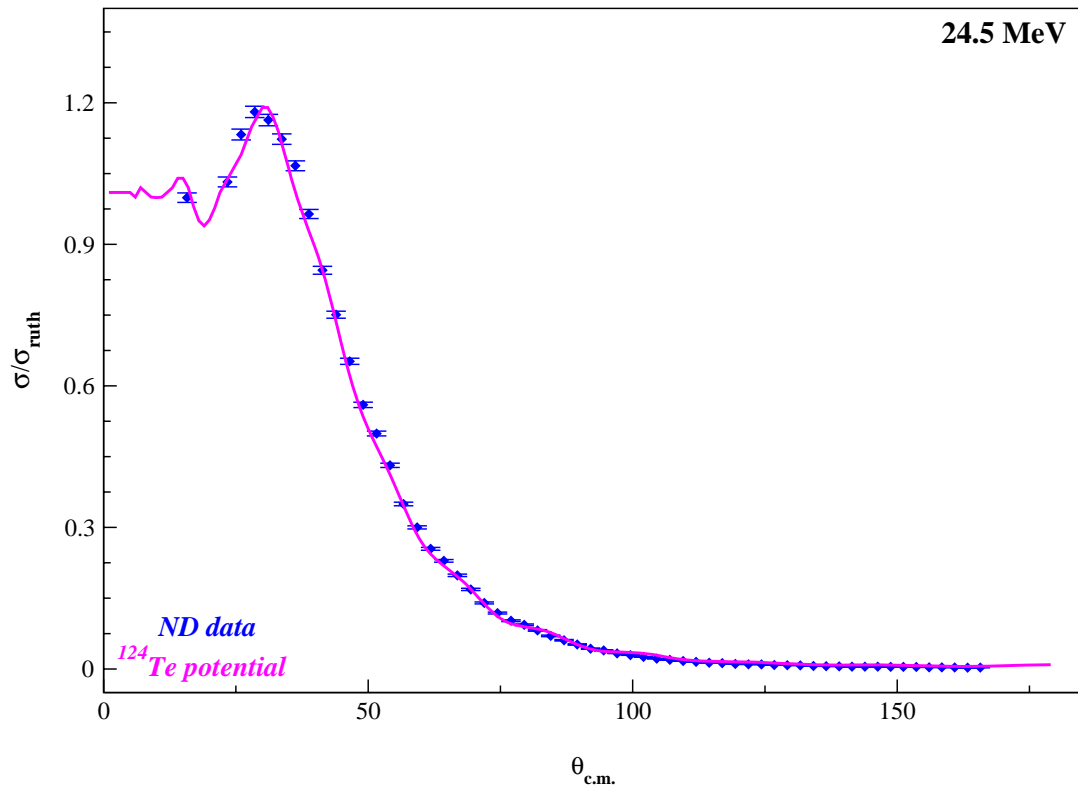
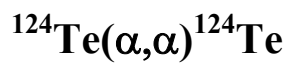




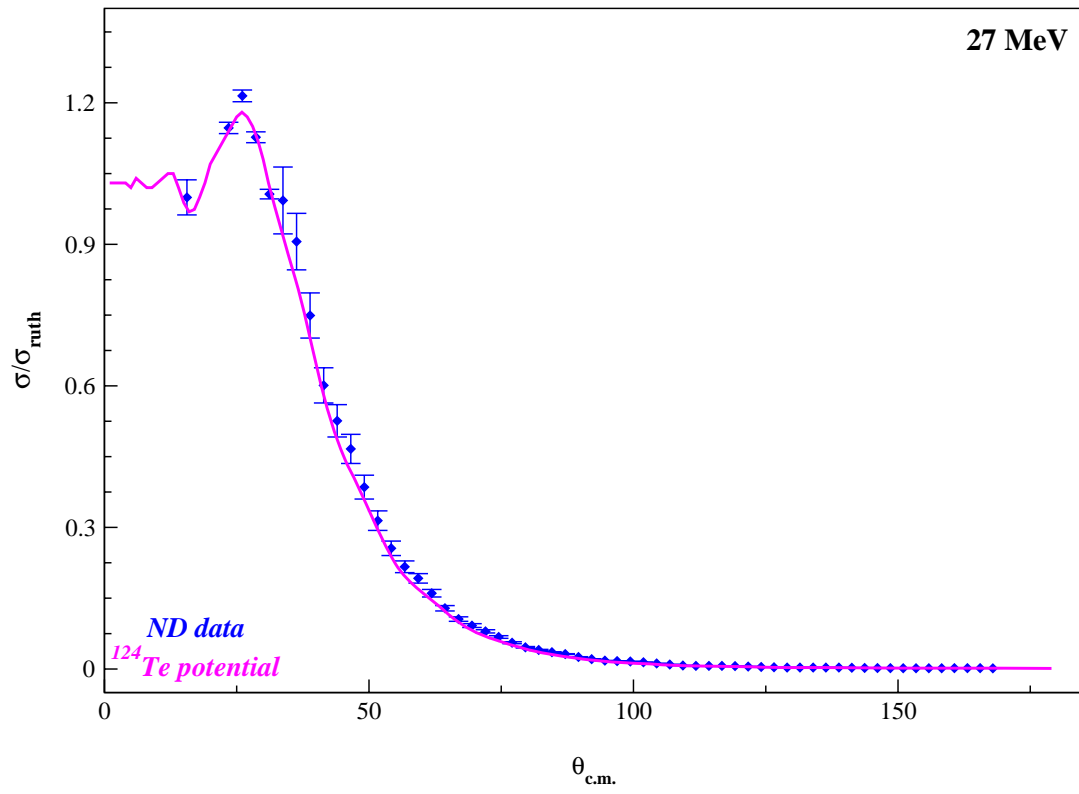


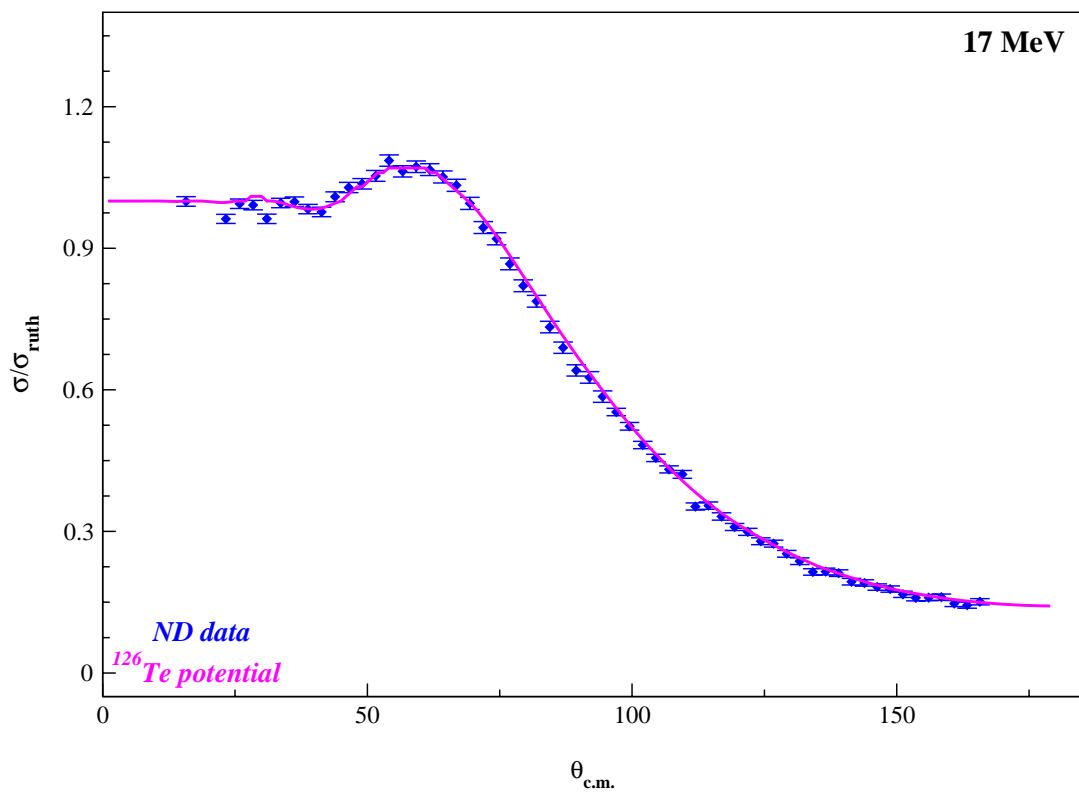
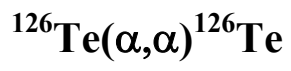


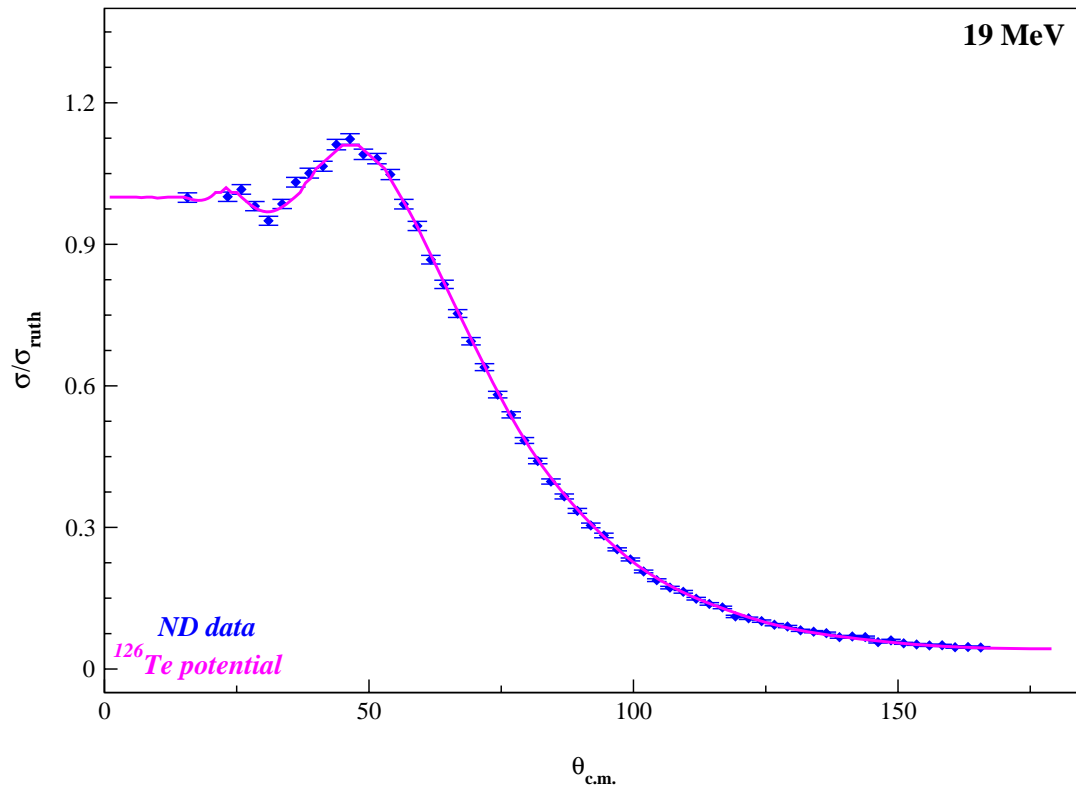
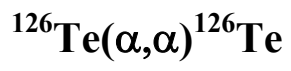




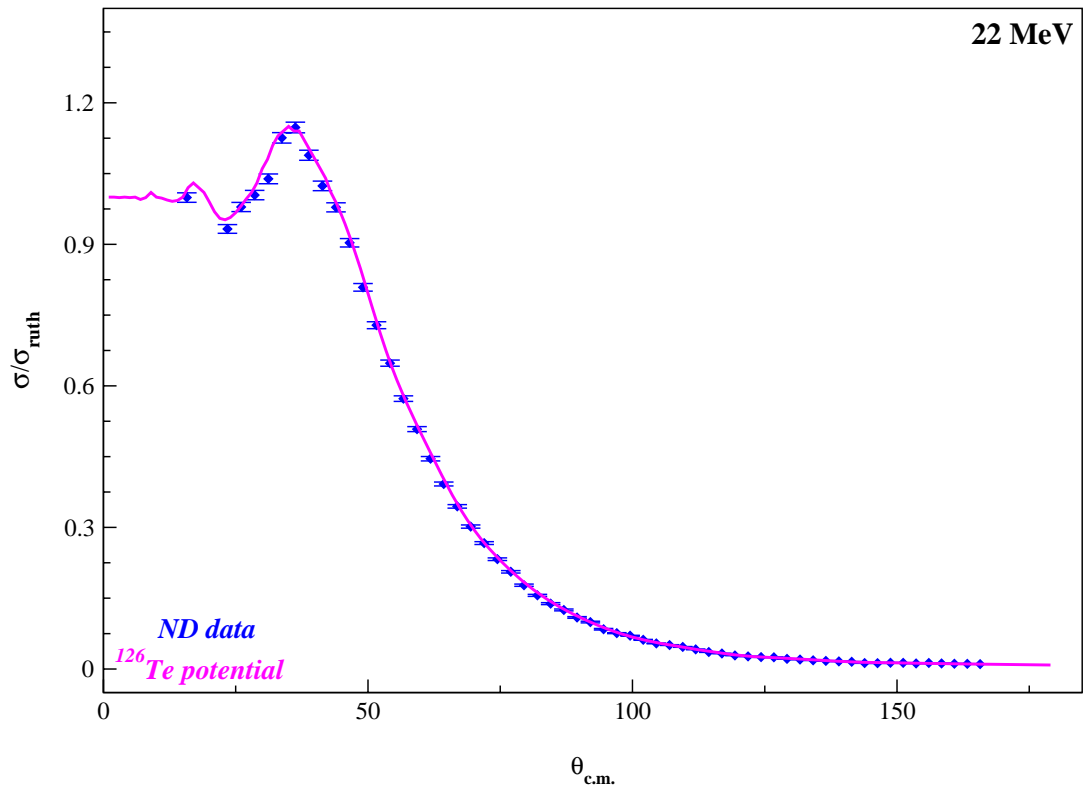
$^{124}\text{Te}(\alpha,\alpha)^{124}\text{Te}$



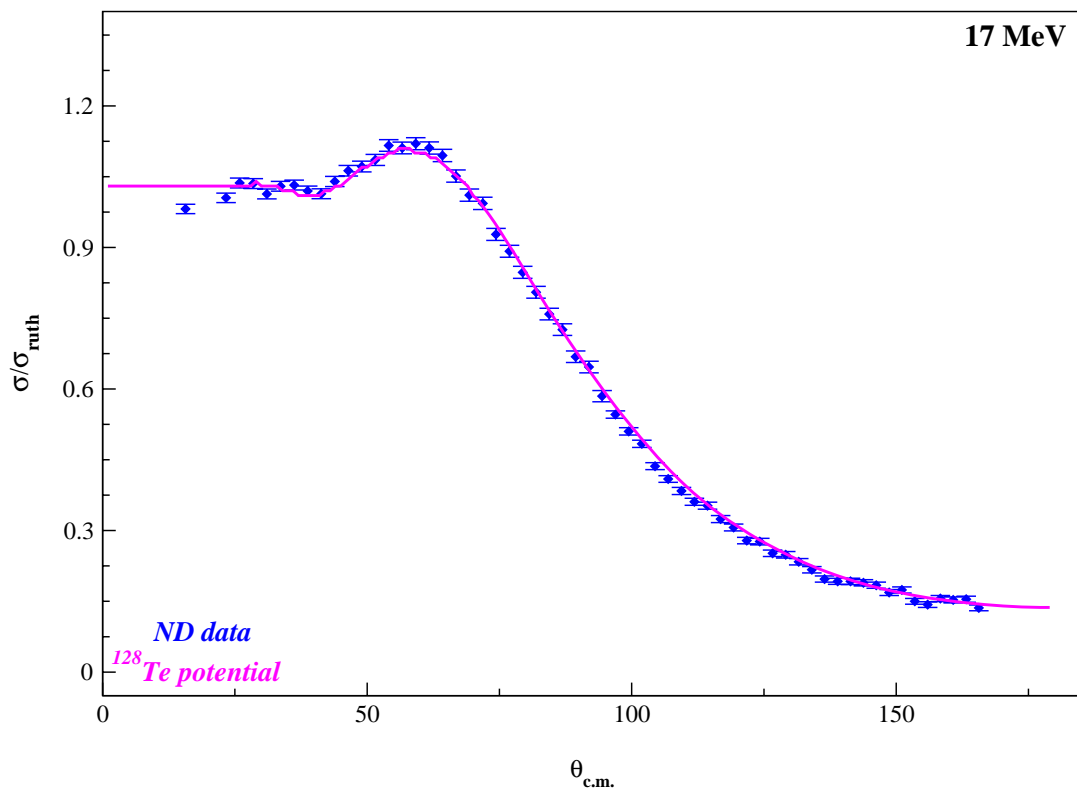




$^{126}\text{Te}(\alpha,\alpha)^{126}\text{Te}$



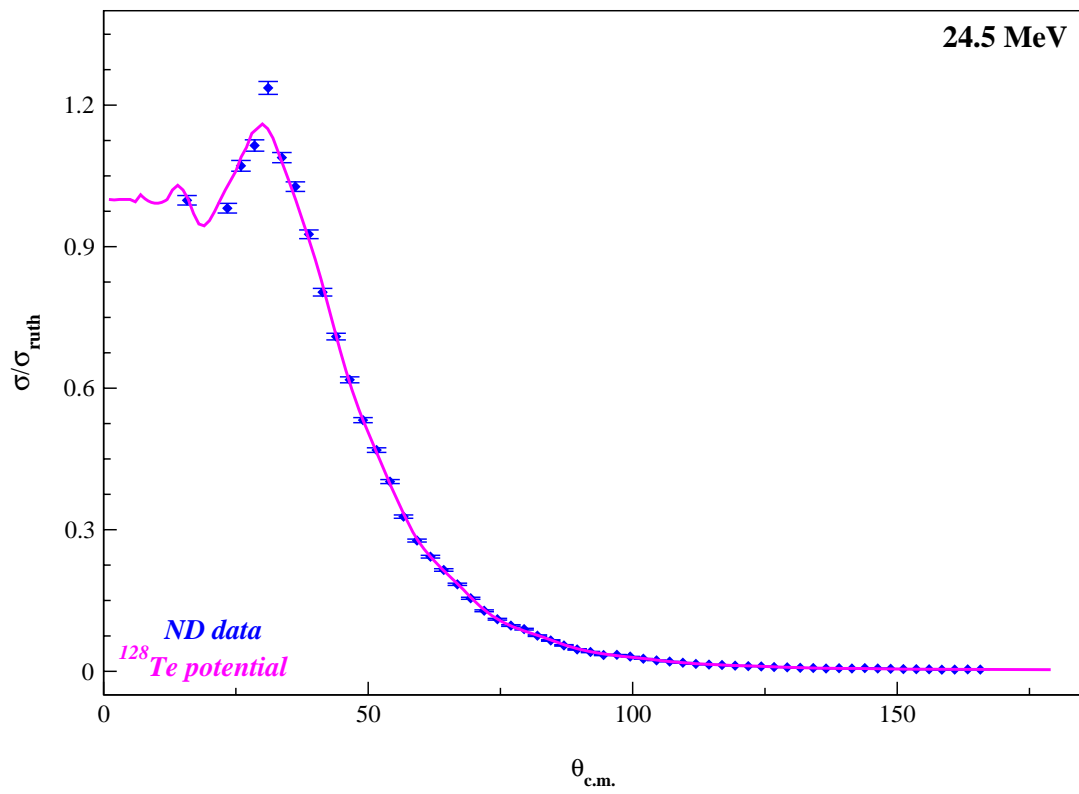
$^{128}\text{Te}(\alpha,\alpha)^{128}\text{Te}$



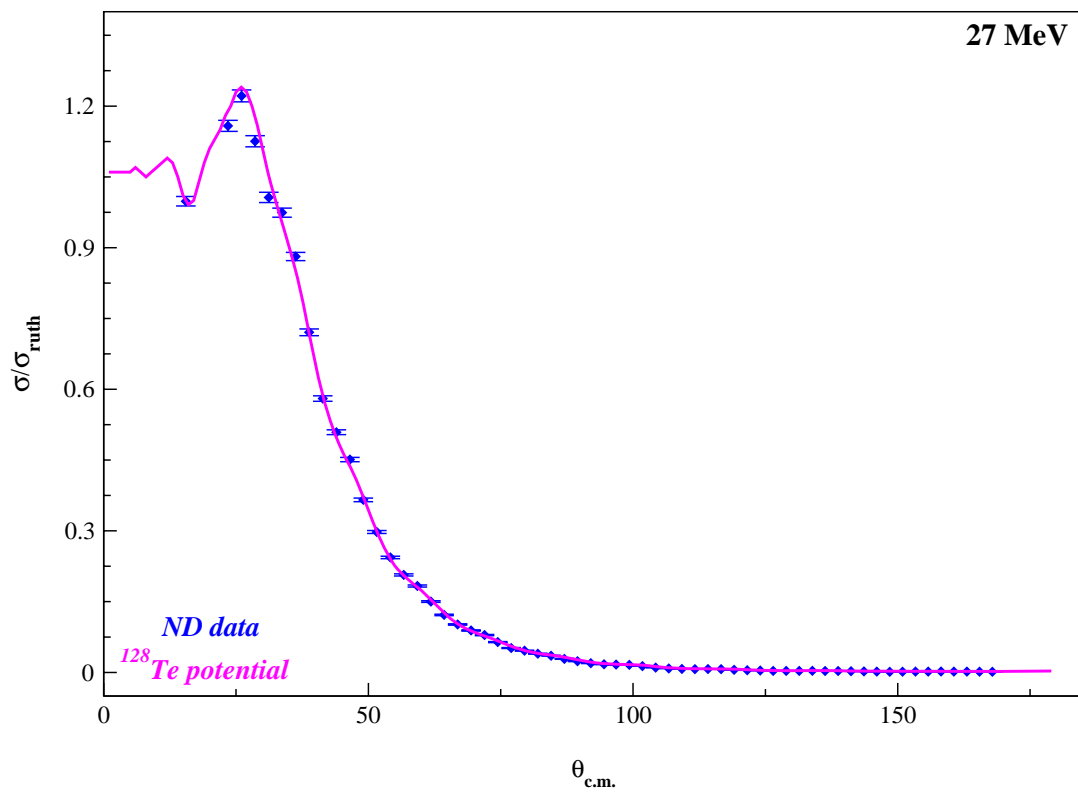


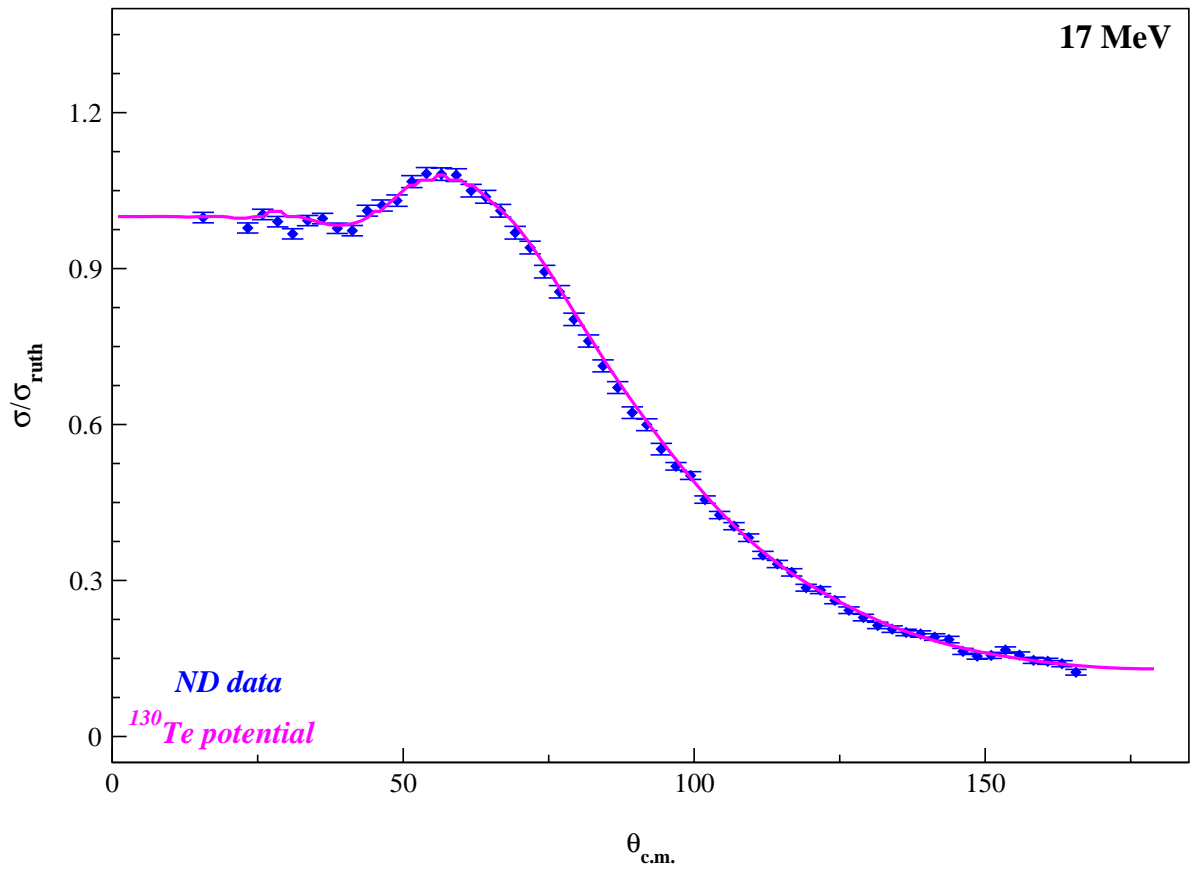
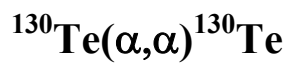


$^{128}\text{Te}(\alpha,\alpha)^{128}\text{Te}$

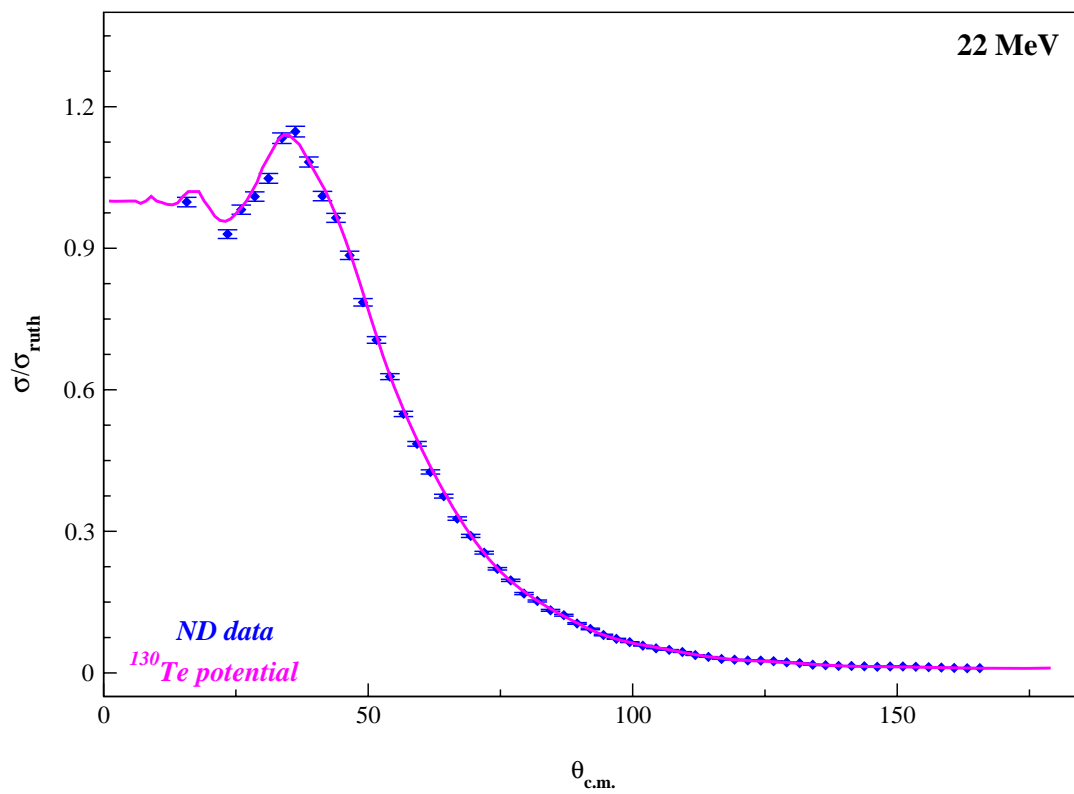
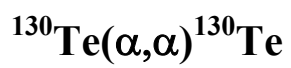


$^{128}\text{Te}(\alpha,\alpha)^{128}\text{Te}$











## REFERENCES

- [1] E. Burbidge, G. Burbidge, W. Fowler, F. Hoyle, *Rev. Mod. Phys.* 29 (1957) 547.
- [2] A. Cameron, Report CRL-41, A.E.C.L. Chalk River, Canada (1957).
- [3] D.D. Clayton, *Principles of Stellar Evolution and Nucleosynthesis*, University of Chicago Press (1984).
- [4] D. Arnett, *Supernovae and Nucleosynthesis*, Princeton University Press (1996).
- [5] C Rolfs, W. Rodney, *Cauldrons in the Cosmos*, University of Chicago Press (1988).
- [6] F. Käppeler, H. Beer, K. Wisshak, *Rep. Prog. Phys.* 52 (1989) 945.
- [7] F. Käppeler, *Prog. Part. Nucl. Phys.* 43 (1999) 419.
- [8] R.D. Hoffman, S.E. Woosley, and T.A. Weaver, *Astrophys. J.* 549, (2001) 1085.
- [9] V. Costa, M. Rayet, R.A. Zappalà, and M. Arnould, *Astron. Astrophys.* 358, (2000) L67.
- [10] Daniel Galaviz Redondo, PhD thesis, Technischen Universität Darmstadt (2004).
- [11] H. Schatz, A. Aprahamian, V. Barnard, L. Bildsten, A. Cumming, M. Ouellette, T. Rauscher, F.-K. Thielemann, M. Wiescher, *Phys. Rev. Letters* 86 (2001) 3471.
- [12] E Anders, N. Grevesse, *Geochim. Cosmochim. Acta* 53 (1989) 197.
- [13] M. Arnould, S. Goriely, *Phys. Rep.* 384 (2003) 1.
- [14] S.E. Woosley, D.H. Hartmann, R.D. Hoffman, W.Haxton, *Astrophys.J.* 356 (1990) 272.
- [15] M.Rayet, N.Prantzos, M.Arnould, *Astron. Astroph.* 227 (1990) 271.
- [16] N.Prantzos, M.Hashimoto, M.Rayet, M.Arnould, *Astron. Astroph.* 238 (1990) 455.
- [17] M. Wiescher, *private communication*, 2006.
- [18] Christian Iliadis, *Nuclear Physics of Stars*, Wiley-VCH (2007).
- [19] W. Rapp, J. Görres, M. Wiescher, H. Schatz, F. Käppeler, *Astrophys. J.* 653, (2006) 474.

- [20] T. Rauscher, A.Heger, R.D. Hoffman, S.E. Woosley, *Astrophys. J.* 576 (2002) 323.
- [21] S.Fujimoto, M.Hashimoto, O.Koike, K.Arai, R.Matsuba, *Astrophys. J.* 585 (2003) 418.
- [22] W.M. Howard, B.S. Meyer, S.E. Woosley, *Astrophys. J.* 373 (1991) 5.
- [23] T. Rauscher, F.-K. Thielemann, *ADNDT* 75 (2000) 1.
- [24] H. Schatz, A.Aprahamian, J. Görres, M. Wiescher, T. Rauscher, J.F. Rembges, F.-K. Thielemann, B. Pfeiffer, P. Möller, K.-L. Kratz, H. Herndl, B.A. Brown, H. Rebel, *Physics Reports* 294 (1998) 167.
- [25] T. Rauscher, A. Heger, R.D. Hoffman, S.E. Woosley, *Astrophys. J.* 576 (2002) 323.
- [26] D.G. Sargood, *Phys. Rep.* 93 (1982) 61.
- [27] J. Holmes, S.Woosley, W.Fowler, and B.Zimmerman, *ADNDT* 22, (1978) 371.
- [28] F.-K. Thielemann, M.Arnould, and J.W. Truran, in *Advances in Nuclear Astrophysics*, edited by E.Vangioni-Flam et al. (Editions Frontière, Gif sur Yvette, 1987), p. 525
- [29] J.J. Cowan, F.-K. Thielemann, and J.W. Truran, *Phys. Rep.* 208, (1991) 267.
- [30] P. Descouvemont, T. Rauscher, *Nucl. Phys.* A777 (2006), 137.
- [31] T. Rauscher and F.-K. Thielemann, in *Stellar Evolution, Stellar Explosions and Galactic Chemical Evolution*, edited by A. Mezzacappa (IOP, Bristol, 1998), p. 519.
- [32] E. Somorjai, Zs. Fülöp, A.Z. Kiss, C.E. Rolfs, H.P. Trautvetter, U.Greife, M. Junker, S.Goriely, M. Arnould, M. Rayet, T. Rauscher, H.Oberhummer, *Astron. Astroph.* 333 (1998) 1112.
- [33] J.M. Blatt and V. Weiskopf, *Theoretical Nuclear Physics*, Wiley and Sons (1952).
- [34] W. Hauser, H.Feshbach, *Phys. Rev.* 87 (1952) 366.
- [35] P. Mohr, T.Rauscher, H.Oberhummer, Z.Máté, Z.Fülöp, E.Somorjai, M.Jaeger, G.Staudt, *Phys. Rev. C* 55 (1997) 1523.
- [36] Zs. Fülöp, G.Gyürky, Z.Máté, E.Somorjai, L.Zolnai, D.Galaviz, M.Babilon, P.Mohr, A.Zilges, T.Rauscher, H.Oberhummer, G.Staudt, *Phys. Rev. C* 64 (2001) 065805.

- [37] G.G. Kiss, Gy. Gyürky, Zs. Fülöp, E. Somorjai, D.Galaviz, A. Kretschmer, K. Sonnabend, A. Zilges, P. Mohr, M. Avrigeanu, J.Phys. G: Nucl Part. Phys 35 (2008) 014037.
- [38] J.B.A. England, S.Baird, D.H. Newton, T. Picazo, E.C. Pollacco, G.J. Pyle, P.M. Rolph, J. Alabau, E. Casal, A. Garcia, Nucl. Phys. A388 (1982) 573.
- [39] D. Galaviz, Zs. Fülöp, Gy. Gyürky, Z. Máté, P. Mohr, T. Rauscher, E. Somorjai, A. Zilges Phys Rev. C71 (2005) 065802.
- [40] F. Michel and R. Wanderpoorten, Phys. Rev. C16, (1977) 142.
- [41] H. Abele and G. Staudt, Phys. Rev. C47, (1993) 742.
- [42] B. Buck, A.C. Merchant, and S.M. Perez, Phys. Rev. C51, (1995) 559.
- [43] P. Mohr, Phys. Rev. C61 (2000) 045802.
- [44] E.B. Shera, M.V.Hoehn, G.Fricke, G.Mallot, Phys. Rev. C39, (1989) 195.
- [45] H. de Vries, C.W. de Jager, C. de Vries, At. Data Nucl. Data Tables 36 (1987) 495.
- [46] G.R. Satchler, W.G. Love, Phys. Rep. 55 (1979) 183.
- [47] A.M. Kobos, B.A. Brown, P.E. Hodgson, G.R. Satchler, A. Budzanowski, Nucl. Phys. A 284 (1977) 399.
- [48] G. Bertsch, J.Borysowicz, H.McManus, W.G. Love, Nucl. Phys. A 284 (1977) 399.
- [49] A.M. Kobos, B.A. Brown, P.E. Hodgson, G.R. Satchler, A.Budzanowski, Nucl. Phys. A384 (1982) 65.
- [50] U. Atzrott, P.Mohr, H.Abele, C.Hillenmayer, G.Staudt, Phys. Rev. C53 (1996) 1336.
- [51] P. Mohr, T.Rauscher, H.Oberhammer, Z.Máté, Zs. Fülöp, E. Somorjai, M. Jaeger,G. Staudt, Phys. Rev. C55 (1997) 1523.
- [52] P. Mohr, *Messung und Analyse von Einfangreaktionen an leichten Kernen bei thermonuklearen Energien*, Dissertation, Eberhard-Karls-Universität zu Tübingen (1995).
- [53] Code DFOLD. Universität Tübingen, unpublished (1989).
- [54] G.R. Satchler, *Introduction to Nuclear Reactions*, The Macmillan Press LTD (1990).

- [55] K. Vogt, P. Mohr, M. Babilon, J. Enders, T. Hartmann, C. Hutter, T. Rauscher, S. Volz, and A. Zilges, *Phys. Rev. C* 63, (2001) 055802.
- [56] P. Mohr, *AIP Conf. Proc.* 704, (2004) 532.
- [57] H. Utsunomiya, P. Mohr, A. Zilges, M. Rayet, *Nucl. Phys. A* 777 (2006) 17.
- [58] G.G. Kiss, Gy. Gyürky, Z. Elekes, Zs. Fülöp, E. Somorjai, T. Rauscher, M. Wiescher, *Phys. Rev. C* 76 (2007) 055807.
- [59] T. Sauter, F. Käppeler, *Phys. Rev. C* 55 (1997) 6.
- [60] J. Bork, H. Schatz, F. Käppeler, T. Rauscher, *Phys. Rev. C* 58 (1998) 524.
- [61] Gy. Gyürky, E. Somorjai, Zs. Fülöp, S. Harissopulos, P. Demetriou, T. Rauscher, *Phys. Rev. C* 64 (2001) 065803.
- [62] Gy. Gyürky, G.G. Kiss, Z. Elekes, Zs. Fülöp, E. Somorjai, T. Rauscher, *J. Phys. G: Nucl. Part. Phys.* 34 (2007) 817.
- [63] T. Rauscher, *Phys. Rev. C* 73 (2006) 015804.
- [64] Gy. Gyürky, G.G. Kiss, Z. Elekes, Zs. Fülöp, E. Somorjai, A. Palumbo, J. Görres, H.Y. Lee, W. Rapp, M. Wiescher, N. Özkan, R.T. Guray, G. Efe, T. Rauscher, *Phys. Rev. C* 74, (2006) 025805.
- [65] N. Özkan, G. Efe, R.T. Guray, A. Palumbo, J. Görres, H.Y. Lee, L.O. Lamm, W. Rapp, E. Stech, M. Wiescher, Gy. Gyürky, Zs. Fülöp, E. Somorjai, *Phys. Rev. C* 75, (2007) 025801.
- [66] R.T. Guray, N. Özkan, C. Yalçun, A. Palumbo, R. deBoer, J. Görres, P.J. LeBlanc, S. O'Brien, E. Strandberg, W.P. Tan, M. Wiescher, Zs. Fülöp, E. Somorjai, H.Y. Lee, J.P. Greene, *Phys. Rev. C*, *in preparation*.
- [67] S. Dababneh, N. Patronis, P. A. Assimakopoulos, J. Görres, M. Heil, F. Käppeler, D. Karamanis, S. O'Brien, R. Reifarh, *NIMA* 517, (2004) 230.
- [68] Hye Young Lee, PhD thesis, University of Notre Dame (2007).
- [69] K. Debertin, R.G. Helmer, *Gamma- and X-Ray Spectrometry with Semiconductor Detectors*, Elsevier Science Publishing Company, Inc., 1988.
- [70] F.J. Schima, D.D. Hoppes, *Int. J. Appl. Radiat. Isot.* 38 (1983) 1109.
- [71] J. Görres, *private communication*, 2005.

- [72] Gy. Gyürky, Z. Elekes, Zs. Fülöp, G. Kiss, E. Somorjai, A. Palumbo, M. Wiescher, Phys. Rev. C 71, (2005) 057302.
- [73] D. De Frenne and E. Jacobs, Nucl. Data Sheets 89, (2000), 481.
- [74] J. Blachot, Nucl. Data Sheets 107, (2006) 355.
- [75] <http://www.nndc.bnl.gov/nudat2/>
- [76] J.F. Ziegler. SRIM-2003. NIM B., 1027, (2004), 219.
- [77] T. Rauscher, F.-K. Thielemann, ADNDT 79 (2001) 47.
- [78] T. Rauscher, F.-K. Thielemann, ADNDT 75 (2000) 1.
- [79] NON-SMOKER (standard settings), <http://nucastro.org/nonsmoker.html>.
- [80] L.C. Chamon, B.V. Carlson, L.R. Gasques, D. Pereira, C. De Conti, M.A.G. Alvarez, M.S. Hussein, M.A. Cândido Ribeiro, E.S. Rossi, Jr., C.P. Silva, Phys. Rev. C 66, (2002) 014610.
- [81] G.G. Kiss, Zs. Fülöp, Gy. Gyürky, Z. Máté, E. Somorjai, D. Galaviz, A. Kretschmar, K. Sonnabend, A. Zilges, Eur. Phys. J. A 27, s01, (2006) 197.
- [82] J.P. Greene, G.E. Thomas, NIM A 282 (1989) 71.
- [83] J.P. Greene, A. Palumbo, W. Tan, J. Görres, M. Wiescher, NIM A 590 (2008) 76.
- [84] S. Raman, C.H. Malarkey, W.T. Milner, C. W. Nestor, J.R. Stelson, P.H. Stelson ADNDT, 36 (1987) 1.
- [85] J. Zhang, Y. Sun, M. Guidry, L.L. Riedinger, G.A. Lalazissus, Phys. Rev. C 58 (1998) R2663.
- [86] L. McFadden and G. R. Satchler, Nucl. Phys. 84, (1966) 177.
- [87] V. Avrigeanu, P.E. Hodgson, M. Avrigeanu, Phys. Rev. C 49 (1994) 2136.
- [88] M. Nolte, H. Machner, J. Bojowald, Phys. Rev. C 36 (1987) 1312.
- [89] M. Avrigeanu, W. von Oertzen, V. Avrigeanu, Nuclear Physics A 764 (2006) 246.
- [90] M. Avrigeanu, W. von Oertzen, A. J. M. Plomben, and V. Avrigeanu, Nucl. Phys. A723, (2003) 104.
- [91] C. Fröhlich, Diploma thesis, University of Basel, Switzerland, (2002).
- [92] T. Rauscher, Nucl. Phys. A719, (2003) 73c; A725, (2003) 295.

- [93] W. Rapp, *Der astrophysikalische p-Prozess: Experimente und Konsequenzen für die Häufigkeitsverteilung*, Dissertation, TH Karlsruhe (2003).
- [94] A. Kumar, S. Kailas, S. Rathi, K. Mahata, Nucl. Phys. A 776 (2006) 105.
- [95] P. Demetriou, C.Grama, S.Goriely, Nucl. Phys. A707 (2002) 253.
- [96] G. Kraft R.Koslek, R.Mundhenke, J.Winter, Nucl Phys. A118 (1968) 25.
- [97] W. Rapp, M.Heil, D. Hentschel, F. Käppeler, R.Reifarth, H.J. Brede, H. Klein, T.Rauscher, Phys. Rev. C 66 (2002) 015803.
- [98] R.L. Hahn, Phys. Rev. 137 (1965) B 1491.
- [99] Zs. Fülöp, A.Z. Kiss, E. Somorjai, C.E. Rolfs, H.P. Trautvetter, T.Rauscher, H. Oberhummer, Z.Phys. A 355 (1996) 203.
- [100] C.P. Silva, M.A.G. Alvarez, L.C. Chamon, D. Pereira, M.N. Rao, E. S. Rossi Jr., L.R. Gasques, M.A.E. Santo, R.M. Anjos, J. Lubian, P.R.S. Gomes, C. Muri, B.V. Carlson, S. Kailas, A. Chatterjee, P. Singh, A. Shrivastava, K. Mahata, S. Santra, Nucl. Phys. A 679 (2001) 287.
- [101] S. Wong, *Introductory Nuclear Physics*, Wiley-Interscience (1999).
- [102] Code A0. Universität Tübingen, unpublished (1989).
- [103] P. Mohr, *private communication*, 2008.
- [104] T. Rauscher, *Prediction of nuclear reaction rates for astrophysics*, arXiv:nuclth/0007070 v1 28Jul00, Departement für Physik und Astronomie, Universität Basel (2000).
- [105] G.E. Brown and M.Rho, Nucl. Phys. A372, (1981) 397.
- [106] C. Grama and S. Goriely, *Nuclei in the Cosmos V* (Edition Frontières, Paris 1998) p.463.
- [107] T. Rauscher, *Proceedings of the IX Workshop on Nuclear Astrophysics* (1998).
- [108] T. Fleissbach, Nucl. Phys. A 315 (1979) 109.
- [109] N. Özkan, A.St.J. Murphy, R.N. Boyd, A.L. Cole, M. Famiano, R.T. Güray, M. Howard, L. Şahin, J.J. Zach, R. deHaan, J. Görres, M.C. Wiescher, M.S. Islam, T.Rauscher, Nucl. Phys. A 710 (2002) 469.
- [110] NON-SMOKER (custom  $\alpha$ -nucleus potential), <http://nucastro.org/websmoker.html>.
- [111] T. Rauscher, F.-K. Thielemann, ADNDT 88 (2004) 1.

[112] L.C. Chamon, G.P.A. Nobre, D. Pereira, E.S. Rossi, Jr., C.P. Silva, L.R. Gasques, B.V. Carlson, Phys. Rev. C 70 (2004) 014604.

[113] M. Blaauw, NIM A 332 (1993) 493.